UNIVERSIDAD COMPLUTENSE DE MADRID

FACULTAD DE CIENCIAS FÍSICAS

TESIS DOCTORAL

Interferometría de Intensidad y Pulsos Rápidos en Radio con MAGIC

Intensity Interferometry and Fast Radio Bursts with MAGIC

MEMORIA PARA OPTAR AL GRADO DE DOCTOR

PRESENTADA POR

Irene Jiménez Martínez

DIRECTORES

Juan Cortina Blanco
Carlos José Delgado Méndez
Tarek Hassan Collado

UNIVERSIDAD COMPLUTENSE DE MADRID

FACULTAD DE CIENCIAS FÍSICAS

TESIS DOCTORAL

Interferometría de Intensidad y Pulsos Rápidos en Radio con MAGIC
Intensity Interferometry and Fast Radio Bursts with MAGIC

MEMORIA PARA OPTAR AL GRADO DE DOCTORA

PRESENTADA POR

Irene Jiménez Martínez

DIRECTORES

Juan Cortina Blanco
Carlos José Delgado Méndez
Tarek Hassan Collado

Agradecimientos

No puedo dar por terminada esta tesis sin antes agradecer a todas las personas que directa o indirectamente me han ayudado a realizarla durante estos años:

A mis padres y a mi hermano, que tanto me han apoyado durante estos últimos cuatro años. Gracias por vuestros proyectos artísticos, por las palizas a las cartas, por los paseos con el perrillo, por los inventos culinarios y por mil cosas más. Sin vosotros no habría podido llegar tan lejos. Especial mención a nuestro perrillo, Alam, porque al acariciarle la barriga se curan todos los males.

A mi familia, pero especialmente a mi abuelo Eloy, que desde pequeña me inculcó su curiosidad insaciable por todo lo que le rodea. Ya sea en pintura, literatura, música, magia o ciencias, su sabiduría no conoce límites. Así como no conoce límites el cariño que demuestra a sus hijos y a sus nietos, y por el que estoy inmensamente agradecida.

A mi pareja, David, por estar siempre ahí, a cualquier hora del día o de la noche, de una forma u otra. Gracias por empujarme y animarme a terminar esta tesis cuando creí que no podía más y por demostrarme tu amor y cariño cuando más lo necesitaba. No creo que nunca termine de creerme la suerte que tengo.

A mi amigo de la infancia, David. Quién nos iba a decir que íbamos a cumplir nuestros sueños de ser doctores cuando nos pasábamos horas y horas hablando en nuestros bancos favoritos de Ávila, o por teléfono, o jugando a las consolas. Gracias por seguir siendo el mejor amigo que he tenido jamás. Te deseo toda la suerte del mundo para finalizar tu propia tesis, que como todo lo que haces, va a ser extraordinaria.

A mis amigos de infinitas tardes de videojuegos y rol, Carlos, Álvaro y Enrique. Es un gusto inmenso compartir con vosotros tantas historias y aventuras. Espero que compartamos muchas más, ya como doctores.

A mis directores de tesis. Gracias Carlos por encontrar un hueco para mí incluso cuando tenías montañas y montañas de trabajo, por enseñarme a ver el mundo en espacio de Fourier y por ser el mejor director de orquesta en Japón. Gracias Juan por presentarme

el maravilloso mundo de la interferometría de intensidad, por tus ‘tenemos que hablar’, por confiarme la corona de ‘scheduler oficial del reino’ y por las horas de discusiones fascinantes sobre la ciencia que vamos a hacer con nuestros datos. Gracias Tarek por todos los cientos de horas de explicaciones, ensayos y correcciones, por presentarme a los fast radio bursts, esos fenómenos fascinantes y misteriosos, y en general por tu infinita paciencia y dedicación a tus estudiantes. Nos sentimos muy afortunados. Los tres os habéis ocupado de velar por mi crecimiento como científica estos cuatro años, solo espero que estéis orgullosos del resultado.

Gracias también al resto de personas del grupo de gammas: Salvatore, Gustavo y Carlos. Por todas las reuniones de grupo en las que me habéis prestado vuestras orejas y vuestras ideas. Gracias en especial a María, cuya estancia fue corta pero dejó mucha huella. Echaré de menos nuestros cafés y nuestros correos urgentes.

A mis compañeros del CIEMAT, pasados y presentes. Empezando por los miembros del Despachito: Miguel Ángel, mi compañero de la Pecera desde el inicio de los tiempos. Gracias por las estratagemas malvadas y malignas, por los memes, por el profesor Layton, por ser un neutrino como yo y en general por ser el mejor compañero de despacho. Espero que bebas mucha agua y que te jubiles pronto. David, que ideas las mejores bromas y también las acabas sufriendo. Gracias por tus postales y por provocar situaciones sociales incómodas totalmente necesarias. Pepe, que no te gustan los agradecimientos pero aquí te va uno. Gracias por ser la banda sonora del Despachito, en vivo y en directo, por tus ‘this is very nice’ y por Alyssa. Juan, gracias por hacer de tu mesa un museo y por la pandemia de mandarinas podridas. Nicola, que has llegado hace nada y parece que lleves aquí años. Gracias por deleitarnos con los mejores dulces italianos. Carmen (¿quién es Carmen?), Molero, Mab, Martín, Héctor e Iker que ya hace tiempo que dejasteis el CIEMAT pero que no habéis sido olvidados. Gracias por enseñarme cómo sobrevivir a las ciematadas del CIEMAT. A los que estáis en la Becacueva, en Neutrinos, en el Inframundo y abajo: gracias a Oliver por tener tan buen sentido del humor y por tus rankings. Gracias a Elvira por aguantar a Oliver. Gracias a Dani por compartir con nosotros tus aficiones más frikis y tus logros de judo. Gracias a Lourdes por enseñaros a todos a no clicar en enlaces sospechosos que llegan por correo. Gracias a Jaime por comer a la velocidad de la luz. Gracias a Antonio por los legos de Pokémon que aún no he terminado de construir. Gracias a Beymar, donde quiera que estés. Gracias a Cecilia porque se puede hablar de cualquier cosa contigo. Gracias a Julia por ponernos los mejores problemas de mates y por enseñarnos cómo se pone acento sevillano. Gracias a Ludo por enseñarnos lo que es una pizza de verdad. Riega la piña, por favor. Gracias a Diego por descubrir el diegón y por sus historias totalmente verosímiles. Riega la piña tú, porque Ludo no lo va a hacer. Gracias a Iñaki por saberse el BOE entero y por hacer un registro de cada comida del CIEMAT. Gracias a Rodrigo por siempre decir lo que nadie se espera y por sus batidos ‘saludables’. Gracias a Sergio por ser la mejor persona del CIEMAT. Gracias a Laura por su arte tanto en la pintura como en la resolución de sudokus hiperdifíciles.

Gracias en especial a mis sucesores, los CTAcitos Yuan y Alejo, con los que he compartido tantas experiencias. Yuan, gracias por los momentos canónicos, por los directos de Nintendo, por los Kologs, por llevarte el kazoo a todas partes y por los karaokes épicos. Organizar contigo el (Menta)Poleo Cuántico ha sido una de las cosas más divertidas que

he hecho en mi vida. Gracias también a Ernesto, que se sacrificó por el resto. Alejo, gracias por los chistes de 'y eso también', por tus historias escalofriantes sobre amigos de tus amigos, por tu té con 'aroma' y por tus consejos de seguridad de escalada totalmente fiables. Sé que el schedule de interferometría se queda en buenas manos. Os deseo toda la suerte del mundo para terminar vuestras tesis, sé que ambas van ser excelentes.

Gracias a todos por las 'roturas del café' en las escaleras y en el aparcamiento, por los tea times, por el número 63, por los jerseys amarillos, por los Premios Radón y por todas las sapadas. Gracias por los grandes momentos que he compartido con vosotros estos años. Os voy a echar muchísimo de menos.

Finally, thank you to all the members of the MAGIC and LST collaborations with whom I have shared working groups, conferences and shifts. Special thanks to Lea, Jarred, Carolin and Joao. I will always remember our shifts together. Thank you for the recipes, the games of Cards Against Humanity, the DnD games on rainy nights, the movies and your delightful company during the long long nights up at the Roque.

Contents

Resumen

Los telescopios MAGIC situados en el Observatorio del Roque de los Muchachos en la isla de La Palma (España) llevan en operación justo 20 años en el momento de escritura de esta tesis. Esta tesis está dedicada a la explotación innovadora de estos telescopios como un interferómetro de intensidad para medir tamaños angulares estelares con precisión de milisegundos de arco en el azul; y a la búsqueda de las posibles contrapartidas de los transitorios llamados pulsos rápidos en radio o fast radio bursts (FRBs) en óptico y muy alta energía.

La estructura de la tesis se divide en tres grandes bloques:

- Introducción a la astronomía de rayos gamma: en este capítulo se detalla cómo se descubrieron los rayos gamma (0.1) y los rayos cósmicos (0.2), dando lugar al la física de astropartículas. También se presentan los diferentes procesos conocidos de producción (1.1), absorción (1.2) y aceleración (1.3) de rayos gamma. Dichos procesos servirán para explicar la emisión de rayos gamma en fuentes galácticas (2.1) y extragalácticas (2.2). Y esa emisión de rayos gamma será recogida por instrumentos en el espacio (3.1) y en tierra (3.2). Se hará especial hincapié en los telescopios MAGIC (3.3), con los que se han tomado los datos presentados en este trabajo.

- Interferometría de intensidad: en este capítulo se hablará del origen de la técnica de interferometría de intensidad, partiendo de la interferometría de amplitud (4.1). Se presentarán los fundamentos teóricos que la gobiernan (4.2) y algunos de los casos científicos que se han propuesto hasta la fecha (4.3). Se mostrará cómo se ha llevado a cabo la implementación de esta técnica en los telescopios MAGIC por medio de varias modificaciones mecánicas y de software (5.1), incluyendo el aprovechamiento de su Active Mirror Control (5.2) que permite seccionar los espejos para lograr diversas medidas. También se presentará cómo construí el catálogo oficial de estrellas (6.1) que he usado para programar (6.2) las observaciones durante casi dos años, acumulando más de 400 horas de observación. Se explicarán los diferentes pasos del análisis: la calibración del flujo de luz (7.1), la corrección temporal (7.2), la con-

volución con el tamaño de los espejos (7.3) y el cálculo del parámetro de calibración del sistema (7.4). También se demostrarán diferentes tests ejecutados para asegurar la consistencia de los resultados obtenidos: la distribución de la anchura y retraso temporal de las señales (7.6.1), la sensibilidad medida en comparación a la esperada (7.6.2), la confirmación del cálculo del parámetro de calibración del sistema obtenido a partir de diferentes medidas (7.6.3) y la comparación entre tamaños angulares medidos con configuraciones ligeramente diferentes (7.6.4). Después, se presentarán las medidas de tamaños angulares para estrellas cuyo diámetro angular había sido directamente medido previamente (8.1.1) y otras que no contaban con una medida directa previa (8.1.2). También se presenta un estudio de los sistemáticos asociados a las medidas (7.7), tales como: el ancho de banda electrónica, el ancho de banda óptica, la ganancia del sistema, el método de substracción del fondo y el filtrado de ruido electrónico. El objetivo principal en este capítulo será obtener diámetros angulares de estrellas nunca antes medidos con tanta precisión en la banda azul y que junto con las distancias a las estrellas medidas por otros experimentos servirán para avanzar en el entendimiento de la estructura y evolución de estrellas masivas.

- Pulsos rápidos en radio (FRBs): en este capítulo se hablará del descubrimiento de los pulsos rápidos en radio (10), enfocándose especialmente en los magnetares (10.1) como una de las fuentes de FRBs. Se hablará del potencial de los telescopios MAGIC para detectar contrapartidas simultáneas en óptico gracias a la configuración especial en los píxeles centrales llamada Central Pixel (CPIX, sec. (11.2)) y en muy alta energía. Se hablará de la campaña que se llevó a cabo para el FRB 121102 en 2017 y cómo ésta sentó las bases del análisis de campañas posteriores como las que se han llevado a cabo durante esta tesis. Se describirá el proceso estándar de análisis de datos de MAGIC de muy alta energía (11.1) y algunos casos de análisis no estándar que se necesitan llevar a cabo en ciertos modos de observación (11.1.1), incluyendo el proceso seguido para analizar los datos del CPIX. Se mostrarán por separado las observaciones y resultados de las campañas de observación de tres fuentes de FRBs: SGR 1935+2154 (12.1), FRB 20200120E (12.2) y FRB 180916.J0158+65 (12.3). El objetivo principal de este capítulo será la búsqueda de emisión en óptico y muy alta energía, transitoria y persistente, en contrapartida a los fenómenos transitorios de pulsos rápidos en radio, de los cuales se desconocen tanto las poblaciones de fuentes que los producen como los mecanismos de emisión.

Abstract

The MAGIC telescopes located in the Roque de los Muchachos Observatory have been active for 20 years at the time of writing this work. This thesis is dedicated to the innovative exploitation of these imaging atmospheric telescopes as an intensity interferometer to measure the angular size of stars with unprecedented precision in the blue band; and to the search for transient fast radio bursts' counterparts in optical (thanks to the central pixel setup in each telescope) and very high energy.

This work is divided into three main blocks:

- Introduction to gamma-ray astronomy: this chapter introduces the history behind the discovery of gamma rays (0.1) and cosmic rays (0.2) that gave birth to astroparticle physics. It also introduces the different production (1.1), absorption (1.2) and acceleration (1.3) mechanisms of gamma rays. These processes are behind the gamma-ray emission of galactic (2.1) and extragalactic (2.2) sources. This emission is then observed and detected by space-based (3.1) and ground-based (3.2) instruments. MAGIC telescopes (3.3) will be showcased in more detail since the results presented in this work have been obtained with them.

- Intensity interferometry: this chapter details the historical background of the intensity interferometry technique starting from its predecessor: amplitude interferometry (4.1). It will also establish the theoretical basis of the technique (4.2) and some of the science cases that have been proposed to exploit it (4.3). The MAGIC telescopes had to undergo several hardware and software modifications in order to implement this technique (5.1), including exploiting its Active Mirror Control to subdivide its mirror dishes into several telescopes (5.2). I will explain how I built the star catalogue (6.1) used for intensity interferometry observations and how I used it to schedule more than 400 h over the curse of 2 years as the official intensity interferometry scheduler (6.2). The different steps of the analysis will be explained: photon flux calibration (7.1), delay correction (7.2), convolution with mirror size (7.3) and zero baseline correlation (7.4). Several tests were performed to ensure the consistency of the analysis: stability of the time delay correction and peak width (7.6.1), comparison of expected

sensitivity with measured sensitivity (7.6.2), compatibility between zero baseline correlation measurements (7.6.3) and compatibility between angular diameters measured with different observation configurations (7.6.4). For stars whose angular diameter has already been measured directly and in the same optical bandwidth, the measured angular diameter by MAGIC will be compared (8.1.1), and for those stars without it the MAGIC angular diameter measurement will be provided. A study of the systematics associated to MAGIC intensity interferometry measurements will be also shown (7.7), such as: electronic bandwidth, system gains, night sky background subtraction and filtering out of electronic noise. The main objective of this chapter will be to obtain stellar angular diameters for stars whose angular diameter has not been measured before with such high precision and/or in the blue band. Together with distances obtained by other instruments, these stellar angular diameters will help to expand the knowledge of the structure and evolution of massive stars.

- Fast radio bursts (FRBs): in this chapter FRB possible origins and mechanisms will be introduced (10), focusing mainly on the magnetar scenario (10.1) as a source of FRBs. The potential of MAGIC to detect simultaneous counterparts of FRBs in optical thanks to MAGIC central pixel (11.2) and in VHE. As a starting point, the searches performed for the source FRB 121102 in 2017 with MAGIC will be introduced, as well as how this work laid the foundations for the searches performed for this thesis. Standard MAGIC analysis techniques will be described (11.1) and some non-standard ones that are needed for certain modes of observation (11.1.1), including the analysis of CPIX data. The results of several observation campaigns of FRB sources will be reported: SGR 1935+2154 (12.1), FRB 20200120E (12.2) and FRB 180916.J0158+65 (12.3). The main objective of this chapter will be the search for optical and very high energy emission, in bursts and persistent, as a counterpart to FRBs, for which the emission mechanism and source populations are still unknown.

Introduction to γ-ray astronomy

0.1 Gamma rays

Gamma rays are the most energetic electromagnetic radiation, with energies starting at 511 keV. They were originally discovered in 1900 by P. Villard when he was investigating radiation emitted from radium. They were called 'gamma' rays in a similar way than the less penetrating forms of radiation alpha and beta rays. Unlike alpha and beta rays they seemed to be undisturbed by magnetic fields. It was confirmed in 1914 that gamma rays had a much shorter wavelength than X-rays and that were a form of electromagnetic radiation since they could be reflected by crystal surfaces: they were made of photons.

The first detection of extra-terrestrial gamma rays would not come until 1961 with the Explorer-11 satellite [1]. The satellite was designed to study gamma rays produced by interactions of cosmic rays with interstellar matter. Later, in 1967 satellite Orbiting Solar Observatory III (OSO-III) detected gamma rays from the Milky Way's disk [2]. In 1969, satellite VELA detected a gamma-ray burst (GRB) while monitoring the nuclear tests activities. In 1972 the Small Astronomy Satellite 2 (SAS-2) observed diffuse gamma-ray emission, linking gamma rays with galactic structure [3]. In 1975 satellite Cos-B built the first all-sky map of the Milky Way's disk in gamma rays, as well as a few sources like the Crab Nebula, Vela pulsar and the 3C 273 quasar [4]. In 1989, the Imaging Atmospheric Cherenkov Telescope (IACT) Whipple discovers TeV gamma-ray emission from the Crab Nebula, giving birth to TeV astronomy [5]. Between 1991 and 2000, the satellite Compton Gamma Ray Observatory (CGRO) studied the isotropic distribution of GRBs and identified AGNs as the most energetic source of cosmic rays [6]. In 1996, the satellite BeppoSAX was designed with improved spatial resolution to identify the origin of GRBs, performing the first observation of a GRB afterglow in X-rays [7]. In 2002 the satellite INTEGRAL was launched, being able to perform observations in gamma rays, X-rays and optical. Results from more recent observatories will be discussed in chapter 3.

0.2 Cosmic rays

Cosmic rays are charged particles and nuclei that move at relativistic speeds through space. One could say that the path to the discovery of cosmic rays started in the 18th century, with independent measurements of the spontaneous discharge rate of electroscopes. A typical electroscope consisted of a vertical metallic rod from which two gold leaves hang, enclosed in a glass bottle [8]. When a charge is applied to the rod, the leaves repel and separate from one another. In 1785 C.A. de Coulomb observed [9], as later M. Faraday confirmed [10], that electroscopes spontaneously discharge by interaction with the air so discharge was not due to defective insulation. What is more, spontaneous discharge was also observed in the presence of radioactive material. In the 20th century, J. Elster and H. Geitel [11] built a better insulated version and put it inside a thick metallic box, observing a decrease in radioactivity and concluding that the discharge was due to highly penetrating ionizing agents. But they were not sure about the origin of this radiation, whether it was coming from within the Earth or originated from extraterrestrial sources. In 1911 D. Pacini observed that ionization was significantly lower underwater than above the sea surface [12]. In 1912 V. Hess confirmed with a series of high altitude flights that the ionization increased with height, supporting an extra-terrestrial source of radiation [13]. The term cosmic rays was not coined until 1926, when R. Millikan and G. Cameron confirmed V.

Hess findings [14].

Since then, many experiments have been designed to unravel the nature of CRs, which has important implications on nuclear physics, particle physics and cosmology.

Data from some of those experiments are shown in Figure 1: The Cosmic Rays' spectrum. The way CRs flux changes with energy can be described by a power law:

$$\frac{dN(E)}{dE} \propto E^{-\gamma} \tag{1}$$

where N is the flux, E is the energy and γ is the spectral index, which is slightly different for each energy range.

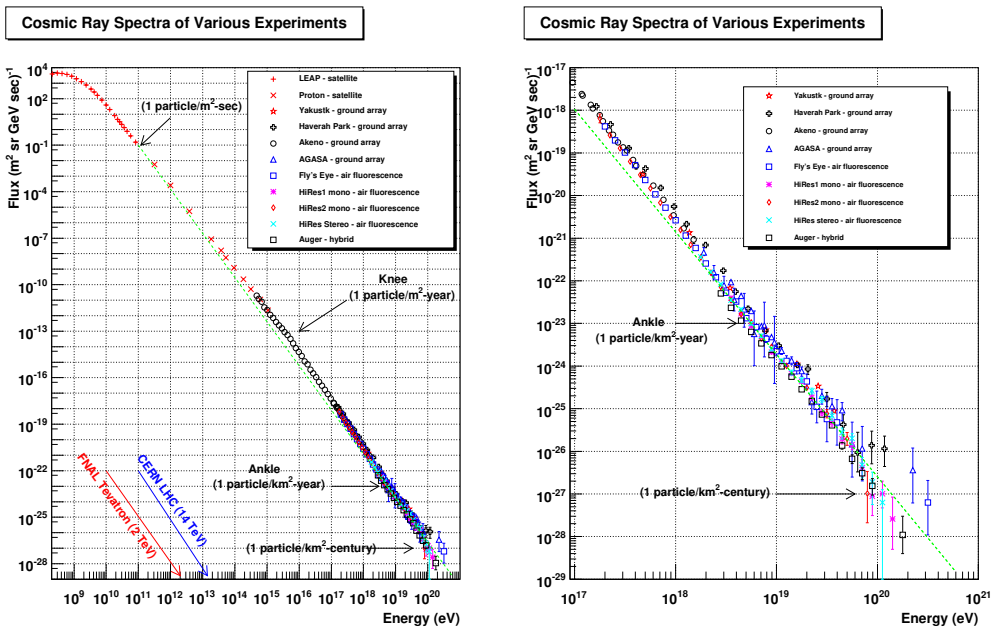

Figure 1: *Cosmic Ray spectra from* `https://web.physics.utah.edu/~whanlon/spectrum.html` *combining data from multiple experiments.*

CRs from a few eV to ∼1 GeV are produced in our solar system via coronal mass ejections and solar flares [15]. From that point and up to $\sim 10^6$ GeV (the knee) the spectral index is 2.7 and CRs are believed to be of galactic origin. Up to 10 GeV there is a phenomenon called solar modulation produced by the interaction between Sun's heliosphere and incoming galactic CRs, which is time-dependent (with solar activity) and produces a suppression in that energy range with a spectral index of ∼5 [16]. The knee is considered to be the maximum energy reachable for most galactic CRs accelerators, like Supernova Remnants. Other theories suggest that this feature is produced by propagation and confinement effects by the Galactic Magnetic Field, explained by a leakage of CRs out of the Galaxy. From the knee up to the second knee at $\sim 10^8$ GeV the spectral index changes to 3.1. The spectral index changes to 3.3 between the second knee and the ankle at $\sim 10^9$ GeV. For energies above the ankle the spectral index changes to 2.7: the charged particles

at these energies are no longer confined by galactic magnetic fields and can travel longer distances without being diverted [17] (i.e. the curvature radius or Larmor radius given by the relationship between the particle's energy, particle's charge and the Galactic Magnetic Field is larger than the galactic disk). This implies that the spectrum starts to be dominated by extragalactic CRs. These CRs are believed to be produced in Active Galaxy Nuclei, Gamma Ray Bursts, radio galaxy lobes and the intra-cluster medium of galaxy clusters [18]. Finally, a cut-off is observed $\sim 5 \cdot 10^{10}$ GeV. This is called the Greisen-Zatsepin-Kuzmin cut-off [19, 20] and it is attributed to inelastic collisions between UHE CRs and photons of the CMB over long travelling distances.

Gamma rays have a close relationship with Cosmic rays. CRs interact with the medium close to their origin, producing gamma rays. Therefore, observing gamma rays can help answer some of the questions on how and where CRs are produced in the Universe. The physics field that studies this relationship is astroparticle physics, combining astrophysics and particle physics.

1. Production, absorption and acceleration mechanisms

Traditionally, wide ranges in energy were dominated by one or two emission mechanisms. However, in the case of gamma-ray astronomy there is a large number of competing processes, even within the same energy range. Gamma-ray production implies not only the emission from thermal relativistic plasmas, but interactions of accelerated charged particles (electrons, protons and nuclei) with different mediums like thermal gas, low-frequency photons and magnetic fields. Gamma-ray emission can be subdivided into several convenient energy bands: low energy (LE, < 30 MeV), high energy (HE, 30 MeV - 100 GeV), very high energy (VHE, 100 GeV - 30 TeV), ultra high energy (UHE, 30 TeV - 30 PeV) and extremely high energy (EHE, > 30 PeV). In this chapter the relevant mechanisms of production, absorption and acceleration associated with gamma rays are presented.

1.1 Production mechanisms

1.1.1 Matter-antimatter annihilation

The most common process of this type produces gamma rays by the annihilation of $e^- e^+$ pairs. The energy produced is typically around $\sim$500 keV in the rest mass frame of reference. A similar process but by a pair $p^+ p^-$ produces mostly pions that later decay into gamma rays. The necessary anti-protons can be generated by energetic protons interacting with matter, but this is a rather inefficient mechanism compared to protons producing pions upon interaction with matter.

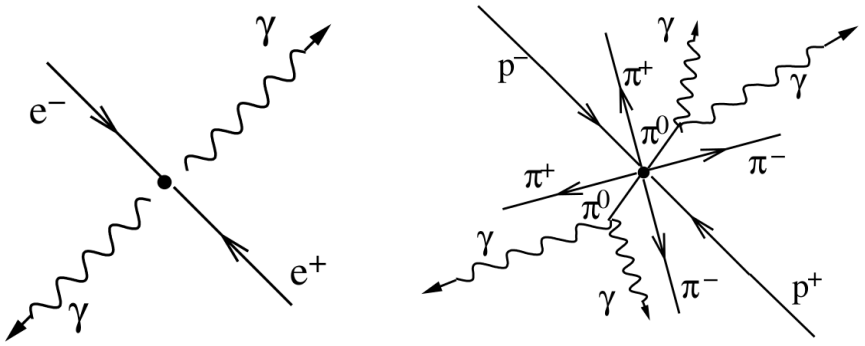

Figure 1.1: *Examples of matter-antimatter annihilation: electron-positron (left) and proton-antiproton (right) [21].*

1.1.2 Radioactive nuclei

It dominates the low energy gamma rays production together with e^-e^+ annihilation. Gamma rays can be produced by radioactive decay or by collisional excitation processes. In the case of radioactive decay other two processes occur: internal conversion (excess energy of the nucleus is transferred to one of its electrons, ejecting the electron from the atom) or internal pair production (excess energy is transformed into a pair e^-e^+ which is ejected from the atom).

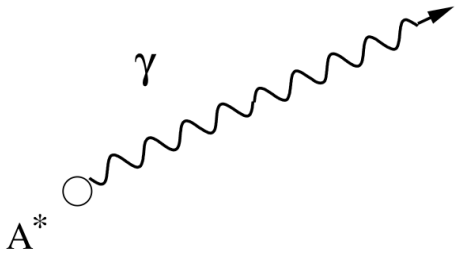

Figure 1.2: *Schematic of radiactive nuclei emission [21].*

1.1.3 Bremsstrahlung

Bremsstrahlung or braking radiation is produced when a charged particle is decelerated by an electric field. The deviated particle emits radiation of electromagnetic amplitude proportional to the suffered deviation. This effect is most common when the particle is an electron or positron and it is in a high density medium, like nebulae with ionized gas, supernova remnants and intracluster medium between galaxies. It is the dominant production mechanism for galactic gamma rays up to $\sim$100 MeV.

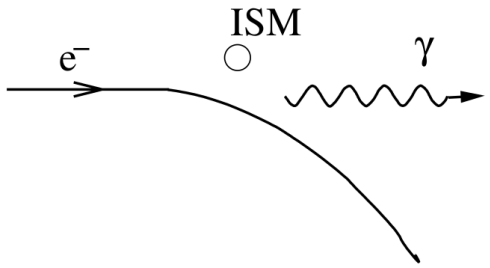

Figure 1.3: *Schematic of bremsstrahlung or braking radiation [21].*

1.1.4 Synchrotron radiation

Occurs when a charged particle moves through a magnetic field. The charged particle will follow a spiral trajectory, with constant speed parallel to the magnetic field lines, while being accelerated towards the center of its orbit at the same time. This kind of radiation of ultra-relativistic particles is the most important contribution to the non-thermal universe (including radio and X-rays). Production of HE gamma rays would require that both the intensity of the magnetic field and the energy of the accelerated particle to be extremely high. However, if there are relativistic electrons present in regions with synchrotron emission, these photons are capable of acquiring higher energies via inverse Compton scattering.

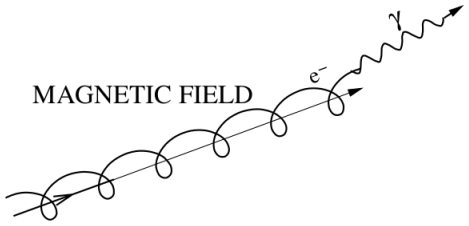

Figure 1.4: *Schematic of synchrotron radiation [21].*

1.1.5 Black body emission and thermal bremsstrahlung

A body with a rather high optical thickness emits thermal radiation according to Planck's law of black-body radiation:

$$B_\nu(T) = \frac{2h\nu^3}{c^2} \cdot \frac{1}{e^{\frac{h\nu}{kT}} - 1} \tag{1.1}$$

where h is the Planck constant, ν is the frequency of the radiation, c is the speed of light in vacuum, k is the Boltzmann constant and T is the temperature of the body. In order to produce a non negligible flux of photons of energy higher than 1 MeV a temperature of 10^{10} K would be necessary. Such high temperatures are believed to be only achieved in the very early stages of the Universe (in which case the cosmological redshift would displace the photons' energies to lower values) or in extremely violent phenomena like Gamma Ray Bursts (GRBs). If instead of an optically thick medium we have a optically thin medium

it is necessary to take into account the absorption coefficient of photons by hot plasma, resulting in a spectrum of thermal bremsstrahlung.

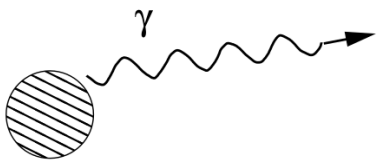

Figure 1.5: *Schematic of hot plasma emitting gamma rays [21].*

1.1.6 Curvature radiation

In the presence of very intense magnetic fields, electrons and positrons spiral around magnetic field lines with a very small rotation radius, effectively following trajectories parallel to the magnetic field lines. Since field lines are warped, the particle emits radiation in the direction of movement called curvature radiation. A common place for this kind of radiation is the surroundings of pulsars, when magnetic fields are specially strong, reaching energies of a few GeV.

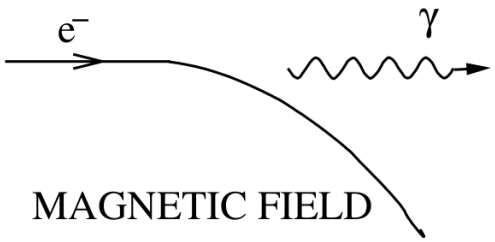

Figure 1.6: *Schematic of curvature radiation [21].*

1.1.7 Inverse Compton

Inverse Compton emission is produced by the inelastic interaction of a charged particle (typically an electron) at relativistic speed that transfers a great amount of its energy to a photon. These kind of interactions are quite common for photons from the CMB (Cosmic Microwave Background), as well as for synchrotron and thermal photons emitted by astrophysical sources. This production mechanism is specially efficient in dense populations of relativistic electrons such as TeV blazars and jets of AGN (Active Galactic Nuclei). It is the dominant mechanism to produce VHE gamma rays.

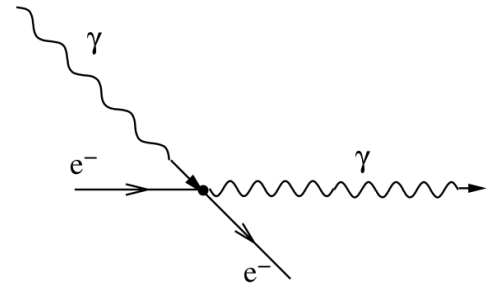

Figure 1.7: *Schematic of inverse Compton emission [21].*

1.1.8 Hadronic collisions

Protons accelerated to relativistic speeds in extreme environments such as strong magnetic fields or jets, can collide with other hadrons producing secondary particles (pions, kaons and other nucleons) that can decay into HE gamma rays. The most efficient production of gamma rays in this case is by neutral pions π^0 which can decay into 2γ (with a branching ration of 99%) or into $e^-e^+\gamma$ (with a branching ratio of 1%). They can also be produced from a $\pi^+ - \pi^-$ pair that decays into a $\mu^+ - \mu^-$ and a gamma ray. The annihilation of π^0 is believed to be the dominant mechanism behind gamma-ray emission from SNR and AGN. Proton collision can also produce charged mesons which decay into neutrinos, so one way of differentiate between leptonic and hadronic emission from a source would be to find a correlation between gamma-ray emission and astrophysical neutrinos (as well as a lack of correlation with X-rays and a different spectrum shape).

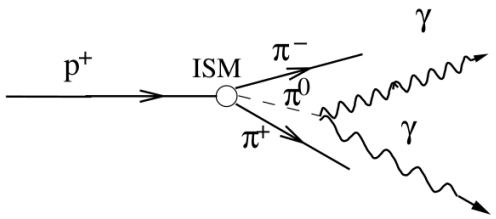

Figure 1.8: *Schematic of hadronic collision [21].*

1.2 Absorption mechanisms

1.2.1 Classical pair production

A photon passing close enough a nucleus and with enough energy ($2m_ec^2$) may produce a pair e^-e^+ by interacting with the nucleus' electric field. This is the very process responsible for gamma-ray absorption in Earth's atmosphere, producing Extended Air Showers (EAS). It is the inverse process to electron-positron annihilation.

Figure 1.9: *Schematic of classical pair production adapted from [22].*

1.2.2 Gamma-gamma pair production

It is possible for two photons to produce a pair $e^- e^+$ if their combined energy is larger than $2m_e c^2$. This mechanism is critical for extragalactic sources of Very High Energy (VHE) gamma rays: low energy photons from the Extragalactic Background Light (EBL) interact with gamma rays, producing an attenuation in the observed spectrum which increases with redshift. Since the EBL absorption is modeled as a function of the distance ([23, 24, 25]), if the redshift of a source is known, the intrinsic spectrum can be estimated. Observations of distant sources in VHE help constraining the EBL [26] and may also allow to estimate the redshift to distant blazars.

1.2.3 Photoelectric absorption

Photoelectric absorption is a process that dominates at photon energies $\ll m_e c^2$. If a photon impinging on an atom has an energy above the binding one of a bound electron, it can strip it, the remaining energy going into the kinetic energy of the stripped electron. The 'absorption threshold' is given by the binding energy of the electron. At sufficiently large energies, the cross-section of this process decreases as one over the cubic of the photon energy.

Figure 1.10: *Schematic of photoelectric absorption adapted from [22].*

1.2.4 Compton scattering

Compton scattering takes place when an incoming photon collides with a stationary electron transferring some of its energy to the latter. Since the photon loses energies it ends up with a longer wavelength. In case of a non-relativistic collision it is simple to show that the change of wavelength is related to the angle through which the photon is scattered as:

$$\lambda_2 - \lambda_1 = \frac{2\pi\hbar}{m_e c}(1 - cos\phi) \tag{1.2}$$

Figure 1.11: *Schematic of compton scattering adapted from [22].*

1.3 Particle acceleration mechanisms

1.3.1 Direct electric field acceleration

This is he process by which charged particles are accelerated by a strong electric field, such as those produced during magnetic field reconnections. Two scenarios depending on the strength of the electric field can be distinguished: sub-Dreicer and super-Dreicer fields. This classification is based on the comparison of the electric field with the critical Dreicer field E_D, which is the electric field necessary for electrons in a collisional plasma to be accelerated into runaway electrons, which can produce plasma waves and turbulence, accelerating particles via stochastic acceleration (see section 1.3.3). In case of a sub-Dreicer scenario, this kind of acceleration is inefficient compared to losses by collisions. In the other case, in a super-Dreicer scenario, the acceleration by the electric field is faster than collisions and thermalisation times. This process is believed to occur in pulsar gaps [27], although the structure and location of these gaps in their magnetospheres is not yet fully understood and has a direct effect on the VHE gamma ray spectra of these objects.

1.3.2 Diffusive Shock or First Order Fermi acceleration

This kind of acceleration is the most important acceleration process in plasmas and could be the power source of supernova remnants (SNR). It takes place near non-relativistic shocks that divide the plasma in two distinct regions: upstream and downstream (in front of the shock and after the shock). If a charged particle going at high speed goes through the front of the shock in either direction, it will get an energy boost proportional to the speed of the front of the shock. Something not fully understood is how the seed particles of energy above the thermal energy were originated in the first place (injection problem). Another problem is that this is a rather slow process, meaning that the particles require crossing the shock several times in order to acquire the observed energies. Additionally, cosmic rays spectrum extends beyond 10^{20}eV while this mechanism has a maximum reachable energy of 10^{14}eV, so it is assumed that magnetic fields can be amplified by several kinds of processes.

1.3.3 Stochastic or Second Order Fermi acceleration

Also known as Fermi process, charged particles moving at speeds close to the speed of light following magnetic field lines with a pitch angle will suffer stochastic collisions or scattering against magnetic gas clouds. Irregularities in the magnetic field cause an overall reflection and acceleration when moving against the particle trajectory (head-on collisions) or braking (head-tail collisions). The main difference with the First Order Fermi acceleration process is the distribution of velocity directions of the irregularities. A partic-

ular case in which this process is relevant is in plasma waves or magnetohydrodynamic turbulences in strongly magnetized plasmas. This would be the scenario in solar wind flows and perhaps also in AGN jets [28].

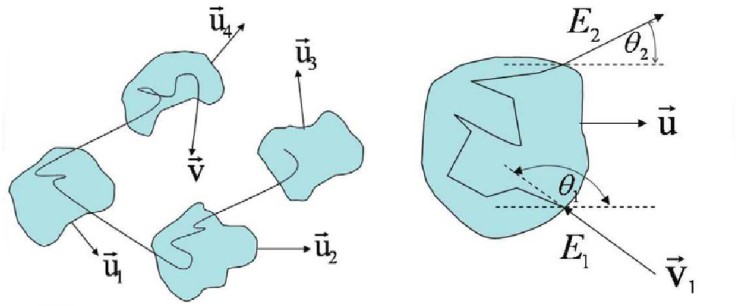

Figure 1.12: *Stochastic acceleration by several magnetic gas clouds (left) and detail of the acceleration for one magnetic gas cloud (right) [29].*

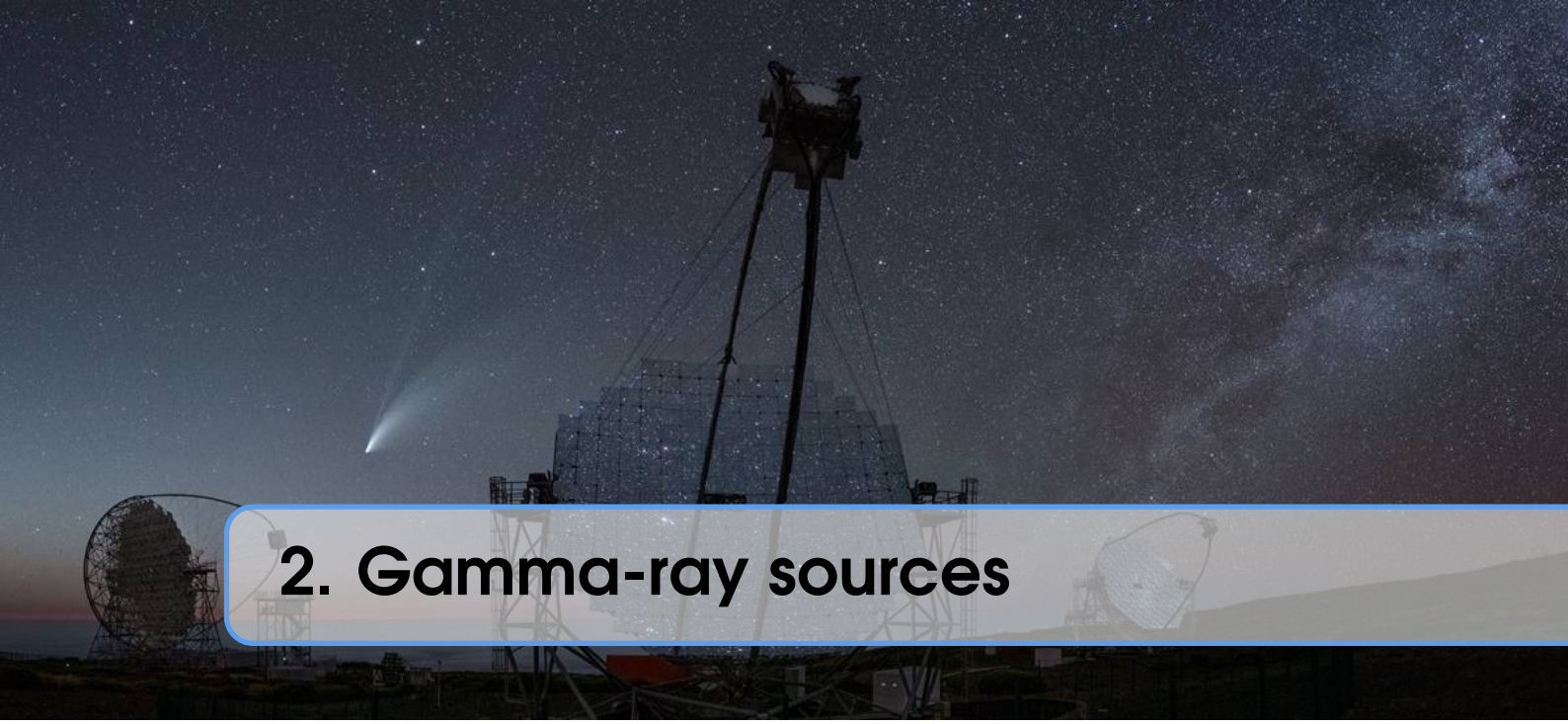

2. Gamma-ray sources

After introducing the different production, absorption and acceleration mechanisms in the previous chapter, this chapter outlines the main gamma-ray sources divided into two groups: galactic and extragalactic.

2.1 Galactic sources

2.1.1 Supernova Remnants

A supernova is an explosion representing the final stage in the evolution of some stars. In this process the brightness suddenly increases while layers of the star's gas are ejected into the interstellar medium in the form of a violent explosion. There are different kinds of supernovae depending on their spectra:

Type I if no hydrogen lines are present. They come from a hydrogen-poor progenitor, usually a white dwarf in a binary system [30]. There are further sub-types: Ia if spectra presents Si lines, Ib if it presents He lines without Si lines and Ic if none of the former [31].

Type II if the spectrum shows hydrogen lines. The progenitor would be a massive star with hydrogen in its outter layers. In this case the explosion is caused by an imbalance between gravitational forces and pressure radiation when fusion reactions of heavier nuclei become inefficient, leading to the collapse of the core into a neutron star or a black hole.

However, from the point of view of the physical mechanism behind the explosion, SNe can be classified into thermonuclear runaways (type Ia, where a white dwarf experiences complete nuclear fusion) and core-collapse SNe (where the core of a massive star undergoes sudden collapse, corresponding to type II and all other type I sub-types).

Supernova remnants (SNR) are the aftermath of a supernova, in which the ejected material has expanded producing a shock wave in the interstellar medium (ISM). There are three kinds of SNR:

Shell-type SNRs they are the most popular candidates for cosmic rays acceleration. Said cosmic rays can produce as byproducts of hadronic interactions with the surrounding gas and dust: pions are generated in the interaction, later decaying into gamma rays. They have no central pulsar, nor strong enough winds that can produce a strong expanding shock. Therefore the main emission mechanism present is the Fermi process [32].

Plerions or Pulsar Wind Nebulae (PWNe) they have a pulsar in the center, with a strong magnetic field that generates streams of particles in the surrounding clouds, forming a pulsar wind. Gamma-ray emission from these sources is generally explained by inverse Compton, produced by the interaction of relativistic particles carried by the pulsar wind with synchotron photons, emitting in the MeV range. They particles also interact with low energy photons in the shock, producing inverse Compton scattering, and with the MeV synchrotron photons (self inverse Compton).

Composite remnants they are a combination of both shell-type and plerions (a plerion surrounded by a shell-type). Since plerions are typically younger objects than shell-type remnants, composite remnants are believed to be an intermediate state between the two.

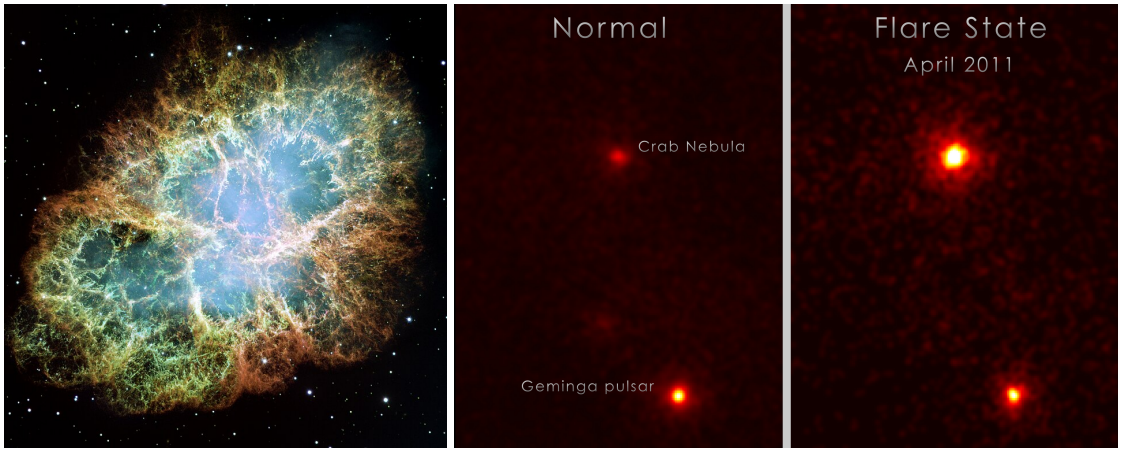

Figure 2.1: *An example of composite remnant: the Crab Nebula. On the left: Crab Nebula as seen by Hubble [33]. On the right: Fermi-LAT TS skymap at E>100 MeV of the Crab Nebula before and during a superflare right next to the Geminga pulsar [34].*

Shell-type SNRs are believed to be the main source of galactic CRs. When accelerated protons interact with nearby matter they generate gamma rays. Therefore SNRs could be the perfect laboratories to study the acceleration of these particles. However it is difficult to establish what is the contribution of protons to the global gamma-ray spectrum because HE electrons also produce gamma rays via bremsstrahlung radiation and IC scattering. In 2011 AGILE observed the pion-decay feature in the SNR W44 spectrum [35], which was later confirmed by Fermi-LAT in 2013 [36], which also detected it for the SNR IC 443, and then later as well for SNR W51C [37], providing direct evidence that cosmic rays are accelerated in SNRs.

2.1.2 Pulsars

They are the most common galactic gamma-ray emitters. Neutrons stars are produced in core-collapse SNe. By conservation of angular momentum, the neutron star is spun up while it rotates. This fast rotation produces strong magnetic fields. If the angle between the direction of the magnetic field and Earth's line of sight is small enough and the rotation axis is not parallel to the magnetic field axis, we see a pulsed emission (mainly synchrotron and curvature from the stripped electrons) with the same period that the period of rotation. Typical periods range from milliseconds to seconds. Consider a particle that co-rotates with the star at a certain radius. The radius for which the particles reaches the speed of light is the radius of the so-called light cylinder (see figure 2.2) and determines the edge of the magnetosphere: beyond the light cylinder magnetic field lines are open. The magnetosphere is powered by rotational energy. Electrons and positrons are accelerated in vacuum regions of the magnetosphere where a electric field can be generated ('gaps'), making them follow the magnetic field lines. High energy photons are also emitted, capable of producing $e^- e^+$ pairs that later emanate from the pulsar in the form of a relativistic magnetized wind. This wind interacts with the sub-relativistic expanding material ejected from the progenitor star during collapse, slowing down via termination shock. More than 200 pulsars have been detected in the HE range [38], some of the brightest are: Crab, Vela, Geminga and Monogem. HE emission up to a few GeV can be produced by synchrotron emission. However IACTs have found out that the pulsed spectrum may extend up to TeV energies (MAGIC, [39]), probably due to IC emission of the same electrons. The exact location of the emission is still unclear.

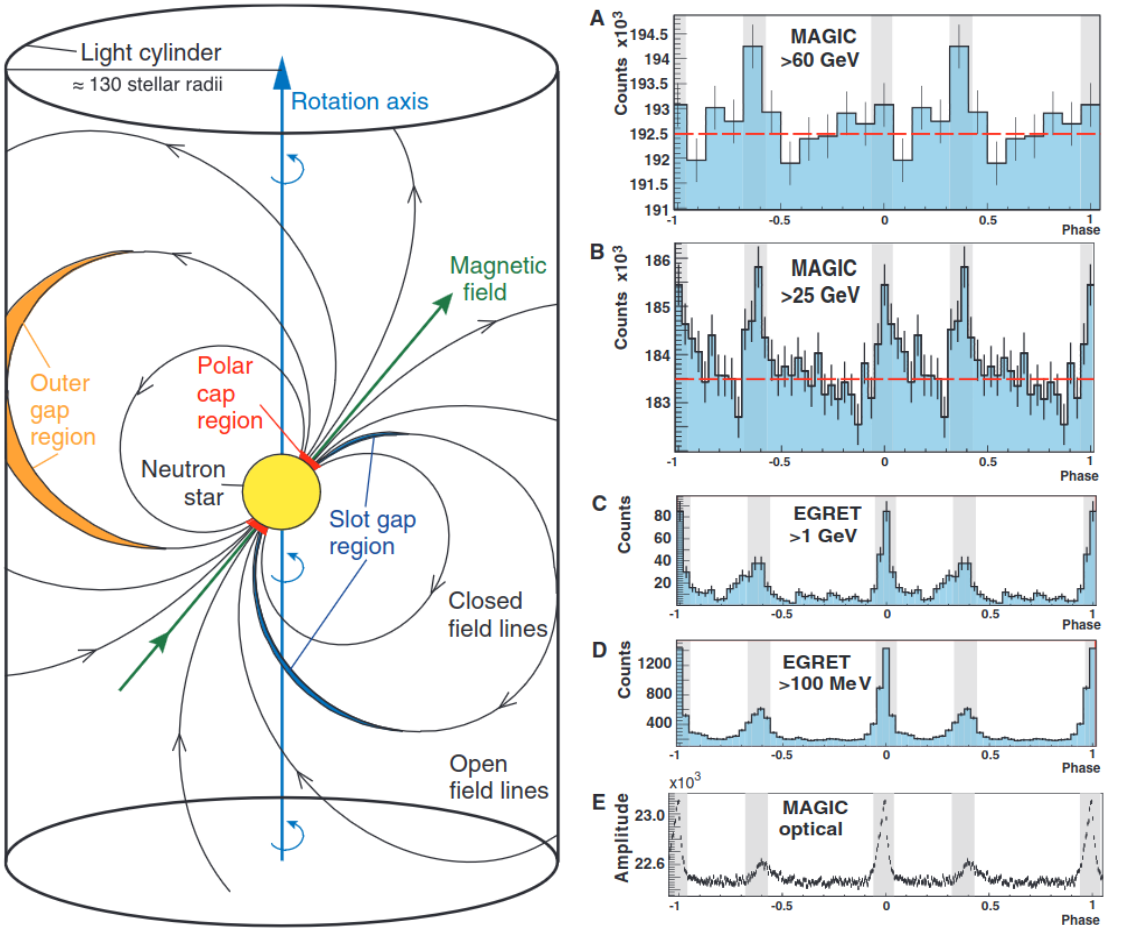

Figure 2.2: *A sketch of the Crab pulsar's magnetosphere (left) and its pulsed emission in different energy bands by MAGIC and EGRET (right) [40].*

2.1.3 Gamma-ray binaries

These systems are typically formed by two objects bound by gravitational forces in which one of them is a massive star and the other is a compact object (neutron star or black hole). The material falling into the compact object produces X-rays via thermal blackbody emission, while the origin of gamma-ray emission is still unclear. In one of the proposed scenarios, the compact object is a pulsar that creates wind shocks with the wind of the massive star, producing gamma rays similarly to plerions [41]. The other proposed scenario is a so-called micro-quasar: the gamma-ray emission is produced in a similar way that in the jets of quasars [42, 43]. Some of these systems have been detected in HE by Fermi-LAT [44, 45], HESS [46] and MAGIC [47, 48]. A few relevant sources are LS I +61 303, Cygnus X-3 and PSR J2032+4127/MT91 213. Another example would be the SS 433 binary system, composed by a supergiant star that has filled its Roche lobe and a compact object (black hole or neutron star). Two jets of ionized material extend from the binary and interact with the surrounding SNR W50. VHE gamma rays have been detected from the regions in which the jets interact with the SNR (lobes) and were discovered by HAWC [49].

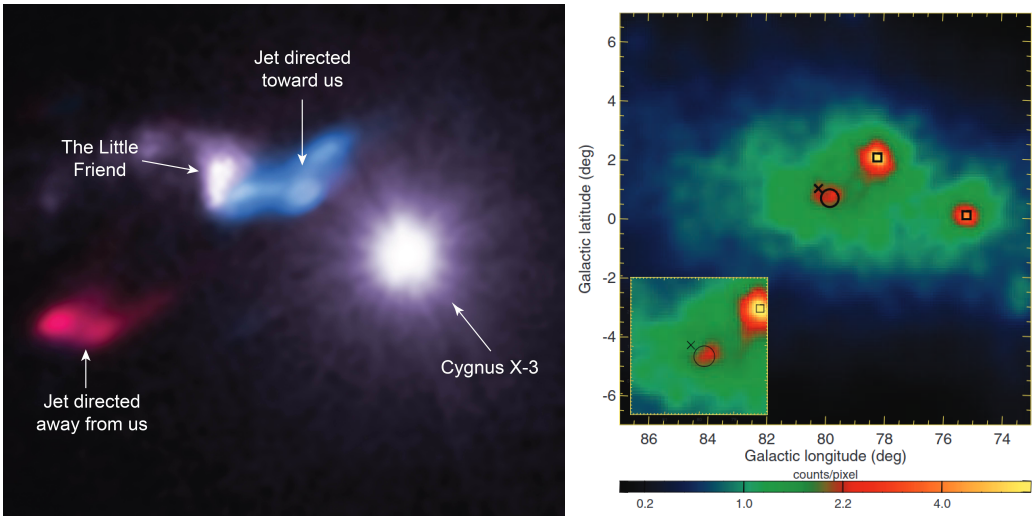

Figure 2.3: *On the left: composite image of Cygnus X-3 as seen by Chandra in X-rays together with radio observations [50]. On the right: Counts map of 14×14 deg centered around Cygnus X-3 (circle), in the 200 MeV - 100 GeV energy range by Fermi-LAT [45]. It shows emission from three pulsars (PSR J2021+4026, PSR J2021+3651 pointed by squares, and PSR J2032+4127 pointed by a cross) and Galactic diffuse emission.*

2.1.4 Novae

A nova occurs in a binary system consisting of a white dwarf and a main sequence star. The white dwarf accretes material from the companion, forming an accretion disk. The hydrogen-rich gas layer in the surface of the white dwarf heats up deeper layers, increasing degeneration and provoking a thermonuclear runaway. This produces an increase in the star brightness that can go on for long periods of time (days or months). In the case of a symbiotic system, the companion does not belong to the main sequence and is more evolved (like a red giant). The interaction between the stellar wind of the red giant and the expanding surface of the white dwarf turns into a favorable environment for particle acceleration. Novae were detected in the HE regime by Fermi-LAT [51, 52, 53] and were expected to be detectable in the VHE [54]. The nova RS Oph was recently detected by MAGIC [55], HESS [56] and LST-1 [57].

2.1.5 Globular clusters

Globular clusters are compact, gravitationally bound spherical distributions of stars, located outside of the galactic plane, forming a spherical halo around the galaxy. They are composed of evolved systems and compact objects, including objects known to produce gamma rays such as pulsars and binary systems. Two models have been proposed to explain the gamma-ray emission coming from these clusters related to Millisecond Pulsars (MSPs): the gamma-ray emission is produced by curvature radiation in their magnetosphere or it is produced by inverse Compton emission by electrons accelerated by optical, infrared or CMB photons [58]. Globular clusters have been detected in gamma rays by Fermi-LAT [59] and HESS [60] and even pulsed gamma-ray emission from individual MSPs [61, 62].

2.1.6 The Galactic Center

The Galactic Center is the region at the center of our galaxy. Due to the presence of dust we cannot see it in visible nor in UV but we can in radio, X-rays and gamma rays. A plethora of MWL observations have shown the galactic center is an extremely rich region of potential VHE emitters: supernova remnants, plerions, stellar clusters and HII regions; and a compact object, the supermassive black hole Sagittarius A* [63]. Both HE [64] and VHE [65, 66, 67] gamma rays have been detected in this region. VHE emission is extended and its spectrum points to a hardening of the primary CR spectrum as one approaches the center [68]. Several scenarios have been proposed to explain its gamma-ray emission: seeing the Milky Way as a former AGN in which gamma rays originated in the base of the jets or due to the accretion disk around the supermassive black hole. Since the region is highly populated, more angular resolution is needed in order to resolve some of the sources, as well as properly identifying gamma radiation coming from other gamma-ray emitters like SNRs, Sagittarius A East and stellar clusters with increased star formation. The rest of the gamma-ray emission is believed to come from high concentration of MSPs (in globular clusters) [69] or even annihilation of dark matter [70].

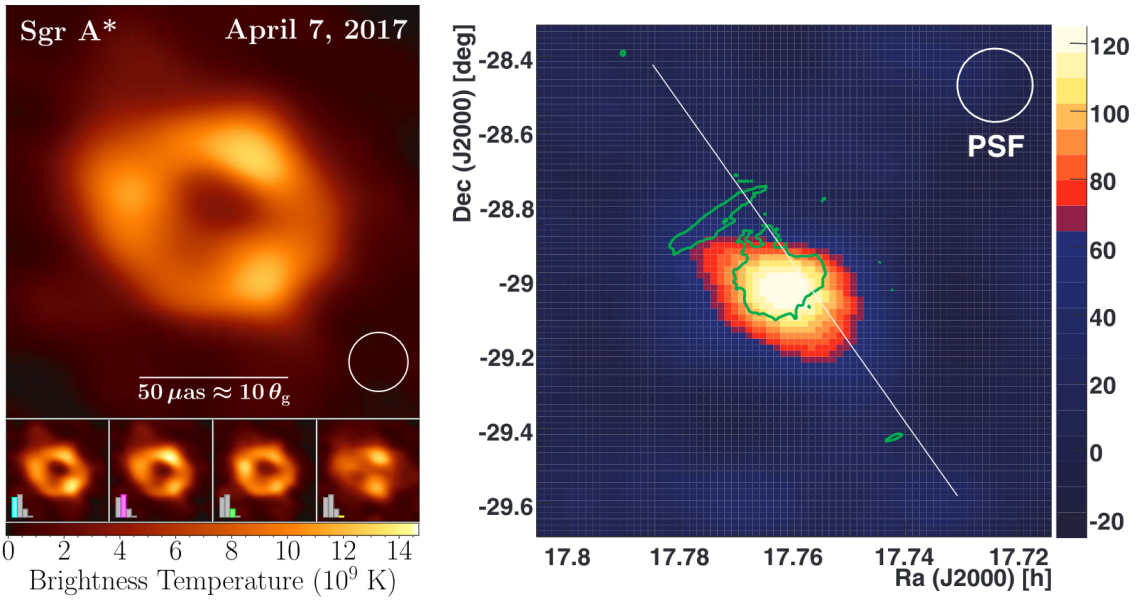

Figure 2.4: *On the left: Event Horizon Telescope (EHT) image of Sagittarius A* observations from 2017 in scale of brightness temperature. The image is consistent with the presence of a supermassive black hole [71]. On the right: smoothed skymap of gamma-ray candidate events in the direction of the Galactic Center with MAGIC [66]. The green contours correspond to 90 cm VLA radio data and the white line indicates the Galactic plane.*

2.1.7 The Fermi Bubbles

Two large bubble-like structures extending 50º above and below the galactic center were reported in Fermi-LAT gamma-ray data [72, 73, 74] in the 2010s. Their gamma-ray emission follows a harder spectrum than that of the diffuse gamma-ray emission from the Galactic disk. Figure 2.5 shows how the structures overlap with other structures in other

wavelengths, suggesting a common origin. They are believed to be what remains of AGN jets that used to outflow from the supermassive black hole in the center of our galaxy.

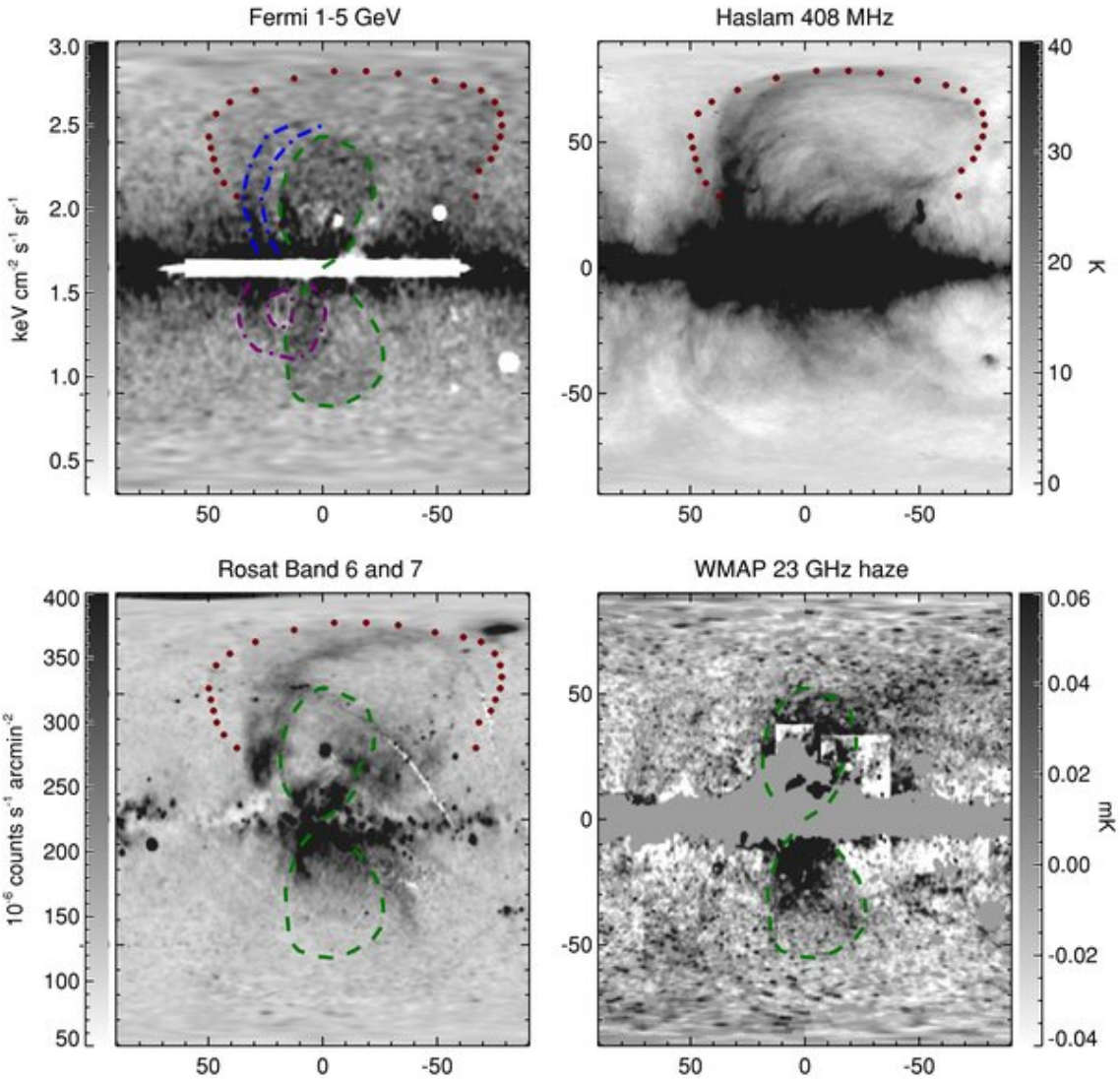

Figure 2.5: *Comparison of the Fermi Bubbles structure overlapping with other maps: On the left: residual Fermi-LAT skymap in which the north and south bubbles are marked with a green dashed line, the north arc in a blue dot-dashed line, the red dotted line marks the edge of Loop I and the purple dot-dashed line outlines a tentative 'donut' structure. On the top right: Haslam 408 MHz map of soft synchrotron emission overlapping with the Loop I. On the bottom left: ROSAT 1.5 keV X-ray map overlapping with part of the Fermi Bubbles and Loop I. On the bottom right: WMAP haze in K-band 23 GHz overlapping with the edges of the FBs [72].*

2.1.8 Galactic PeVatrons

The detection of UHE photons from the Crab Nebula [75] suggests the existence of a PeV accelerator (a pevatron) within the nebula. In 2021, LHAASO published a list of 12 galactic cosmic accelerators from which Ultra High Energy (UHE) photons have been detected [76], that is, in the PeV range, managing to detect the highest photon to date

with an energy of 1.4 PeV. Most of the sources have not been identified yet, but they are usually spatially correlated with leptonic accelerators like pulsars and PWNe. However the emission is consistent with primary electrons/positrons so it is not a proven source of hadrons up to the Knee (a so-called PeVatron).

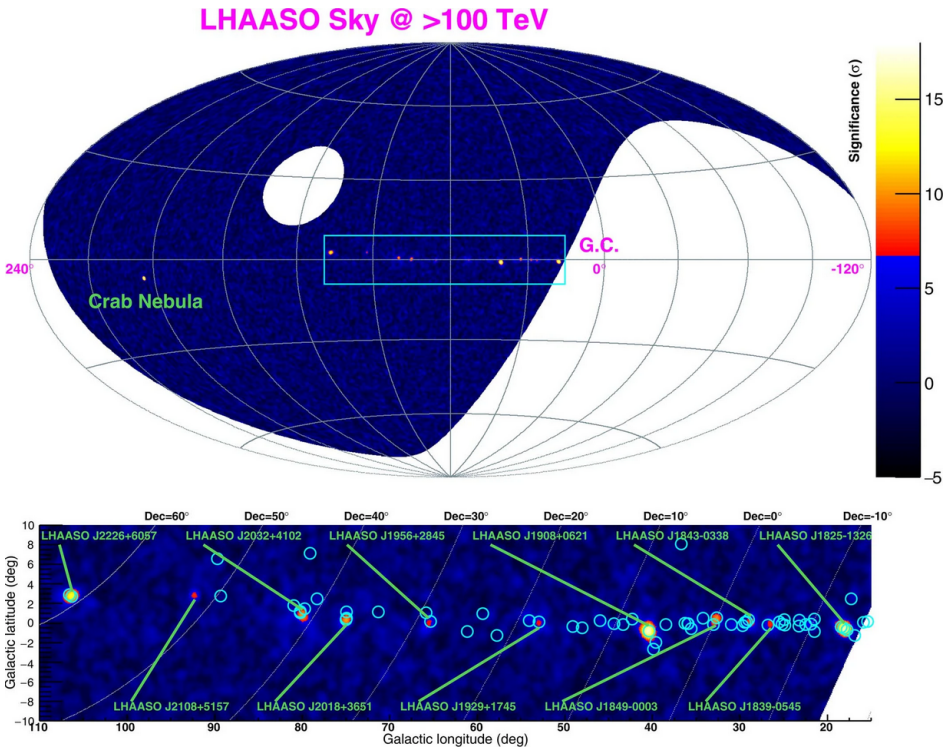

Figure 2.6: *LHAASO skymap at E > 100 TeV. The position of known VHE gamma-ray sources are circled in blue, overlapping with detections in some cases [75].*

2.2 Extragalactic sources

2.2.1 Active Galactic Nuclei

They are the brightest source of gamma rays. The emission is believed to be powered by falling material into the central supermassive black hole of a galaxy. The black hole attracts surrounding material by gravitational force, forming an accretion disk that emits energy in form of UV light and X-rays [77]. AGN are broadly classified into two types:

Radio-loud they present radio emission related to relativistic jets of plasma coming out of the BH and flowing perpendicular to the accretion disk. These jets accelerate particles to ultra-relativistic energies, producing radiation from radio to gamma rays [78]. If the angle between the line of sight to Earth and the direction of the jets is small enough, we see even stronger emission and call these objects blazars. Blazars can be classified into: FSRQ if their spectrum shows strong broad optical emission lines, and BL Lac if they present weaker lines with fast flux variability and polarization in optical. They constitute only 10% of AGN [79]. AGNs observed in the HE and VHE ranges are overwhelmingly jetted and typically blazars. Other kinds of radio-loud AGNs are the Fanaroff-Riley classes I and II (FR-I and FR-II). The first class corresponds to AGNs whose surface brightness decreases

with the distance to the center while the second class corresponds to AGNs whose surface brightness is higher in the end of their lobes.

Radio-quiet they are three orders of magnitude weaker in radio than their 'loud' counterparts. They do not show jets nor present HE non-thermal emission. They can be further classified into quasi-stellar objects (QSO) and Seyfert (1 and 2).

The *unified scheme* proposes that morphological and spectral differences observed in AGN are caused by perspective (see figure 2.7) rather than intrinsic differences of the sources [77].

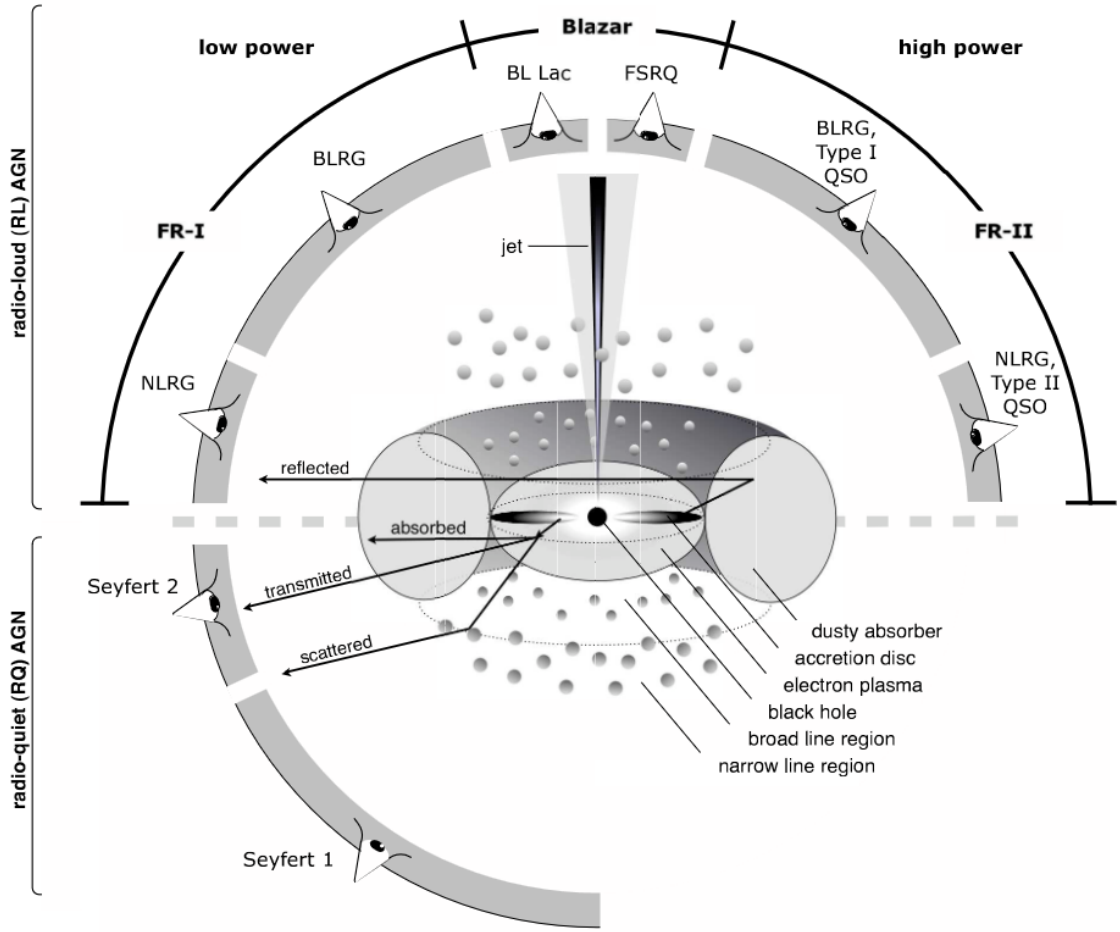

Figure 2.7: *Unified scheme for AGN from [80]. It shows different AGN types depending on the view angle.*

2.2.2 Gamma Ray Bursts

They are the most luminous kind of transient observed. Sudden bursts of gamma rays capable of emitting the same radiation of the whole Milky Way over several years in a matter of seconds (short GRBs), minutes (long GRBs) or hours (ultra-long GRBs):

Short GRBs they last less than 2 seconds and are believed to be associated to mergers of neutron stars or black holes in evolved regions. In 2017 Fermi-GBM detected the

event GRB 170817A just 1.7 seconds after LIGO triggered on a binary compact merger candidate [81] of two pulsars.

Long GRBs they last from 2 seconds up to a few minutes. They seem to occur in stellar formation regions, most likely by supernova explosions of massive stars. They are usually followed by an afterglow in all wavelengths and can be detected years after the event, which allows for a deeper study. For example, in 2019 MAGIC detected TeV emission from GRB 190114C from about one minute after the burst, identifying a distinct emission of the afterglow comparable to the synchrotron emission component [82].

Ultra-long GRBs they last thousands of seconds. Their origin is unknown so far, but several scenarios have been proposed like magnetars, tidal disruption events and extended massive stars, such as blue super giants [83].

2.2.3 Starburst galaxies

Starburst galaxies are galaxies with specially high star formation rate (SFR), typically caused by interaction with nearby galaxies or mergers. Since this ratio is highly correlated with the ratio of supernova explosions, gamma rays detected from these sources are expected to come from supernova remnants. The detection of gamma rays from these sources is essential to understand the acceleration efficiency of cosmic rays in supernova remnants and how they travel through different interstellar mediums. Two starburst galaxies have been detected in the VHE range NGC 253 and M82 [84, 85, 86], other two galaxies with enhanced SFR in the HE range: NGC 4945 and NGC 1068 [87, 88], and seven are associated with 4FGL (Fermi) sources [38].

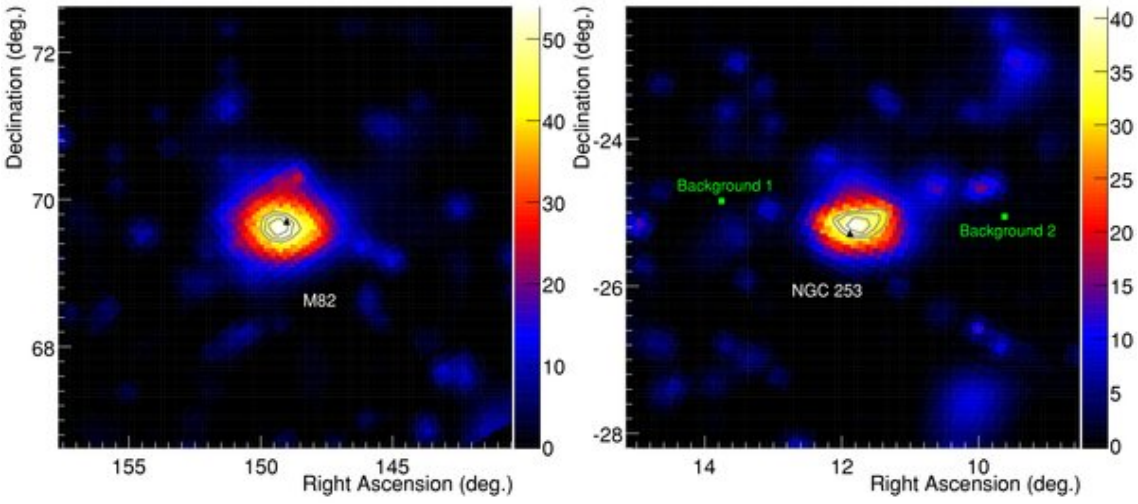

Figure 2.8: *Fermi TS skymaps of M 82 and NGC 253 for energies > 200 MeV [86].*

2.2.4 Galaxy clusters

Galaxy clusters are the largest gravitationally bound structures in the universe. Their main component is dark matter (70-80%) whilst ordinary matter is concentrated in the galaxies,

filaments and intracluster medium. The mergers that take place inside the cluster scatter energy in the form of shocks that heat up the surrounding gas and/or displace it great distances. Part of that energy is invested in the acceleration of particles to relativistic speeds, producing cosmic rays. These sources are expected to be a source of HE photons produced by IC scattering of CMB photons interacting with ultra-relativistic electrons or by neutral pion decay. In 2018, Fermi-LAT detected extended emission of gamma rays in the Coma cluster, apparently correlated with a halo in radio [89].

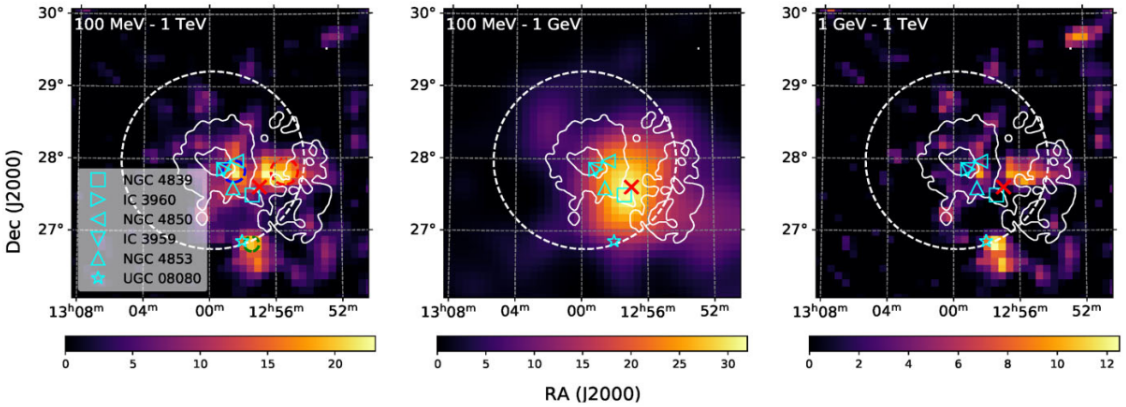

Figure 2.9: *Fermi TS skymap of the Coma cluster for three energy ranges. The dashed white line is the virial region of the Coma cluster, the solid white contours are the radio measurements of the halo, the cyan markers are a few AGN in the region and the red cross is 4FGL J1256.9+2736. The dashed green, red and blue circles in the first panel correspond to 68% containment radii for three point-like sources [90].*

2.2.5 Neighbouring galaxies

Several galaxies of the Local Group have been observed and detected in gamma rays. They are so close that even some individual sources have been identified within them. The Large Magellanic Cloud (LMC) is a dwarf barred spiral galaxy with high SFR, visible from the southern hemisphere. Gamma-ray emission has been detected from it by EGRET [91] and later in HE by Fermi-LAT [92, 93, 94] and in VHE by HESS [95, 96]. The Small Magellanic Cloud (SMC) is a close companion to the LMC, being gravitationally bounded to it. It has been detected as well in gamma rays by Fermi-LAT [97]. The Andromeda Galaxy (M31) and the Triangulum Galaxy (M33) have been detected as well in HE by Fermi-LAT [98, 99].

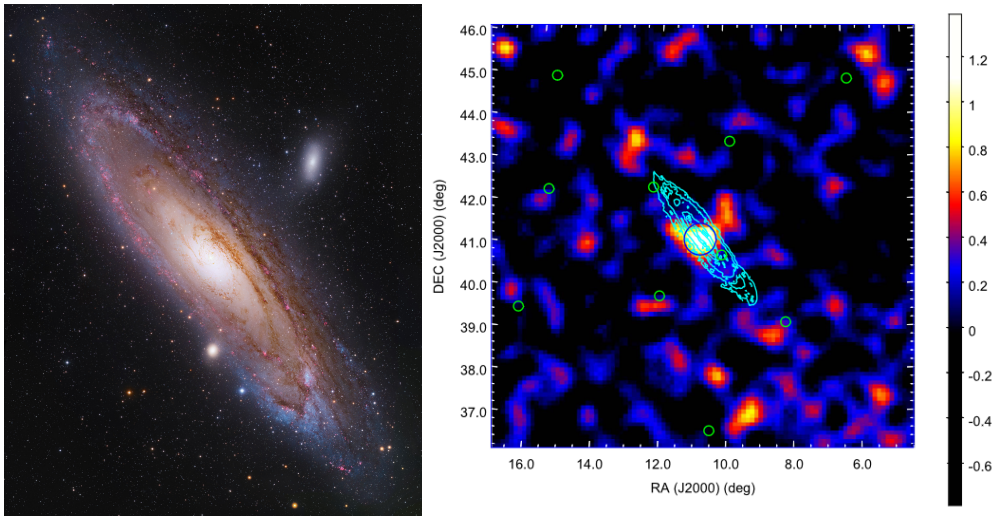

Figure 2.10: *On the left: Composite image of the Andromeda Galaxy in optical and H-alpha [100]. On the right: Fermi's residual counts map after background subtraction. The cyan contours represent the atomic gas column density map, the blue circle is the best-fit disk model and the green circles are 3FGL point sources [99].*

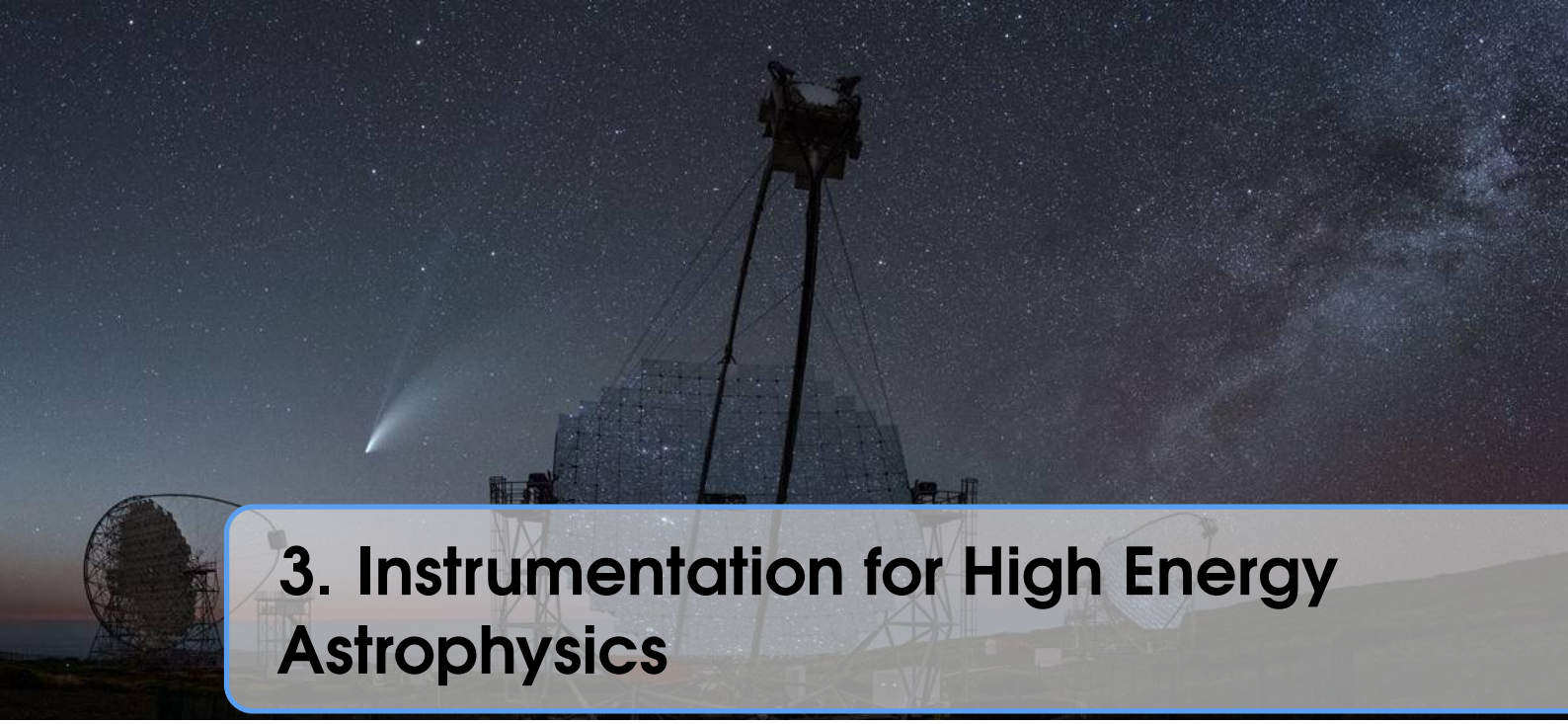

3. Instrumentation for High Energy Astrophysics

This chapter showcases several gamma-ray detection techniques exploited by space-based and ground-based instruments. Space-based instruments can detect cosmic rays and gamma rays directly, enjoying a wide FOV and good background rejection. However, their space-based nature makes them technically challenging to build and put into orbit, limiting their size considerably. This is reflected in their reduced light collection areas of just a few m^2. Ground-based instruments are less technically demanding and easier to maintain, allowing for larger structures (and therefore much larger collection areas). The naturally ocurring extended atmospheric showers (EAS) allow for collection areas of several orders of magnitude larger than those for space-based instruments, increasing the maximum observable energy. Not only that, but by performing stereoscopic observations (several telescopes observe the same event simultaneously) the direction and energy reconstruction is improved. The main disadvantage for ground-based instruments would be the extremely high background rate of showers caused by cosmic rays in comparison to the rate of showers caused by gamma rays.

3.1 Space-based telescopes

3.1.1 Based on Compton effect

The Compton effect or Compton scattering is the process by which a photon interacts with a charged particle (mainly electrons), resulting in a recoil for the charged particle and a loss of energy for the photon. This is the dominant matter-light effect in the 20 keV - 30 GeV energy range. Telescopes based on this effect have scintillators in which the process takes place. The trajectory of the scattered photon is measured in order to reconstruct its original direction. Then, the photon is absorbed by a calorimeter to measure its energy. Some examples on telescopes based on this effect are COMPTEL on board satellite CGRO (1991-2000) [101] and IBIS on board satellite INTEGRAL (2002-present) [102].

3.1.2 Based on pair production

As described in section 1.2.1, a photon with energy equal or more than $2m_e c^2$ passing close enough to a nucleus will interact with its electric field, producing a $e^- e^+$ pair. Detectors based on this effect are composed by several layers of heavy materials in which the process is expected to take place, interleaved with tracking materials to measure the position of the particles over time in order to reconstruct the direction of the original gamma-ray. Similarly to Compton effect detectors, they make use of a calorimeter to measure the energy of the resulting particles. They also use an anti-coincidence detector to identify events caused by background (like CRs). Some telescopes that exploit this effect are the satellite Cos-B (1975-1982) [103], the instrument EGRET on board the satellite CGRO (1991-2000) [104], AGILE (2007-2020) [105] and the instrument LAT on board satellite Fermi (2008-present) [106, 107].

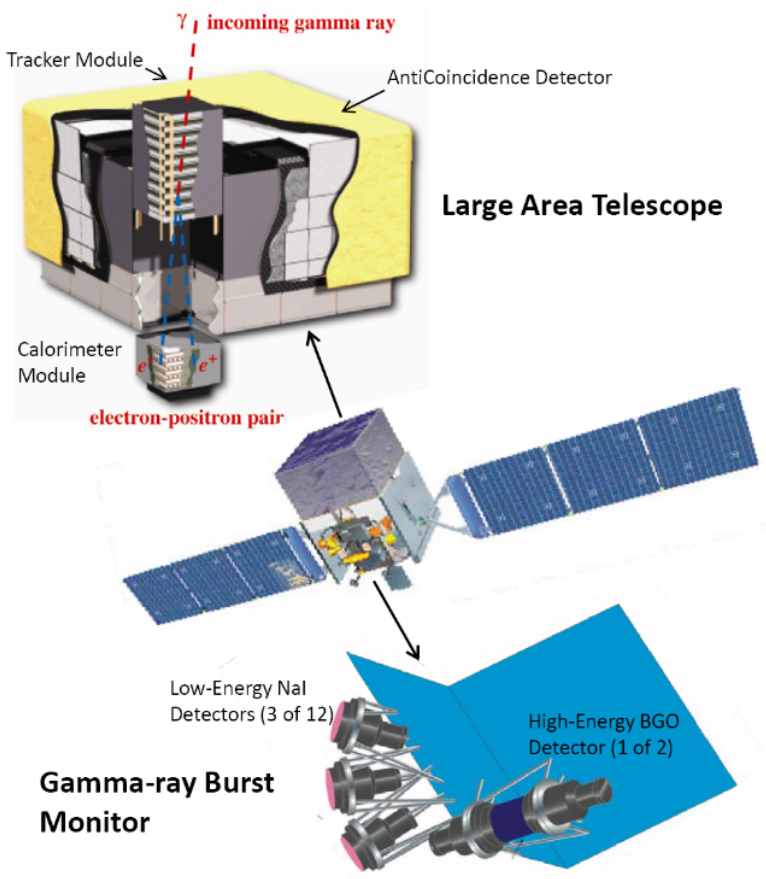

Figure 3.1: *Schematic view of the Fermi Gamma-ray Space Telescope (middle) with its instruments: The Large Area Telescope (LAT) (on top) that images the sky in the 20 MeV - 300 GeV energy range, and the Gamma-ray Burst Monitor (GBM) (on the bottom) that monitors transients such as GRBs in the 8 keV - 40 MeV energy range [108].*

3.1.3 Combination of Compton effect and pair production

There are new telescopes being developed that combine both effects: ComPair [109] which will study the energy range from 200 keV to more than 500 MeV and Gamma Cube which will function as a pair production telescope at HE and as a Compton telescope at lower

energies [110, 111].

3.2 Ground-based detectors

While space-based detectors dominate the LE and HE gamma rays energy ranges, ground-based detectors are better suited for VHE and UHE gamma rays. Instead of measuring the gamma ray photons directly, ground-based detectors measure the output of their interaction with Earth's atmosphere in the form of secondary particles and Cherenkov light produced in Extensive Air Showers (EAS).

Since most EAS are produced by CRs, it is important to distinguish between different showers in order to correctly determine the direction, energy and nature of the primary:

Electromagnetic showers when a VHE gamma ray reaches Earth's upper atmosphere and interacts with the electric field of an atomic nucleus, it produces an $e^- e^+$ pair and initiates a cascade of Bremsstrahlung and pair production processes in the atmosphere. Secondary electrons and positrons have enough energy to move faster than the speed of light in the air, producing Cherenkov radiation. The Cherenkov photons are mostly uniformly contained within a circular light-pool of radius 130 m perpendicular to the angle of incidence of the primary with a density of 100 photons m^{-2} for a primary of energy 1 TeV [112].

Hadronic showers they are produced by relativistic CRs, mainly by protons. The relativistc CR interacts with a nucleus in Earth's atmosphere, fragmenting it and producing lighter nuclei and charged mesons that further collide with other particles and producing charged mesons (pions and kaons). Most of the secondary particles produced in these showers are pions, of wich 1/3 are neutral pions that together with the neutral pions produced by the decay of charged kaons further decay into HE photons that generate electromagnetic showers. Charged mesons can also decay into muons and neutrinos. Hadronic showers present more lateral dispersion than electromagnetic showers and are more irregular, which is useful for detectors to distinguish between the two types.

Electronic showers they are produced by cosmic electrons and positrons interacting with the upper atmosphere. The electron or positron produces HE photons via Bremsstrahlung when they encounter atmospheric nuclei and said photons produce $e^- e^+$ pairs, producing a chain of processes just like the electromagnetic showers. These showers are practically indistinguishable from showers produced by gamma rays.

There are two subcategories of ground-based detectors: particle detectors and atmospheric Cherenkov detectors.

3.2.1 Particle detectors

They collect secondary particles produced by EAS. Only VHE (or more energetic) gamma rays produce showers capable of reaching the ground, so this kind of detectors are often located at high altitudes (> 2000 m).

Particle counter arrays they are arrays of classical particle detectors that measure the direction and arrival time of the particles in order to reconstruct the direction and energy of the primary. Some instruments that use this technique are or were: CASA-MIA (1987-1997) [113], HEGRA scintillator and muon detector array (1987-2002) [114], Tibet AS-gamma Experiment (1990-2019) [115] and LHAASO-KM2A (2019-present) [116].

Cherenkov detectors in water they consist on large arrays of water tanks or big water pools. The refractive index of water is higher than that of the air, increasing Cherenkov photons emission. Cherenkov radiation is detected by PMTs. A fit to the light density distribution measured at the PMTs allows to reconstruct the direction. Some examples of detectors that use or used this technique are: MILAGRO (2000-2008) [117] and HAWC (2015-present) [118].

3.2.2 Atmospheric Cherenkov detectors

Instead of collecting the secondary particles produced by EAS, atmospheric Cherenkov detectors measure the Cherenkov radiation produced by them in the atmosphere.

Sampling detectors an array of optical detectors (typically PMTs) is spread over a wide area on the ground in order to collect the Cherenkov light of EAS, measuring its density and temporal distribution to reconstruct the direction and energy of the primary. These detectors operate in the VHE and UHE energy ranges. An example of this kind of detector was AIROBICC (HEGRA) (1987-2002) [119].

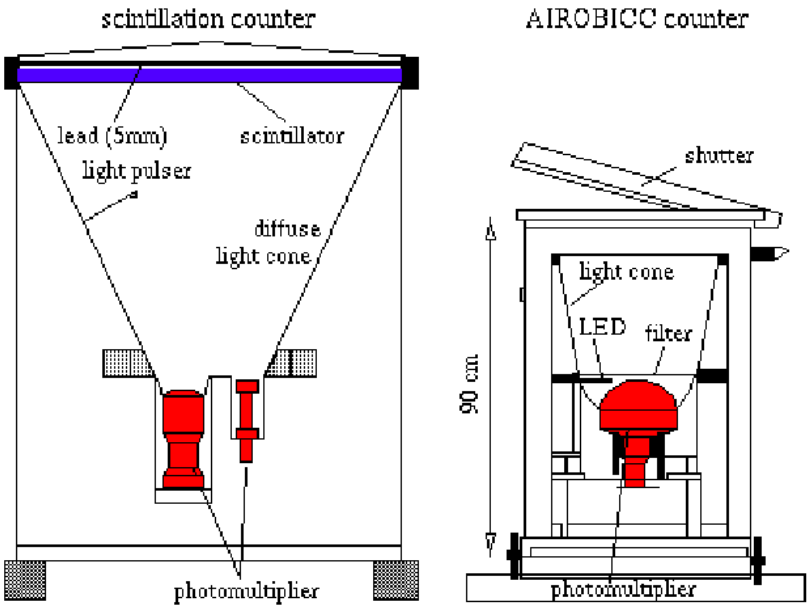

Figure 3.2: *Diagram of a scintillation counter (left) and an AIROBICC counter from HEGRA [120].*

Imaging Atmospheric Cherenkov Telescopes (IACTs) they use mirrors to focus the Cherenkov light of the EAS into a camera of photodetectors (PMTs or SiPMs), similarly to classical optical telescopes. The image together with the time gradient information is parametrized in order to reconstruct the origin, energy and nature of the event. This parametrization allows to distinguish between gamma-like events and background events much better than with sampling detectors, which is why nowadays this is the preferred technique in the VHE energy range. To further improve the parametrization they come in arrays of two or more telescopes in order to observe the showers from different angles simultaneously (stereo observations). Examples of IACTs are: Whipple (1968-2006) [121], HEGRA IACT array (1987-2002) [114], CANGAROO (2004-2008) [122], HESS (2003-present) [123], MAGIC (2004-present) [124, 125], VERITAS (2007-present) [126], FACT (2011-present) [127] and LST-1 (CTA) (2019-present) [128].

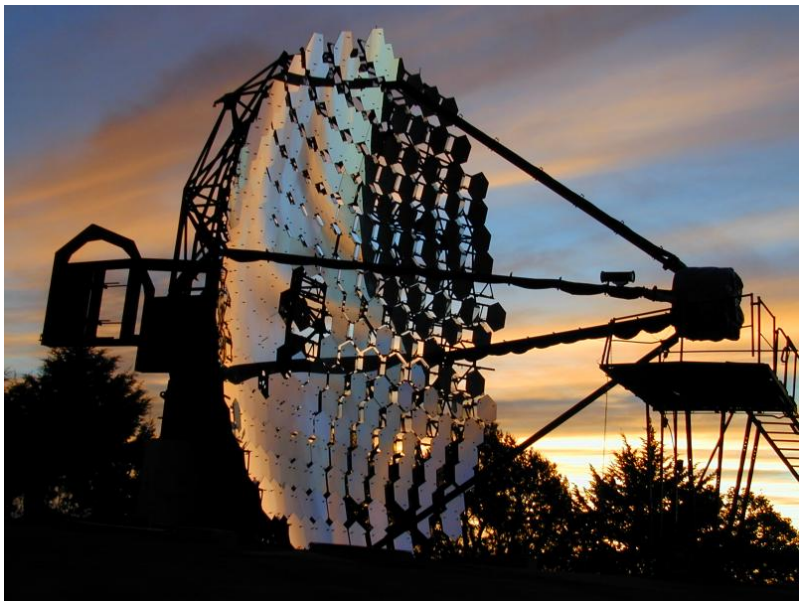

Figure 3.3: *Picture of the 10 m dish diameter IACT Whipple [129].*

3.2.3 Hybrid detectors

They combine components from several kinds of detectors simultaneously. Some examples are the Pierre Auger Observatory [130] which combines water Cherenkov detectors with optical telescopes, HEGRA that combined atmospheric Cherenkov detectors like AIROBICC with scintillation counters or LHASSO that combines electromagnetic particle detectors, muon detectors, water Cherenkov detectors, wide field-of-view air Cherenkov telescopes and a electron-neutron detector array [131].

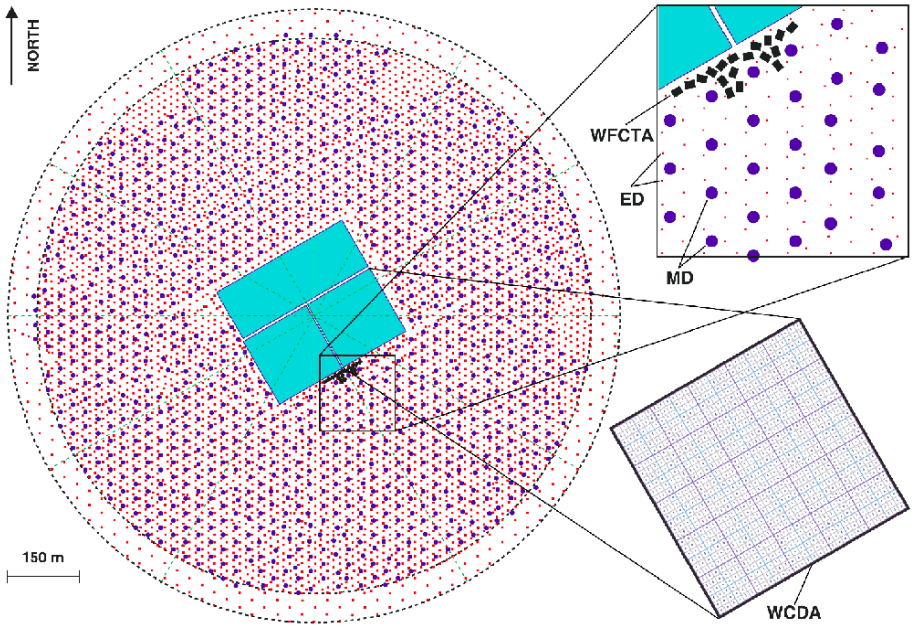

Figure 3.4: *Diagram of different KM2A LHASSO detectors: electromagnetic particle detectors (ED), muon detectors (MD), water Cherenkov detectors (WCDA), wide field-of-view air Cherenkov telescopes (WFCTA) and electron-neutron detector array (ENDA) [131].*

3.3 The MAGIC Telescopes

The MAGIC telescopes are a system of two IACTs with parabolic mirror dishes of 17 m diameter, located at an altitude of 2200 m above sea level, at the Roque de los Muchachos Observatory in La Palma, Canary Islands (Spain). They provide an integral sensitivity of 0.66 ± 0.03 % of the Crab Nebula flux above 220 GeV in 50 h of observation, and allow the measurement of photons in the energy range from 50 GeV to above 50 TeV [124, 132].

Figure 3.5: *Astronomy Picture of the Day of 24th July 2020 by Urs Leutenegger (taken on 20th July 2020). From left to right: telescopes LST-1, MAGIC 2 and MAGIC 1 on the ground, and in the sky: the Neowise commet between LST-1 and MAGIC 2 and the Milky Way on the right [133].*

They have different operation modes, and some of them are: VHE observations, Central Pixel observations and Intensity Interferometry observations. The results presented in this work have been obtained using the MAGIC telescopes and make use of those three modes.

Next to the MAGIC telescopes is another IACT which is the first prototype of Large-Sized Telescope (LST) of CTA: LST-1, which can be seen on the left-most part of figure 3.5. LST-1 has a parabolic mirror dish with a diameter of 23 m, a trigger threshold of $\pm$30 GeV after cuts and a sensitivity in 50 h at 100 GeV about 1.5 worse than MAGIC (mainly because MAGIC observes in stereo with two telescopes instead of in mono) [128]. Given their proximity, all three have been used simultaneously to perform successful stereo observations [134].

IACTs are systems of multiple large-aperture (>10 m diameter) telescopes designed to study VHE gamma rays by detecting the nanosecond-scale flashes produced within extended air showers (see HESS [123], MAGIC [124, 125] and VERITAS [126]). Their very large reflecting surfaces and detectors sensitive to the Cherenkov light (UV/blue) with extremely fast time response (1 ns) make them world-class instruments to explore optical transients from millisecond down to nanosecond timescales. These capabilities were tested with off-the-shelf implementations of the MAGIC CPIX setup for testing timing accuracy [135, 136], but recently their scientific interest has been revived (lead by the PI): IACTs performed the highest angular resolution star diameter measurements [137], set the strongest available limits on optical counterparts of Fast Radio Bursts [138] and

performed ns optical searches for extraterrestrial intelligence (OSETI) [139]. The current generation of IACTs, such as MAGIC (Roque de los Muchachos, Spain) and VERITAS (Tucson, Arizona), has been fully operational for over a decade and producing high-impact results [140, 141, 142, 143]. The new generation is already on its way: the Cherenkov Telescope Array (CTA). Currently in the pre-production stage, CTA will be composed of two sites, one in each hemisphere, with a multitude of IACTs: 15 telescopes at the northern-hemisphere site and 99 at the southern site [144, 145, 146]. These telescopes will come in three different sizes: few Large-Sized Telescopes (LSTs, 23 m diameter), tens of Medium-Sized Telescopes (MSTs, 12 m diameter) and 70 Small-Sized Telescopes (SSTs, 4.3 m diameter) [147, 148, 149].

As already introduced and as proven by the results from the current generation of IACTs, these instruments are very competitive fast optical detectors [137, 138, 150], mainly due to their extremely-large reflecting surface and camera electronics. Their sensitivity (maximum brightness detectable over a given observation time) is limited by the very-large FOV they integrate over a single pixel (6 arcmin). Even if they are still competitive, the irreducible shot noise added by the night sky background makes them less suitable for discovering very faint signals. For instance, a single MAGIC telescope is able to detect millisecond-duration flashes of 13th in B band, while HiPERCAM (the most sensitive fast optical camera, mounted on the 10.4 m GTC [151]) is able to reach 15th mag in g' band (also optical). This comparison significantly changes when comparing the signal-to-noise on brighter targets: when observing bright stars (9th mag), a single MAGIC telescope provides better signal-to-noise for short observation times than HiPERCAM when comparing an equivalent filter (u'). IACTs are the most competitive instruments to search for fast diffraction features produced by serendipitous stellar occultations: by observing a bright star using a system of several very-large-aperture IACTs with inter-telescope distances of 100 m, for instance the two 17-m MAGIC telescopes and a 23-m LST, one is able to maximize the signal-to-noise achieved by each individual telescope while reducing an order of magnitude the rate of atmospheric-scintillation-induced false positives by requiring a simultaneous detection.

II Intensity Interferometry

4. Introduction

4.1 Historical introduction

Spectroscopy and imaging are the best known techniques of astronomy nowadays. The amplitude and wavelength of spectral features allow us to study the composition and movement of distant objects, while imaging focuses on how those objects look like. Both of these methods rely on their light-gathering power. In the case of spectroscopy, the critical characteristic is the spectral resolution while for imaging is the angular resolution.

Broadly speaking, the larger the telescope aperture, the higher is its angular resolution. The limit in angular resolution of a telescope is given by the ratio between the light's wavelength and the aperture of the telescope λ/D but in the case of ground-based telescopes, there is an extra ingredient to take into account: the atmosphere. In order to get as close as possible to this limit, ground-based telescopes make use of techniques like adaptive optics (correction in real time, technically challenging to implement) and speckle interferometry (correction afterwards in the analysis, technically not so demanding) that correct the effects of the turbulence of the atmosphere.

But instead of building even larger and more expensive telescopes in order to improve angular resolution there is another option: interferometry. For an interferometer made up of several telescopes, the limiting resolution is not given by λ/D but by λ/B, where B is the baseline or maximum distance between apertures (telescopes).

Applying interferometry to stellar observations was first suggested in 1868 by H. Fizeau [152]. He reported that interference fringes produced by a source of light of finite dimensions must be smeared by a factor depending on the size of the source. Therefore, if a star of a certain angular diameter is observed by two distant-enough apertures (telescopes), we could put an upper limit to the star's angular diameter.

About a decade later, M. Stéphan [153] masked the aperture of the 80 cm reflector at the Marseille Observatory, leaving two identical apertures at the edges. He observed fringes for both of the stars that he pointed at and calculated an upper limit of 0.158 arcsec

for all of them, reaching the highest resolution in those days.

Another decade later, A. A. Michelson described the technical implementation of the stellar interferometry technique, by observing the fringes produced by a pair of slits with variable separation in a mask in front of the 30 cm refractor at Mount Hamilton. He describes in [154] how to measure the fringe visibility as a function of aperture distance in order to reconstruct the profile of stars. He also discussed the expected results from assuming different profiles: uniform disks, binaries and limb-darkened stars. The instrument evolved and became what we know today as the Michelson stellar interferometer. Michelson used this interferometer to measure the diameter of Betelgeuse [155] in 1921 and F. G. Pease added another six stars then years later. They measured the few big bright stars that could be measured with baselines of a few meters and the field came to a halt for over 30 years.

The concept of the stellar interferometer was revived in radio astronomy by the development of aperture synthesis by M. Ryle. The longer wavelenghts in radio made technical implementation easier for them than for optical wavelenghts, which had to wait until the invention of the intensity interferometer by R. Handbury Brown and J. Q. Twiss in 1956 [156]. They mounted two telescopes in a circular rail, so that they could vary their orientation and the distance between them, similar to how Michelson used slits with variable separation, in the Narrabri Observatory. The group measured the diameter of 32 stars with this equipment [157], but had to abandon the technique due to the lack of faster photo-sensors and a larger collector area. Both elements are needed in order to measure the faint correlation of light's intensity fluctuations and to overcome the $\sim$1 kHz atmospheric turbulence.

The intensity interferometry resurfaced with the IACTs era. IACTs serendipiously have the perfect specifications for intensity interferometry with few technical adjustments: very large reflective surfaces, sensitivity to individual photons, temporal resolution of nanoseconds and the fact that they come in groups of several telescopes. In fact, the telescopes used by R. Handbury Brown and J. Q. Twiss were later converted into IACTs [158, 159, 160]. The technique has since been implemented, with a few technical differences, in VERITAS, MAGIC and HESS.

4.2 The Intensity Interferometry technique

The idea behind this technique is that an extended object of angular size α made up by many incoherent emitting sources, produces a speckled wavefront at the position of the observer with a typical size of λ/α. Therefore, a pair of observers at a distance less than λ/α observe the same intensity fluctuations (i.e. they are within the same speckle). Observers at longer distances are more likely observe from different speckles and see less correlated fluctuations.

The explanation for this phenomenon can be approached in a classical way, through classical waves, or in a quantum way, through Bose-Einstein condensate fluctuations. For the purpose of this thesis we will focus on the classical interpretation.

The waveform of light from a quasi-monochromatic source ($\delta\omega/\omega_0 << 1$), can be described as the sum of sinusoidal waves of frequencies ω in the band $\omega_0 \pm \delta\omega$. The coherence time $\tau_c = 1/\delta\omega \approx \lambda^2/(c \cdot \Delta\lambda)$ is the time during which the phase is more or less stable, i.e. coherence is expected.

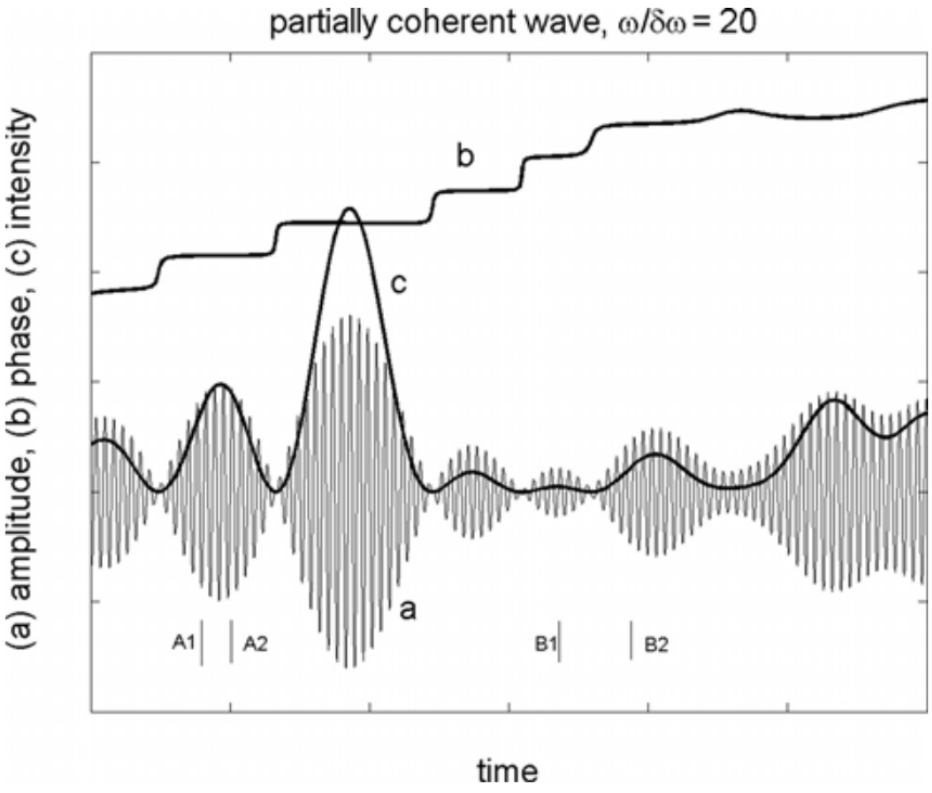

Figure 4.1: *Simulated partially coherent wave, where (a) is the wave amplitude, (b) is the phase and (c) is the fluctuating intensity [161].*

Measuring the correlation between intensity fluctuations is measuring the deviations of the envelope from its mean value. If we take two points in time like A1 and A2 in Fig. 4.1, separated by $\tau << \tau_c$, they are very likely to be within the same wave group or to be close to a minimum. This means that the sign of their deviations from the mean will probably be the same, so the correlation between them is strong. If we take instead two points at $\tau >> \tau_c$ like B1 and B2 in Fig. 4.1, they are most likely to be in different wave groups. This means that the probabilities of their deviations having the same sign or the opposite are the same, rendering the correlation insignificant.

Intensity fluctuations correlations relate to physical properties of the source through the Van Cittert-Zernike theorem [162]: when observing a thermal (non-coherent) light source through a narrow spectral band, the coherence of light measured between two points is proportional to the Fourier transform of the intensity pattern of the source at the distance between said two points in units of wavelengths. In the case of non-polarized light this relationship follows the equation:

$$g^{(2)}_{1,2} = \frac{\langle I_1(t) \cdot I_2(t+\tau)\rangle_t}{\langle I_1(t)\rangle \cdot \langle I_2(t+\tau)\rangle_t} = 1 + \frac{\Delta f}{\Delta \nu} \cdot |V_{1,2}(\tau)|^2 \tag{4.1}$$

where $g^{(2)}_{1,2}$ is the second-order intensity correlation function, $I_i(t)$ is the intensity of light at the point i (1 or 2) at the time t, τ is the delay between measurements (given by the optical path difference between the detectors), $\langle x\rangle_t$ represents the time average of x, Δf where $\Delta f << \Delta \nu$ is the electronic bandwidth, $\Delta \nu$ is the width of the frequency distribution of the detected light and $V_{1,2}(\tau)$ is the normalized degree of first-order mutual coherence of the light at the aforementioned delay τ (which is equivalent to a certain baseline). In other words, $V_{1,2}(\tau)$ is the Fourier transform of the source intensity pattern and is also called visibility.

The relationship described in (4.1) describes how to measure the modulus of the visibility through intensities I_i. Note that since it depends on the modulus, phase information is 'lost', and imaging cannot be performed with just two detectors, but could be done with at least three (see [163] and [164]). The MAGIC Stellar Intensity Interferometer performs correlations between two detectors for the moment.

The modulus of the visibility can take different forms depending on the brightness profile of the source in question. The most simple case is an uniform disk, for which the expression is:

$$|V_{1,2}| = 2 \cdot \frac{J_1(\pi \cdot d_{1,2} \cdot \theta/\lambda)}{\pi \cdot d_{1,2} \cdot \theta/\lambda} \tag{4.2}$$

where J_1 is the Bessel function of the first kind, $d_{1,2}$ is the baseline between the detectors, θ is the angular size of the equivalent uniform disc and λ is the effective wavelength. The angular diameter of the source can be therefore inferred by measuring:

$$\frac{g^{(2)}_{1,2} - 1}{g^{(2)}_0 - 1} = \frac{|V_{1,2}(d)|^2}{|V_{1,2}(0)|^2} \tag{4.3}$$

where $g^{(2)}_0$ and $V_{1,2}(0)$ are respectively the second-order intensity correlation and the visibility at zero baseline. The term $g^{(2)}_0$ is also referred to as the zero baseline correlation or ZBC.

We can also define the term of the normalized contrast of the visibility pattern for a given baseline like:

$$c(d) = g^{(2)}_{1,2} - 1 = \frac{\Delta f}{\Delta \nu} \cdot |V_{1,2}(d)|^2 \tag{4.4}$$

which returns:

$$\frac{c(d)}{c(0)} = |V_{1,2}(d)|^2 \tag{4.5}$$

where $c(0)$ is a correlation normalization factor called zero-baseline correlation (ZBC), and is the value of the correlation at baseline 0, in other words, the correlation that would be measured for a point-like source. This value together with measurements of the correlation at different time delays or baselines is used to reconstruct the brightness distribution of the thermal emission of the source.

For an uniform disk model (appropriate for a single star), only the spatial coherence and the baselines are needed in order to reconstruct the angular size of the star because radial symmetry is expected, but this is not the case for more complex models and physical scenarios like fast rotators and binary stars. For these cases, radial symmetry is not expected, and therefore one must take into account the projection of the baseline on the plane perpendicular to the direction of the object, in units of wavelength, i.e. the UV plane, which is defined as $(u,v) = (x,y)/\lambda$ where (x,y) are the coordinates in the ground plane as seen in figure 4.2.

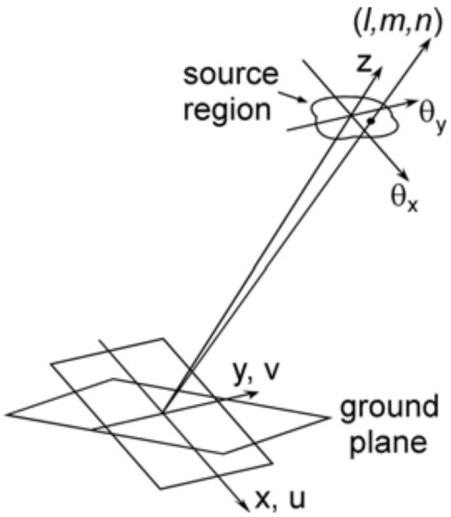

Figure 4.2: *Geometrical diagram of the Van Citter-Zernike theorem (Fig. 3.17 from [161]), where (l,m,n) are the direction cosines, (θ_x, θ_y) are the angular coordinates, (x,y) are the ground coordinates and (u,v) are the ground coordinates in units of wavelength.*

These are some examples of UV plane patterns for four different models that will be further explained in the next section:

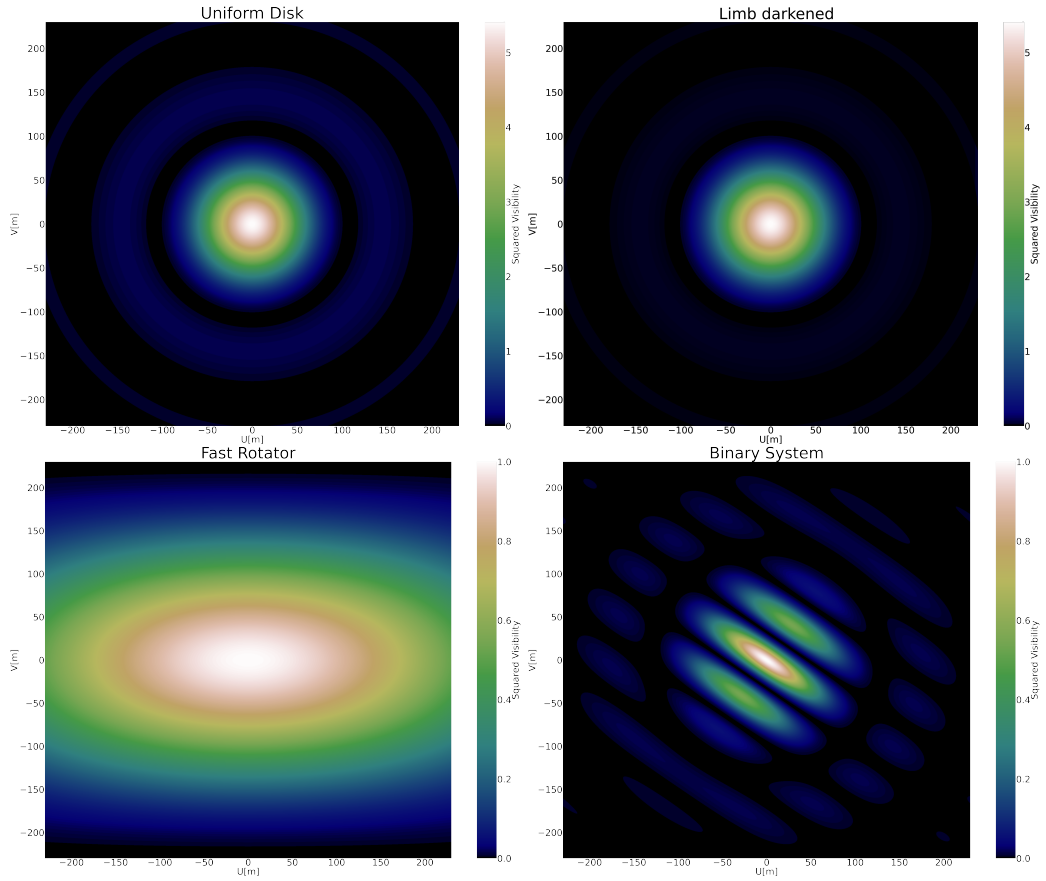

Figure 4.3: *Examples of visibility patterns in the UV plane. Top left: Uniform disk, top right: limb darkened disk, bottom left: fast rotator, bottom right: spectroscopic binary.*

4.3 Main science cases

The main targets for the use of the intensity interferometry technique with the MAGIC telescopes are stars with an angular diameter between 0.5 and 2 mas and bright in the blue (B < 4 mag). These are generally main sequence massive stars. The most simple scenario is the determination of their **stellar radii** by fitting the spatial coherence measurements to an uniform disk model (see expression 4.2). By measuring the angular diameter of a star of known distance one can obtain an independent measurement of the physical star radius that can be used to test different stellar models and determine other physical parameters like mass, age or temperature.

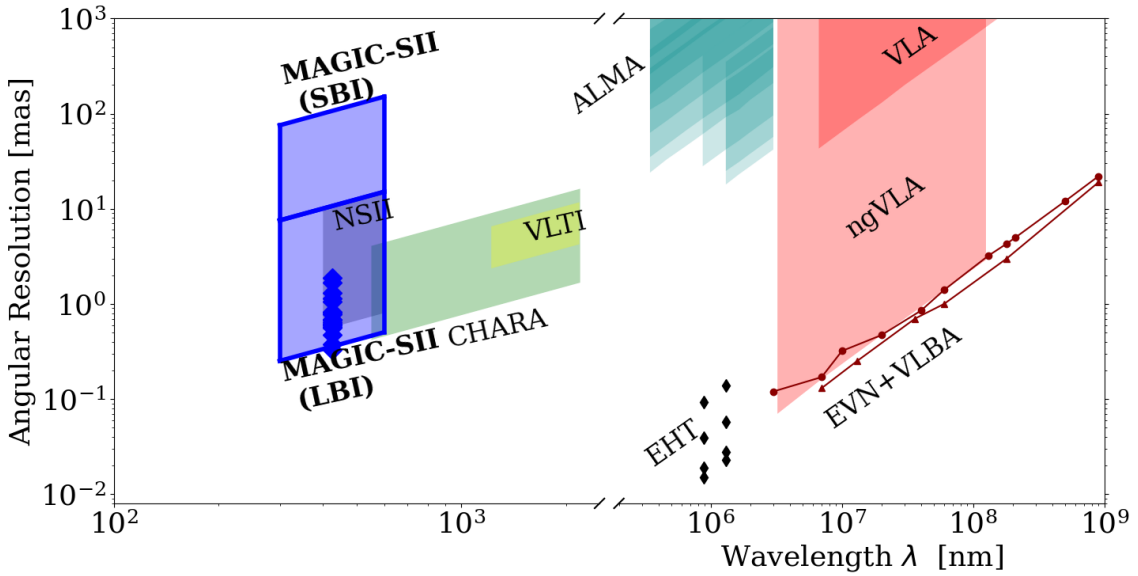

Figure 4.4: *Angular resolution versus wavelength for several instruments and experiments. MAGIC angular resolution with intensity interferometry for short baselines (SBI) and long baselines (LBI) is shown in blue areas, together with angular size measurements performed so far (blue diamonds).*

There are some stars that show oscillation modes that can produce periodical changes in the diameter (pulsations). The study of these oscillations is called **asteroseismology**, and it is based on how the sound speed changes within a star depending on the density, temperature, composition, age and the internal movement and mixing of material.

One step further is to add to the uniform disk model a monotonically decreasing radial dependence of the brightness: **limb darkening**. This effect is the result of the combination of decreasing optical depth and effective temperature of the photosphere with radius. It is also dependent of the wavelength, so the apparent angular diameter will be different for different wavelengths.

Another case is that of the **fast rotators**: stars that spin so rapidly that the photosphere becomes oblate: the effective gravity decreases towards equatorial regions (gravity darkening), even producing mass loss that form circumstellar disks. These kind of stars when observed in the Fourier space would not present a radially symmetric pattern but an elliptical one, allowing to measure a changing angular diameter and therfore the oblateness.

Another example without radial symmetry would be **binary stars** and particularly spectroscopic binaries: stars that are close enough to suffer gravitational interaction between each other and are usually discovered by measuring variations in radial velocity by changing positions of spectral lines (Doppler effect). In this kind of stars the diameters and the separation are of the same order of magnitude. This produces varying UV patterns that depend on both their radii, relative brightness and relative distance and position angle (which change within their orbital period).

5. Setup

5.1 The MAGIC Stellar Intensity Interferometer

The main objective of IACTs, such as the MAGIC telescopes, is to observe the gamma-ray sky. Gamma rays are absorbed in our atmosphere but they interact with it, producing EAS that emit faint fast blue flashes of Cherenkov light (see section 3.2). By characterizing the intensity and the spatial and temporal pattern of this light, one can study different properties of the primary: its nature (gamma photons or otherwise), its direction (the astronomical source) and its energy (to reconstruct their spectrum). In order to perform this kind of observations, IACTs have several technical features that make them incidentally well suited for intensity interferometry observations: they come in groups (each combination of telescopes is a different baseline), they have time resolution of nanoseconds (needed to resolve the correlation peak), they are sensitive to single photo-electrons (and therefore coherence of individual photons) and they have large mirror areas (more photons means more statistics and better S/N).

In recent years, the MAGIC telescopes have undergone several technical modifications ([165, 166, 167]) like the implementation of a digitizer and GPU-based real-time correlator, special configuration of its AMC (to focus the light to the infinite instead of the typical altitude of EAS of 10 km and to concentrate it into just one or two photo-multipliers or PMTs) and the automatic deployment of optical filters using the white target holder, that allows the system to transform into an intensity interferometer in less than a minute and then back to VHE observations just as quickly (useful for transients). This makes MAGIC Intensity Interferometer an extremely high duty cycle instrument, having taken more than 500 hours of observations since 2021. These observations were mainly performed during full Moon breaks, which are periods with bright moonlight conditions in which IACTs are less performing in VHE, but can still operate in interferometry mode, because the optical filters strongly attenuate the moonlight that gets into the PMT (see 5.1).

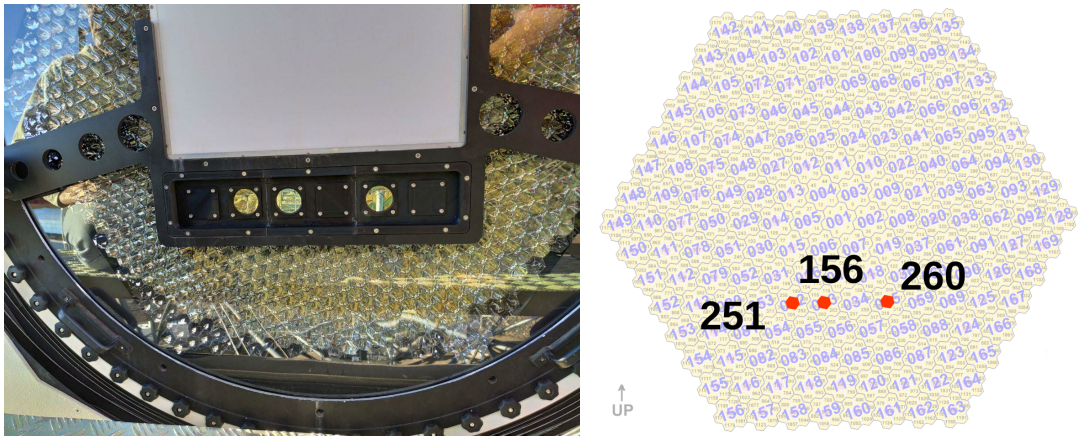

Figure 5.1: *Left: picture courtesy of Juan Cortina of one of MAGIC camera white target filter mount. The structure has been adapted to hold up to 6 filters in front of 6 pixels, from which 3 are already being used for intensity interferometry observations on each telescope. Right: diagram of the front view of a MAGIC camera with pixels 251, 156 and 260 highlighted in red (modified from MAGIC hardware school slides).*

Each telescope has a parabolic primary dish of 17 m diameter. The Active Mirror Control AMC allows to focus the starlight into two (or four) of the filter holes. Each filter hole has a Semrock 425-26 nm optical filter and falls in front of a Winston cone that further concentrates the light into a PMT at the end of it. The AC coupled electrical signal of the PMT is amplified ($\sim$25 dB) and transmitted in two separate ways. One goes to the camera slow control that stores the DC with a rate of 1 Hz. The other one goes by means of vertical cavity surface emitting lasers (VCSELs) through a multimode optical fiber into a separate readout. The optical signal is transformed back to electrical signal and amplified by a Femto HSA-Y-2-40 amplifier with a 40 dB gain and a 2 GHz bandwidth. This amplified signal is processed by the digitizer boards Spectrum M4i.4450-x8 PCIe 2.0 with a sampling rate of 500 MSamples/s. The digitized signals from each channel/pixel are sent to the correlator setup that consists on two processors (20 cores), HDDs for long-term storage, SSDs for fast access and a Nvidia Tesla V100 GPU. The correlation between channels is computed in the GPU by software developed in CUDA C that makes use of the convolution theorem in Fourier space with Fast-Fourier-Transforms (FFTs) of the data in $\pm$2048 ns time delay windows. For each combination of channels the cross-correlation is stored, and for each channel the auto-correlation and the standard deviation of the input signal are stored as well. The data is written into disk in the form of binary files (.bin) that can be later analyzed together with the slow control DC reports [168].

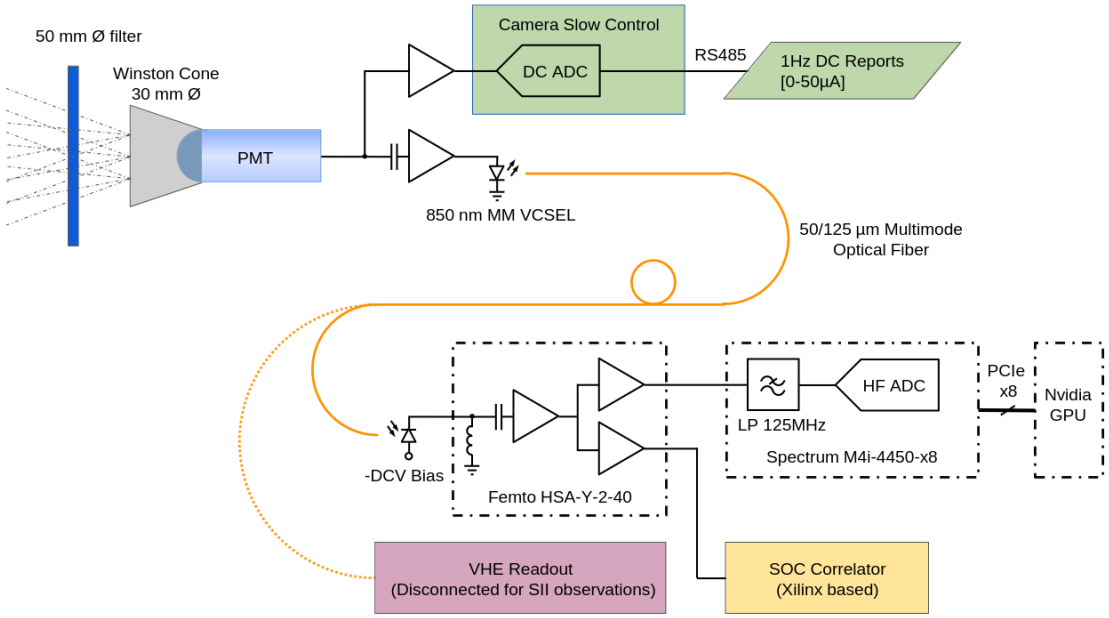

Figure 5.2: *Diagram of the hardware setup of the MAGIC Stellar Intensity Interferometer (image from a private communication for a paper in preparation).*

5.2 MAGIC AMC

5.2.1 Finding the focusing parameters

During regular VHE observations, the MAGIC telescopes focus their reflectors to the typical distance of EAS, $\sim$10 km, in order to get as sharp a shower image as possible. When performing intensity interferometry observations, we are looking at stars that are at several pc away, so by all intents and purposes at 'infinite' distance, and we are trying to get as much light as possible into the pixel that has the filter in front of it, besides, this pixel is not at the center of the camera. This means that the AMC parameters, that control how each of the actuators behind the mirrors behave, cannot be the same for both kinds of observations.

In order to find the AMC parameters that allow the telescopes to focus to infinite distance and not to the center of the camera, we pointed at a non-variable bright star (B magnitude $\sim$1, like Adhara or Alnilam), at low zenith (<30 deg) to start with as much light as possible, but being careful that the measured DC did not go beyond the safety limit of 40 μA. We then made a preliminary guess of the AMC parameters (X, Y ,Z) and performed 5x5 quick sweeps in RA/DEC in steps of 0.05 arcdeg, in which the center position is the position of the star. We refer to this procedure as a 'dcTpoint'. In each of these positions we measured the DC in the interferometry pixel. One must measure the DC always in the same pixel instead of measuring the 6 pixels around the target pixel because each pixel has a different gain and therefore we could not be sure that the differences in DC would come because of the focusing parameters alone. This method has another advantage because the FOV of each pixel is 0.1 arcdeg, whereas our steps are 0.05 arcdeg, which translates into better spatial resolution.

I wrote a python tool (dcTplotter.py) to read the DC reports and produce plots to visualize the light distribution. The observed distribution of light can be described with a 2-dimensional gaussian with two different widths and shared amplitude and constant. We tried several AMC parameters until we minimized the two widths of the gaussian and maximize the DC value in the central position.

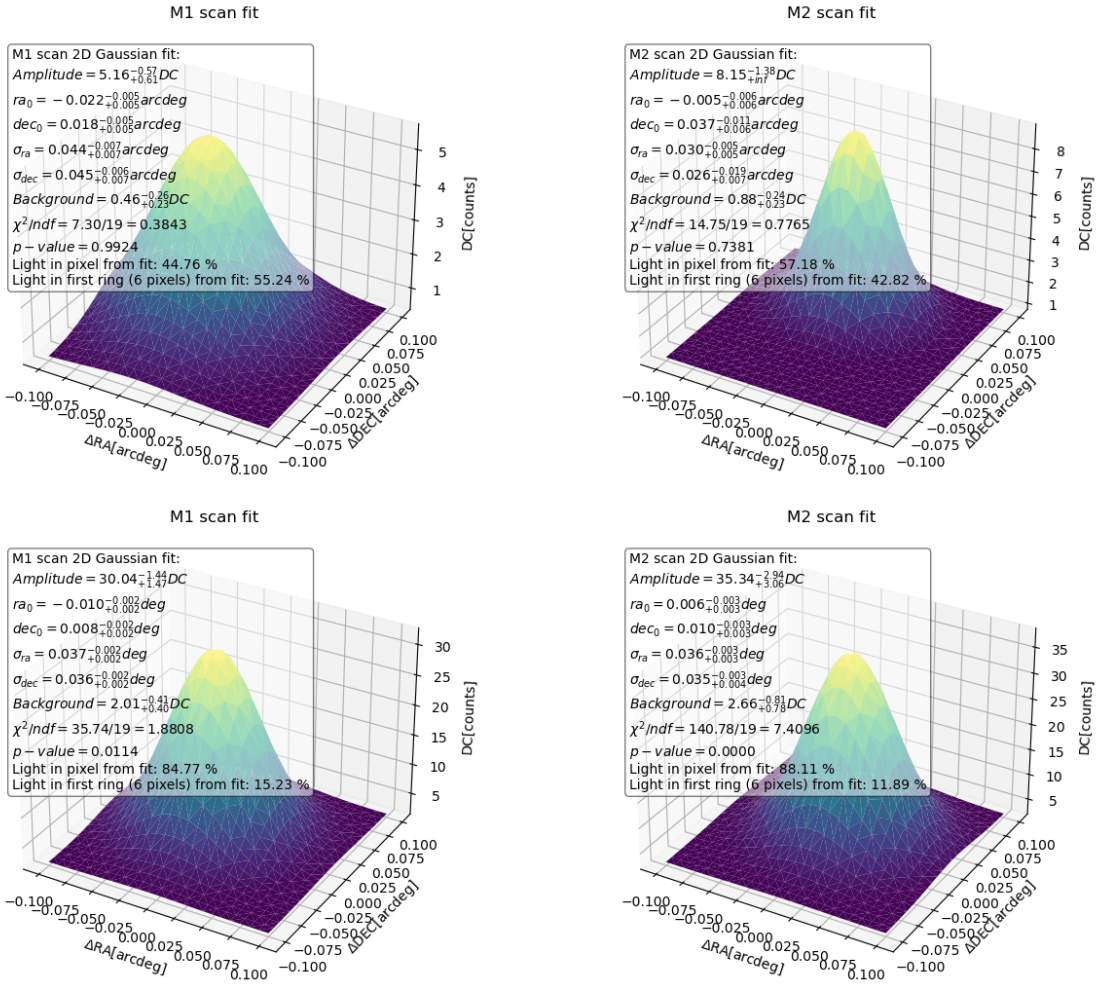

Figure 5.3: *dcTpoints using the star Alderamin. Top two plots: observed distribution of light for a preliminary set of parameters for MAGIC 1 (top left) and MAGIC 2 (top right). No more than 57% of light is contained within the target pixel, most of it is lost in the surrounding 6 pixels. Bottom two plots: observed distribution of light for a different set of parameters after a few tries, for MAGIC 1 (bottom left) and MAGIC 2 (bottom right). In this case ∼85% or more of light is contained within the target pixel, meaning that these focusing parameters are much better than the other ones.*

Once the distribution did not get any narrower or better centered, the parameters were set and were used in all observations with pixel 251 from that point on. When the upgrade of adding the second filter in front of pixel 260 was made, since the position in the camera is mirrored from 251, only the X parameter needed to be changed into its mirrored value.

5.2.2 Mirror configurations

Intensity interferometry observations are typically performed using the whole dishes of 17 m diameter (full mirror configuration) in order to collect as much starlight as possible, but thanks to MAGIC's AMC the individual facets that compose each dish can be focused into different pixels independently.

Full-mirror configuration In this configuration all the facets of each mirror dish are focused into one pixel. Pixels 251 and 260 of each telescope have filters that fall in front of them when the white target is deployed, and are connected to the interferometry setup. Full-mirror observations can be performed focusing the light of both telescopes to their respective pixels 251 ('Full-mirror to 251') or to pixels 260 ('Full-mirror to 260').

Checkerboard or chessboard configuration In this configuration, half of the facets of each dish are focused into one pixel and the other half into other pixel, following a chessboard pattern (see figure 5.4. This configuration allows to measure 6 cross-correlations simultaneously but with half the mirror area. Two of these 6 cross-correlations are made within the same telescope, which translates into measurements at roughly 0 baseline that can be used to calculate the ZBC for those combinations of channels.

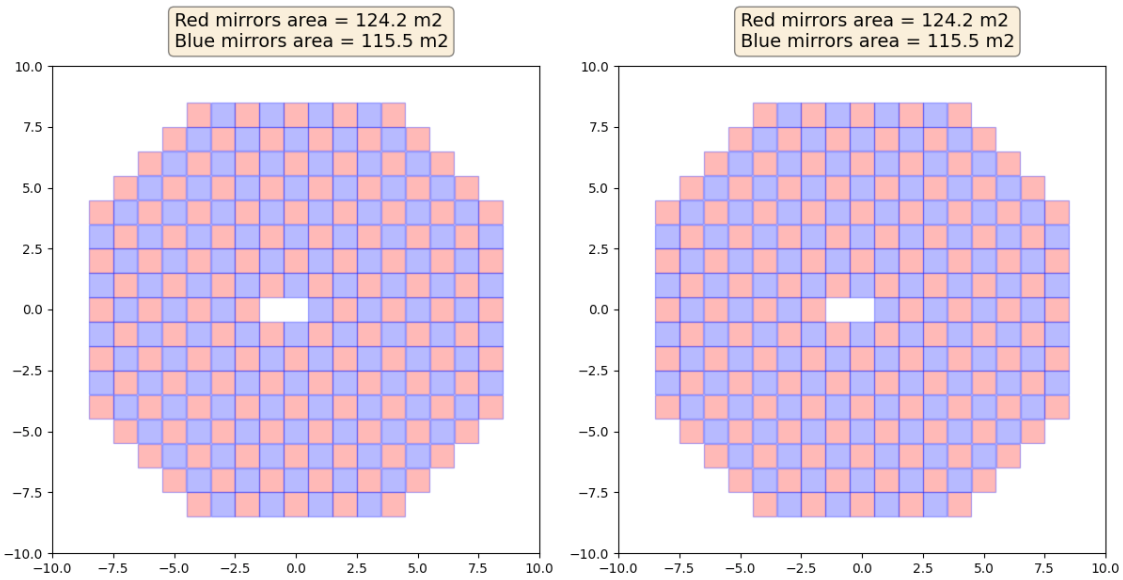

Figure 5.4: *Chessboard configuration for MAGIC 1 and MAGIC 2. The red facets focus the light into one pixel and the blue facets into another. Axis are in arbitrary units. The total mirror areas are similar with: 124.2 m^2 for the red facets and 115.5 m^2 for the blue ones. Plots by courtesy of T. Hassan.*

Submirrors configurations Instead of using the whole mirror, one can create virtual smaller telescopes by focusing groups of facets into different pixels. This kind of observations make use of smaller mirror areas, so they are ideal for larger and brighter stars: the bigger the star the stronger is the effect of the convolution of the mirror size with the spatial coherence (see 7.3) so smaller mirror sizes allows to resolve it better by accessing shorter baselines, and since the mirror area is smaller the magnitude should be smaller in

order to have enough photon flux to make a correlation detection.

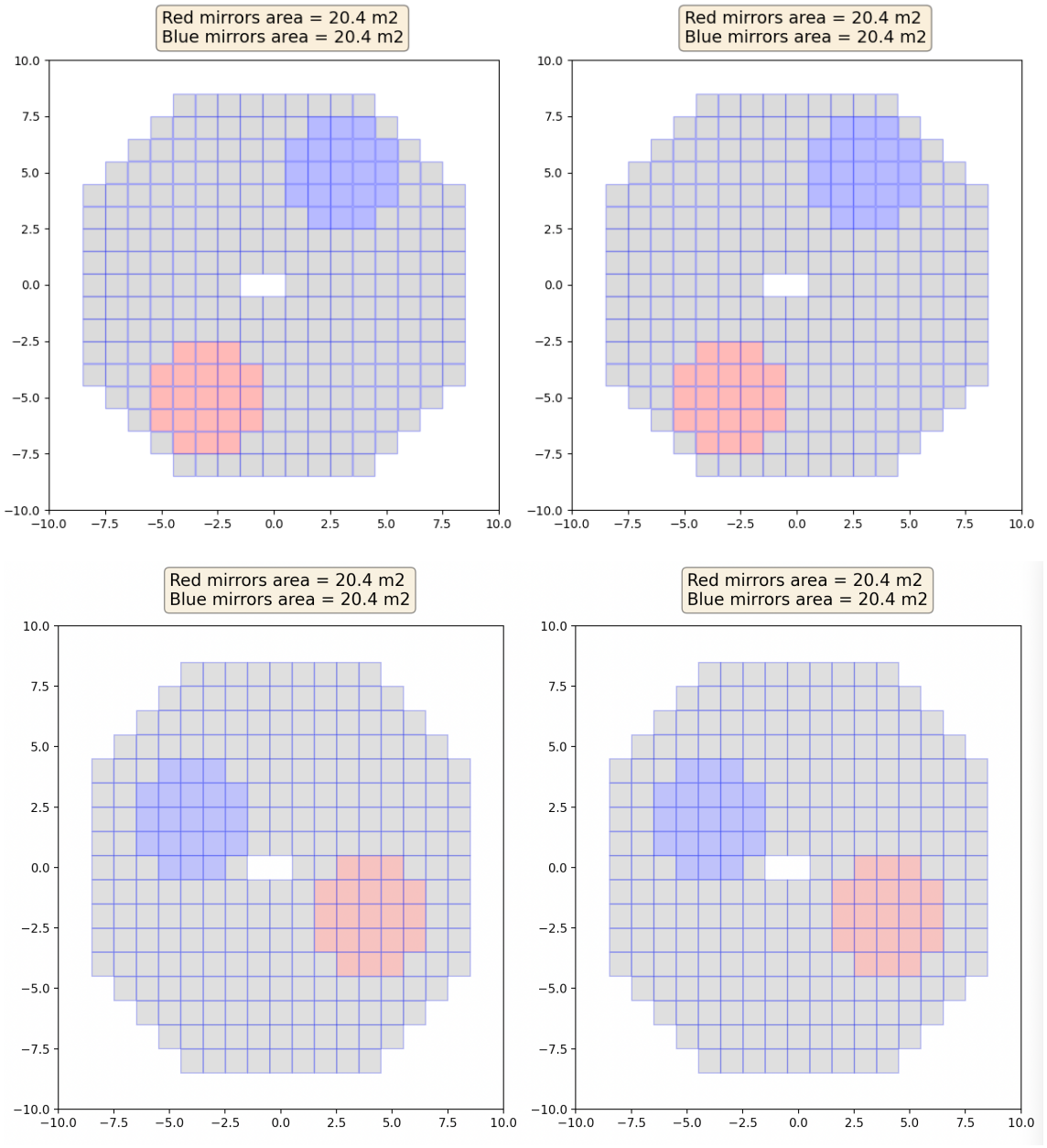

Figure 5.5: *Submirrors configurations 22 (top) and 28 (bottom) for MAGIC 1 (left) and MAGIC 2 (right). Axis are in arbitrary units. Both configurations have submirrors of 20.4 m^2 but the orientation and distance between them is different. Plots by courtesy of T. Hassan.*

6. Intensity interferometry observations

Over the course of a year, around 5 nights each month have too much moonlight to allow for sensitive VHE observations. Before the implementation of MAGIC's intensity interferometry setup, operations stopped during these nights, also called 'Moon breaks'. But intensity interferometry observations do not need the same dark conditions as VHE observations, mainly thanks to the filters that block out most of the blue moonlight. This translates into the necessity of properly allocate extra $\sim$300 h a year, deciding the best science targets and when to observe them. For this purpose, as the intensity interferometry scheduler for 2 years, I was tasked with building a catalogue of intensity interferometry targets and use said catalogue to build a schedule throughout the year.

6.1 Building the candidates and calibrators catalogue

In order to identify the best targets for intensity interferometry observations with the MAGIC telescopes I built a star catalogue combining three catalogues of measured and expected stellar angular diameters:

Swihart catalogue [169] contains modeled diameters for 1510 stars, with a declination between $-15°$ and $81°$, B magnitudes between 1.34 and 7.54 and angular diameters between 0.077 and 2.48 mas. The modeled diameters have been calculated by fitting the observed spectral energy distributions from literature to spectral templates.

JSDC v2 catalogue [170] contains modeled diameters for 465877 stars, covering all declinations, B magnitudes between -1.431 and 19.76 and angular diameters between 0.002 and 41.4 mas. It provides the both UD diameters and LD diameters in several bands (BVRIJHKLMN) as well as the respective magnitudes in these bands. The catalogue was built using the SearchCal tool [171, 172]: each diameter is modeled using a surface brightness method and calibrations for color indexes (B-V), (V-R) and (V-K) as described in [173]. The LD diameters are computed using the V magnitude together with the (V-K) color index and the UD diameters are obtained using linear limb-darkened coefficients from [174, 175].

JMDC catalogue [176] contains measured diameters for 1478 stars, covering all declinations, B magnitudes between -1.46 and 16.55 and angular diameters between 0.05 and 420 mas. The diameters have been measured by three methods: optical (amplitude) interferometry, lunar occultations and intensity interferometry. The objective of using this catalogue is to find a set of stars that we can use as calibrators or at least as reference stars to understand the performance of the MAGIC intensity interferometry setup at any given time.

Once I cross-referenced all three catalogues, I applied some filters in order to select the a set of stars observable with the MAGIC telescopes:

- Declination $> -51°$: so that they can be observed from the MAGIC telescopes site, Roque de los Muchachos Observatory, with a maximum zenith of 80 deg at least at some point in the year.
- Minimum necessary time for detection (5σ) of less than 5 hours at least at some point in the year: to focus first on stars that are easier (faster) to detect.
- B mag < 7 mag: magnitude affects the necessary detection time greatly, as seen in expression 6.6.
- Not being a spectroscopic binary: since they do not present radial symmetry in the UV plane.
- Not being in a double or multiple system in which the brightest companion is not at least 2.2 mag in B fainter or at a separation of more than 10 mas or both: depending on their brightness and position, they could affect the apparent shape of the star and the B magnitude.

Furthermore, in order to decide which stars are well suited as calibrators or reference stars from the JMDC catalog, I applied additional filters:

- The measurement of the diameter must have been performed in our same bandwidth (400-440 nm).
- Their combination of B magnitude, angular diameter and declination must allow for them to be detected by our interferometer in very short observation times (5 - 10 min per baseline bin).
- Not being a known fast rotator (star that rotates so rapidly that is elongated along the perpendicular to the rotation axis, see 4.3)..
- In case of being in a multiple system: not having a bright close companion (ΔB>2.2 or angular distance greater than 10mas).
- Not being too variable in magnitude (ΔB<1).
- In order to be a calibrator (and not just a reference star) the measured diameter must have better or similar precision to our own measurements.

The resulting reference/calibrator stars can be found in table 6.1.

Historical Name	Bayer Name	Spectral Type	B (mag)	Measured θ (mas)	Source
Adhara	eps CMa	B1.5II	1.29	0.77 ± 0.05	Narrabri
Bellatrix	gam Ori	B2V	1.42	0.704 ± 0.04	Narrabri
Alnilam	eps Ori	B0Ia	1.51	0.631 ± 0.017	VERITAS
Mirzam	bet CMa	B1II-III	1.73	0.523 ± 0.017	VERITAS
Saiph	kap Ori	B0.5Ia	1.88	0.44 ± 0.03	Narrabri
Naos	zet Pup	O4I(n)fp	1.98	0.41 ± 0.03	Narrabri
Gienah	gam Crv	B8III	2.47	0.72 ± 0.06	Narrabri

Table 6.1: *Table of reference/calibrator stars selected from JMDC, sorted by B magnitude. The spectral types and B magnitudes have been extracted from SIMBAD [177]. The measured angular diameters are from Narrabri ([157]) at 443 nm and VERITAS ([178]) at 420 nm.*

The total number of stars in this initial catalogue is 380, with declination from $-50°$ to $87°$, magnitudes in B band from 0.03 to more than 5 mag and angular diameters from 0.1 to more than 3 mas. Their spectral types are mostly early types: O (7 stars), B (211 stars), A (147 stars) and F (15 stars). This catalogue has been later expanded with a few more stars from special science cases and constitutes the input for the scheduling tool described in the next section.

6.1.1 The software: ii_scheduler

I built a tool specifically designed to schedule observations with the MAGIC telescopes in order to produce a schedule every Moon break or whenever VHE observations could not be performed.

First, a few inputs are necessary:

- The catalogue described in the previous section 6.1.
- The date and time of start and end of the observations. Typically starting at 19:30 UTC and ending at 7:30 UTC of the following day.
- MAGIC telescopes parameters: Geographical coordinates, altitude above sea level, distance between telescopes.
- MAGIC Intensity Interferometer setup parameters: central wavelength, quantum efficiency of the PMTs, the efficiency of the optical system, effective cross-correlation electrical bandwidth, excess noise factor of the PMTs, total mirror area and the normalized spectral distribution of the optical pass-band.
- Optional filters: maximum/minimum B mag, maximum/minimum zenith, maximum/minimum detection time, maximum/minimum angular diameter.

Then, the zenith and azimuth are calculated every half hour using the Python library astroplan from the Python library astropy. They are used to calculate the delay, baseline, B magnitude corrected by atmospheric extinction (B_{corr}), and differential stellar photon flux (n):

$$delay = \Delta x \cdot sin(zd) \cdot sin(Az) + \Delta y \cdot sin(zd) \cdot cos(Az) + \Delta z \cdot cos(zd) \tag{6.1}$$

$$baseline = \sqrt{separation^2 - delay^2} \tag{6.2}$$

$$B_{corr} = B + \frac{0.23}{cos(zd)} \tag{6.3}$$

$$n = \frac{0.0000869}{2.5^{B_{corr}}} \tag{6.4}$$

Where Δx, Δy and Δz are the separation between MAGIC 1 and MAGIC 2 respectively along the east-west direction, the north-south direction and the vertical direction and were obtained a few years ago with 0.1 mm precision (see Figure 6.1.

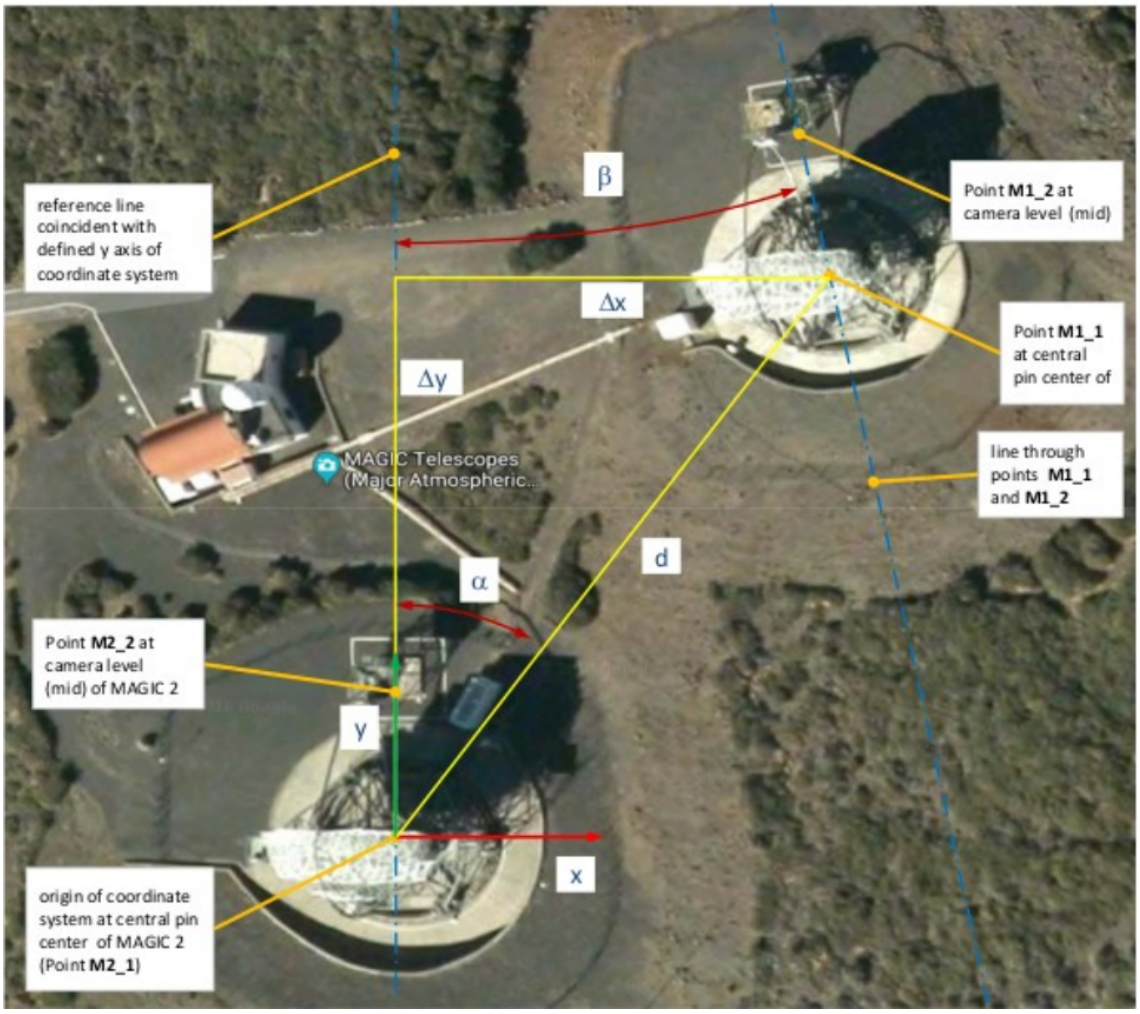

Figure 6.1: *Satellite view of the MAGIC telescopes with some lines and arrows that show the positions, angles and distances of the telescopes from Google Earth .*

These parameters together with the UD visibility already defined in expression 4.2, allow to calculate the expected signal-to-noise using the expression 5.6 from [157]:

$$S/N = Area \cdot \alpha(\lambda) \cdot q(\lambda) \cdot n(\lambda) \cdot |V|^2(\lambda, baseline) \cdot \sqrt{(}b_v) \cdot F^{-1} \cdot \sqrt{(}T/2) \cdot \sigma \cdot (1+\beta)^{-1} \tag{6.5}$$

and the necessary observation time to get a detection (5σ) of the correlation:

$$T(5\sigma)[s] = \frac{50}{(A \cdot \alpha(\lambda) \cdot q(\lambda) \cdot n(\lambda) \cdot |V|^2(\lambda, baseline) \cdot \sqrt{(}b_v) \cdot F^{-1} \cdot \sigma \cdot (1+\beta)^{-1})^2} \tag{6.6}$$

For both expressions the parameters are: the mirror area A, the PMT quantum efficiency at the peak of the optical pass-band $\alpha(\lambda)$, the efficiency of the optical system, the differential stellar photon flux $n(\lambda)$, the effective cross-correlation electrical bandwidth b_v, the excess noise factor of the PMTs F, the observation time T, the normalized spectral distribution σ and the ratio between starlight and background light β. (These parameters can be found in table 1 of the 2020 MAGIC intensity interferometry publication [167]).

The zenith, azimuth, delay, baseline, visibility, T(5σ) and S/N together with the angular distance from the Moon are presented in different tables and plots in a LaTeX-PDF report, which includes the following sections:

Summary table of the stars that are observable in at least one of the half hour slots within the time-slot given as input. It is a quick look into what stars are going to be more easily detected.

Name	RA(hh mm ss) DEC (dd mm ss)	Bmag (mag)	θ (mas)	min T(5σ) (min)	Best hour (UTC)	zd at best hour (dd mm ss)
eps CMa	06 58 37.54876 -28 58 19.5102	1.29	0.77	0.3	00:00	66d38m53.26273786s
bet CMa	06 22 41.9853527 -17 57 21.307352	1.73	0.523	0.5	23:00	54d20m14.88387895s
eps Ori	05 36 12.81335 -01 12 06.9089	1.51	0.631	0.6	23:00	48d48m07.51863663s
kap Ori	05 47 45.3888404 -09 40 10.577707	1.88	0.44	0.6	22:30	48d03m06.39532444s
gam Ori	05 25 07.86325 +06 20 58.9318	1.416	0.704	0.8	23:00	46d21m11.6465129s
eta UMa	13 47 32.43776 +49 18 47.7602	1.751	0.937	1.1	22:30	68d39m01.43795846s
zet Pup	08 03 35.04754 -40 00 11.3321	1.98	0.41	1.1	23:30	69d35m37.11678716s
eps UMa	12 54 1.75 +55 57 35.36	1.738	1.4448455	1.8	20:30	75d09m06.79689564s
eta Cen	14 35 30.42 -42 9 28.17	2.173	0.569879	2.1	06:30	72d58m17.02135978s
eta CMa	07 24 05.70228 -29 18 11.1798	2.367	0.72	2.3	00:00	64d08m13.30462358s
gam Crv	12 15 48.37081 -17 32 30.9496	2.473	0.72	2.9	05:30	59d16m36.35306724s
alf Cyg	20 41 25.91514 +45 16 49.2197	1.342	2.041944	3.1	04:30	78d21m37.51740577s
ups Sco	17 30 45.84 -37 17 44.93	2.521	0.483078	3.8	07:30	66d49m06.40021686s
bet UMa	11 01 50.4765370 +56 22 56.733912	2.373	1.133	4.2	19:30	68d26m06.68607859s
sig Sgr	18 55 15.92650 -26 17 48.2068	1.923	0.678677	4.4	07:30	62d52m33.94003802s
gam Peg	0 13 14.15 +15 11 0.94	2.64	0.4174095	4.5	19:30	63d59m17.02176581s
omi02 CMa	7 3 1.47 -23 49 59.85	2.943	0.47685	4.6	23:30	58d20m16.27998368s
alf02 CVn	12 56 1.67 38 19 6.15	2.775	0.649454	5.9	22:30	63d13m54.04066528s
eta Aur	05 06 30.8933734 +41 14 04.112721	3.032	0.444	7.0	19:30	13d09m57.79352203s
del Crv	12 29 51.86 -16 30 55.55	2.928	0.764645	7.5	06:00	60d59m27.07650265s
eps Cas	1 54 23.73 63 40 12.36	3.2	0.3561515	7.6	19:30	44d21m25.11043478s
mu. Lep	5 12 55.90 -16 12 19.69	3.19	0.579853	8.5	22:00	54d03m54.19802617s
eta Lup	16 0 7.33 -38 23 48.15	3.214	0.35494	9.4	07:30	68d09m37.93636732s
zet Per	03 54 07.9224751 +31 53 01.081262	2.97	0.531	9.8	19:30	11d43m34.75725842s
bet CMi	7 27 9.04 8 17 21.54	2.793	0.6830885	10.0	01:00	44d57m49.15119548s
alf Cep	21 18 34.77 62 35 8.07	2.707	1.3310365	10.7	05:00	71d05m24.48801483s
zet Cas	00 36 58.2841866 +53 53 48.867311	3.494	0.305	12.8	19:30	51d06m51.64167933s
gam Lyr	18 58 56.6224137 +32 41 22.400295	3.201	0.696373	17.2	04:30	65d15m37.46598079s
bet Cas	00 09 10.68518 +59 08 59.2120	2.66	1.835882	17.4	07:30	74d57m01.16002572s
tau Her	16 19 44.43666 +46 18 48.1123	3.759	0.354	17.5	04:00	39d16m25.79459807s

Table 6.2: *Sub-sample of the summary table generated for the night of the 27th to 28th of February of 2023. For each star it includes: the Bayer designation, RA/DEC coordinates, B magnitude, angular size, minimum observation time to get 5 σ in minutes, best hour to observe (defined as the time in the night where the S/N per unit time is the highest) and the zenith at that time.*

Tables of expected parameters every half hour typically starting at 19:30 UTC and ending at 7:30 UTC sorted by observation time to get 5σ. Each row shows the value of each parameter at the beginning of the 30 min slot and right at the end for a given star. This allows to see the evolution of the different parameters within 30 min. For example one could check if a star is getting too close to the Moon, or the zenith getting too high, or the baseline range not being the best for getting a good diameter measurement, or checking that the measurement would be in a baseline range not yet covered by previous observations, or the necessary observation time for detection getting too high. The final purpose is to help the scheduler decide when to start and stop observing each star in order to efficiently distribute the targets in the given time-slot.

name	zd(deg)	Az(deg)	delay(ns)	baseline(m)	$\|V\|^2$	T(5σ)(min)	S/N(T=1s)(σ)	Moon sep(deg)
kap Ori	38.43 – 39.07	179.70 – 191.51	-148.74 – −168.45	72.71 – 68.74	0.72 – 0.75	0.74 – 0.69	0.75 – 0.78	38.01 – 37.98
bet CMa	47.52 – 46.75	168.48 – 178.19	-149.05 – −170.25	72.65 – 68.34	0.62 – 0.66	0.81 – 0.72	0.72 – 0.76	49.08 – 49.04
eps Ori	30.06 – 31.50	185.35 – 199.80	-128.18 – −147.32	76.15 – 72.97	0.46 – 0.49	0.87 – 0.76	0.69 – 0.74	29.08 – 29.05
eps CMa	60.24 – 58.61	162.00 – 169.40	-153.21 – −174.28	71.87 – 67.42	0.35 – 0.40	1.45 – 1.06	0.54 – 0.63	62.74 – 62.69
gam Ori	22.97 – 25.52	193.94 – 211.13	-107.76 – −125.93	78.94 – 76.48	0.35 – 0.37	1.26 – 1.10	0.57 – 0.61	21.05 – 21.01
eps UMa	75.15 – 71.39	33.81 – 35.80	274.02 – 268.30	23.00 – 28.42	0.70 – 0.57	1.82 – 1.95	0.48 – 0.46	84.30 – 84.20
zet Pup	75.77 – 73.12	153.74 – 159.05	-136.81 – −156.59	74.79 – 71.22	0.74 – 0.76	2.72 – 1.98	0.39 – 0.46	79.61 – 79.55
gam UMa	68.21 – 63.93	39.74 – 41.14	261.52 – 252.01	33.62 – 39.61	0.68 – 0.58	4.28 – 4.90	0.31 – 0.29	78.31 – 78.19
alf Col	62.85 – 63.46	181.77 – 188.72	-215.40 – −231.46	55.73 – 49.61	0.51 – 0.59	7.05 – 5.37	0.24 – 0.28	60.88 – 60.89
bet UMa	60.35 – 56.19	38.83 – 39.28	244.54 – 233.32	43.62 – 48.83	0.44 – 0.35	6.68 – 9.63	0.25 – 0.21	70.41 – 70.30
omi02 CMa	55.71 – 53.77	158.90 – 166.99	-135.93 – −158.13	74.93 – 70.91	0.66 – 0.69	7.58 – 6.69	0.23 – 0.25	59.02 – 58.96
eps Cas	50.45 – 53.70	330.93 – 330.07	96.06 – 97.63	80.28 – 80.11	0.77 – 0.77	8.21 – 8.61	0.23 – 0.22	47.46 – 47.50
zet Per	24.41 – 30.79	284.56 – 284.96	-43.16 – −51.42	84.30 – 83.89	0.51 – 0.52	9.89 – 10.02	0.21 – 0.20	13.74 – 13.86
gam Peg	77.06 – 79.86	280.54 – 282.00	-112.30 – −106.69	78.37 – 79.07	0.71 – 0.70	11.78 – 19.92	0.19 – 0.14	65.04 – 65.11
zet Cas	59.92 – 64.25	318.50 – 319.48	58.70 – 65.70	83.46 – 82.99	0.81 – 0.82	15.06 – 17.06	0.17 – 0.16	53.94 – 54.01
alf02 CVn	79.92 – 79.58	51.77 – 51.96	266.43 – 265.84	29.95 – 30.43	0.89 – 0.88	16.26 – 15.14	0.16 – 0.17	95.66 – 95.65

Table 6.3: *Sub-sample of the table generated for the night of the 27th to 28th of February of 2023, for the time slot of 20:30 to 21:00 UTC. Each line corresponds to a different star and shows: the Bayer designation, zenith, azimuth, delay, baseline, visibility, necessary observation time to get 5σ, S/N per 1 second, and angular separation from the Moon.*

Plots several plots are generated for each star: zenith vs time, visibility vs time, baseline vs time, delay vs time, time to get 5σ vs time, visibility vs baseline and visibility vs zenith. For stars for which different estimations/measurements of the angular size are available, several curves are shown for: time to get 5σ vs time, visibility vs baseline and visibility vs time. See example for gam Ori in Figure 6.2. They display the same information as the previous tables but in a graphical way, being every point 30 min apart. This allows to follow the evolution of the parameters over the whole night.

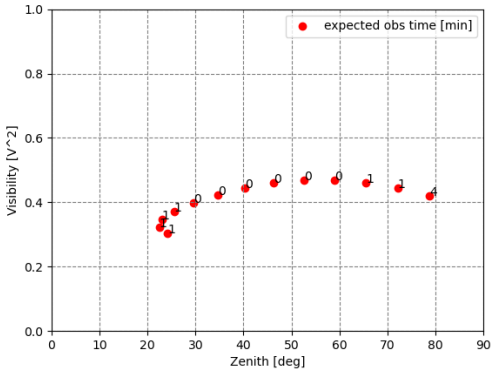

(a) *Visibility vs zenith with $T(5\sigma)$ in minutes on each point.*

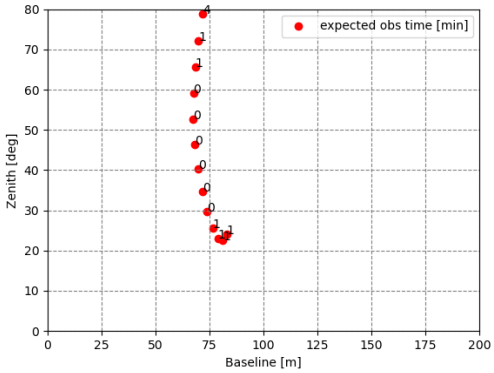

(b) *Zenith vs baseline with $T(5\sigma)$ in minutes on each point.*

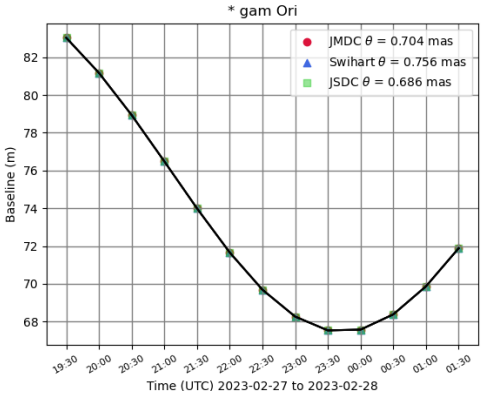

(c) *Baseline change along the whole time-slot.*

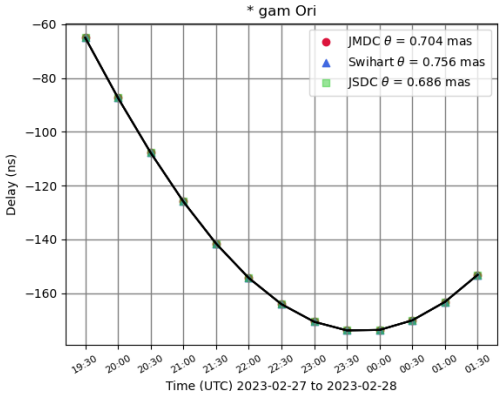

(d) *Delay change along the whole time-slot.*

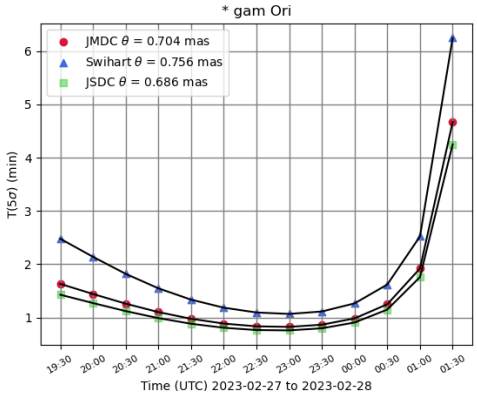

(e) $T(5\sigma)$ *change along the whole time-slot.*

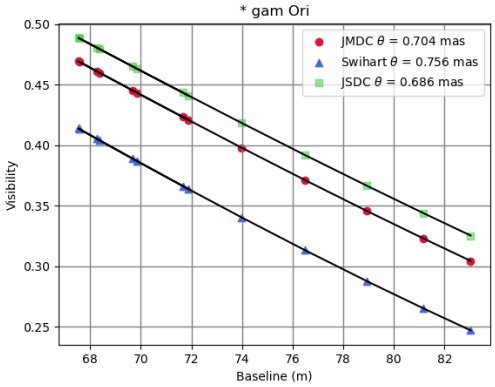

(f) *Accessible range of baseline vs visibility along the whole time-slot.*

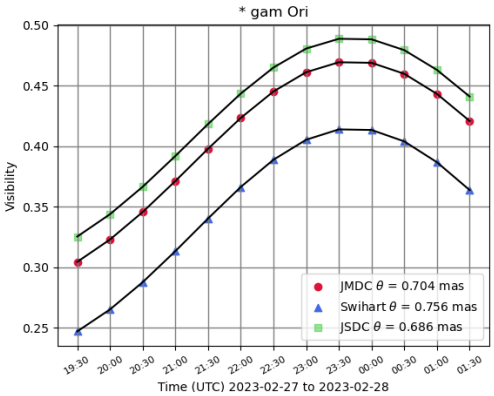

(g) *Visibility change along the whole time-slot.*

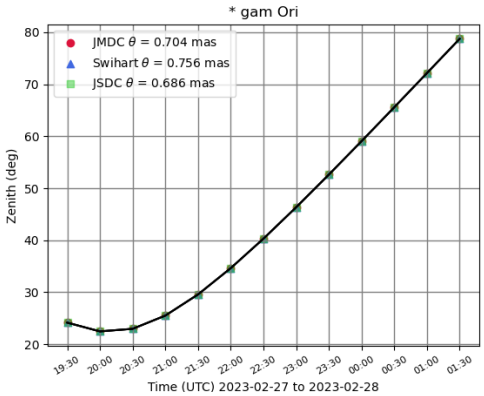

(h) *Zenith change along the whole time-slot.*

Figure 6.2: *Examples for gam Ori for the night of the 27th to 28th of February 2023.*

6.2 Building a schedule

When building a schedule for observations of an astronomical source, one usually aims at observing when the zenith distance is as low as possible, so as to minimize the atmospheric

extinction. One also tries to minimize the amount of background light in the FOV from other sources (Sun at sunrise/sunset, Moon, or other astronomical sources). While this still applies to intensity interferometry observations there are a few differences.

Single stars For the most simple kind of intensity interferometry observations, looking at a single non-variable symmetrical star, it is necessary to have into account not only the above-mentioned points in order to successfully schedule the best moment of observation, but to have in mind that what we are not just trying to maximize the flux of photons, but to optimize the distribution of visibility measurements over the baseline range.

The position in the sky of the star at any given moment (zenith/azimuth) will translate into a certain delay/baseline between the telescopes with its correspondent degree of spatial coherence or visibility, which depends on the wavelength and angular size of the star.

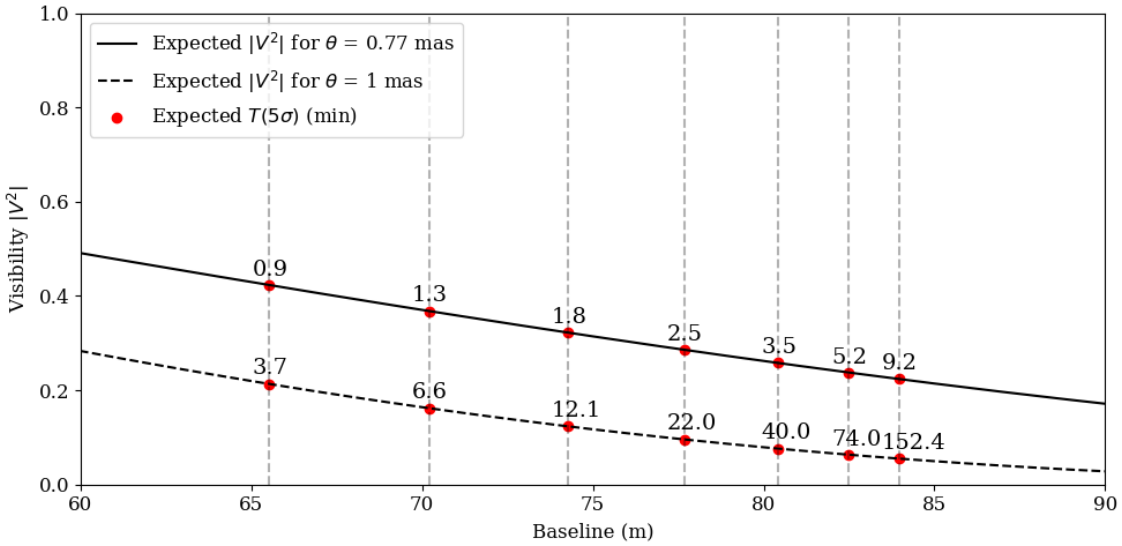

Figure 6.3: *Comparison for an Adhara-like star (same angular diameter, coordinates and B mag) between having the literature diameter of 0.77 mas (black full line) or 1 mas (black dashed line) for every half hour for a certain night. For a smaller diameter the spatial coherence is higher for the same baseline and the observation time (values above each red dot) required for a 5σ detection is lower.*

But getting a good visibility signal in a single delay/baseline is not enough to get a good measurement of the angular diameter. The visibility changes more slowly with baseline for smaller stars than for bigger as shown in figure 6.3. This means that the range of baselines that needs to be covered for the smaller star is wider than for the larger star (both being in the same position in the sky and with the same magnitude) in order to get the same precision in the angular diameter measurement. Figure 6.4 shows how measurements performed at the same baselines for a smaller and a larger star retrieve different precision in the angular diameter measurement, being lower for the smaller star than for the larger one (11% vs 7% relative error respectively). However, figure 6.5 shows that measurements with same significance as the previous case but performed at longer baselines for the smaller star now result in a better measurement of the angular diameter (7% relative error).

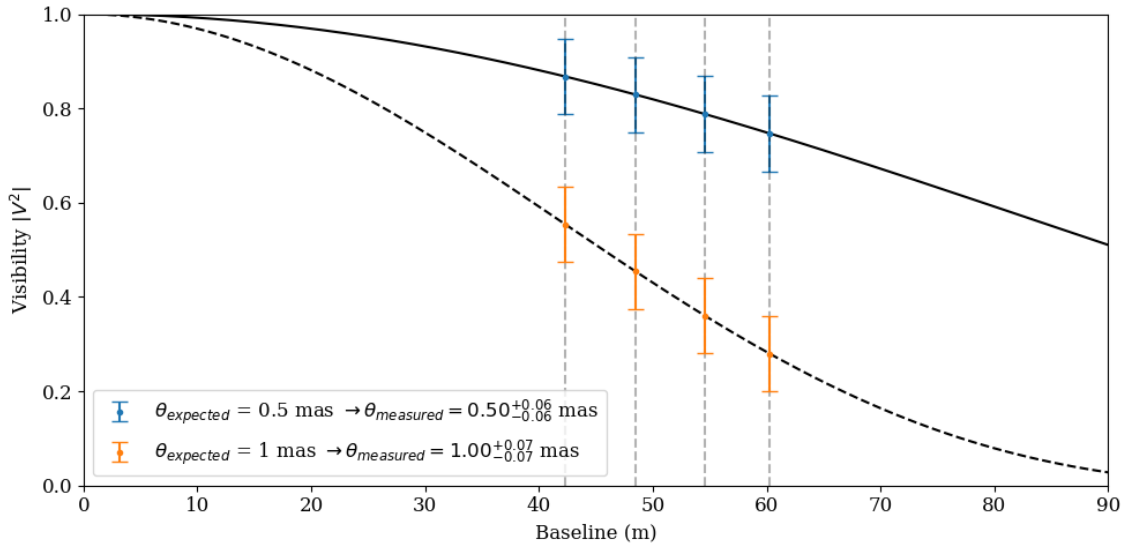

Figure 6.4: *Comparison between reconstructed values of the diameter for an Adhara-like star of 0.5 mas or 1 mas diameter. Eachvisibility point is the theoretical value given by the uniform disk model expression 4.2 for each corresponding baseline. Additionally, every point has the same error value of 0.08 in visibility. A bootstrap fit of each set of values gives a relative error of 11% for the smaller case of 0.5 mas and 7% for the bigger case of 1 mas.*

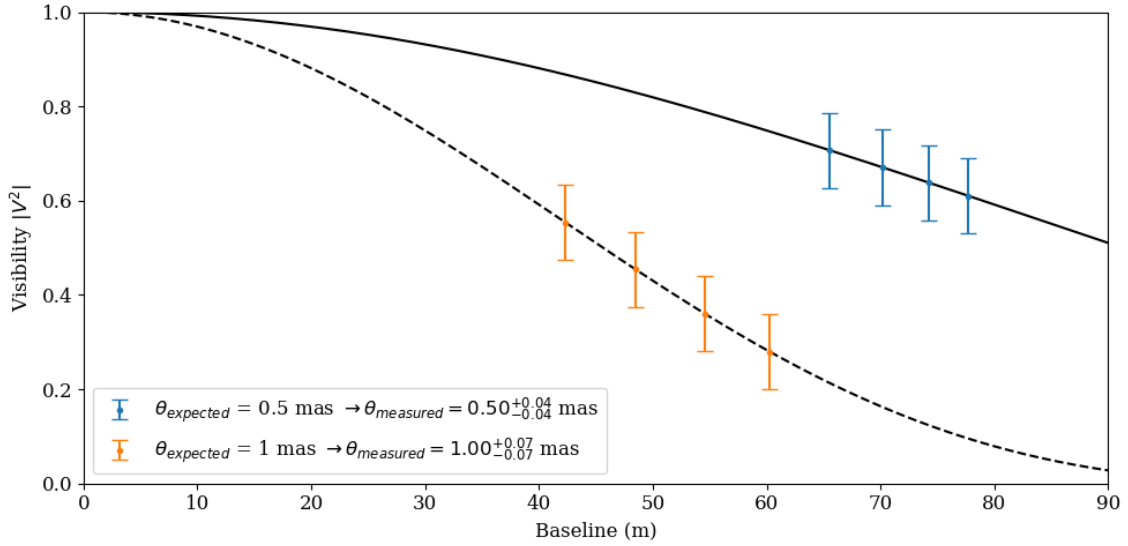

Figure 6.5: *Same as the above but covering longer baselines for the 0.5 mas case, that results in achieving the same relative error than the 1 mas case (7%).*

The range of accessible baselines is given by the position of the star with respect to the telescopes, therefore it is possible that even though one can physically point at certain stars and get good visibility signals from them, will not be able to get a good measurement of the angular diameter, or at least not the best possible. Figure 6.6 shows that for a star of 1 mas, measurements performed at longer baselines return a better measurement of the angular diameter than measurements performed at shorter baselines (with the same significance).

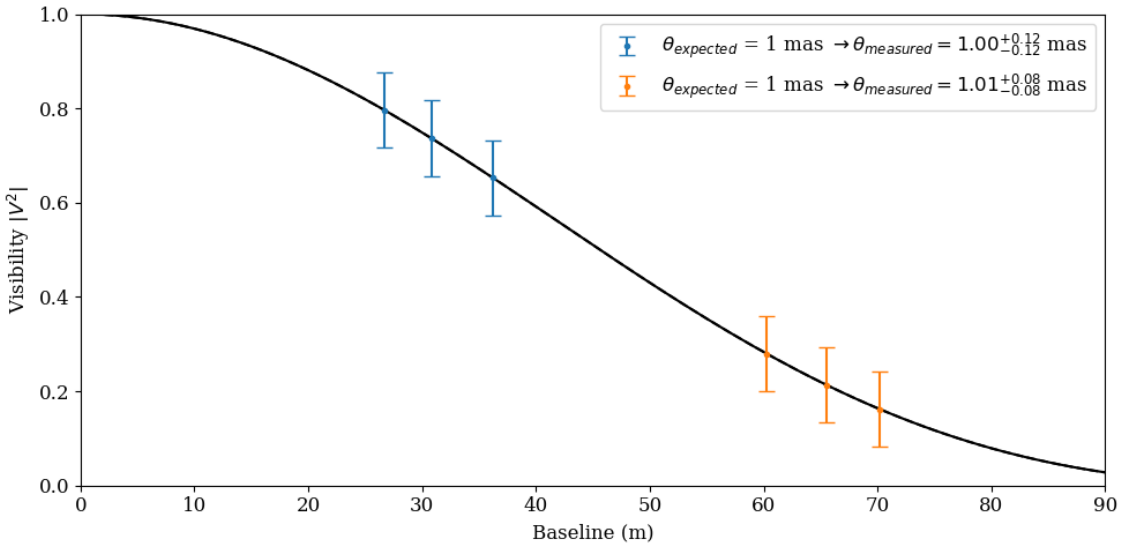

Figure 6.6: *Comparison between two bootstrap fits using different sets of measurements at shorter (blue) and longer (orange) baselines. The resulting diameters are compatible but for longer baselines the relative error is lower (8%) than for shorter baselines (12%).*

Since intensity interferometry observations are taken during Moon breaks, we have full Moon conditions for the vast majority of the observations. This effect is less intense than for VHE observations since interferometry observations require the use of optical filters. This means that most of the light from the Moon is filtered out, but some still goes through the filter and is our main source of background light. The ratio between Moon's flux of uncorrelated photons and the correlated photons from our source can affect our S/N ratio and by proxy the necessary observation time to get 5σ (see parameter β in expression 6.5). In order to minimize this ratio and keeping it below the 30%, only observations in zenith/azimuth positions that are at least at 50 deg distance from the Moon are scheduled.

If a star has been previously observed, it is needed to perform at least a preliminary analysis in order to know how much more time is needed at certain baselines. If some of the observations were performed during bad weather the visibility signal could not be significant enough and more time needs to be invested in the same baselines. Or if some observations could not be/have not been performed yet at the rest of the necessary baselines to get a good measurement of the angular diameter, then those are the ones that take priority.

In cases in which radial symmetry is not expected it is needed to take into account even more parameters:

Fast rotators As described in chapter 4.3, fast rotators are stars that spin so rapidly that they exhibit an elongation perpendicular to the axis of rotation. Depending on the oblateness or ratio between the semi-major and semi-minor axis of the star and the orientation of their axis of rotation with respect to the position of the telescopes, one could see more or less difference between the angular diameter measurement when observing in one orientation or another at $\pm 90°$. This translates into the necessity of taking into account not only the delay/baseline of each observation, but its orientation in the UV plane (UV angle), since the expected visibility distribution in said UV plane will not have radial symmetry,

but will appear elongated as well.

The orientation of the rotation axis and the oblateness of fast rotators are not always perfectly known and therefore is needed to calculate the necessary observation time to get 5σ using a preliminary expected average value of the angular diameter usually provided from stellar models and spectroscopy, but keeping an eye on the UV positions that can be covered so that as many measurements at $\pm 90°$ between them as possible can be performed. Examples of stars with 'good' and 'bad' UV coverage are shown in figure 6.7. In the figure, the UV coordinates that can be covered from the position and orientation of the MAGIC telescopes throughout the year is shown, together with the necessary observation time to get 5σ (with a limit of 5 h per observation). For the star with $-15°$ of declination, the UV coverage is not 'good', meaning that there are not many measurements that can be performed at ± 90 from each other, while the opposite happens for the star at 48°, which is considered to have a 'good' UV coverage.

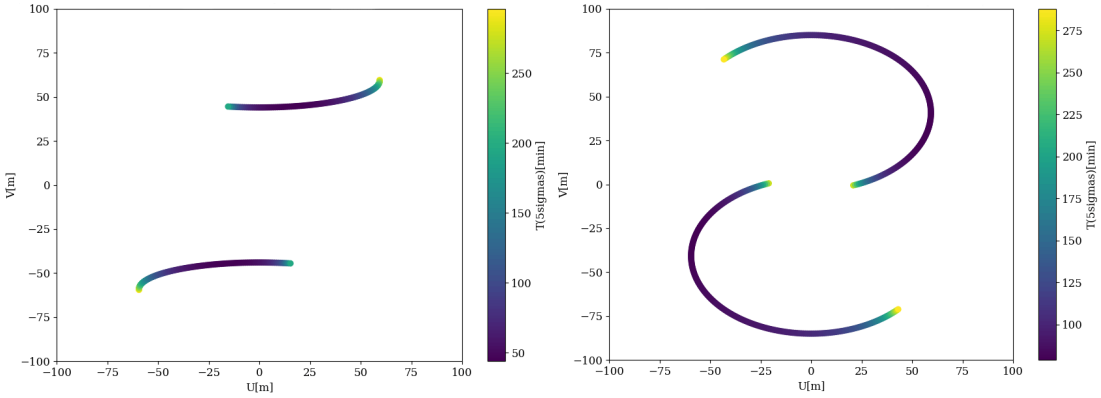

Figure 6.7: *UV points covered stars of declination* $-15°$ *(left) and* 48° *(right) over the course of a year, if measured each night at midnight. The color represents the necessary observation time to get* 5σ *in minutes, only points with less than 5 h of observing time are shown. For the star with lower declination (left) the covered UV angle is much more limited than for the star with larger declination (right).*

Binaries In this case not only is needed to take into account all of the parameters above, including the UV coverage, but also the expected position of the binary components at any given time, because this will translate into different visibility patterns in the UV plane. This can be calculated if orbital parameters are known beforehand from the literature.

Provided the UV angle coverage is wide enough (in a single night or within a few days), more or less information can be derived from the UV pattern. If the orbital period is long enough (tens of days or more) or if the components are in (or close to) the apoastron (when they are the most far away from each other), then the UV pattern should change very slowly, and more visibility points in the UV plane can be probed (with 2 telescopes one can only probe one point at a time), allowing a good understanding of that particular pattern (see right side of figure 6.8). If on the contrary the orbital period is very short (a few days or less) or the components are in (or close to) the periastron (when they are the closest), the pattern changes greatly in a manner of minutes or hours, making increasingly difficult to resolve it (see left side of figure 6.8). In any case, the expected visibility can be

calculated at any given time, and therefore the expected necessary observation time to get 5σ. In order to observe each of this patterns that the components produce in their orbital motion it is important to take into account the orbital phase of the system and try to cover as many different phases as possible.

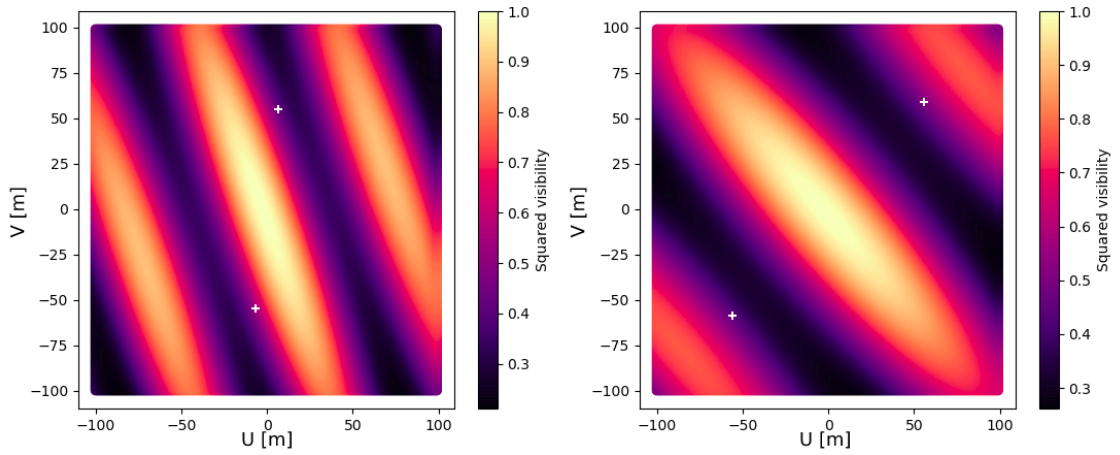

Figure 6.8: *Comparison of visibility patterns in the UV plane for a spectroscopic binary in the periastron (left) and apoastron (right). The white crosses represent the UV points seen by the telescopes at each of those moments.*

Sometimes the orbital parameters are not fully known or the period of the apsidal motion (precession of the line that connects the periastron with the apoastron) is too short, therefore for every studied system a initial guess of the missing parameters is made, and then is constantly revised through analysis of the data.

6.3 Summary

Each time I had to prepare a schedule, I followed this prescription: first, schedule enough calibrator observations to keep track of the performance of the setup. Then, schedule 'main science-case' observations (fast-rotators, binaries and asteroseismology targets) to fulfill the main science-case objectives of our yearly proposal of observations. Finally, schedule single (in principle) stars with unknown angular diameter in order to build a catalogue of angular diameters that can be exploited in the future. During the course of my PhD I have been responsible to schedule about 420 h of MAGIC observation time, most of it during Moon breaks and some of it in dark time. I was the official intensity interferometry scheduler for 2 years and I was tasked with leading the last observation proposal of the MAGIC interferometry team which was awarded the highest category grade and was 3rd in the list of approved proposals.

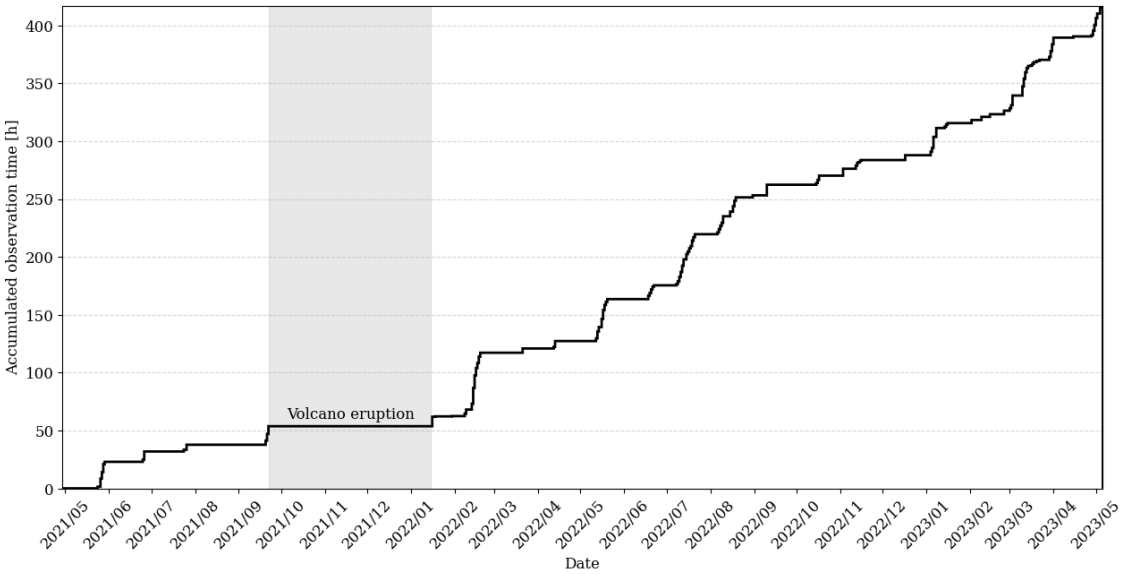

Figure 6.9: *Accumulated observation time since the end of April 2021 until the beginning of May 2023, including a brief interruption due to Cumbre Vieja volcano's eruption.*

7. Analysis procedure and evaluation of systematics

Measuring our signals using the same kind of PMTs that we use for VHE observations means that we are not measuring the signal intensities directly I_i but the anode currents of the PMTs which are proportional to them $\langle I_i \rangle \propto DC_i$. Since the intensity fluctuations follow a Poisson distribution, it can be shown as well that $\sqrt{\langle (I_i(t) - \langle I_i \rangle)^2 \rangle} \propto \sqrt{DC_i}$.

Camera reports are produced every second, keeping track of the DCs and other parameters, while the signal from the pixels is digitized at 500 MSamples/s. The digitized signal is later processed by the GPU-correlator which computes the Pearson's correlation as:

$$\rho(\tau) = \frac{\langle (I_1(t) - \langle I_1 \rangle) \cdot (I_2(t+\tau) - \langle I_2 \rangle) \rangle}{\sqrt{\langle (I_1(t) - \langle I_1 \rangle)^2 \rangle} \sqrt{\langle (I_2(t+\tau) - \langle I_2 \rangle)^2 \rangle}} \tag{7.1}$$

We correct for the time delay coming from the hardware setup, which is different for each pixel due to different lengths of the optical fibers, the different transit times inside the PMTs (which in turn depends on the HV) and the additional delay coming from the different optical paths between the telescopes when tracking the source at different zenith/azimuth positions. We divide the data into baseline bins of 5 m, performing an average of frames for each bin weighted by the inverse of background variance (more background variance, less weight). We apply a 12 MHz frequency high-pass filter to remove slow residual noise, and then we extract the amplitude of the cross-correlation signal at 0 ns delay as the value of the Pearson's correlation and its error as the standard deviation of the correlation background region defined between (-140,40) and (40,140) ns.

Finally, we combine the Pearson correlation and the DCs to calculate the contrast, which is proportional to the modulus of the complex visibility squared:

$$c(\tau) = \frac{\langle (I_1(t) - \langle I_1 \rangle) \cdot (I_2(t+\tau) - \langle I_2 \rangle) \rangle}{\langle I_1(t) \rangle \cdot \langle I_2(t+\tau) \rangle_t} = K \cdot \frac{\rho \beta \sqrt{G_1 G_2}}{\sqrt{DC_{1,Star} DC_{2,Star}}} \tag{7.2}$$

where K is a setup constant, G_i are the gains of the PMTs, $DC_{i,Star}$ are the DCs of the pixels for which the starlight has been focused into and β is the ratio between the light

coming from the night-sky background (NSB) and the star:

$$\beta = \sqrt{\frac{(DC_{1,Star} + DC_{1,NSB})(DC_{2,Star} + DC_{2,NSB})}{DC_{1,Star} DC_{2,Star}}} \tag{7.3}$$

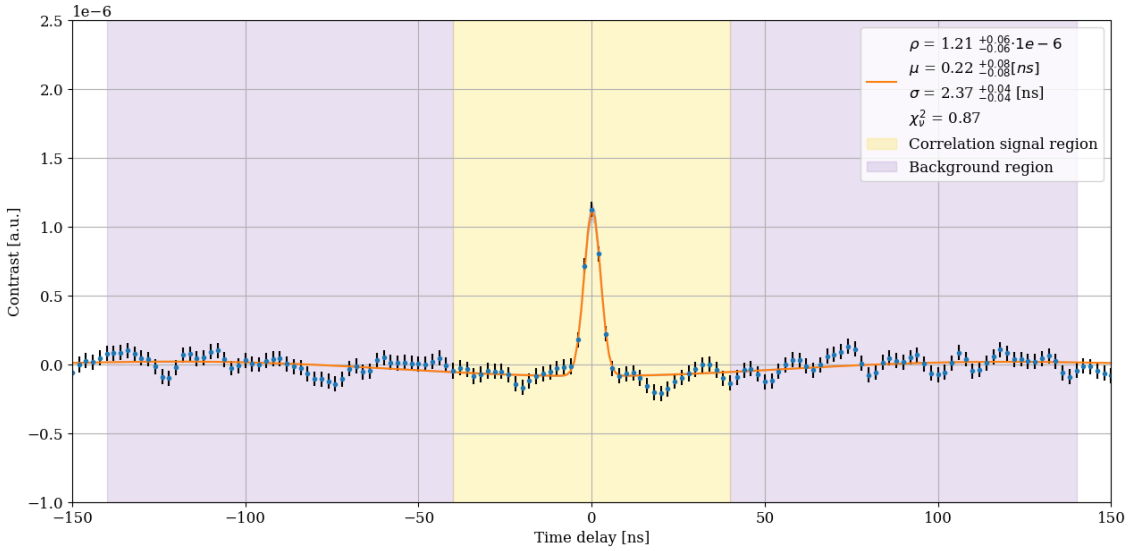

Figure 7.1: *Contrast of the cross-correlation peak.*

The contrast can be normalized in order to calculate the visibility:

$$c(d) = g^{(2)}_{1,2} - 1 = \frac{\Delta f}{\Delta \nu} \cdot |V_{1,2}(d)|^2 \rightarrow \frac{c(d)}{c(0)} = |V_{1,2}(d)|^2 \tag{7.4}$$

where $c(0)$ is a correlation normalization factor, also called zero-baseline correlation (ZBC), and it is the value that the correlation takes at baseline 0 or in other words, the correlation that would be measured for a point-like source at any baseline. There are several ways to estimate or directly measure its value that can be found in [165]. This value together with measurements of the correlation at different time delays or baselines (and different UV plane coordinates for cases without radial symmetry) can be used to reconstruct the brightness distribution of the thermal emission of the source.

The value of the ZBC is expected to be constant for each pixel pair, but several scenarios are described in the next section that can affect its value over short and long periods of time.

7.1 Photon flux calibration

Since photon flux can not be directly measured an alternative is needed in order to quantify the amount of light received by the setup: the DC from the camera slow control which are proportional to the photon flux. As described in section 5.1, the slow control of MAGIC cameras stores the DC at a rate of 1 Hz, which is much slower than the sampling frequency

of the correlation measurements (500 MHz). For this reason, it is necessary to interpolate between DC reports so that each frame can be properly corrected by DC following expression 7.2.

Several features can be discerned in the evolution of the DC. The best-case scenario is shown in figure 7.2 in which the night was clear with no clouds, calima or wind. The star's DC from both channels are mostly stable with a slow decline barely perceptible due to the change of zenith (higher zenith less starlight) and some kind of serrated pattern caused by the tracking system that corrects the position of the telescopes every few seconds. The AMC also corrects the focusing of the mirrors every 5 degrees change in zenith. For the background DC (mainly from the Moon) the behaviour is very stable since background pixels are receiving diffuse light.

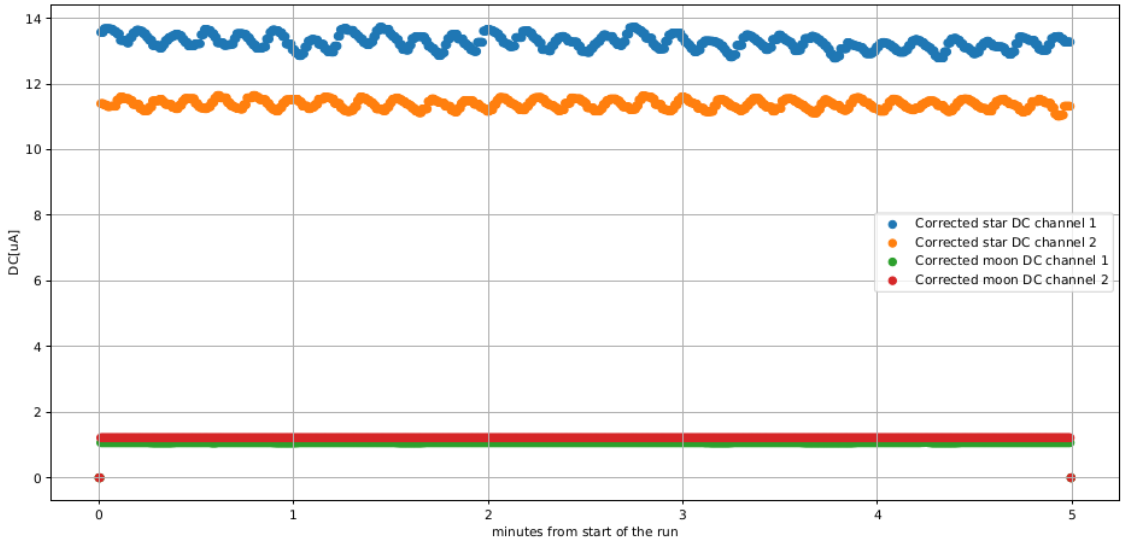

Figure 7.2: *Corrected DC from pixels 251 (star) and 260 (background) during a 5 min observation of Adhara.*

In presence of wind, one or both telescopes can have more difficulty keeping track of the source, which is reflected in the DC as more exaggerated serrated structures and even peaks and valleys as can be seen for the 'star DC channel 1' (blue points) in figure 7.3.

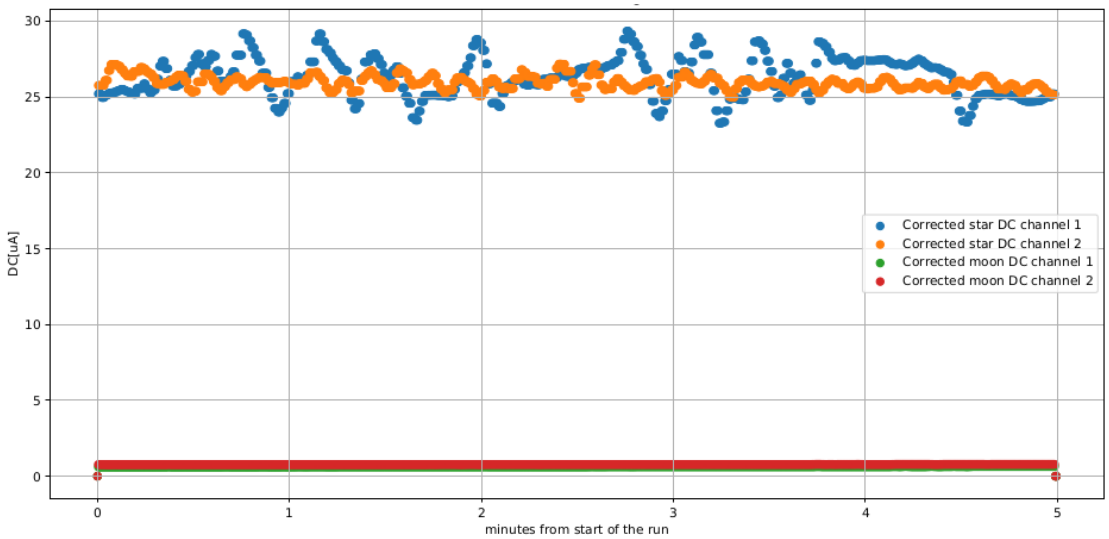

Figure 7.3: *Corrected DC from pixels 251 (star) and 260 (background) during a 5 min observation of Adhara, wind affects one of the telescopes.*

Similarly, in the presence of clouds in front of the source, the DC will suffer a strong drop until the cloud has passed as can be seen for both star channels in figure 7.4. This can also produce the background DC to increase due to scattering (see small increase in background DCs while there is a decrease in star DCs in 7.4).

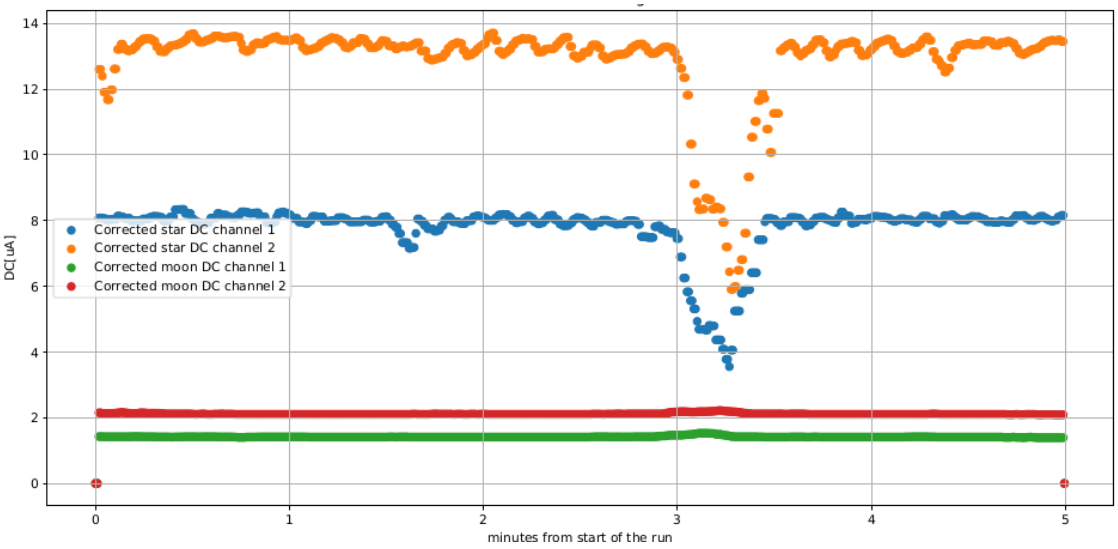

Figure 7.4: *Corrected DC from pixels 260 (star) and 251 (background) during a 5 min observation of gam Cas, a cloud passes producing a drop in the star DCs.*

For lower DC the cross-correlation is dominated by electronic noise but for higher DC it is dominated by starlight photons, following a poissonian distribution. Therefore in order to properly weigh each cross-correlation frame the variance of the cross-correlation at a background region defined in the range time delays of(-140,-40) and (40,140) ns is used. Frames with lower background variance have more probability to come from direct starlight, while frames with higher background variance are more likely to come from bad

quality observations.

An example for a baseline bin of the analysis of Adhara is shown in figures 7.5 and 7.6. In the first figure the DC combined from several observations in the same baseline range shows strong variations and drops. The second figure displays a 2D histogram of the value of the background region variance versus the DC showing that for higher DCs the variance is indeed smaller and contained within small values ($(0.2-0.4)\cdot 10^{-10}$ u.a.) while for lower DCs the distribution of the background variance gets broader.

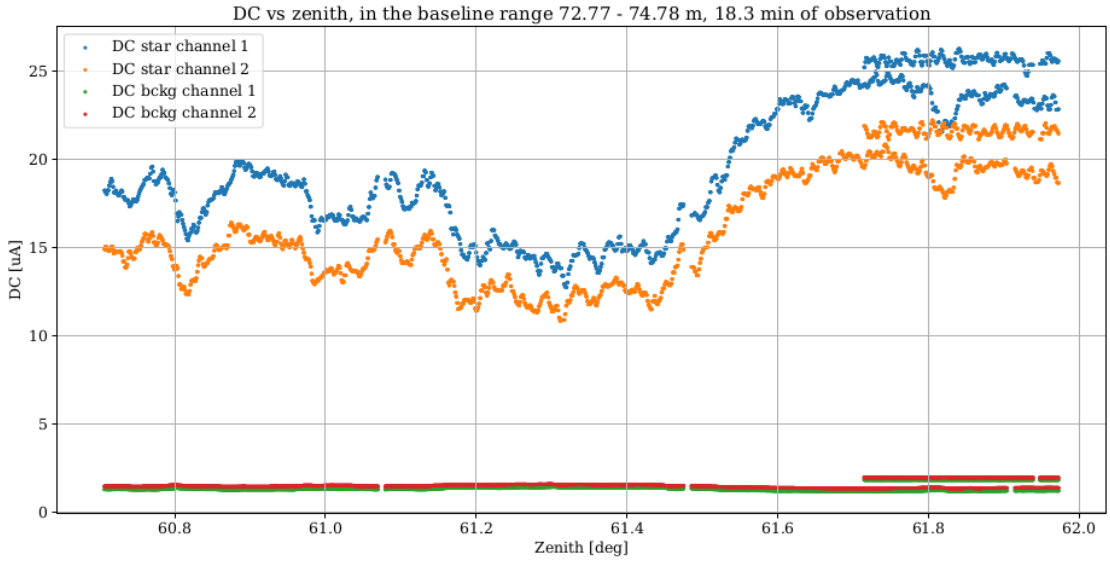

Figure 7.5: *DC in the baseline range of 72.77 to 74.78 m for an observation pointing at Adhara. Two populations of DCs are seen since several runs taken in different nights have been stacked within the same baseline bin. The first population of runs is restricted to zenith range 61.7-62° with average DC of 25 and 21 µA for star channels 1 and 2 respectively. This population shows mostly stable DC values. The other population shows strong variations of DC along the whole zenith range caused by passing clouds in the FOV.*

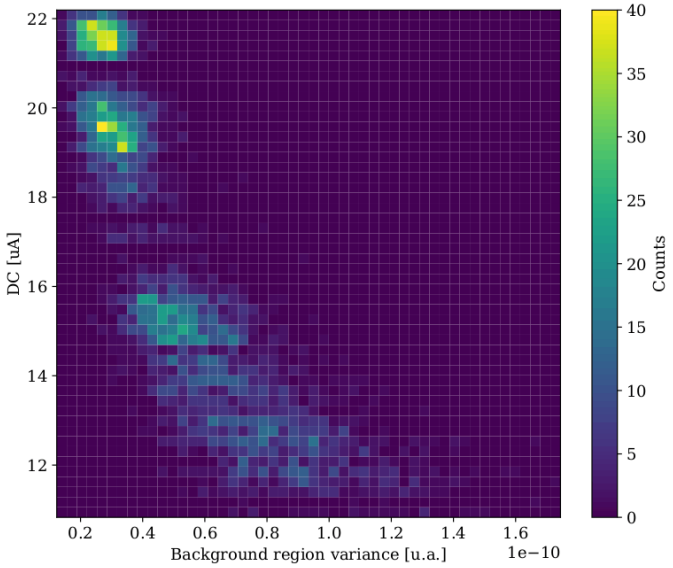

Figure 7.6: *Relationship between DC and cross-correlation background variance in the baseline range of 72.77 to 74.78 m for Adhara. The higher the star DC (i.e. starlight photon flux) the lower is the background region variance, meaning that the measured cross-correlation is dominated by starlight photons.*

The DC of the PMTs is limited by the camera control software in order to avoid degradation of the anode and last dynodes. The safe limit established for MAGIC's PMTs is 50 μA. When performing intensity interferometry observations the amount of light observed by each PMT is, even with the narrow pass filter that is used for interferometry, much higher than during VHE observations, since light from bright stars is being focused into individual pixels.

Some measurements were performed in order to determine adequate HV values for each PMT so that even when observing bright stars (B mag $\sim$ 1) the DC would not surpass the safe limit while leaving enough range to measure dimmer stars. A bright star such as Adhara was selected and observed at low zenith. Its starlight was focused into each of the PMTs and the HV was gradually changed until the DC observed by all of them allowed for enough range below and above that value (without reaching the safe limit in any case). The resulting HV are built into a table (shown in 7.1) that is loaded by the camera control software when intensity interferometry observations are performed.

Pixel	Nominal HV (V)
M1 251	1050
M1 260	850
M1 156	702
M2 251	1090
M2 260	1025
M2 156	694

Table 7.1: *Nominal intensity interferometry HV settings.*

The HV for each pixel is not perfectly stable during observations: the observed DC

are produced at values very close but not always exactly the nominal HV values. This is why a small correction is applied taking into account the overall behaviour of each PMT with HV (shown in figure 7.7), i.e. the gain of the PMT. This is even more important when observing especially bright stars (magnitude $\sim$1 or less) for which the HV may need to be reduced tens of volts. The gain and DC are expected to behave like $\sim HV^{kn}$ where k depends on the structure and material of the dynodes and n is the number of dynode stages in the PMT [179]. For MAGIC PMTs, the number of dynode stages is 6 and the constant k is expected to be around 0.7, therefore the DC is expected to follow a power law with the supply voltage (HV) of index ~ 4.

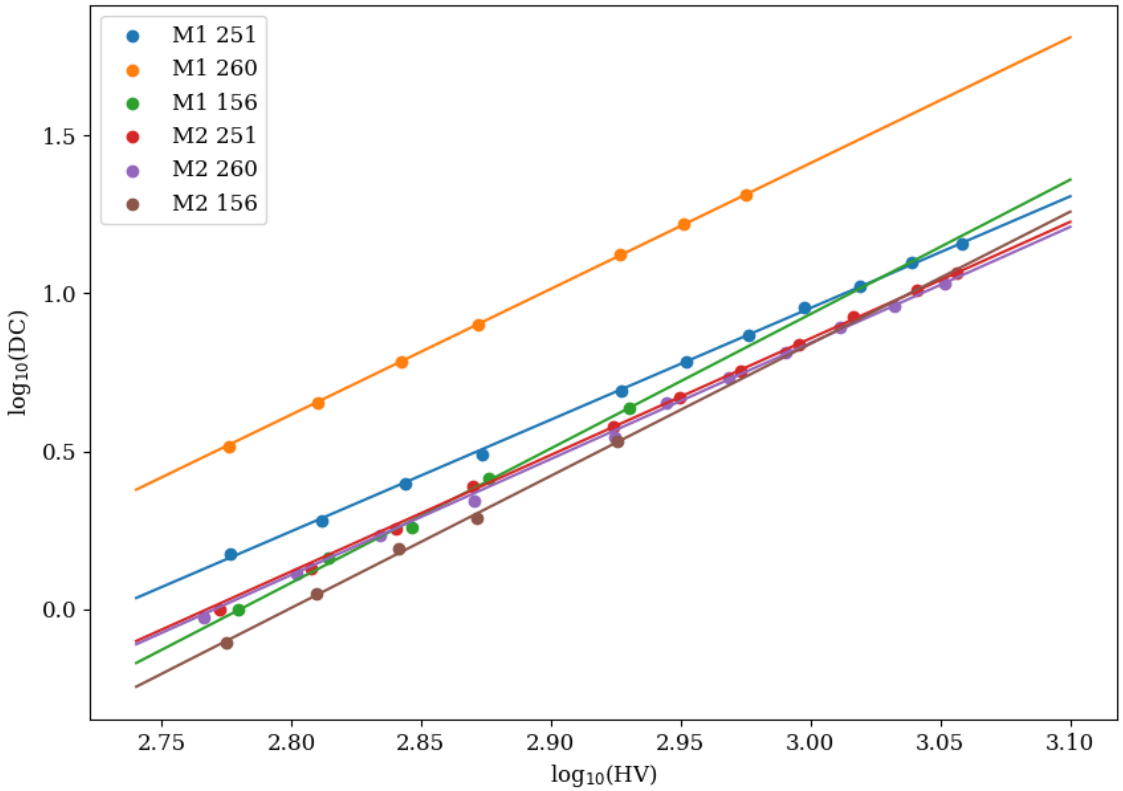

Figure 7.7: *Measurements of HV and DC for each pixel in log_{10} with each of the corresponding linear fits.*

In order to obtain the exact power law index for each pixel, a linear fit of $log_{10}(HV)$ vs $log_{10}(DC)$ is performed, obtaining the values of table 7.2, which are used to interpolate DC values for different HV values close to the nominal ones. The reported index values ('Slope' column) are consistent with the expected value of $\sim$4.

Pixel	Slope	Intercept
M1 251	3.55 ± 0.03	-9.68 ± 0.08
M1 260	4.01 ± 0.01	-10.62 ± 0.03
M1 156	4.2 ± 0.1	-11.7 ± 0.4
M2 251	3.75 ± 0.02	-10.38 ± 0.07
M2 260	3.73 ± 0.04	-10.3 ± 0.1
M2 156	4.2 ± 0.1	-11.7 ± 0.3

Table 7.2: *Best fit parameters of log(HV) vs log(DC) data.*

The observed DC for 'star pixels' (pixels used to focus the light of the stars and not the background like 251 and 260) is proportional to the received flux from the star and the background. This is why the pixels that are not being focused on (pixels 156 mainly but also 260 when focusing on 251 and 251 when focusing on 260) are used to monitor the diffuse background light. In order to properly subtract this contribution, the previous step of correcting the DC by the gain of each pixel is needed, but also an extra pixel-to-pixel factor is applied.

This factor is the relationship between how each pair of pixels behave when observing diffuse light, instead of direct starlight. In order to calculate this factors, hundreds of hours of data were combined and the DC from the background were compared and fitted to a line, of slope 'p1' and intercept 'p0' (see expressions 7.5 and 7.6.

$$DC_{pixelcorr} = \frac{DC_{gaincorr} - p_0}{p_1} \tag{7.5}$$

$$\Delta DC_{pixelcorr} = \sqrt{\left(\frac{\Delta DC_{gaincorr}}{p_1}\right)^2} \tag{7.6}$$

The parameters that better described the behaviour of the background measured DC are shown in the following table from and to each of the 6 channels (pixels) used for intensity interferometry observations.

From: \ To:	M1 251	M1 260	M1 156	M2 251	M2 260	M2 156
M1 251	-	0.09, 0.86	0.11, 0.56	-	-	-
M1 260	-0.10, 1.16	-	0.02, 0.65	-	-	-
M1 156	-0.19, 1.78	-0.03, 1.54	-	-	-	-
M2 251	-	-	-	-	0.03, 1.06	0.02, 0.69
M2 260	-	-	-	-0.03, 0.94	-	-0.02, 0.65
M2 156	-	-	-	-0.02, 1.46	0.02, 1.54	-

Table 7.3: *Parameters (p0, p1) of the empirical expressions 7.5 and 7.6 that allow to calculate the equivalent DC between any two of the three pixels of the same camera.*

Once all these corrections have been applied the DC from the background are subtracted so that the DC from the star are obtained and the contrast can be calculated.

7.2 Delay correction

As seen in section 4.2 the intensity interferometry technique is based on measuring the spatial coherence of the brightness distribution of a source throughout a certain range of baselines or delays. For detectors fixed in place (like MAGIC telescopes) the variations in baseline/delay come from the apparent movement of the source in the sky. The expected baseline/delay can be easily calculated using the source's zenith and azimuth and the position of the telescopes following expression 6.1.

But this is not the only source of delay. The starlight is collected in to the PMTs and then transmitted through optical fibers and other components until it reaches the correlator, several tens of meters after. This translates in to a 'hardware delay' that is slightly different for each channel and needs to be taken into account as well. In order to find out the hardware delay introduced to each channel, simultaneous 6-correlation measurements were performed pointing to a bright star for which a clear cross-correlation signal was expected. I compared the position of the cross-correlation peak corrected by the expected star's delay with respect to 0 ns delay and preliminary values of hardware delays based on approximate differences in cable lengths between channels for many frames (see figure 7.8. Then I calculated the median of the observed deviation with respect to 0 ns and subtracted it for each channel combination (see figure 7.9).

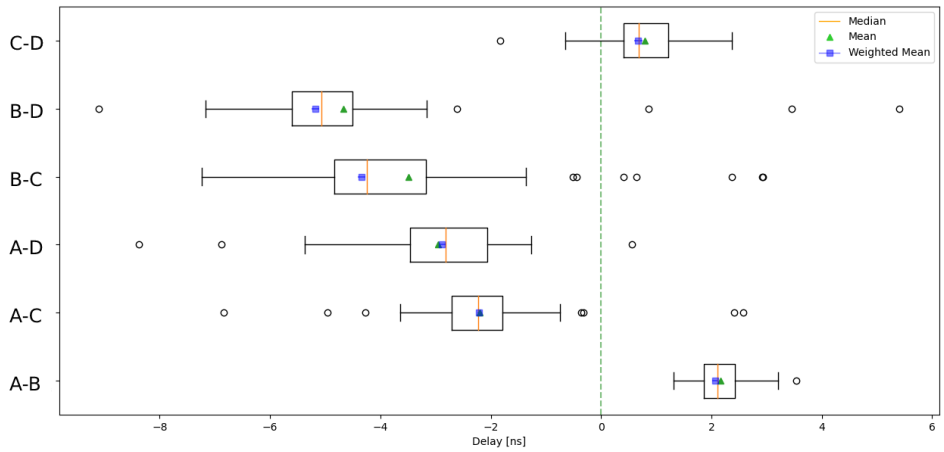

Figure 7.8: *Box and whisker plots that represent the distribution of the measured cross-correlation peaks deviation from delay 0 ns: each box represents the interquantile interval (where half of the data values are found), the orange lines represent the median, the blue squares represent the weighted mean, the green triangles represent the mean, the whiskers outside each box extend to the minimum and maximum values and the clear circles outside each box+whiskers represent the ouliers.*

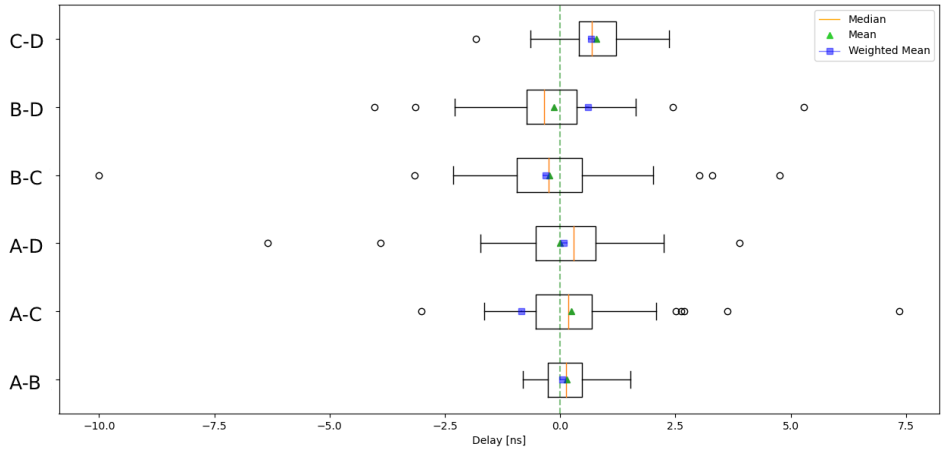

Figure 7.9: *Box and whisker plots that represent the distribution of the measured cross-correlation peaks deviation from delay 0 ns after applying the median as a delay correction for each channel combination.*

In the analysis, the expected star's delay is calculated for each frame and subtracted to the ±2048 ns time delay as well as the hardware delay for each combination of channels so that the expected position of the cross-correlation peak is at delay 0 ns following expressions 7.7 and 7.8. This allows to perform the average of several frames, increasing the significance of the cross-correlation peak.

$$\tau_{corr} = \tau - \Delta\tau_{hardware} - \Delta\tau_{star} \tag{7.7}$$

$$\Delta\tau_{hardware} = \Delta\tau_{Channel1} - \Delta\tau_{Channel2} \tag{7.8}$$

$\Delta\tau_{star}$ is obtained for every frame using expression 6.1 and $\Delta\tau_{hardware}$ depends on the combination of channels. The median values of the measured time delays for each channel were added to the preliminary values of the hardware delays, and the final values are reported in table 7.4.

Pixel (Channel)	Hardware delay (ns)
M1 251 (C)	550.45
M1 260 (D)	5.18
M2 251 (A)	645.46
M2 260 (B)	0

Table 7.4: *Hardware delays introduced by optical path differences to each channel.*

7.3 Convolution with mirror size

Each cross-correlation measurement is not only the cross-correlation at a certain baseline given by the combination of the zenith/azimuth and the separation of the telescopes, but

the convolution between all the distances between all the individual facets of the mirror dishes of the telescopes. This means that the observed contrast and hence the visibility will not be simply the expected one from expression 4.2, but the average of all the contrasts or visibilities that would be measured for each combination between mirror dish facets.

With MAGIC 17 m diameter dishes this effect is less than 1% for stars of diameter of $\sim$1 mas but for stars of several mas it becomes noticeable as can be seen in figure 7.10.

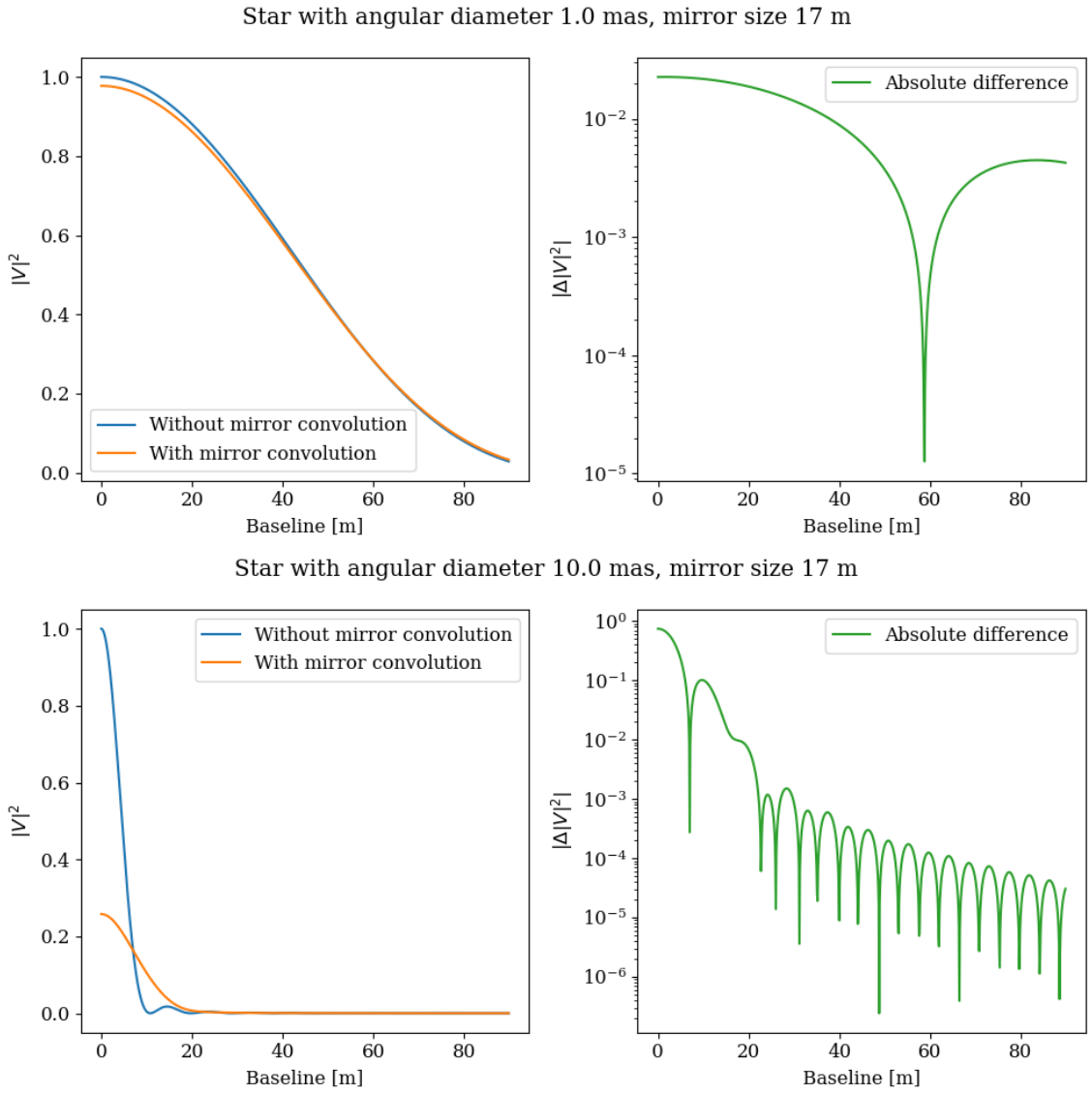

Figure 7.10: *Examples of how mirror size convolution affects $|V|^2$ measurements for stars of different sizes. For each star, the left plot shows a simulation of the $|V|^2$ with (orange line) and without (blue line) taking into account the convolution with the mirror size, and the right plot shows the absolute difference between the two models in units of $|V|^2$. Top: star of 1 mas with 17 m mirror (usual scenario for MAGIC). Bottom: star of 10 mas with 17 m mirror, the visibility is heavily reduced by the convolution with the size of MAGIC mirror dishes compared with not taking the mirror convolution into account.*

The result is a smoothing effect that can affect observations with no radial symmetry as well, diluting the visibility patterns in the UV plane. Figure 7.11 illustrates how the UV pattern of a binary star is affected.

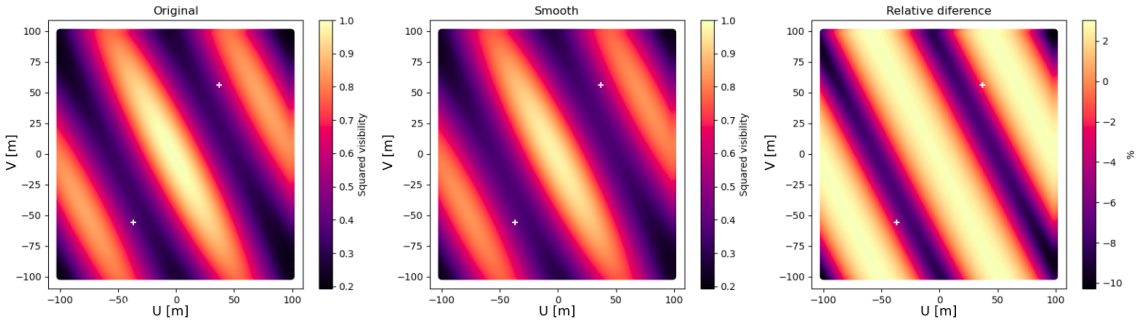

Figure 7.11: *Smoothing calculated by the convolution of the size of the mirrors with the visibility pattern in the UV plane for a spectroscopic binary (center) compared to the non-smoothed pattern (left). The relative difference in visibility in % is shown on the right.*

To increase significance of the cross-correlation peak, the data is divided into baseline bins of 5 m and the corresponding delay-corrected frames are averaged. In order to calculate the mean baseline value for each baseline bin a weighted average is performed taking into account the distribution of baselines weighted by the background variance of the cross-correlation (frames with less background variance weight more) and the distribution of baselines given by all the distances between individual mirror facets. Figure 7.12 shows the normalized original baseline distribution extracted from telescope pointing positions (orange), the same distribution but weighted by the background variance of the correlation (blue) and the distribution after taking into account all the combinations between facets (green).

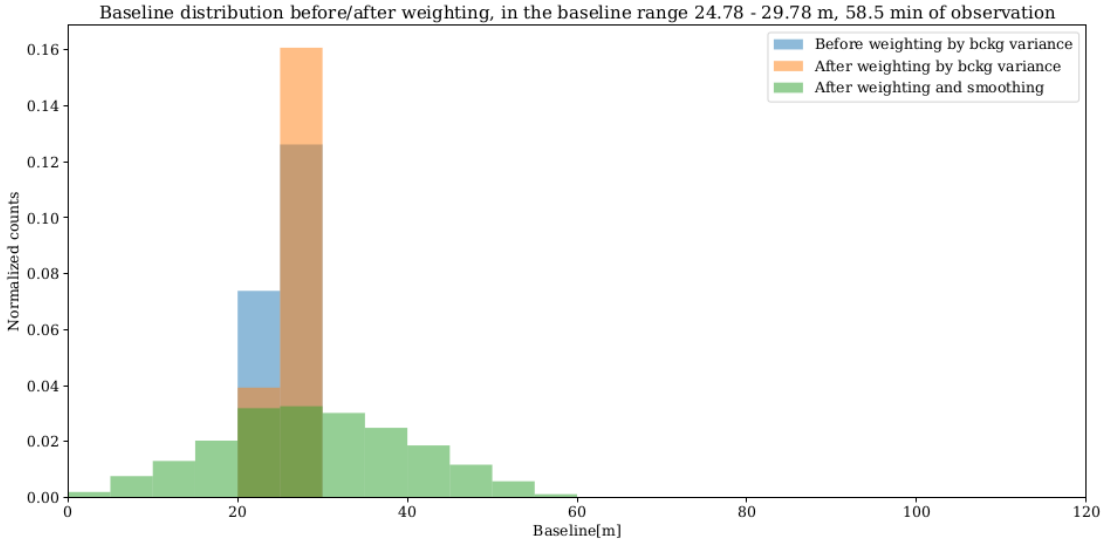

Figure 7.12: *The blue histogram shows the normalized distribution of baselines extracted from telescope pointing positions. The orange histogram is the normalized distribution of baselines after weighting by background variance (more background means less weight). The green histogram shows the normalized distribution of baselines after weighting the blue distribution by the convolution with the mirror size (all baselines combinations between the two 17 m dishes).*

7.4 Zero baseline correlation

The zero baseline correlation is the value of the correlation at baseline 0 and it is a constant for all measurements performed with each pair of channels for as long as the instrumental setup does not change. All correlations between channels pixel 251 of MAGIC 1 and pixel 251 of MAGIC 2 (A-C configuration) would have the same value if measured at baseline 0 and the same would happen for any other combination of channels, each combination having a distinct ZBC value.

The ZBC can be measured performing chessboard observations (see section 5.2.2) because the corresponding effective baseline is roughly zero or by fitting observations of a well known star that can be used as calibrator. I performed 5 independent joint bootstrap fits for 5 of the 7 reference stars defined in table 8.1. For each star a bootstrap fit was performed combining the A-C and B-D configurations data sets (see example for Adhara in figure 7.13). The parameters of the fits were ZBC_{AC}, ZBC_{BD} and the angular diameter to represent the fact that each data set has a different calibration parameter but both must reconstruct the same UD model of the star, since the angular size of the star, and ultimately its physical diameter, does not depend on the setup.

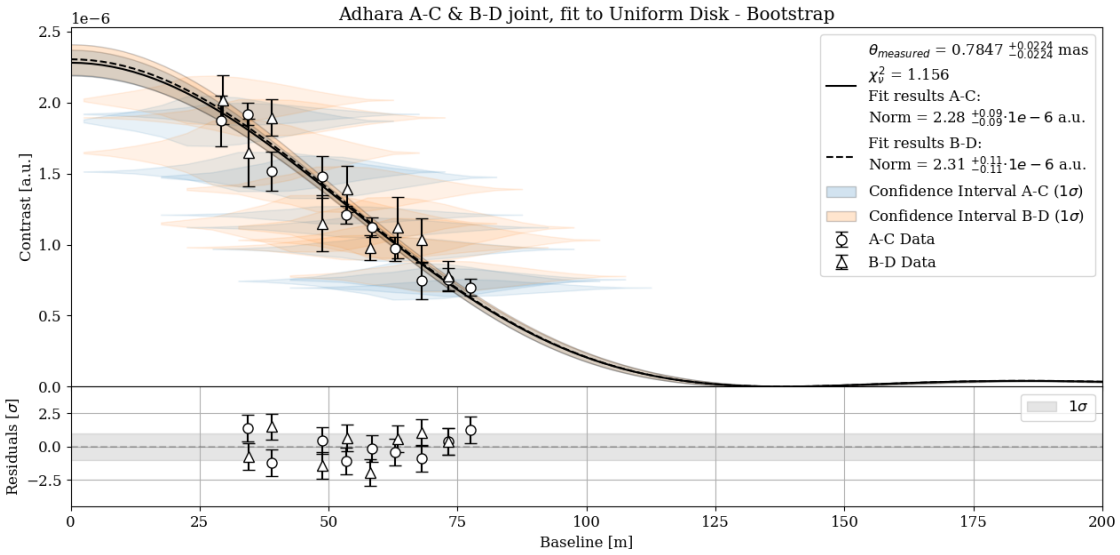

Figure 7.13: *Joint bootstrap fit of A-C (circles) and B-D (triangles) data sets of eps CMa (Adhara). The true distribution of baselines normalized an scaled to fit within the size of the error bars is shown as violin plots for each A-C (blue) and B-D (orange) measurement (this is equivalent to the green histogram in figure 7.12 for each point). The 1 σ CL is shown for the A-C (blue) and B-D (orange) reconstructed UD models. In the lower part the residuals of each measurement are also shown.*

The result of the fit for each star can be found on table 7.5. In the table, the angular diameters measured from other instruments are compared with the ones measured with MAGIC-SII, being all of them compatible and with better or similar precision.

Bayer Name	HD Number	Spectral Type	B (mag)	Reference θ (mas)	Measured θ (mas)	χ^2_ν	Obs. Time (hours)
eps CMa	52089	B1.5II	1.29	0.77 ± 0.05 (1)	0.78 ± 0.02	1.2	9.6
eps Ori	37128	B0Ia	1.51	0.631 ± 0.017 (2)	0.61 ± 0.02	0.5	3.1
bet CMa	44743	B1II-III	1.73	0.523 ± 0.017 (2)	0.59 ± 0.03	1.1	3.8
kap Ori	38771	B0.5Ia	1.88	0.44 ± 0.03 (1)	0.56 ± 0.05	3.9	1.7
gam Crv	106625	B8III	2.47	0.72 ± 0.06 (1)	0.82 ± 0.04	1.9	1.7

Table 7.5: *Table of reference stars selected from JMDC, sorted by B magnitude for which enough MAGIC-SII data was available in order to perform an analysis. The spectral types and B magnitudes have been extracted from SIMBAD [177]. The angular diameter measurements performed by other instruments such as Narrabri (1) [157] and VERITAS (2) [178] are shown alongside MAGIC-SII measurements for comparison. The reduced χ^2 and the devoted observation time in hours are also shown.*

As can be seen in figure 7.14 the star for which we have devoted more observation time is Adhara, and is the star that has yielded the best precision in the measurement of both ZBC values and has a previous angular diameter measurement of 0.77±0.05 mas by Narrabri [157] which is compatible with our 0.78±0.02 mas measurement.

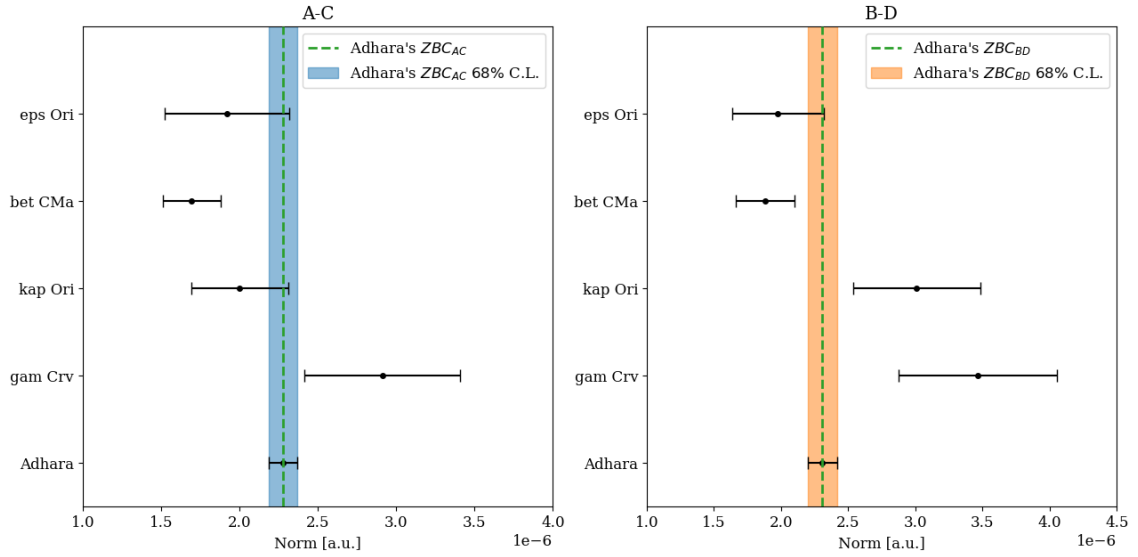

Figure 7.14: *Comparison of the precision of the different ZBC measurements for A-C and B-D modes with the 5 reference stars.*

For this reason I chose to use Adhara as a calibrator in order to calculate the ZBC for two combination of channels: A-C (pixels 251 from MAGIC 2 and MAGIC 1) and B-D (pixels 260 from MAGIC 2 and MAGIC 1), being the resulting ZBCs $(2.28 \pm 0.09) \cdot 10^{-6}$ a.u. for A-C and $(2.31 \pm 0.11) \cdot 10^{-6}$ a.u. for B-D. These values will be used as extra measurements for other stars in their respective A-C and B-D data sets at zero baseline.

7.5 Angular diameter estimation

For some stars, only measurements in A-C or B-D configuration have been performed. In those cases the corresponding ZBC have been added as an extra measurement at baseline 0 m and then the diameter has been found by performing a bootstrap fitting of the contrast measurements versus baseline. In some cases, both A-C and B-D measurements have been performed. For these cases, a joint bootstrap analysis has been performed: the data sets from A-C and B-D with the added corresponding ZBC values as extra measurements (shown in figure 7.15 as 'Adhara's A-C ZBC' and 'Adhara's B-D ZBC') are treated as separate fits but imposing the condition that both data sets must reconstruct the same angular size diameter, leaving very little room for variation of the ZBC values (within the uncertainties obtained from Adhara ZBC values). The distribution of the fit parameters for the star eta UMa (Alakid or Benetnasch) are shown in a corner plot in figure 7.16.

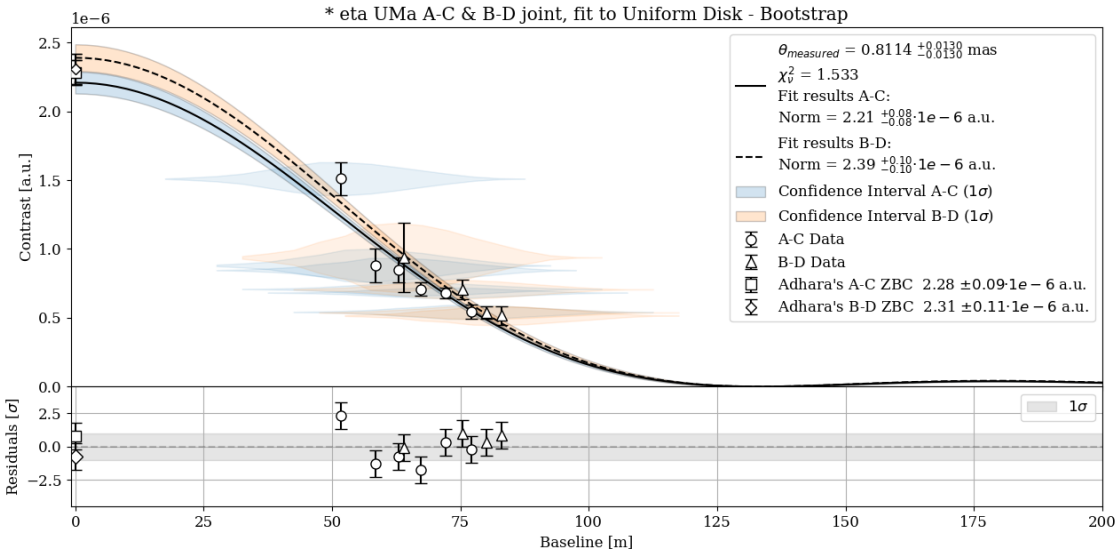

Figure 7.15: Result of the joint bootstrap fit of A-C (circles) and B-D (triangles) data sets for eta UMa (Alkaid). The upper part of the plot shows the two reconstructed UD models with same angular size diameter but different ZBC values together with their CL regions for A-C (blue) and B-D (orange). The lower part of the plot shows the residuals of each measurement with respect to the model.

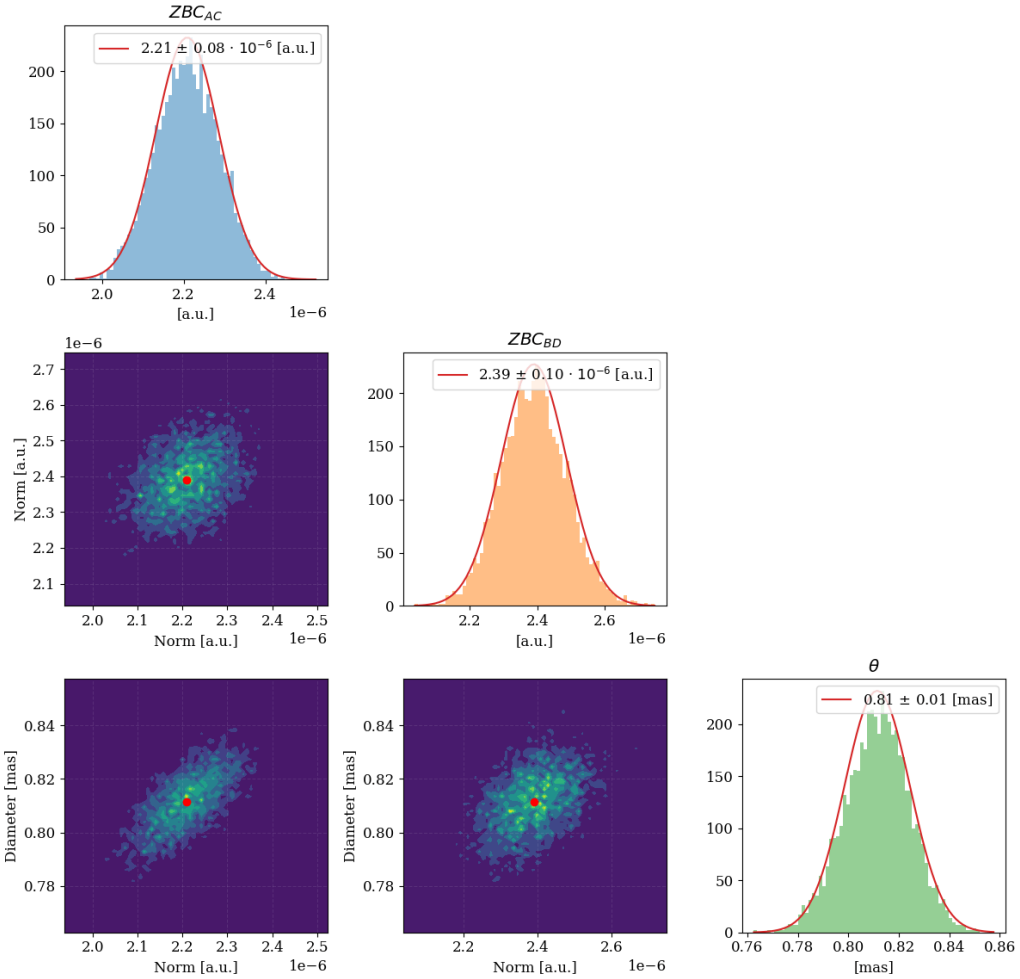

Figure 7.16: Corner plot that show the normal distributions of the parameters from the joint bootstrap fit showed in figure 7.15 for the star eta UMa (Alkaid).

This procedure has been applied for each star. The resulting angular diameters are presented in section 8.1 and the contrast or visibility curves are shown in the appendix A.

7.6 Data quality and consistency

Several test have been performed to ensure that measured data meets the expectations from the theoretical basis and hardware specifications, such as studying the distribution of corrected time delays and correlation peak width to ensure a proper delay correction has been performed for all the signals, a comparison between the expected and the measured sensitivity of the signals in order to validate both the scheduling tool and that observations are being taken in nominal conditions, a study of different measurements of the ZBC in order to check for possible biases in its estimation, a study of the consistency between angular diameters obtained with different hardware configurations to ensure that the calculated diameters are independent of the combination of channels used.

7.6.1 Time delays and correlation peak width

If the delay has been properly corrected for all frames, all correlation peaks are expected to fall close to 0 ns time delay and have a width close to 2 ns. The following figures show the distribution of the gaussian parameters μ and σ for the A-C and B-D modes combined:

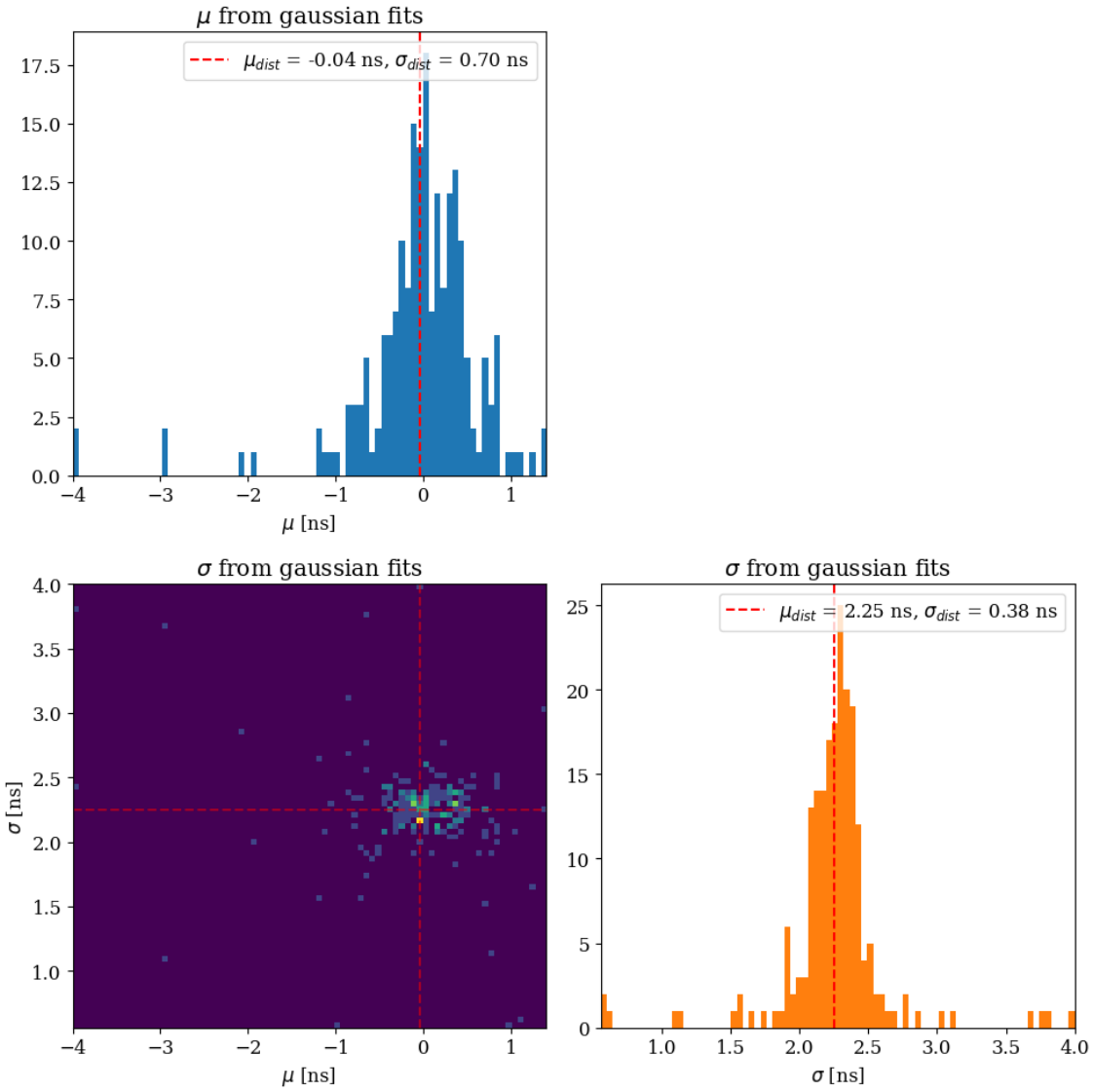

Figure 7.17: *Corner plot of the distribution of μ and σ from the gaussian fits of the correlation peaks of A-C and B-D combinations of channels.*

As shown in figure 7.17 both averages of the gaussian fit parameters $\mu_{avg} = -0.04 \pm 0.70$ ns and $\sigma_{avg} = 2.25 \pm 0.38$ ns are consistent with the expected values of 0 ns and ~ 2 ns of delay and width, respectively.

7.6.2 Sensitivity

The expected signal-to-noise of the cross-correlation peak is calculated with expression 6.5 assuming a background magnitude of 5 mag. It is important to check if our predictions

agree with our measurements to ensure that our setup works as intended. It also means that the scheduling tool returns realistic observation times to get 5σ.

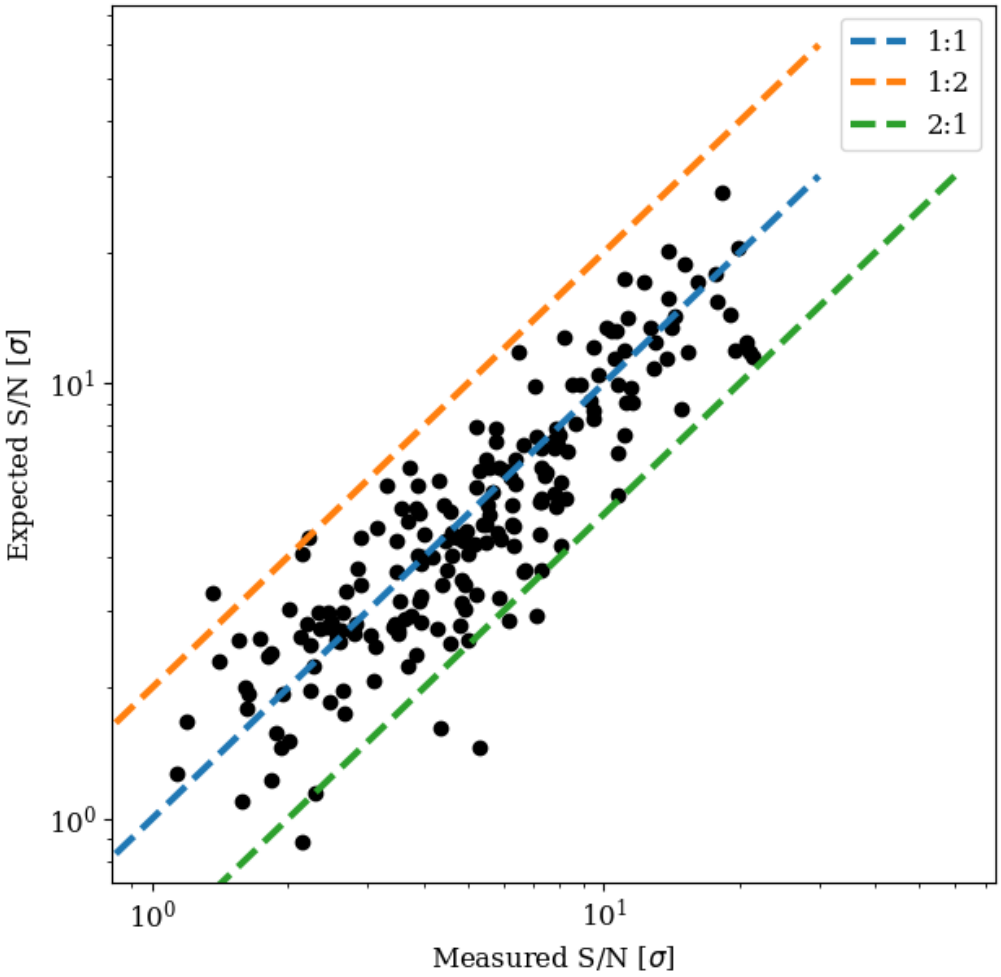

Figure 7.18: *Expected signal-to-noise vs measured signal-to-noise of the correlation peak for the full dataset.*

Figure 7.18 shows that the vast majority of the cross-correlation peaks are detected within $(-2SN_{expected}, +2SN_{expected})$, meaning that our measurements match our predictions successfully. The differences up and down the expected values can be produced by several factors such as higher/lower background illumination levels than the one used for the predictions (5 mag) trough the β parameter or a variety of weather conditions.

7.6.3 ZBC consistency

To check the consistency of the ZBC for each combination of channels I performed bootstrap fits first without using Adhara's ZBC as an extra measurement and then adding it as an extra measurement at baseline 0 m. If all data from each channel is consistent, all the ZBCs should agree with Adhara's ZBC for the corresponding combination of channels.

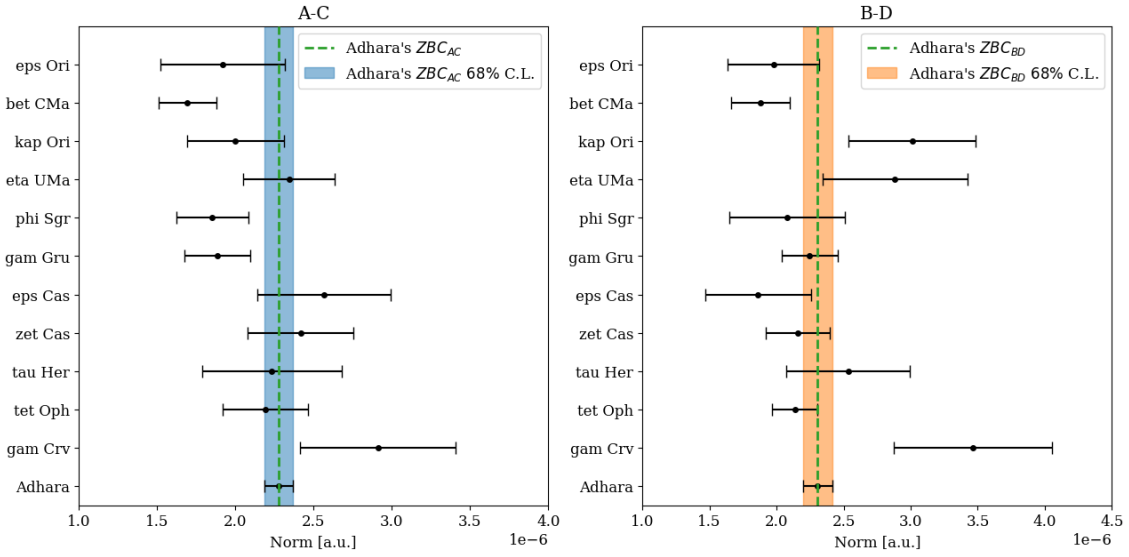

Figure 7.19: *ZBC measurements for A-C and B-D using the combined data sets (A-C & B-D) for each star, without adding Adhara's ZBC as an extra measurement.*

In figure 7.19 only ZBC values obtained with less than 30% relative error are shown. Most of the measurements for both combination of channels agree with the measurement with best precision (Adhara's).

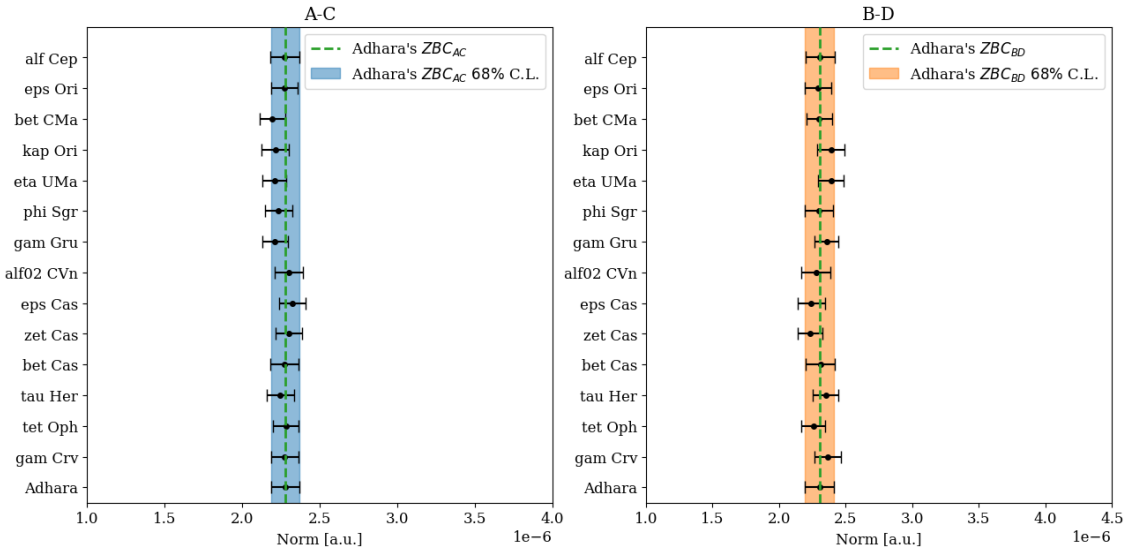

Figure 7.20: *ZBC measurements for A-C and B-D using the combined data sets (A-C & B-D) for each star adding Adhara's ZBC as an extra measurement.*

In figure 7.20 the ZBC it can be seen that all the ZBC measurements are in agreement with Adhara's ZBC since it (Adhara's ZBC) was used as an extra measurement at baseline 0 m. The higher precision measurement in the ZBCs will translate into better diameter measurements.

7.6.4 Consistency between A-C and B-D

If the ZBCs calculations from the previous sections are correct, then one should get the same diameter for each star for A-C and B-D independently.

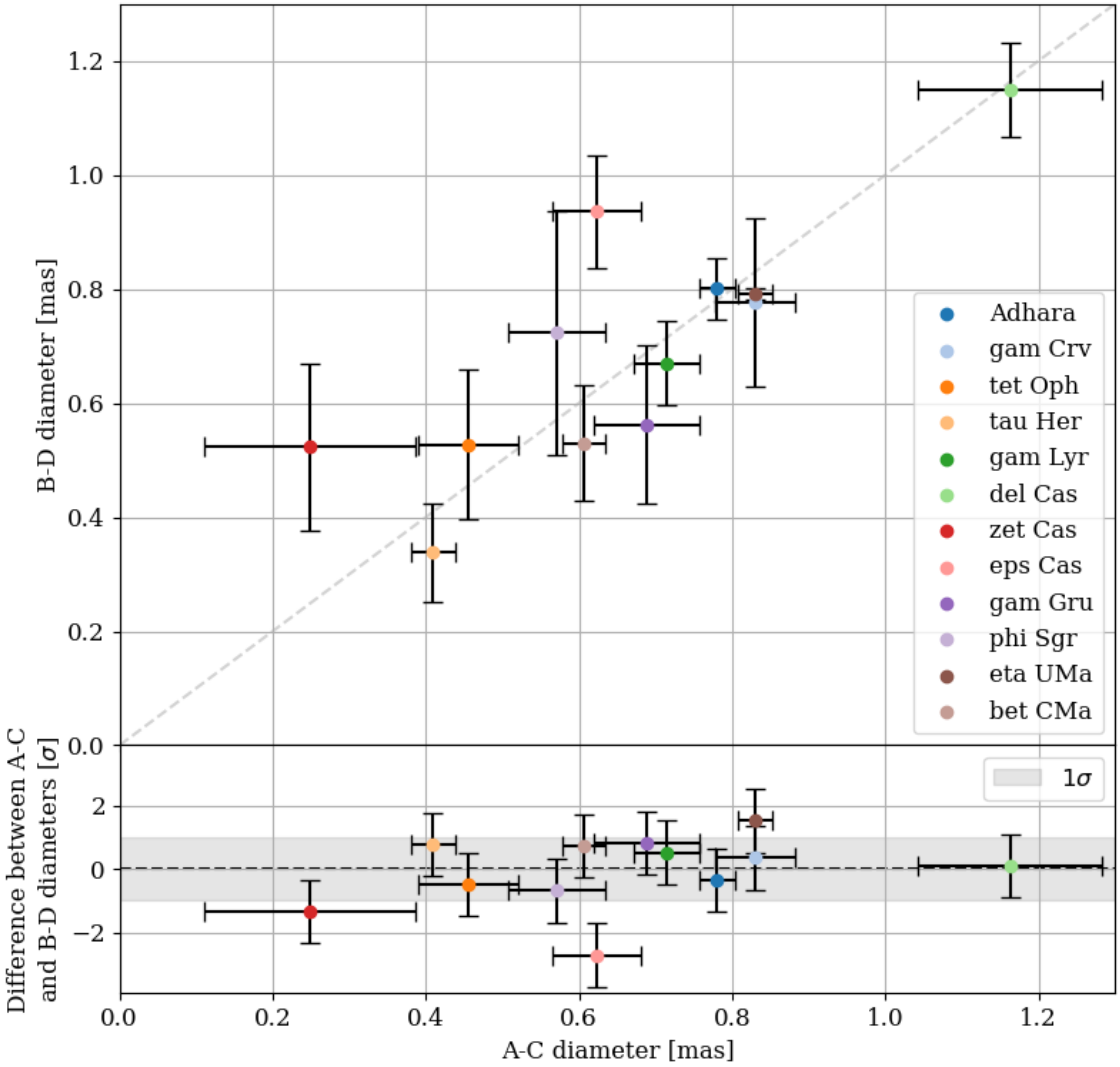

Figure 7.21: *Comparison between diameters obtained with A-C channels data and B-D channels data.*

Figure 7.21 shows that the difference between most diameters measured independently in A-C and B-D is less than 1σ, meaning that most of them agree between the two combinations of channels.

7.7 Systematics

The MAGIC Collaboration carefully evaluated the main systematics affecting their VHE gamma-ray analysis [132, 180]. Given the very different nature of the measurement, these systematics actually do not affect interferometry observations the same way. For instance, the uncertainty in the amount of light detected by IACTs mainly affects S/N (see [181]),

but does not add as a systematic.

There are factors that can change not only the S/N of the correlation signal, but also the ZBC (which could lead to a wrong calibration of the setup and a wrong calculation of the visibility). We have performed an extensive study of the effects that can and can not add systematic uncertainties to our intensity interferometry analysis.

Some effects that do not add systematic uncertainty are: the amount of light that hits the PMTs (provided that the stored DC values properly account for the average photon flux that reaches the PMTs) and the gain evolution of components after DC/ADC branch (Pearson's correlation needs to be unit-less and so does the visibility, so changes in gain coming from the vertical cavity surface emitting lasers (VCSels) or any component after the DC/ADC branch cancel out when we calibrate our measured correlation with the average photon fluxes (see Eq. 7.2)).

Electronic bandwidth While the single photo-electron response of the PMTs is fairly stable, the VCSels' signal transmission could change in short timescales, producing a time-dependent variation of the electronic bandwidth. Thanks to the versatility of the GPU correlator, we are able to compute the auto-correlation simultaneously to the cross-correlation. This means that we can keep track of the electronic bandwidth of each channel (pixel) over time. Our measurements represented in Figure 7.25 show that for values of photon flux (which is proportional to the measured DC) higher than a certain threshold, the width of the auto-correlation signal, and therefore the electronic bandwidth, remains constant (less than 1% deviation for all pixels). This is because for lower photon fluxes the signal is dominated by electronic noise, but for higher fluxes it follows a poissonian.

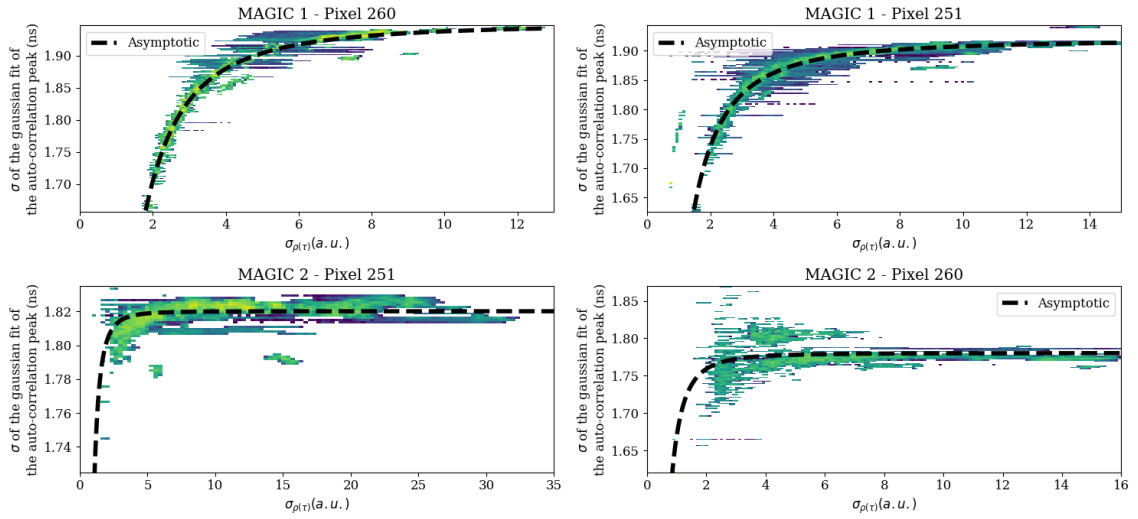

Figure 7.22: *Width of the auto-correlation peak versus different values of photon flux for pixels 251 and 260 of the telescopes MAGIC 1 and MAGIC 2. A preliminary asymptotic fit is added on top of the 2D density distributions to better visualize the behaviour. For lower photon fluxes the correlation signal is dominated by electronic noise, but for higher fluxes it follows a poissonian.*

Optical bandwidth The distribution of photons that pass through the narrow-band filters has a certain QE ($\alpha(\lambda_0)$) but this factor is affected by the angle of incidence (AOI) of the photons that reach them. Simulations of AOIs up to 26 deg (which is the cut-off angle of the Winston cones in front of every PMT) show how this affects the shape of the optical band-pass in Figure 7.23.

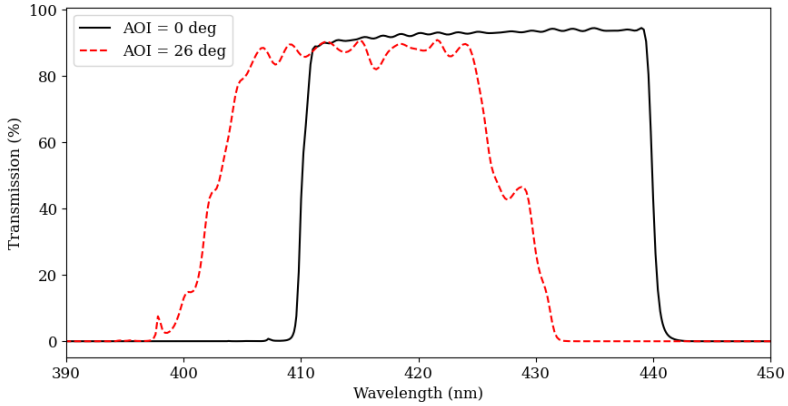

Figure 7.23: *Filter transmission curve for 0 and 26 deg AOI produced with the official tool at* https://searchlight.idex-hs.com/ *for our Semrock 425-26 nm filters.*

Sometimes the communication is lost between the AMC and the actuators of the mirrors, resulting in mirrors focused at the position of a previous observation or not focused at all due to other problems with the actuators. This means that the number of mirrors focusing the light into the pixels is not always constant and some light might be missing. MAGIC's AMC allows to keep track of the number of disconnected mirrors, so we can check when this happens. Simulations in which the number of missing mirrors was up to 10 in different locations (random, outer ring, center) showed that this systematic effect is in any case less than 1%.

The weight of the mirror dishes can produce deformations in the overall shape of the dish when pointing at different zenith/azimuth coordinates, changing the distribution of AOIs. This deformation is countered by producing Look Up Tables (LUTs) for the AMC that correct for this effect and maintain the focusing performance in nominal conditions, independent of the zenith/azimuth coordinates.

Gain of the DC/ADC branch The gain is the relationship between the number of photo-electrons that are detected at the PMT and the anode current reported by the anode current monitoring system. As seen in Eq.7.2, this value is necessary to properly account for the amount of light that goes into each pixel and to properly compare $DC_{i,Star}$ with $DC_{i,NSB}$, and has a direct effect on the calculation of the contrast and visibility. We have identified several factors that can have an effect on the evolution of the gains, such as: temperature variations, sudden jumps in current that need a few minutes to recover, PMT degradation and changes in high voltage (HV). We perform special HV vs DC calibrations to ensure that changes in $log(HV)$ are proportional to changes in $log(DC)$ for the observed DCs in our nominal set of HV for the pixels. We estimate an overall systematic effect of 1% or less.

NSB DC subtraction During interferometry observations we keep track of the NSB in order to properly account for the starlight following Eq.7.3. We extract $DC_{i,NSB}$ from the 'background pixels' that are not being focused on (up to two in each camera, reserving the third one to observe the star). See picture in Figure 7.24 from when we had just two filters in each camera. Most of the time they receive diffuse light from the Moon. It could happen that a star brighter than the NSB crosses the field of view (FOV) of the background pixels, producing an increase in $DC_{i,NSB}$. This would result in an overestimation of the NSB and a wrong calculation of the contrast and later the visibility. Fortunately, we have two background pixels in each camera when performing full-mirror observations, and can see if one of the $DC_{i,NSB}$ values gets unexpectedly higher than the other. This effect, although occurring in a very small percentage of observations, can be avoided by using the $DC_{i,NSB}$ value from the unaffected background pixel. If this distinction is not made, the effect is in any case less than 3% for stars up to 3.5 B mag.

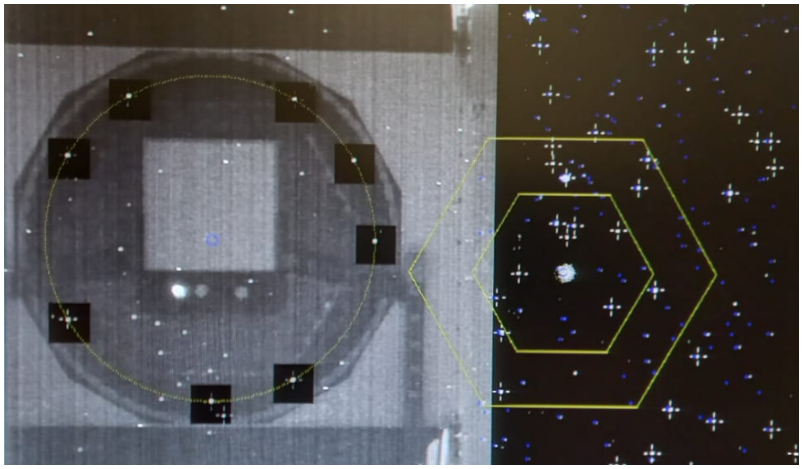

Figure 7.24: *Picture of one of MAGIC cameras during an intensity interferometry observation. The light from the target star, which can be seen within the yellow hexagons on the right, is focused by the AMC into one of the holes with filters in the target holder (left hole), while the other holes are illuminated by diffuse background light (right holes).*

Residual electronic noise in the correlation There are two kinds of residual electronic noise that can affect our correlation measurements. One of them is a slow noise (one order of magnitude slower than the sampling frequency), coming from the digitizers and correlators. When the amount of received photons is very low, the correlation is dominated by this noise, which has a stable shape over time (see Figure 7.25) and can be easily removed by applying a 12 MHz high-pass filter to the correlation. When the amount of received photons is high (i.e. for bright stars) the correlation is no longer dominated by this noise and the effect is much smaller, but we apply the filter in any case. The other kind of noise is a high-frequency noise we believe is coming from different electronic devices within the MAGIC counting house, which where the setup is located. This one cannot be removed because the frequency is much closer to the sampling frequency. The best we can do is shield the setup as much as possible.

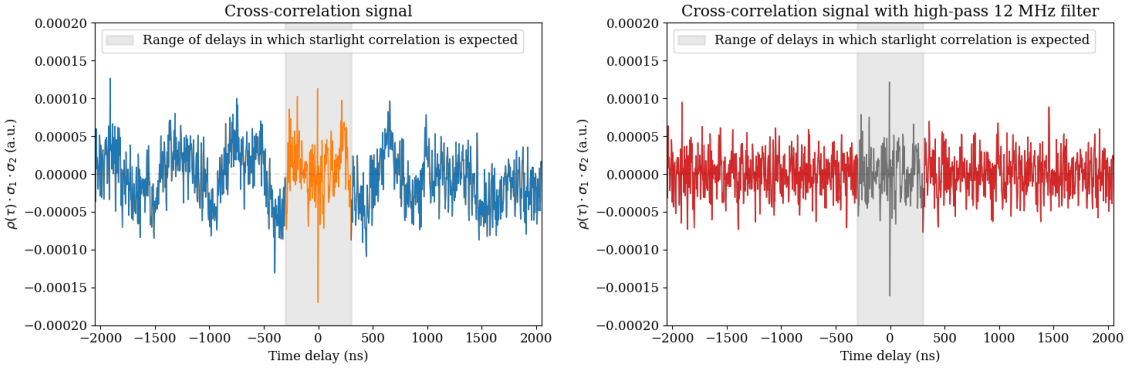

Figure 7.25: *Average of the accumulated cross-correlation data frames in units of* $\rho(\tau) \cdot \sigma_1 \cdot \sigma_2$. *The total integrated time is over 70 h, for pixel pair MAGIC-1 pixel 260 and MAGIC-2 pixel 260, taken over the course of year 2022. The stable shape of the residual slow electronic noise (left) can be removed by applying a high-pass 12 MHz filter (right). The greyed out zone between* ± 300 *ns is the range of delays in which we typically expect a correlation signal from the star. Within this zone, the shape of the slow electronic noise is intertwined with the stars' correlation signals. After applying the high-pass filter, only the slow noise is subtracted.*

8. Results

8.1 Stellar angular diameter measurements

The main and most simple of the science cases discussed in section 4.3 was the measurement of stellar radii by constructing a UD model of the star's surface brightness distribution by measuring the spatial coherence (visibility) over a range of baselines. This implies the assumption that the selected stars are uniformly illuminated symmetrical stars, leaving out the calculation the dependence of the optical depth and the effective temperature with stellar radius (limb darkening).

8.1.1 Comparison with reference diameters

Considering that there are previous estimations and measurements for the stars that we have measured, it would be interesting to test how close or far away are our measurements from those values, since that would imply differences between direct observations performed by different instruments.

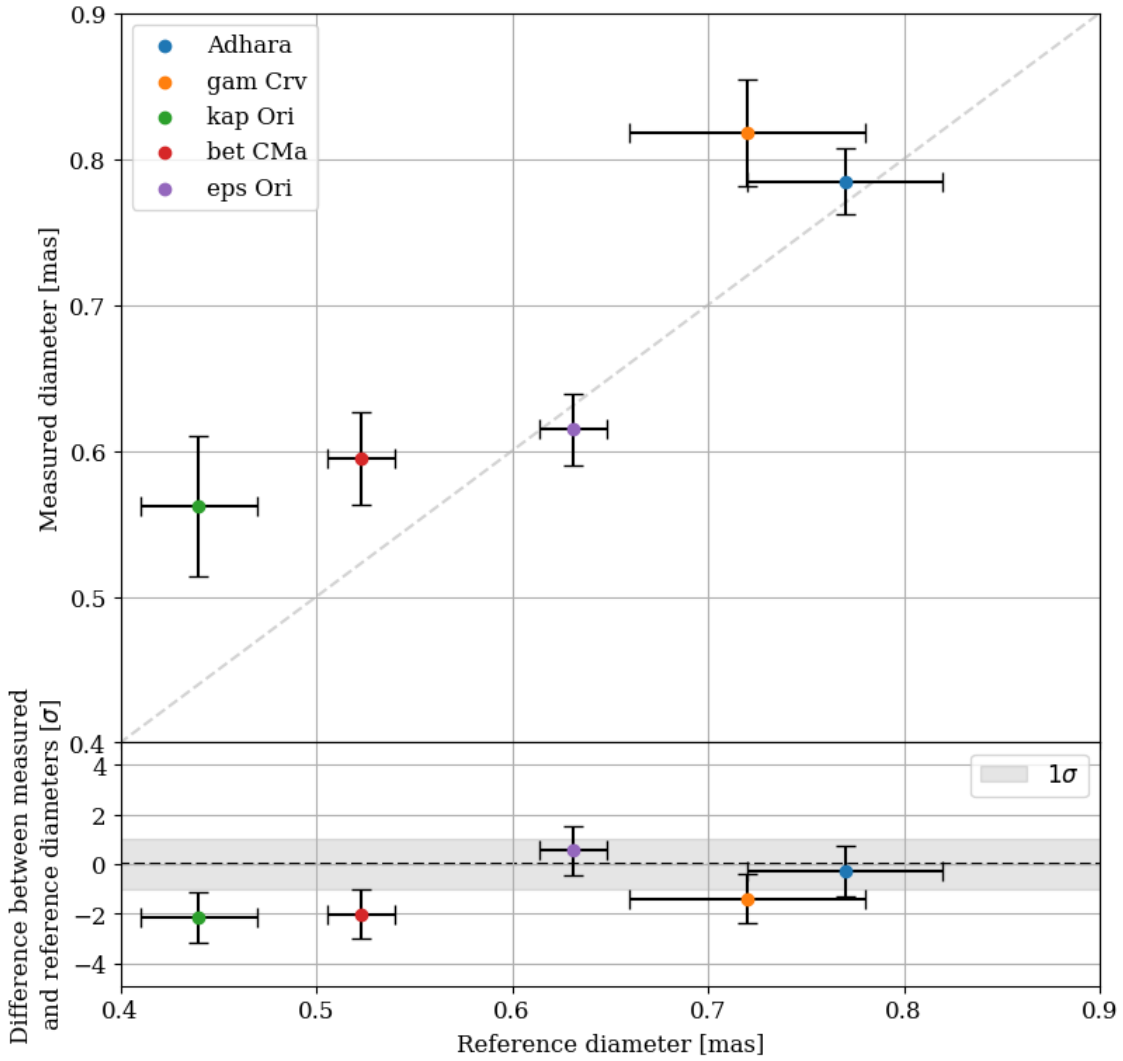

Figure 8.1: *Comparison between reference diameters obtained by Narrabri and VERITAS and measured angular diameters obtained with MAGIC-SII, for 5 of the 7 reference stars. The grey zone in the lower plot shows the* $\pm 1\sigma$ *region of the difference between measured and reference diameters.*

As seen in figure 8.1 and table 7.5 the diameters for Adhara, gam Crv and eps Ori are compatible with measurements performed by Narrabri and VERITAS but for bet CMa and kap Ori they are not. For kap Ori more measurements at different baselines are needed: the fit was performed with just two measurements from A-C and one from B-D, being the measurement from B-D in the same baseline range than one of the measurements in A-C (see figure A.4). For bet CMa the discrepancy could come from the fact that it is actually a Beta Cephei variable star: it is possible that measurements from VERITAS and ours have been performed in different modes of pulsation.

8.1.2 New diameters

Stellar angular diameters have been computed for a total of 16 stars for which the angular diameter had not been measured before in our bandwidth (400-440 nm) or for which there

are measurements in our bandwidth but the precision was too low to be considered as reference stars. They are mostly early-type stars with B magnitudes between 1.67 and 3.73 and modeled angular diameters between 0.05 and 2 mas.

The resulting angular diameters are shown in table 8.1 together with their Bayer designation, HD number, spectral type, B magnitude, modeled value of the angular diameter, measured diameter with the MAGIC stellar intensity interferometer and the reduced χ^2 of the fit. A comparison with the modeled diameters from stellar models is shown in figure 8.2.

Bayer Name	HD Number	Spectral Type	B (mag)	Modeled θ (mas)	Measured θ_{UD} (mas)	χ^2_ν	Obs. Time (hours)
eta UMa	120315	B3V	1.67	0.67 ± 0.14 [2]	0.81 ± 0.01	1.5	9.2
				0.74 ± 0.09 [1]			
bet Per	19356	B8V	2.07	1.2 ± 0.1 [1]	0.82 ± 0.04	7.3	1.6
eta Cen	127972	B2Ve	2.12	0.57 ± 0.06 [1]	0.75 ± 0.08	$4 \cdot 10^{-3}$	0.9
ups Sco	158408	B2IV	2.48	0.48 ± 0.05 [1]	0.92 ± 0.06	1.4	1.5
gam Peg	886	B2IV	2.61	0.36 ± 0.04 [1]	0.48 ± 0.03	0.4	2.9
				0.47 ± 0.02 [2]			
bet Cas	432	F2III	2.61	1.8 ± 0.2 [1]	1.7 ± 0.2	2.4	0.9
				2.0 ± 0.1 [2]			
alf Cep	203280	A8Vn	2.68	1.34 ± 0.14 [1]	1.3 ± 0.1	0.3	2.9
alf02 CVn	112413	A0VpSiEu	2.76	0.71 ± 0.07 [1]	0.68 ± 0.04	3.3	5
				0.6 ± 0.1 [2]			
del Cas	8538	A5IV	2.810	1.2 ± 0.1 [1]	1.14 ± 0.07	0.8	4.7
				1.1 ± 0.1 [2]			
gam Gru	207971	B8IV-Vs	2.89	0.69 ± 0.06 [1]	0.64 ± 0.05	1.9	9.5
zet Per	24398	B1Ib	2.97	0.052 ± 0.001 [1]	0.65 ± 0.08	0.7	3.4
				0.61 ± 0.06 [3]			
phi Sgr	173300	B8III	3.050	0.63 ± 0.07 [1]	0.58 ± 0.05	1.3	6.4
gam Lyr	176437	B9III	3.200	0.70 ± 0.08 [1]	0.68 ± 0.04	1.2	8.3
				0.6 ± 0.1 [2]			
eps Cas	11415	B3Vp_sh	3.22	0.35 ± 0.04 [1]	0.68 ± 0.06	0.9	7.0
				0.36 ± 0.08 [2]			
zet Cas	3360	B2IV	3.47	0.29 ± 0.03 [1]	0.34 ± 0.06	2.1	10.2
				0.32 ± 0.01 [2]			
tau Her	147394	B5IV	3.73	0.37 ± 0.03 [1]	0.38 ± 0.03	1.1	19.4

Table 8.1: *Table of MAGIC's measured UD angular diameter for stars with modeled diameters from different sources. Spectral types and B magnitudes are from SIMBAD. The modeled angular diameters are from the (1) JSDC catalog v2 ([170]), the (2) Swihart catalog ([169]) and the (3) SearchCal tool ([171, 172]). The stars that were found both in JSDC and SearchCal presented no difference in the value nor in the error between them, except for zet Per for which the value was very different.*

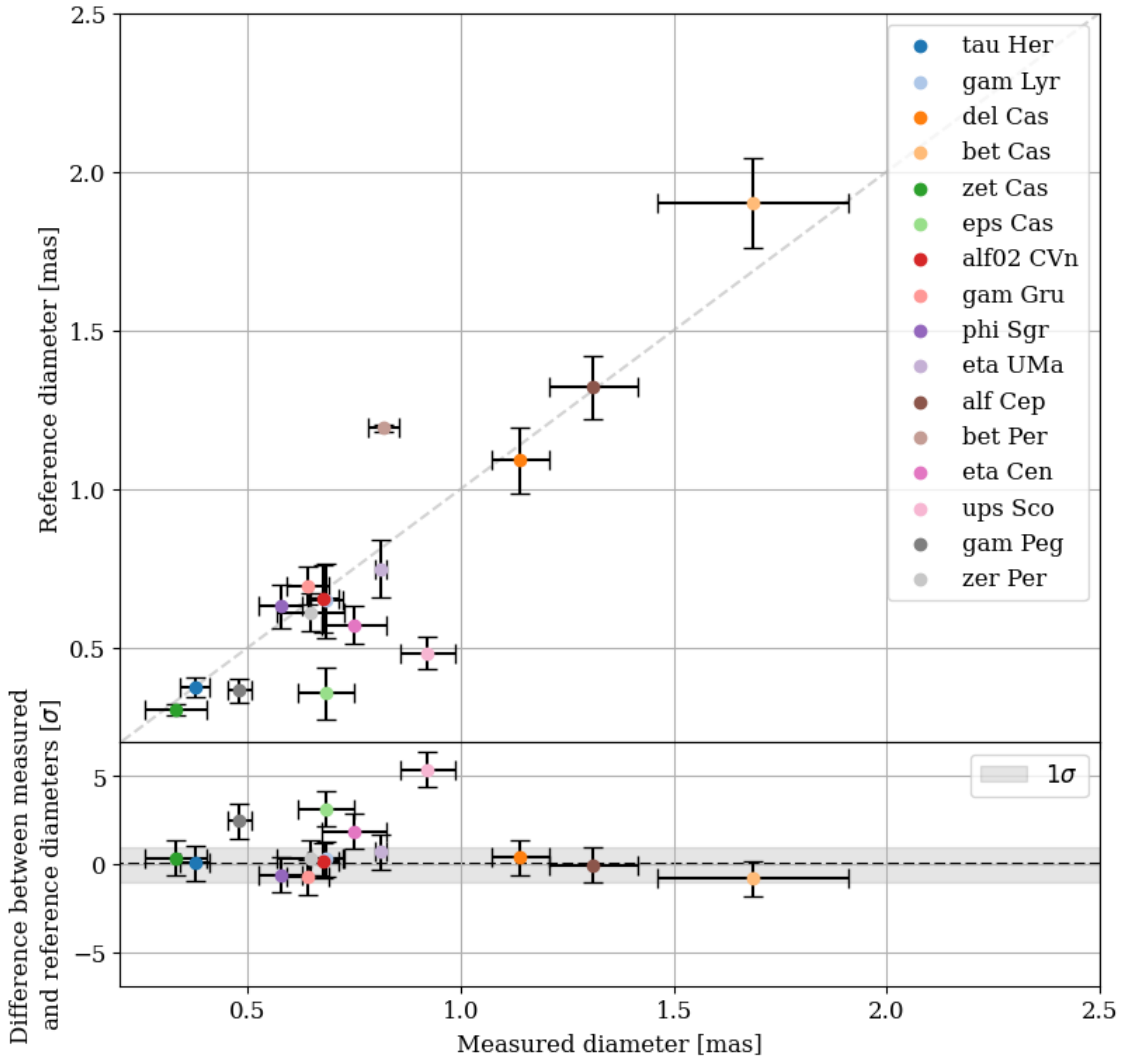

Figure 8.2: *Comparison between modeled and measured angular diameters for stars without a direct angular diameter measurement in our optical band.*

For vast majority of cases, the modeled diameter agrees with the measured diameter and previous measurements in other wavelengths:

eta UMa: also known as Alkaid or Benetnasch, is a fast rotator with a rather small oblateness of 0.05 [182]. CHARA reported measurements in [183] with CHARA/PAVO at 630-950 nm of 0.818±0.060 mas. Our measurement is compatible with this measurement and with the the modeled diameters from Swihart, JSDC v2 and Underhill et al. [184].

bet Per: more widely known as Algol, is a triple system in which Algol A and B interact as an eclipsing binary in a close orbit of ∼3 days period and Algol C orbits the first pair with a period of ∼ 680 days [185]. In [186], CHARA reports angular diameter measurements in H band for the three components: UD_A = 0.88 ± 0.05 mas, UD_B = 1.12 ± 0.07 mas and UD_C = 0.56 ± 0.10 mas. Our measurement is compatible with the measurement reported by CHARA in H band but not with the modeled value from JSDC v2. Since the A component is much brighter than the B and C components, we consider that we are only seeing component A most of the time, but it is possible that some

observations have been performed during one of the eclipses of the component B over component A. More measurements at different orbital phases would be needed.

eta Cen: is classified as a Be star with multiperiodic magnitude variations interpreted as non-radial pulsation modes [187]. It is a fast rotator with 0.16 oblateness [182]. The incompatibility of our measurements with the expected value could be explained by its fast rotating nature: maybe this property has not been taken into account in the model for the predicted angular diameter and measurements performed at different UV angles would retrieve different angular diameters. Our measurements have not been separated by UV angle and the UV coverage that we have covered, which could explain the poor quality of the fit and the discrepancy with the modeled values.

ups Sco: is a subgiant B star. Our measurement differs a lot from the modeled value of 0.48±0.05 mas from JSDC v2 and 0.438 mas from [184]. It is not a known fast rotator nor a known multiple star system. A naive calculation of the star radius using the distances from GAIA DR3 [188] and Hipparcos [189] and our measurement of the angular diameter retrieves 220±30 $R_\odot$ and 16 ± 2 $R_\odot$ respectively. The angular diameter obtained in this work of 0.92±0.06 mas is compatible with the one obtained by other analyzers from the MAGIC intensity interferometry group, such as the one presented in C. W. Wunderlich thesis of 0.94±0.09 mas [190]. Measurements at more baselines are needed to improve the angular diameter measurement.

gam Peg: is a Beta Cephei variable star, with radial pulsations with 3 or more pulsational frequencies, ranging from ∼3 hours to ∼ 7 days [191]. Our measurement is compatible with the prediction from Swihart but not with the one from JSDC v2 nor the one from [184] of 0.432 mas. More measurements would be needed to get a better fit, but our measured angular diameter seems to be in the ballpark of what it is expected for this star.

bet Cas: is a Delta Scuti variable star [192] and is a fast rotator [193] spinning at more than 90% of its critical velocity, causing a radius difference of 24% [194]. Our measurement of the angular diameter seems to be in agreement with modeled values from Swihart and JSDC v2. Other measurements in other wavelengths seem to be pretty similar as well: 2.145±0.058 mas at 700 nm [195] and 2.05±0.05 mas at 740 nm [196].

alf Cep: better known as Alderamin, is a fast rotator with oblatenes 0.21 [182]. Our measured angular diameter agrees with the modeled value from JSDC v2. More measurements are needed at different UV angles to improve the quality of the fit.

alf02 CVn: is a binary star together with alf01 CVn, which is much fainter (2.76 vs 5.94 mag). It gives name to the α^2 Canum Venaticorum variable star classification [197]: stars that present specially strong magnetic fields originating starspots that produce visible variations in their light curves and spectra with a period equal to the star rotation. Our measurement is compatible with the modeled angular diameters from Swihart and JSDC v2, but more measurements at different baselines are needed in order to improve the angular diameter estimation.

del Cas: it is an eclipsing binary with a very long orbital period of 759 days [198]. Our

measurement is compatible with the modeled angular diameters by Swihart and JSDC v2.

gam Gru: is a variable [199] high proper motion star [200]. Our measurements agree with the modeled values from Swihart, JSDC v2 and Underhill (0.666 mas) [184].

zet Per: is a blue super-giant [201]. Its angular diamter has been measured by CHARA/VEGA 0.531±0.007 mas at 734 nm [202]. The modeled angular diameters by SearchCal and Underhill (0.702 mas) [184] while the modeled value by JSDC v2 seems to be quite different.

phi Sgr: is another high proper motion star [200]. Our measurements seem to agree with the modeled angular diameter by JSDC v2.

gam Lyr: CHARA has reported measurements for this star in different wavelengths, like 0.74±0.01 mas with CHARA/VEGA at 480-850 nm [202] and 0.712±0.028 mas with CHARA/PAVO at 630-950 nm [183]. Our measurement is compatible with the modeled angular diameters from Swihart and JSDC v2.

eps Cas: according to [201, 203, 204] this is a 'shell star', presenting diffuse helium lines and sharp hydrogen lines. These kind of stars can present episodes in which they display shell characteristics in their spectrum and other episodes in which they do not, appearing sometimes as a Be star or a B star. The incompatibility observed between the modeled angular diameters and our measurement could be caused by a wrong value of E(B-V) (color excess) used in the predictions, as briefly discussed in [184] for which the predicted angular diameter was 0.468 mas. Another reason could be that this star is a fast rotator and our measurements have been performed in a direction in which it appears very elongated.

zet Cas: it is a candidate to be a Beta Cephei variable star [205]. Its diameter has been measured by CHARA/PAVO in the 630-950 nm with a value of 0.273±0.018 mas [183]. Our measurement is compatible with the CHARA/PAVO value and with the modeled values from Swihart, JSDC v2 and Underhill (0.303 mas) [184].

tau Her: it is a pulsating variable [206]. CHARA/PAVO measured its angular diameter in the 630-950 nm with a value of 0.354±0.020 mas [183]. Our measurement is compatible with this value and with the modeled values by JSDC v2 and Underhill (0.358 mas) [184].

9. Conclusions and prospects

Over the course of this thesis, the MAGIC stellar intensity interferometry setup has been upgraded in several ocasions [165, 166, 167]. For this setup, I have participated by finding MAGIC AMC focusing parameters that better focused the light into the designed interferometry pixels. In order to exploit this setup, I built a catalogue of almost 400 target stars with modeled and/or measured angular size diameter in the blue band. This catalogue has been gradually extended with new sources and science cases such as fast rotators or spectroscopic binaries whose results are not showed in this work for being too preliminary still. I developed a tool to schedule over 400 h of observations over the course of the last two years as the official scheduler MAGIC intensity interferometry observations.

I present the different steps of the analysis that I implemented on an pipeline independent from other three different pipelines within the MAGIC intensity interferometry working group, obtaining consistent results with them. I also present several consistency tests in order to ensure data quality, such as: the distribution of corrected delays and widths of the correlation peaks with being compatible with the expected 0 ns delay and 2 ns width, sensitivity measurements and sensitivity estimations that prove that the scheduling tool reproduces well the observed sensitivities, compatible ZBC measurements from different analysis and comparsion of angular diameter measurements from two different hardware configurations that ensure that the measured angular diameters do not depend on the hardware configuration used.

Part of the scientific results obtained with the 400 h of data is presented in this thesis, mainly angular diameters for stars with known angular diameters and for stars whose diameter had not been measured before in blue band. The angular diameters obtained with MAGIC-SII were compared with values from other instruments (Narrabri and VERITAS), showing compatible results for all but one star. For the stars that did not have previous measurements of the angular diameter in blue band, MAGIC-SII measurements were compared with modeled values from different sources based on spectroscopy and stellar models. For all but 3 of the 16 stars, an agreement between modeled and measured diameter was obtained. Some of the stars are known fast rotators according to [182], so the reported diameter values should be taken as an average.

The reported diameter measurements uncertainties in this thesis do not include the contribution of systematics. Still, a systematics study was performed and several sources of systematics were found: 1) The electronic bandwidth could change over short timescales due to changes signal transmission of the VCSels. This returned a systematic of less than 1% for all pixels. 2) The AOI of incident affects the shape of the transmission curve of the optical filters. Simulations were performed within the MAGIC-II working group for different AOIs, which returned in a systematic of less than 1% for all the mirror facets. 3) Changes in gain of the DC/ADC branch due to temperature variations, sudden jumps in current and degradation of the PMTs. The gain values are used to account for the amount of light that goes into each pixel, and properly subtract the NSB contribution to the star's DC. Again, the found systematic value for this effect is less than 1%. 4) Stars different from the target star that cross the FOV of the defined background pixels. It can happen for some stars, in which case very different NSB levels are observed in the two background pixels. The effect can be removed by selecting the unaffected background pixel, but in any case the effect is less than 3% for stars up to 3.5 mag. 5) Residual noise in the correlation caused by the electronic components such as digitizers and correlators. When the amount of starlight photons is low, this noise dominates the correlation, while for higher amount of starlight photons the correlation is dominated by a poissonian. Since frequency of this noise is slower than the sampling frequency and mainly affects observations with low star DC, a 12 MHz high-pass filter is applied to all data.

MAGIC already proved that it can function as a stellar intensity interferometer with the previous setup [167] and is on the process of proving that again with the upgraded setup in a performance paper in preparation of which I will be a corresponding author. Several new configurations are being assessed making use of the neighbour LST-1 and the soon-to-be LST-2, and 4. Combining the two MAGIC telescopes with one or several telescopes, would translate into several advantages: 1) more different baselines would be measured simultaneously and at longer distances, desirable for small stars (< 0.5 mas) and measurement of limb darkening for larger ones ($\gg 1$ mas). 2) The larger collection areas from LSTs with 23 m diameter mirror dishes would reduce necessary observation times for detection compare to those of MAGIC with its 17 m diameter mirror dishes, and lower the star magnitude threshold and relative statistical error in the diameter measurements, as shown in figure 9.1. 4) since different baselines are measured in different relative orientations, the UV coverage would be greatly improved with 3 and 15 simultaneous correlations for MAGIC+LST and MAGIC+4LSTs respectively. This would help to unveil the structure of non-symmetric targets such as fast rotators and spectroscopic binaries and even some asteroseismology modes.

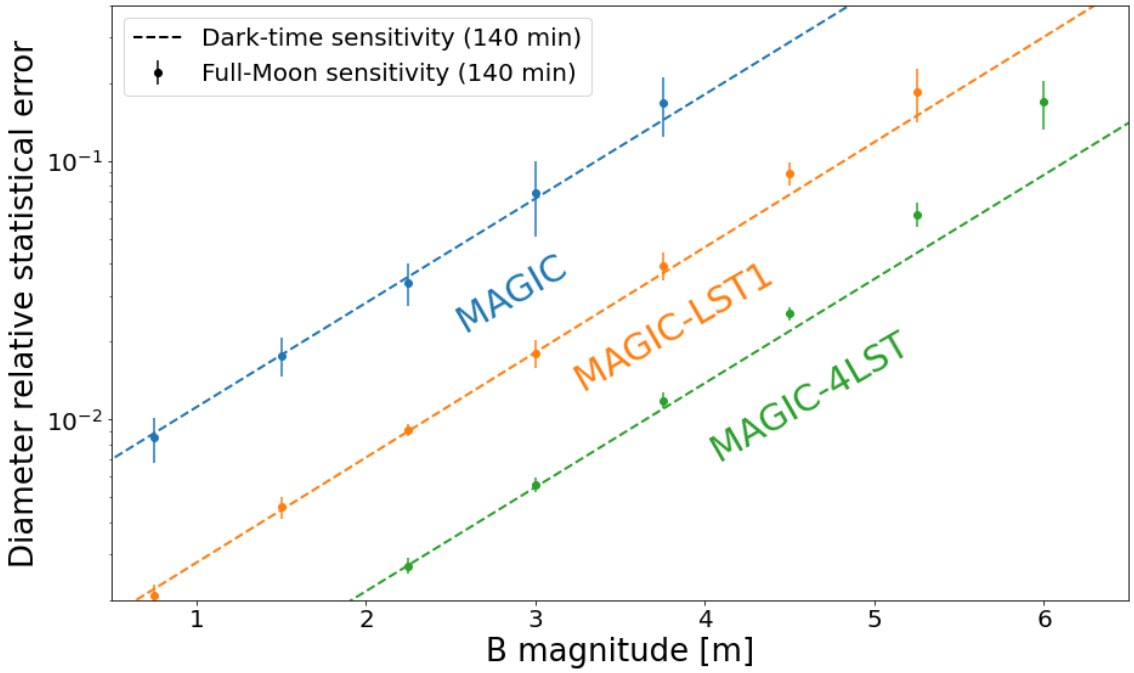

Figure 9.1: *Plot from [166]. The expected error in the measurement of an angular diameter as a function of magnitude is calculated for MAGIC, MAGIC-LST1 and MAGIC-4LSTs. The dashed lines show the the results assuming dark-sky conditions while the points are simulated under full-Moon conditions, both with 140 minutes of observation per step.*

II Fast Radio Bursts

10. Introduction

Fast Radio Bursts (FRBs) are a kind of astrophysical transient that consist on fast, bright radio flashes. They were first discovered with the Parkes Radio Telescope in Australia in 2007 [207]. Since then, over 600 FRB sources have been detected, displaying a wide range of characteristics. So far, 24 of them exhibit a repeating behaviour but others do not, which may suggest different emission mechanisms. At least 2 of the repeaters also display periodic states of activity: FRB 20121102A [208] and FRB 20180916B [209], with periods of 157 [210] and 16.35 [211] days respectively. For this kind of FRB sources (repeaters), young magnetars are the prime candidates (and perhaps also for non-repeating ones). This is supported by the detection of FRBs coming from the galactic magnetar SGR 1935+2154 [212], which was the first known FRB emitter associated to a known source within our galaxy. In case of the non-repeaters, more cataclysmic scenarios have been proposed like the merging of neutron stars [213].

Most FRB emissions have been identified to come from outside of our galaxy by studying their dispersion measures (DMs): depending on from where and from how far away the FRB was produced with respect to Earth, the pulse gets more dispersed by the free electrons in our galaxy (different column depths) the farther away the source is, which has a direct effect on the delay of the pulse observed in different frequencies. Given that there is a maximum dispersion measure in any given direction within our galaxy (that can be explained by the models of free galactic electrons), if a significantly greater dispersion is observed, then we are looking at an extragalactic event. This is one of the main reasons why these events remain a mystery: most of them come from cosmological distances and yet we observe them with such a great brightness that the energy involved in their production must be huge. Another reason is that they have only been detected in radio and very few of them simultaneous to other wavelengths.

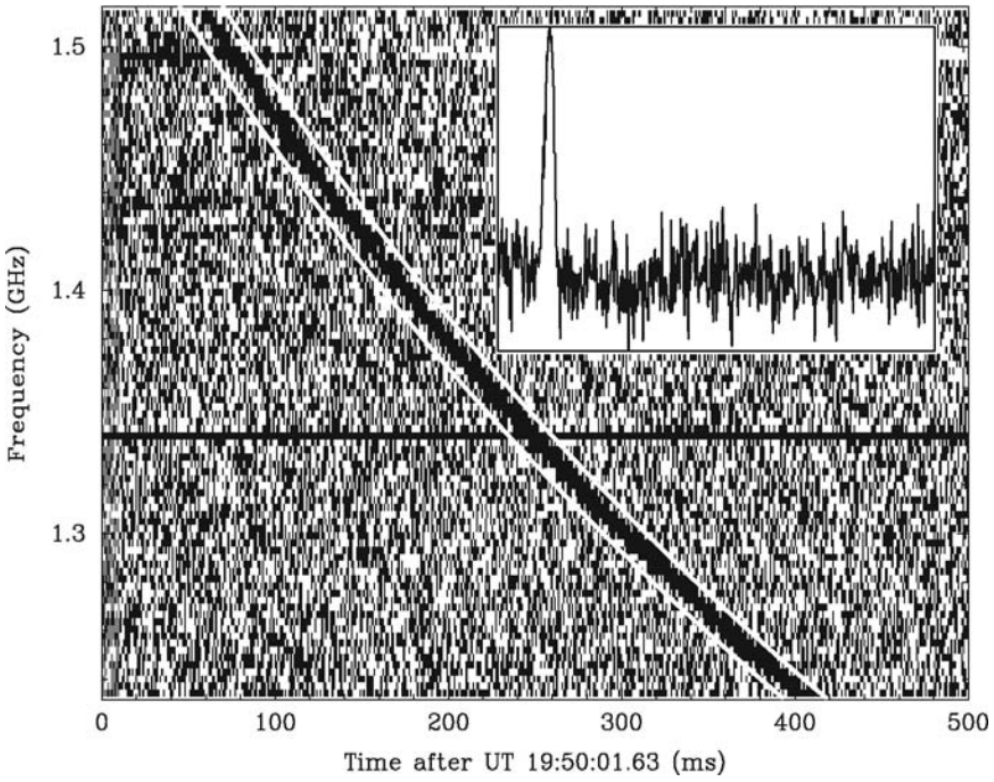

Figure 10.1: *Waterfall plot of CHIME data collected on August 24th, 2021. It shows a quadratic shift in the position of the pulse across the frequency band, which translates into a dispersion measurement of 375 ± 1 pc cm^{-3}. This DM is much higher than the expected DM for this line of sight which is 25 pc cm^{-3}. This fact together with the galactic latitude of the source b = -41.8° makes it highly improbable that the source is located within our Galaxy and suggests a cosmological origin [207].*

10.1 Main suspects: Magnetars

Magnetars are neutron stars with specially strong magnetic fields (B = $10^{14} - 10^{15}$ G) and short spin periods (1 - 10 s) [214]. They are known to display persistent and transient emission:

Persistent Their strong magnetic field decays, powering persistent X-ray emission via thermal radiation from the neutron star's hot surface which gets reprocessed in the magnetosphere via cyclotron resonant scattering [215]. This emission has only been detected up to a few keV. Fermi-LAT has set strong upper limits in HE gamma rays for 20 galactic magnetars from observations taken over the curse of six years [216]. MAGIC set upper limits in VHE gamma rays for magnetars 4U 0142+61 and 1E 2259+586, observing no significant emission above 100 GeV for 14 and 25 h of observation respectively [217]. These non-detections agree with theoretical models that predict that magnetars are not expected to emit gamma-ray radiation via synchro-curvature processes since magnetospheric particles are not sufficiently accelerated in order to emit any detectable HE gamma-ray signal [218].

Transient Magnetars have been known to produce flares or bursts that have been detected in radio and X-rays, on different time-scales. They are most likely caused by large-scale changes in the surface or the magnetic field. The bursts can be divided by their duration and intensity into short, large and giant flares. Giant flares have been observed to display very intense short hard spike emission followed by a weaker pulsating phase and a thermal afterglow in X-rays [219] as seen in figure 10.2. Fermi-LAT detected one of these events in the HE range [220] proving these sources have the energy budget to emit at energies above 1 GeV.

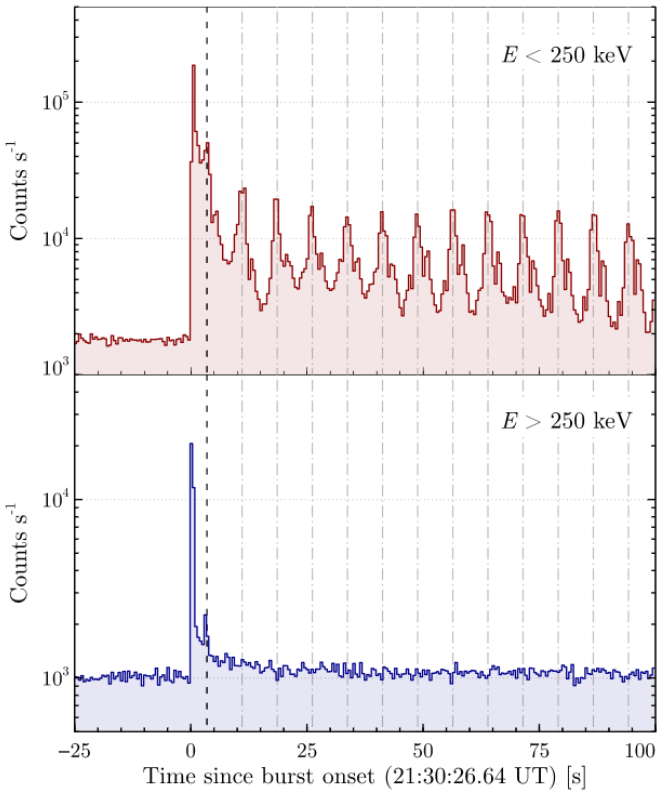

Figure 10.2: *Count rates of the RHESSI solar telescope during a giant flare on December 27, 2004 of the magnetar SGR 1806-20 [219, 221]. Top plot shows the flare and the oscillations at E < 250 keV while the bottom plot at E > 250 keV shows the flare but no oscillations. The dot-dashed lines mark the spin period of the neutron star, coincident with the pulsations on the top plot.*

10.2 MAGIC potential to detect FRBs counterparts

Magnetars show very diverse transient activity with short, large and giant flares. For the moment there is no link between short flares and HE emission, but giant flares have been detected by Fermi-LAT (E $>$ 1 GeV) as showed in the previous section. This proves that magnetars have the energy budget to emit in HE. If the emission mechanism is able to accelerate photons to even higher energies, MAGIC would actually be better suited than Fermi-LAT to detect such bright transient emission. As shown in figure 10.3, IACTs are $\sim$3 orders of magnitude more sensitive than Fermi-LAT to brief transients in the VHE regime.

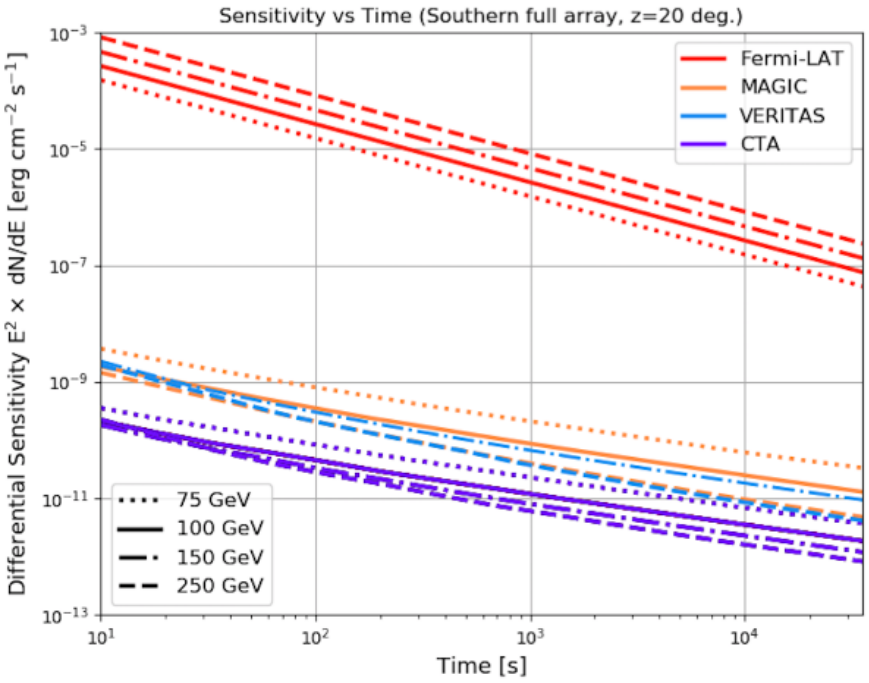

Figure 10.3: *Differential sensitivity as a function of observation time for Fermi-LAT, MAGIC, VERITAS and CTA (South array) at four energies from 75 to 250 GeV [222].*

Current magnetar models support the possibility of observing optical bursts [223]. In fact, ultra-fast optical emission was detected in 2007 from the direction of the galactic magnetar candidate SWIFT J195509.6+261406 [224]. They detected strong optical flares of magnitude > 6 mag and durations between 2 and 100 s. The morphology of the optical flares resembled X-ray outbursts of SGRs. MAGIC's Central Pixel setup described further ahead (section 11.2) has enough sensitivity and time resolution to observe similar bursts.

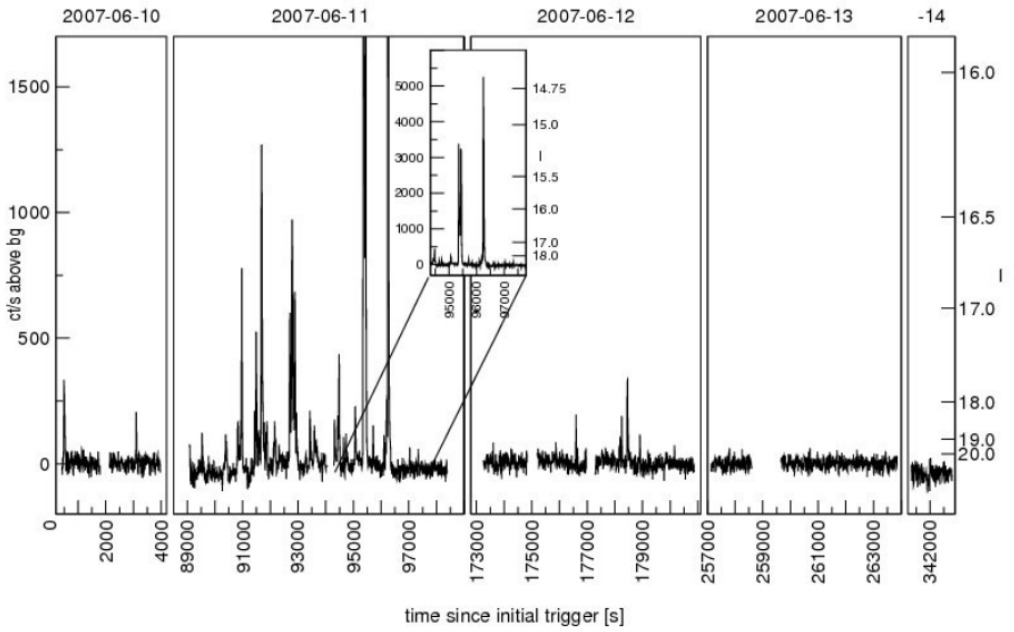

Figure 10.4: *Optical light-curve of SWIFT J195509.6+261406 obtained with OPTIMA-Burst at Skinakas Observatory. Several fast optical flares are seen within the first 50 h from the initial trigger [224].*

As introduced in this chapter, most detected FRBs are one-time transient events, while a reduced subset of them show a repeating behaviour. Over the last decade radio surveys have shown that these repeaters have periods of higher activity, in which the average burst frequency reaches values well above 1 FRB/h. These properties make FRB repeaters the ideal target to constrain the multi-wavelength emission of these transient phenomena: they allow the scheduling of strictly simultaneous observations between several facilities during active periods. Although rather time consuming, this observational approach has achieved multiple milestones, such as the localization of FRB repeaters by employing multiple radio antennas [225], the detection of X-ray burst simultaneous to FRB burst for SGR 1935+2154 or the setting of UL in optical and VHE by MAGIC [138].

Among FRB repeaters, FRB 121102 was the first known FRB repeating source and the second known repeater with periodic activity with a period of 157 ± 7 days [210]. Thanks to its repeating behaviour it was possible to localize the source with sub-arcsecond precision, identifying radio and optical persistent sources in its direction [225, 226]. It seems to be located in a star-forming region with low metallicity [227] within a dwarf galaxy of redshift $z \simeq 0.193$ [228] at a projected separation of 40 pc from a compact persistent radio source [225]. The FRBs from this source have been observed with an average DM of 557 pc cm^{-3} [208]

FRB 121102 was observed by MAGIC in 2017 in both VHE and optical [138] and by Arecibo in radio [229]. Five radio bursts were detected simultaneous to MAGIC observations, but no counterpart was found for any of the radio pulses as shown in figure 10.5 in the optical. The emission was constrained in both VHE and optical. A bright 12 ms optical flash occurred 4.3 s before one FRB but it was consistent with meteors' irreducible background (2.2σ). Still, MAGIC was able to provide the most stringent constraints to

simultaneous optical and VHE emission available at the time.

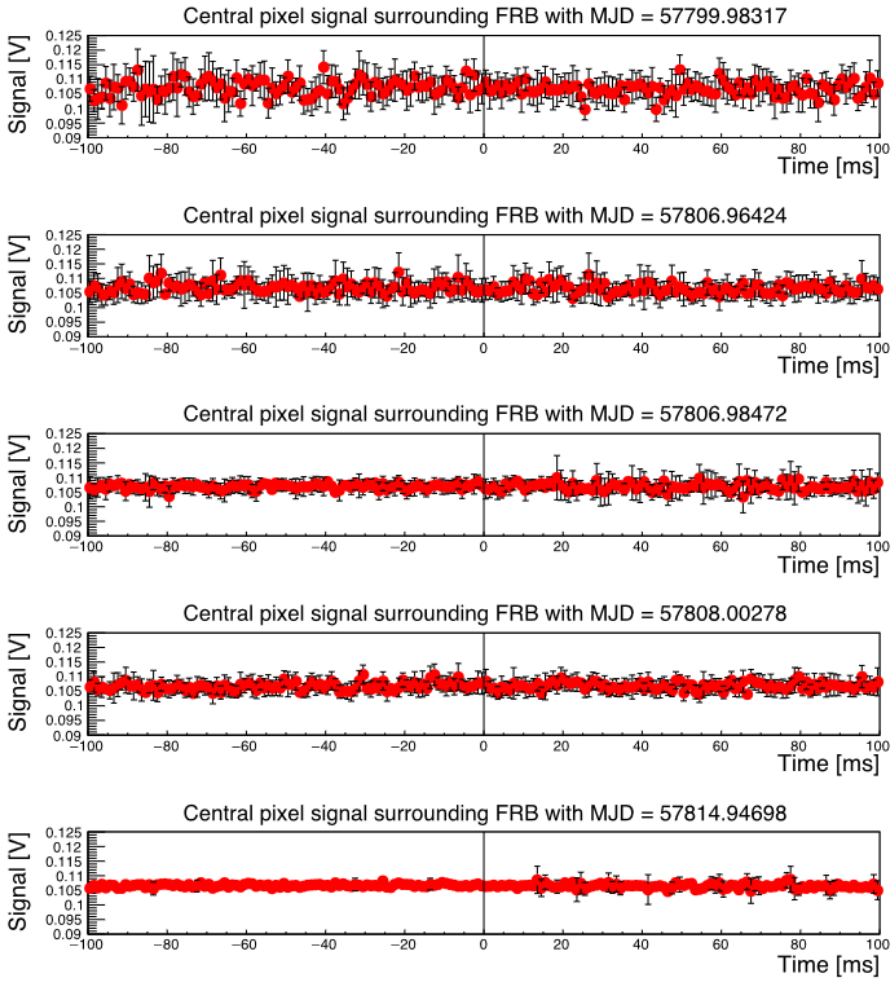

Figure 10.5: *Optical light-curves of FRB 121102 taken with MAGIC's CPIX from [138], covering ±100 ms around the Arecibo's TOAs [229]. No significant excess is observed simultaneous to any of the bursts.*

These observational results demonstrate the potential IACTs may have on detecting MWL counterparts to FRB emission. For this reason, the FRB observation program has been proposed within the MAGIC Collaboration since 2017, and multiple observing campaigns have been performed on multiple FRB repeaters showing high burst frequencies triggered by radio observations. The results of some of these observing campaigns are presented in the following sections.

11. MAGIC analysis

11.1 VHE analysis

The VHE analysis has been performed using the MAGIC Standard Analysis Software (MARS) [230, 231]. MARS is a collection of programs written in C++ embedded within the ROOT framework [232]. In this section a brief description of the MAGIC analysis is presented. For a more in-depth description of the analysis, see [21, 233, 234] and references therein.

The overall flow of the analysis is divided into the following steps:

Initial data quality assessment

1. Source data selection: it is necessary to establish the conditions in which the source's data has been taken: zenith range, ON or Wobble mode, stereo or Mono, with standard or SumT trigger, good/bad weather, high/medium/low background illumination levels, analysis period.

2. MC data selection: Given the impossibility of directly calibrating IACTs, these telescopes heavily rely on simulated Monte Carlo (MC) data. VHE gamma-rays MC data needs to be selected, matching the type of trigger of the data (standard or SumT), analysis period (since the performance of the telescopes varies with time), and zenith range. It will be necessary to train and test the random forests later used in event classification, energy estimation and direction estimation.

3. OFF data selection: Select OFF data, empty of known VHE gamma-ray sources, with similar observing conditions to those of the source (zenith range, observation mode, trigger, analysis period). It will be needed to train the random forests used for gamma/hadron classification.

4. Crab Nebula data selection: Select Crab Nebula data with similar conditions to the source's data (zenith range, observation mode, trigger, analysis period). The Crab Nebula acts as a 'standard candle' since it is a bright and stable VHE emitter. It

is needed to test that the random forests are properly trained and that the analysis chain is capable of reconstructing the Crab Nebula spectrum properly (agreeing with previous publications).

Signal extraction A trigger system is implemented that evaluates the events and decides whether storing or not the received signals. Its main objective is to store as many Cherenkov showers as possible, leaving out as many events caused by the NSB as possible. The pixels involved in the first three levels of the system are the inner-most ones, favouring those events recorded close to the center of the camera (where most of the Cherenkov image is expected to be seen completely):

- Level 0: this level evaluates if the digitized signal from each channel surpasses a discriminator threshold (DT) which is different for different source and observation conditions (galactic or extragalactic source, with or without moon-light) and whose objective is to limit the amount of background events (mainly CRs) while maintaining a sufficient and stable rate of gamma-like events.

- Level 1: this level looks for spatial and temporal correlation within several overlapping regions for events that passed the Level 0 trigger. The events that present N adjacent pixels forming a compact group are accepted since gamma-like events are expected to produce compact Cherenkov images (ellipses).

- Level 2: this level evaluates the shape of the events that passed the Level 1 trigger providing additional discrimination, although it is not enabled for standard MAGIC data taking modes. It is used for monitoring the event rate, rate scaling, coordination of the Level 1 trigger with the calibration system and the merging of stereo triggers.

The last trigger level is the Level 3 and is used in stereoscopic observations (which is the standard for VHE observations with MAGIC). This level evaluates which events have triggered both telescopes within a certain time window at trigger level 1. The PMT signals and arrival times of events that successfully trigger this level are stored for further analysis.

Signal calibration Given the different properties of each PMT in the camera, a step is needed to ensure the signal coming from each pixel are calibrated (both in charge and arrival time). The pedestal signal is subtracted and each pixel's charge is converted from ADC to photo-electrons via the F-factor method [235]. The arrival times are corrected by their corresponding cable length differences.

Image cleaning In addition to the elliptical-shaped Cherenkov showers, IACT camera images contain NSB photons and electronic noise. Image cleaning algorithms are applied to identify those pixels dominated by Cherenkov photons. Calibrated images are 'cleaned' by identifying clusters of pixels with charge above a given threshold and similar arrival time.

Image parametrization Hillas parametrization [236] is applied to describe the properties of cleaned images of the events.

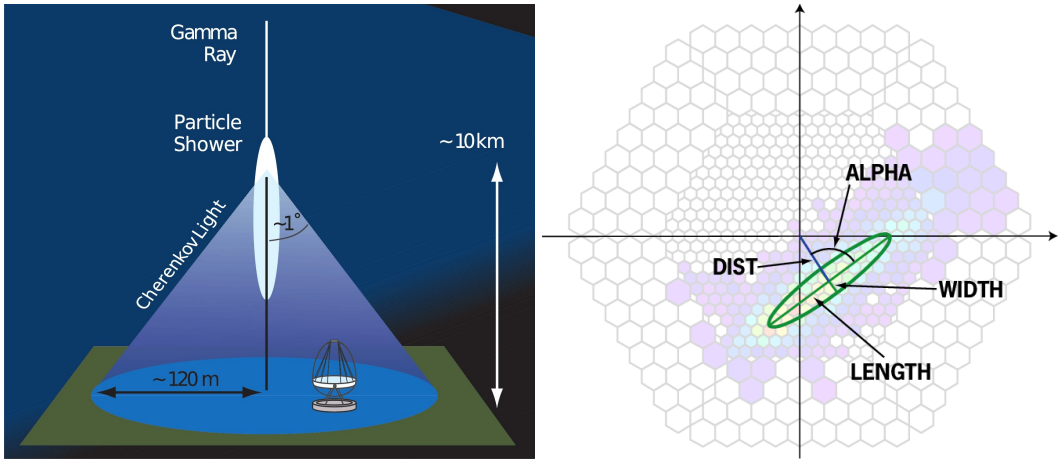

Figure 11.1: *On the left: diagram of a gamma-ray shower development from [237]. On the right: image of a cleaned shower with a superimposed diagram of some of the Hillas parameters that describe it [231].*

The most relevant Hillas parameters, determined from single calibrated images, are:

- **Size:** total charge in photo-electrons of the cleaned image. It is strongly correlated with the energy of the primary.

- **Length:** corresponds to the length of the major axis of the image. It accounts for the longitudinal development of the shower. It is usually larger for hadronic showers than for gamma ray showers.

- **Width:** corresponds to the length of the minor axis of the image. It accounts for the lateral development of the shower. Hadronic showers usually appear broader than gamma ray showers.

- **Center of gravity (CoG):** center of gravity of the image in camera coordinates.

- **Conc N:** concentration or compactness, it accounts for the fraction of the photoelectrons within the n brightest pixels.

- **Dist:** it is the angular distance between the center of gravity of the image and the source position in the camera. It is used to provide an estimation of the impact parameter of the shower, which is the distance between the shower axis and the telescope axis.

- **Alpha (α):** it is the angle between the major axis of the image and the line that connects the center of gravity of the image with the source position in the camera. The images of showers produced by gamma rays coming from the assumed position of the source in the camera will have low alpha values, since the major axis will point to it.

- **Time gradient:** it is the slope of the linear fit of the arrival times with the spatial coordinate along the major axis. It accounts for the temporal development of the source.

- **Time RMS:** corresponds to the RMS of the arrival times. It will be different for gamma ray showers and for hadronic showers so it is used as one of the discriminators between them.

- **M3Long:** third longitudinal moment of the image along the major axis. It is used to account for the asymmetry along the major axis to distinguish the head from the tail.

- **Asymmetry:** it is the distance between the pixel with the highest charge and the center of gravity of the image, projected onto the major axis. It accounts for the head-tail arrangement of the image.

- **Leakage N:** it accounts for the fraction of charge in the Nth outermost ring of the camera. It helps to estimate how much of the image is lost outside the camera. The greater it is, the less of the image is seen by the camera and a correct reconstruction will be more difficult.

- **Number of islands:** corresponds to the number of isolated groups of pixels. Images produced by gamma ray showers will typically generate a single island while hadronic showers may generate more than one within a single event.

In case that at least two telescopes are triggering simultaneously the same events (MAGIC standard observations are in stereo, so all events fulfill this condition), more parameters can be extracted to describe the event:

- **Shower axis:** it is the 3-dimensional direction of the development of the shower. It is characterized by the arrival direction (point in which the major axes of the images would cross if they where in a common camera plane) and the impact parameter with respect to each telescope.

- **Maximum height:** it is an estimation of the altitude at which the development of the shower was at its maximum. It is strongly correlated to the energy of the primary and it is an important discriminator at low energies.

- **Cherenkov radius and photon density:** they correspond to the radius and density of the Cherenkov light pool on the ground.

- **theta^2 (θ^2):** similar to the alpha angle in monoscopic observations. It corresponds to the squared distance between the true and reconstructed position of the source. Showers with a reconstructed position closer to the source position are more likely to actually come from the source.

All these parameters are calculated for both acquired data and Monte Carlo simulations of VHE gamma-ray showers. Machine learning algorithms (random forest) are trained to identify, using these parameters, the nature (mainly gamma vs hadrons), energy and direction of the primary particle of the shower.

Secondary data quality assessment A second quality assessment is performed making use of MARS 'quate' tool to establish good-time-intervals of data by checking several parameters:

- That the trigger rates are mostly stable and between 200-300 Hz, which are the expected cosmic-ray trigger rates under good-quality sky and hardware conditions.

- Cloudiness/Number of stars: MAGIC counts with a subsystem that monitors and improves the pointing accuracy of the telescopes called Starguider. It uses a CCD camera to record the position of bright stars in the region around the pointing position of the observation and compares their position with their expected ones, making use of reference LEDs around each camera as well. In presence of clouds or calima the system will not be able to see as many stars as in good-weather conditions. About 20 - 40 stars should be seen at any given point. A low number of recognized stars not only implicates bad weather conditions but also possible reduced pointing precision.

- That the average DC (NSB brightness) is not too high. Higher average DC means higher background illumination levels, so it should be as low and stable as possible. If it is too bright (>3000 nA) it could be due to the presence of the Moon or that the data has been taken during sunrise/sunset.

- The presence of aerosols, clouds, calima and high humidity diminish the performance of the telescopes, therefore the quality of the atmosphere needs to be constantly monitored to ensure the best data quality. This monitoring is performed in MAGIC by the use of a LIDAR (Light Detection and Ranging) setup [238, 239]. The LIDAR information shows the atmospheric transmission for different altitudes. Times in which the transmission is too low (typically less than 55% at 9 km) are not used in the standard analysis.

The following image is a screenshot of the output of the tool quate for an observation performed with good weather at low zenith:

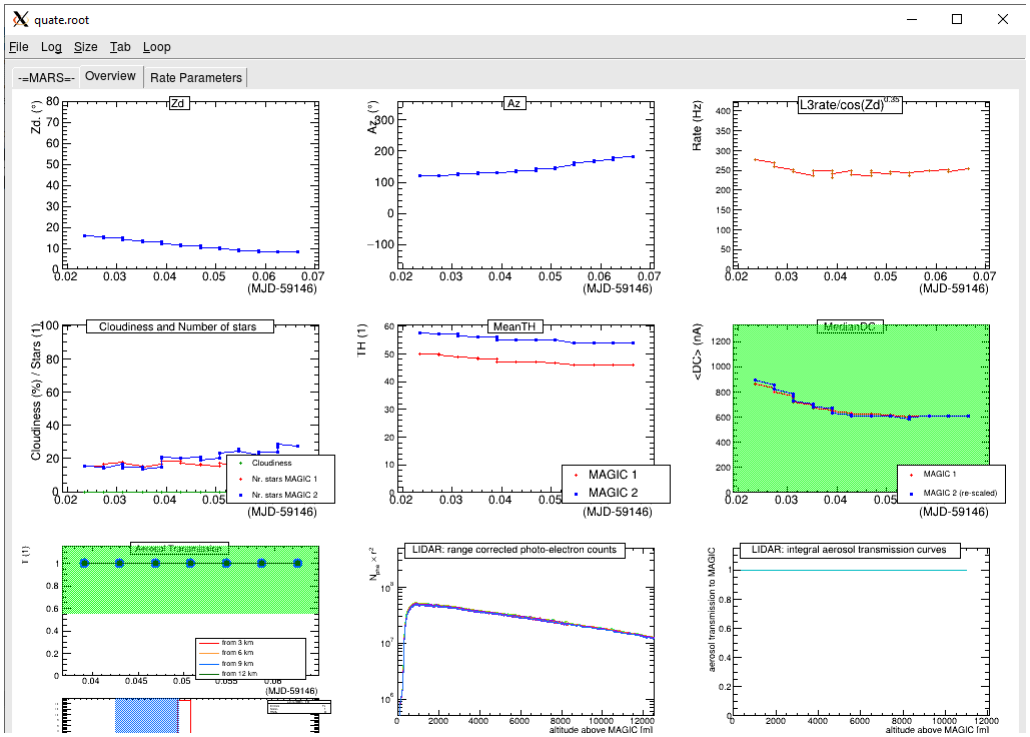

Figure 11.2: *Example of the output of quate for good quality data. Several plots show the conditions in which the data was taken: low zenith, azimuth between 100 and 200 deg, L3 trigger rates between 230 and 280 Hz, Cloudiness(%)/Stars shows around 20 stars or more, TH or trigger threshold seems stable, Mean DC is between 600 and 900 nA, Atmospheric Transmission is around 1 for the whole time, LIDAR data shows no spikes in the curve, meaning no presence of clouds at any of the altitudes, LIDAR integral aerosol data shows a transmission of 1 for all altitudes.*

Random forests training The selected OFF data together with half of the VHE gamma-ray MC data is used to train random forests that are later used to distinguish gamma-like events from hadron-like events, and estimate the energy and direction of the primary.

Random forests testing The selected Crab data is analyzed with the trained RFs to test if the reconstructed spectrum agrees with the Crab Nebula spectrum. This is usually called the 'Crab test'.

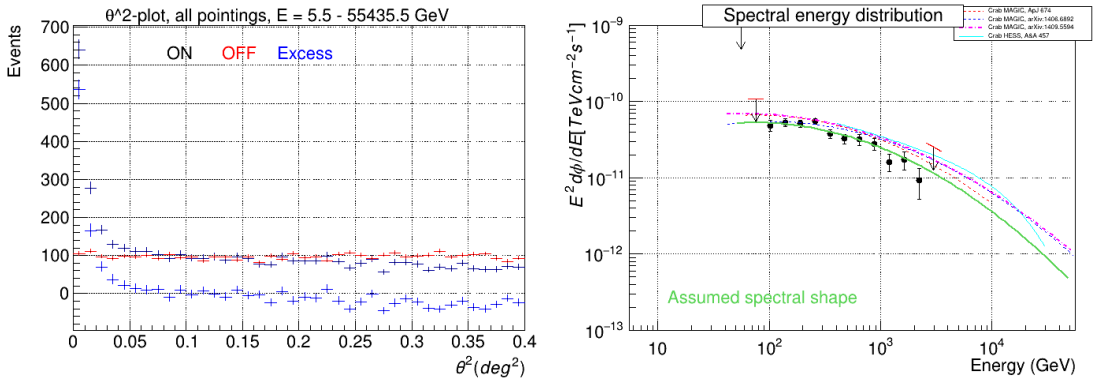

Figure 11.3: *Crab test for the analysis period of ST.03.14. On the left: θ^2 distribution. On the right: spectral energy distribution that shows an overall agreement between this analysis and previous analysis.*

Source's data analysis If the 'Crab test' was successful, then the performance of the analysis chain is proven, and it can be used to produce high-level data products such as the SED and the light curve of the target source. Only the selected good-time-intervals are used to generate these products.

Significance calculation In order to calculate the significance of the VHE signal it is necessary to reduce the number events that are more likely produced by hadronic showers. This is achieved by filtering out those events with a high probability of being hadronic showers, which is quantified by the *hadroness* parameter. The lower its value, the most likely is that the shower was produced by a gamma ray. For further suppression of the background the angle parameters alpha and theta^2 are used. In stereoscopic observations the theta^2 is used to take advantage of using more than one telescope. Since theta^2 is defined as the squared distance between the true and reconstructed position of the source, events that come from the true position of the source will have lower theta^2 values. A *signal region* is defined from 0 to a certain value of theta^2. In case of gamma-ray emission coming from the expected direction of the source, an excess on the source events (ON events) above the background events (OFF events) would be observed. For higher theta^2 no signal will be expected and the ON and OFF events are expected to have the same behaviour, slowly decreasing according with the declining acceptance of the camera with radius.

In order to calculate the excess events over the background the number of events are compared following the expression:

$$N_{ex} = N_{on} - \kappa N_{off} \tag{11.1}$$

where κ is the ratio between on-source and off-source times and N_{on} and N_{off} account for the amount of photons within the defined signal region coming from the ON and OFF regions. The quantity κN_{off} amounts for the background events. The significance is then calculated with the null hypothesis that the observed photons come from the background (i.e. no photons coming from the source) following expression 17 from [240]:

$$S = \sqrt{2}\left\{ N_{on} ln\left[\frac{1+\kappa}{\kappa}\left(\frac{N_{on}}{N_{on}+N_{off}} \right) \right] + N_{off} ln\left[(1+\kappa)\left(\frac{N_{off}}{N_{on}+N_{off}} \right) \right] \right\} \quad (11.2)$$

For a measurement obtained with a single observation (one trial), with enough N_{on} and N_{off}, one can say that the significance of said event is the result of equation 11.2 (in units of number of sigmas) [240]. Unless otherwise stated, the significances of VHE emission are calculated following this expression. In case further cuts and restrictions are applied to the data, the number of trials needs to be taken into account to correct the value of the significance to avoid false detections. By convention, an emission is detected from a source if the significance level is equal or above 5σ.

11.1.1 Modes of observation: Wobble and ON/OFF

IACTs have a wide field of view when compared to optical telescopes, with the peculiarity that the acceptance to VHE gamma-rays across the field of view falls quickly when approaching the edges of the camera. In addition, this acceptance changes with many environmental parameters (zenith distance, azimuth, night-sky background illumination, etc...). Because of these peculiarities, IACTs generally use the following observing modes:

Wobble observations They are performed tracking a position with a given angular offset from the source of interest. This offset is chosen so that acceptance in the ON region is still good while enough OFF regions with comparable acceptance fit in the FOV. This allows for simultaneous measurement of signal and background events at positions on the camera with the same acceptance. These observations are usually carried out tracking four Wobble positions around the source of interest as seen for the two examples in figure 11.4. MAGIC usually employs a Wobble distance of 0.4°. Each Wobble position is observed every 15-20 min to avoid a systematic bias due to detector inhomogeneities.

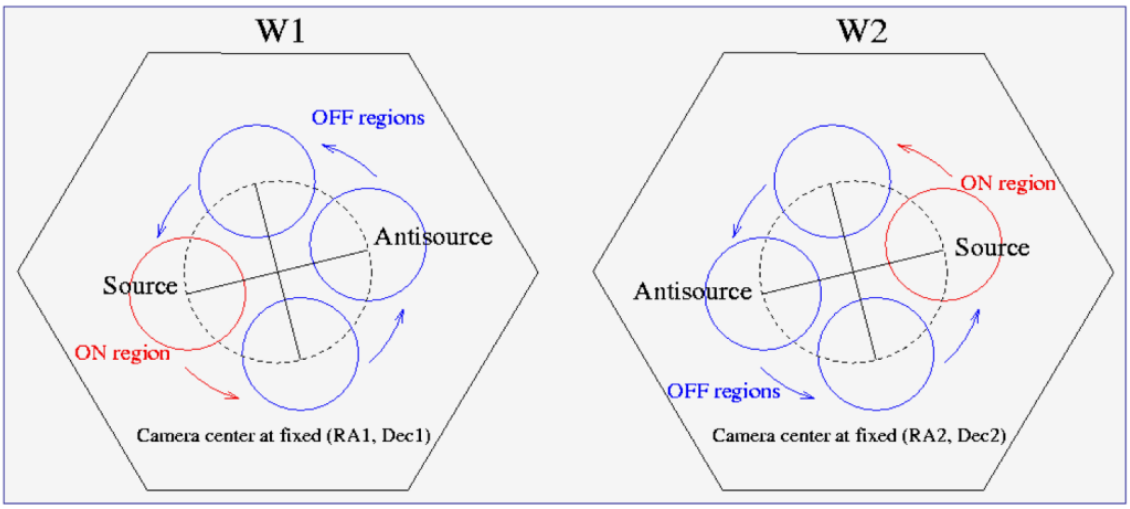

Figure 11.4: *Diagram of how two wobble positions in which one ON region and 3 OFF regions are defined from [234].*

ON/OFF observations They are performed by pointing the source of interest directly (falling into the center of the camera, i.e. ON observations). As the background in this observation mode is not measured simultaneously, devoted OFF observations need to be carried out pointing to a close-by sky position (so that you expect similar telescope performance) with no known VHE emitters. These observations are generally carried out intermittently between the ON and OFF positions.

For repeating FRBs, observations are generally carried out simultaneous to MWL partners, and the key science driver is to observe the extremely brief and transient events strictly simultaneously. ON observations are preferred because:

1. In ON mode, the acceptance is maximized in the source region, slightly improving sensitivity.

2. The duty cycle of ON observations may be close to 100%, once you completely neglect taking devoted OFF observations.

3. The source is located at the center of the FOV, location of the MAGIC Central Pixel. As will be explained in the next section, this system allows MAGIC to perform fast optical photometry simultaneous to VHE observations.

This observation mode (ON mode observations, without interleaved OFF observations) presents a problem in the VHE analysis: no observations are devoted to measure the background. For this reason, other observations with similar observing conditions are used to model the expected background.

11.2 Fast optical photometry with MAGIC's Central Pixel

The Central Pixel System (CPS or CPIX) consists of a modified photosensor-to-readout chain at the center of each MAGIC camera [136]. MAGIC's pixels are comprised of a PMT and a preamplifier that splits the signal into an AC branch that processes Cherenkov light pulses and a DC branch that monitors the anode current. The goal of implementing the Central Pixel System is to increase the bandwidth to over 3 kHz by splitting the DC branch into the slow-control DC monitoring system and to an additional optical transmitter. The signal of the optical transmitter is then read by both the MAGIC DAQ system (Domino readout) and a dedicated PC. This allows for fast (10 kHz) optical photometry observations without disturbing VHE data-taking [150]. In order to reduce the noise at kHz frequencies caused by the electronics, the CPIX is only sensitive to signals between 5 Hz and 10 kHz. A diagram of the DC branch is shown in figure 11.5.

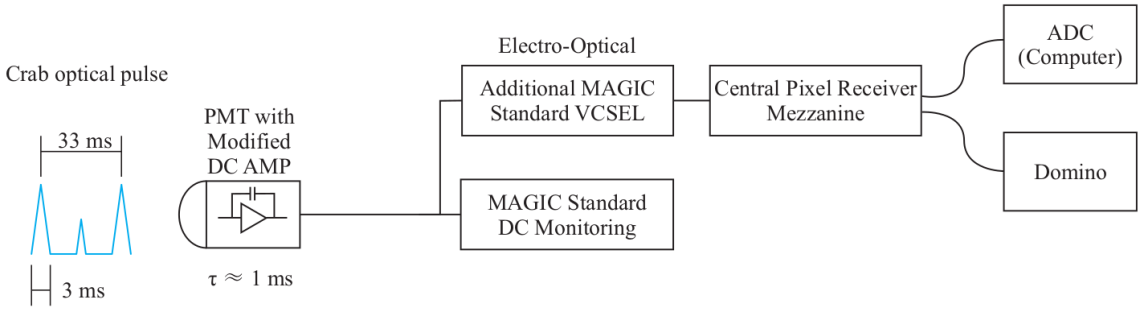

Figure 11.5: *Block diagram of the CPIX showing the modified DC branch [150].*

The main science driver of this system are fast optical variable sources such as:

- **Pulsars:** pulsated emission has been detected from pulsars in several wavelengths: radio, optical [241], X-rays [242] and even in HE [243] and VHE [39, 231] gamma rays. Given the observed phenomenology of pulsars in different wavelengths, it would make sense to exploit MAGIC capability to perform optical and VHE searches of pulsated emission.

- **Stellar angular diameters via asteroid occultation:** it has been proved (with the VERITAS telescopes [137, 244]) that is possible to use IACTs to perform direct stellar angular diameters with sub-milliarcsecond precision by studying the diffraction pattern projected by stars when they are occulted by asteroids from the main belt. Since MAGIC CPIX sensitivity can reach down to a magnitude of ~ 13 these kind of measurements could help to close the gap between predicted and measured stellar sizes for K-type stars [245].

- **Microquasars:** system of a compact object (neutron star or black hole) with a donor star from which material is falling into the compact object, forming an accretion disk around it. The fraction within the accretion disk from falling particles causes it to heat up, emitting in radio, optical, X-rays and even in gamma rays. The characteristics of the emission vary between accretion modes, such as fast quasi-periodic oscillations in the optical and X-rays during transitional periods. Studying the correlation of the ultra-fast variability of emission in different wavelengths simultaneously would help to understand the different states of activity of these objects [246, 247, 248].

- **FRBs and FOBs:** several scenarios have been proposed for the emission of FRBs that could include fast optical bursts (FOBs). Some of these scenarios have been studied involving several IC scattering processes with one-zone and two-zone models. In order to allow for the same emission mechanism of the FRB to emit in optical wavelengths a neutron star with an extremely strong magnetic field and extremely fast spin would be needed or a very young SNR surrounding the FRB source [223]. If detected, this FOBs would reveal extremely energetic environments.

- **Meteors:** Earth is constantly being bombarded by objects coming from outer space of varying size and composition. Upon interaction with the atmosphere they heat

up and produce flashes of light that, depending on the size and composition of the object, can be detected by optical telescopes [249]. These brief optical transients are observed as 'orphan' pulses by MAGIC CPIX and are its main source of background events when trying to observe other optical transients or variable sources. If their frequency was monitored over long periods of time, they could help to verify the theory proposed by Campbell-Brown [250] in which the brightness and frequency of meteors seem to be strongly correlated with solar activity.

11.2.1 Analysis of Central Pixel data

This system stores the voltage coming from the central pixel of each camera at 10 kHz frequencies. The CPIX DAQ also tags in time each voltage value with excellent precision (< 1 ms). The generated files are stored in ASCII format, with the time stamping in MJD local time.

Within MARS, the standard library to analyze CPIX data is *psearch*. This software, developed by M. López, performs a local to barycentric time calibration and, as it was developed for pulsar optical lightcurve analysis, folds the voltage with the pulsar ephemerides provided by the user.

As introduced in this work, the central pixel was mainly used to test the validity of the timing of the MAGIC telescopes [251], but recently new science cases are arising. These science cases require to transform the voltage detected by the CPIX system to calibrated optical magnitudes.

Calibration of the system As the CPIX system is not a DC-coupled device, calibrating this system is tricky: it is simply not possible to use reference calibrated stars for the calibration. The method used to calibrate central pixel signals is the one introduced in [150]. The voltage of the central pixel signal is transformed to U band magnitudes by employing Crab Pulsar observations. This method uses two assumptions: 1) That we know the average flux of the Crab Pulsar in the U band and 2) that we know the Crab Pulsar's light-curve shape, using the one measured by Aqueye [252].

By using these priors, the calibration is performed as follows (see figure 11.6 as reference):

1. We perform Crab Pulsar observations with the CPIX system.

2. By employing psearch and updated Crab Pulsar ephemerides from [253], we calculate the MAGIC CPIX phaseogram.

3. We match the location of the two peaks from the Aqueye phaseogram to that of the CPIX phaseogram.

4. As Aqueye has better timing resolution than MAGIC CPIX, we re-bin their phaseogram to match the binning of the CPIX phaseogram.

5. As the linearity and background level of the Aqueye phaseogram are excellent, we use their phaseogram to relate average counts to the known average flux of the Crab Pulsar.

6. As Aqueye and CPIX phaseograms have been matched, we compute the relation between CPIX voltage and U-band magnitude.

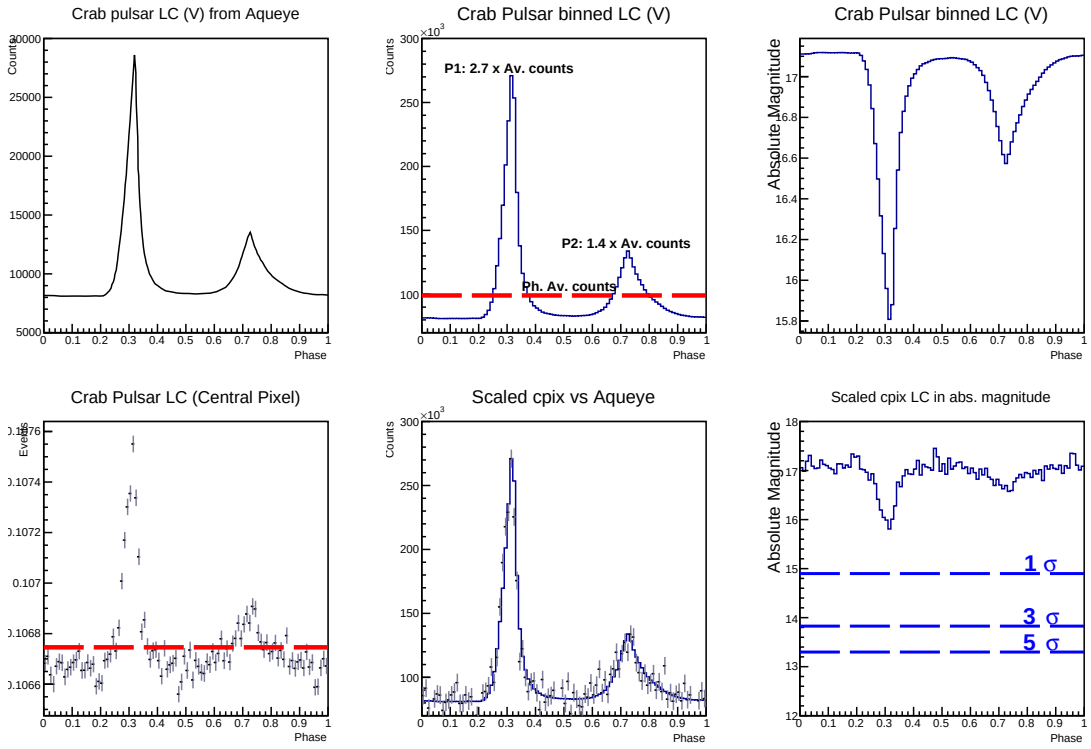

Figure 11.6: *Comparison of the Crab Pulsar light-curve by Aqueye [252] (top-left) with the most recent light-curve obtained with MAGIC CPIX (bottom-left). The bottom-center subplot shows how the scaled light-curve of the central pixel matches the one from Aqueye.*

Optical lightcurves Once the CPIX voltage is calibrated, the only step missing to interpret MAGIC fast optical observations is the timing analysis of the data. If radio observatories detect a FRB simultaneous to our observations, they will provide a barycentric TOA. The timestamps of the CPIX are converted from topocentric to barycentric in order to compare strictly simultaneous observations in different wavelengths (radio or X-rays). CPIX data is affected by high frequency noise. In order to reduce this noise and therefore improve the sensitivity of CPIX observations, averaging filters of 1, 2 and 10 ms are applied as done in [138].

Sensitivity to optical burst emission The sensitivity of the CPIX system has been studied in detail in several publications [138, 150]. At the time the system was commissioned, the main scientific objective was optical pulsars analysis, and therefore noise patterns affecting the acquisition which are not periodic over pulsar's timescales do not really affect sensitivity.

Unlike in the case of pulsars, when searching for brief transient phenomenal no periodic folding is applied, and therefore any noise pattern affecting the data will limit the system sensitivity. Unfortunately, strong high-frequency noise features affect the CPIX data, and limit the sensitivity a single telescope is able to achieve.

The negative effect of this high-frequency noise is mitigated by:

1. Having a CPIX system installed in each telescope. Noise patterns are independent between telescopes. This means that if a brief optical pulse appears in both telescopes, it is likely to come from an optical signal, and not from electronic noise.

2. A time averaging over millisecond timescales may be applied to significantly reduce the impact of the high-frequency noise. The bottom-right panel of Figure 11.6 shows the 1, 3 and 5σ levels observed in CPIX data from the MAGIC 2 telescope under dark conditions after applying a 10-ms averaging filter.

Sensitivities to standalone optical flashes of 12.4, 13.3, 14.1 and 14.4 mag in U band over 0.1, 1, 5 and 10 ms were reported in [138] respectively. In case CPIX observations are performed under higher night-sky background conditions, these sensitivities are expected to worsen, as we will show in this work.

The excellent millisecond-scale sensitivity of MAGIC to optical flashes brings certain drawbacks. An irreducible background of brief optical pulses affect these observations: the $\sim$ 10 ms scale flashes of light generated by meteors serendipitously passing through the MAGIC central pixel field of view. The rate of these events is low, roughly one per several hours, rate decaying with their brightness. Even if the rate is small, this places a limitation for MAGIC to associate these brief optical signals with the source observed. For this reason, simultaneous multi-wavelength coverage is crucial.

12. Studied sources

12.1 SGR 1935+2154

This galactic magnetar is a soft gamma repeater discovered in hard X-ray bursts with Swift-BAT in July 2014 [254]. Follow up X-ray observations confirmed that it is a magnetar with a spin period of P = 3.25 s [255]. In April 28 2020, a bright millisecond-duration radio burst (FRB 200428) was detected by CHIME [212] in the direction of the magnetar with temporal and spatial coincidence to a X-ray burst detected by INTEGRAL [256], establishing a link between young magnetars and FRBs. Moreover, the magnetar has been proposed to be associated with the SNR G57.2+0.8. With a dispersion measurement (DM) of 332.7 pc cm^{-3}, if the magnetar and the SNR are indeed physically associated, the estimated distance is 6.6 $\pm$ 0.7 kpc [257]. Since 2020, the SGR has presented several episodes of burst activity. This activity is monitored by several telescopes, triggering multiwavelength observation campaigns.

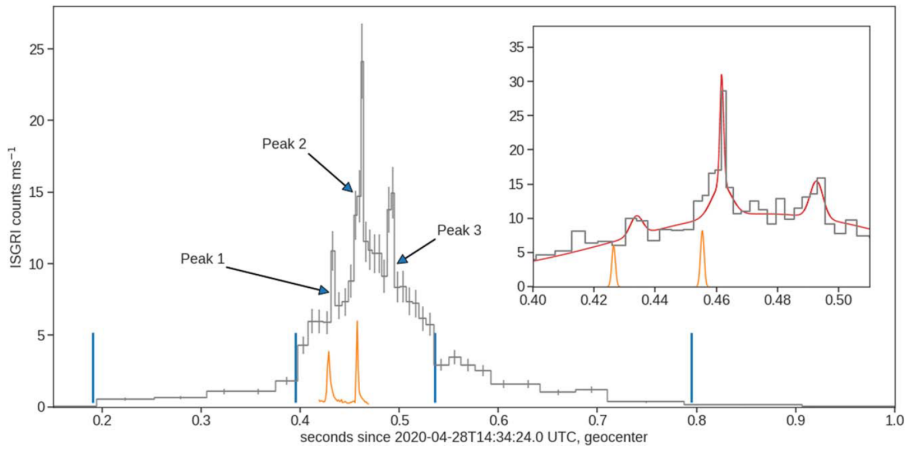

Figure 12.1: *Light-curve in the 20-200 keV energy range obtained with the IBIS/ISGRI instrument [256] with (orange line) radio pulses observed by CHIME [212].*

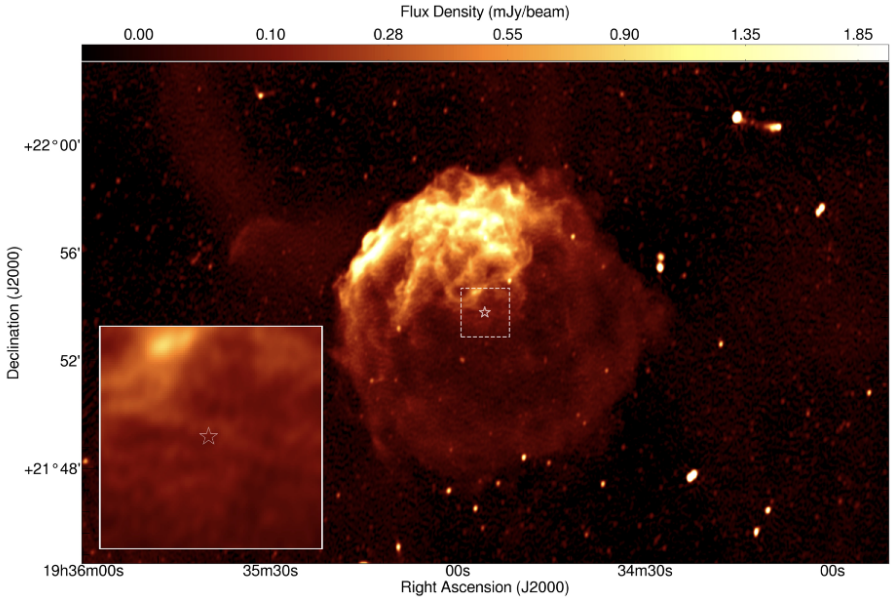

Figure 12.2: *MeerKAT observations of SNR G57.2+00.8 from May 2020. The star marks the location of SGR 1935+2154, which can be seen zoomed in in the bottom left pannel [258].*

MAGIC observations of this source may constrain multiple emission mechanisms expected from this source: 1) magnetar giant flares that could be detected in optical and VHE, since Fermi already detected one of these events from a extragalactic source in HE [220] and this SGR is a galactic source, 2) short magnetar flares linked with optical sub-second emission (as reported by [223]) and 3) VHE persistent emission from the surrounding SNR since there are no known SNRs whose emission is fueled by a magnetar.

12.1.0.1 Observations

MAGIC has performed several multi-wavelength campaigns of SGR 1935+2154 over the last years, generally triggered by active states detected either in X-rays or radio. Observations were coordinated with other observatories such as Westerbork and Onsala in radio, the SiFAP2 camera on the Telescopio Nazionale Galileo in optical and Swift in X-rays. In this work, I present the analysis of 14.8 h of MAGIC VHE data during the July-October 2020 campaign [259].

Since the data was taken over the course of a few months, different analysis periods are covered (ST.03.14 and ST.03.15) requiring the training of two sets of RFs. Observations were scheduled in Wobble mode (mainly to look for persistent VHE emission) and ON+CPIX mode (to look for strictly simultaneous short-timescale bursts in VHE and optical). ON observations were requested when there was strictly simultaneous multi-wavelength observations planned. The summary of these observations is shown in table 12.1, that sum up to a total observation time of 14.8 h.

The night of October 9th the radio telescope FAST reported several FRBs and pulsed emission in radio [260], so a target of opportunity request was submitted to observe simultaneously with MAGIC (VHE and optical), Swift (X-rays) and Onsala (radio) telescopes,

and observations in ON+Central Pixel mode were scheduled for MAGIC. However, the simultaneous radio data by the Onsala telescope did not show any radio bursts.

Analysis period	Date	Mode	CPIX	Observation time (h)	Zenith range (deg)
ST.03.14	2020 07 24	ON	OFF	2	0-35
	2020 08 14	ON	OFF	1.9	0-35
	2020 08 20	ON	OFF	2	0-35
	2020 09 11	ON	OFF	2	0-50
ST.03.15	2020 09 18	Wobble	OFF	2	0-50
	2020 09 19	Wobble	OFF	1.7	0-35
	2020 09 20	Wobble	OFF	2	0-35
	2020 10 10	ON	ON	1.2	0-62

Table 12.1: *Summary of observations for SGR 1935+2154, with a total of 14.8 h of observation after quality cuts.*

12.1.0.2 Results

It is unlikely that persistent VHE emission is detected during this observation since Fermi-LAT [216] and MAGIC [138] already placed strong limits for persistent emission in HE and VHE respectively. Still, it is worth to search for this emission since it can be performed simultaneously to fast optical observations with the CPIX and it is interesting to test the extended gamma-ray emission from the associated SNR.

Figure 12.3 shows both the accumulated theta^2 distribution for the full energy range and the differential flux upper limits over the full 14.8 h. The theta^2 distribution shows that the scaled acceptance between ON and OFF observations match remarkably well, but no detection was achieved, with a (Li&Ma) significance of 0.2 σ.

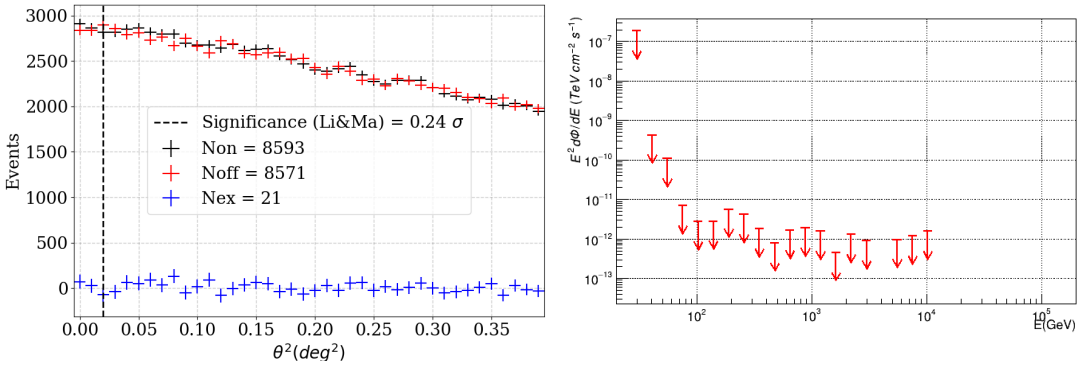

Figure 12.3: *Left: accumulated ON, OFF and excess events for the full data set. No detection is observed with a calculated significance of 0.2 σ. Right: the differential UL on the VHE persistent emission are shown in the form of the spectral energy distribution with photon index $\Gamma = 2$.*

The integral flux UL for the persistent VHE emission has also been calculated using the Poisson likelihood method described in Rolke [261] with a 95% CL for a photon index

$\Gamma = 2$ for energies greater than 100, 300 and 600 GeV: $17.17 \cdot 10^{-12}$, $1.50 \cdot 10^{-12}$ $cm^{-2}s^{-1}$ and $0.42 \cdot 10^{-12}$ $cm^{-2}s^{-1}$. The UL obtained for E > 600 GeV constrains more the VHE emission than the one provided by HESS of $1.5 \cdot 10^{-12}$ $cm^{-2}s^{-1}$ in [262].

No run-wise neither night-wise flaring VHE emission was detected either. As no simultaneous X-ray nor radio bursts were detected during ON observations, and the irreducible background of meteor-induced optical flashes would mitigate the significance of detected standalone optical flashes, no optical observations will be reported here.

12.2 FRB 20200120E

It is the closest known extragalactic source of FRBs with a DM = 87.82 pc cm^{-3} ($\sim$40 times closer than the second closest known extragalactic FRB source FRB 180916 discussed in the next section). It is a repeating source of FRBs and it appears to be located in the globular cluster [PR95] 30244 in the outskirts of M81 [263, 264], although the possibility of being part of the Milky Way halo has not been rejected. If it is located in a globular cluster, it would challenge the current models that support the formation of magnetars via standard core-collapse supernovas.

Authors of [264] present an extremely precise localisation of the FRB as seen in figure 12.4. In this work authors propose several scenarios to explain the FRB production mechanism. In the first scenario they suggest that this FRB source is a highly magnetized neutron star, formed by accretion-induced collapse of a white dwarf or by a merger of compact stars (white dwarfs and/or neutron stars) in a binary system. This scenario would agree more with the extremely high stellar densities in globular clusters that are known to form short-orbital-period binaries at specific high rate [265, 266, 267]. No persistent radio or X-ray emission is expected in this case, as the emission generated during collapse would fade on short time scales (< 1 year). In the second scenario it is suggested that the FRB source could be a compact binary system in which the components are interacting magnetically, such as a close white dwarf-neutron star system in a pre-merger state or a highly magnetized neutron star with a planetary companion [268, 269]. In the third scenario, the FRB emission would be originated by a binary millisecond pulsar with a strong magnetic field via accretion-induced collapse that has accelerated its rotation via accretion [270, 271]. In this scenario, the source could be observed as a low mass X-ray binary similarly to an accreting black hole. The radio bursts would be a result of magnetic reconnection in a relativistic jet or via the interaction of the jet shocks with the surrounding medium, creating a synchrotron maser [272].

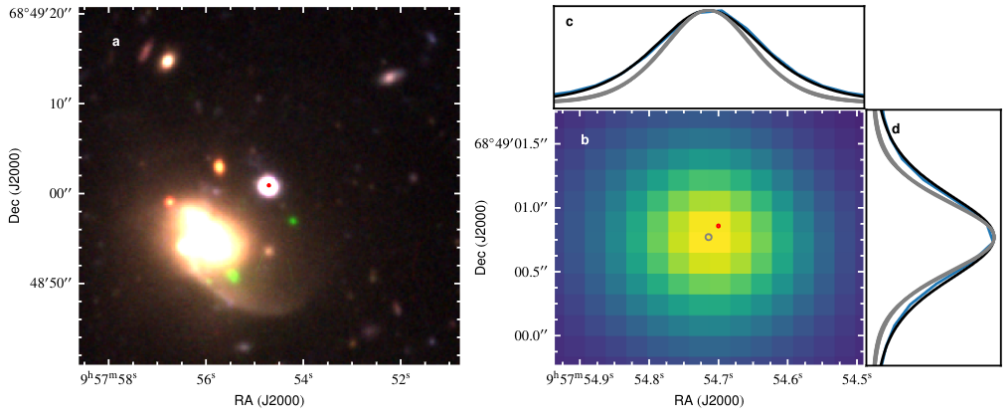

Figure 12.4: *Left: composite Subaru image with bands g', r' and i' of M81 with the globular cluster [PR95] 30244. The position of FRB 20200120E is marked with a red ellipse. Right: zoomed-in image in r' band where the red ellipse marks the location of FRB 20200120E and the grey circle marks the estimated position of the center of the globular cluster. Both images from [264].*

12.2.0.1 Observations

MAGIC performed two deep MWL observation campaigns with large radio antennas and X-rays. The first campaign was performed in April-May 2021, with Effelsberg and Torun observatories in radio and XMM-Newton in X-rays, accumulating 6.3 h of MAGIC data. The second campaign was performed in March-April 2022 with Onsala, Westerbrock and Torun observatories in radio, accumulating 10.7 h. None of the partners reported FRB for the strictly simultaneous observations.

Since the data was taken with almost a year of difference, different MAGIC analysis periods were covered (ST.03.16 and ST.03.17), requiring independent RF training. The summary of the observations is summarized in table 12.2, with a total observation time of 17 h.

Analysis period	Date	Mode	CPIX	Observation time (h)	Zenith range (deg)
ST.03.16	2021 04 17	ON	ON	0.3	35-50
	2021 04 19	ON	ON	3.1	35-50
	2021 05 01	ON	ON	2.4	35-70
	2021 05 14	ON	ON	0.5	35-62
ST-03-17	2022 03 30	ON	ON	0.1	35-50
	2022 03 31	ON	ON	2.5	35-50
	2022 04 01	ON	ON	2.7	35-50
	2022 04 02	ON	ON	3.5	35-50
	2022 04 06	ON	ON	1.9	35-50

Table 12.2: *Summary of observations for FRB 20200120E, with a total of 17 h of observation.*

12.2.0.2 Results

Since no FRBs were reported by any of the partners, no searches for VHE nor optical bursts have been performed. In optical, the calculated significance would be heavily affected by the irreducible meteor background. Current suggested scenarios for this source do not predict persistent VHE emission (and no radio nor X-ray persistent emission has been detected from its location), but since it is the closest extragalactic source of FRBs, UL have been calculated in order to help constrain the possible FRB production mechanisms.

Figure 12.5 shows the accumulated distribution of theta^2 for the full energy range and the differential flux upper limits over the full 17 h. The theta^2 distribution shows the scaled acceptance between ON and OFF observations matching well, but no detection has been achieved, with a (Li&Ma) significance of 3.7 σ. No run-wise neither night-wise burst VHE emission has been detected either.

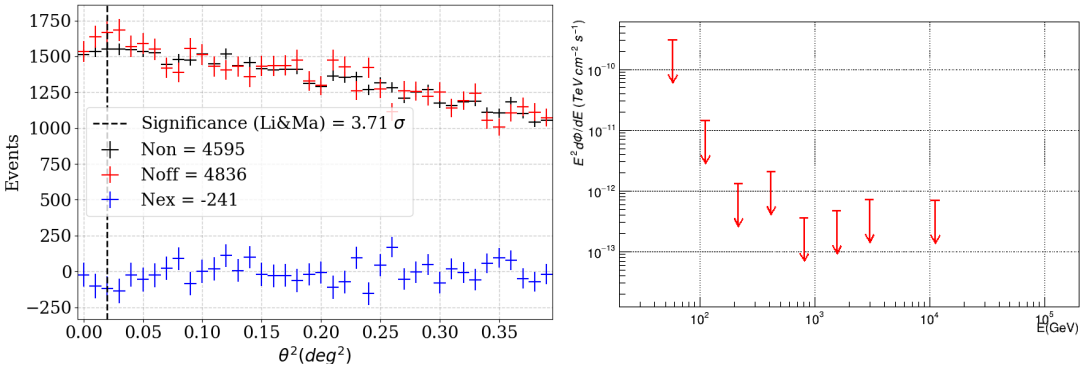

Figure 12.5: *Left: accumulated ON, OFF and excess events for the full data set. No detection is observed with a calculated significance of 3.7 σ. Right: the differential UL on the VHE persistent emission are shown in the form of the spectral energy distribution with photon index* $\Gamma = 2$.

The calculated integral flux UL for the persistent VHE emission (using the Poisson likelihood method described in Rolke [261]) with a 95% CL for a photon index $\Gamma = 2$ for energies greater than 100, 300 and 600 GeV is: 6.77 $\cdot 10^{-12}$, 1.61 $\cdot 10^{-12}$ cm^{-2}s^{-1} and 0.29 $\cdot 10^{-12}$ cm^{-2}s^{-1}. These ULs are more constraining than the ones found for SGR 1935+2154 for E > 100 and 600 GeV even though this source is at a longer distance but not for E > 300 GeV.

12.3 FRB 180916.J0158+65

This extragalactic repeating FRB source was discovered by CHIME/FRB [209]. It was the first FRB source that showed periodic episodes of activity with repeating bursts over 4 days every 16.35±0.18 days [211].

Thanks to its repeating behaviour, measurements were performed to get a precise localization of the source as seen in figure 12.6, obtaining a DM for the observed burst of 349.2±0.3 pc cm^{-3} and placing the source in a star-forming clump within a nearby (z =

0.0337 $\pm$ 0.0002) massive star-forming spiral galaxy [273].

Similarly than for FRB 121102 which also presents periodic episodes of activity, several families of models have been proposed to explain the periodic emission [273]. One of these models states the existence of a young (20-50 years old) SNR and nebula whose emission is fueled by a young magnetar [274, 275, 276, 277] in order to explain the persistent radio emission from FRB 121102. The lack of persistent radio emission from FRB 180916 could be explained if the system is older than the one for FRB 121102 and the emission has already faded. A similar model [274] places ULs on the persistent radio emission that are consistent with a system at least five times older than the FRB 121102 one (200-500 years old). The same model predicts a decay of the rotation measurement (accounts for the Faraday effect or of scattering suffered by the light upon interaction with a magnetic field in its travel through different mediums). For a rotation measurement as large as the one observed for FRB 121102 [278] to drop down to the rotation measurement observed for FRB 180916 [209] about 300 years would need to pass, which is consistent with the aforementioned ages.

Other models suggest interaction between a neutron star's magnetosphere and a nearby plasma stream [279]. Given FRB 121102 large RM [278] and the similarity of the morphology of its persistent radio source with a low-luminosity AGN, it is suggested that the burst could be produced in a massive black hole or neutron star in the vicinity. The accretion black hole could provide a strong plasma stream that interacts with a neutron star magnetosphere [280]. For FRB 180916 there is no persistent radio counterpart and it is located on the spiral arm of its galaxy, making such a model less likely for this FRB source.

Its periodic repeating nature has allowed for the organization and coordination of MWL campaigns in radio, optical, X-rays and gamma rays. One of those campaigns was organized to perform extrictly simultaneous observations with uGMRT in radio, MAGIC CPIX in optical, NuSTAR and XMM-Newton in X-rays and INTEGRAL and MAGIC in gamma rays.

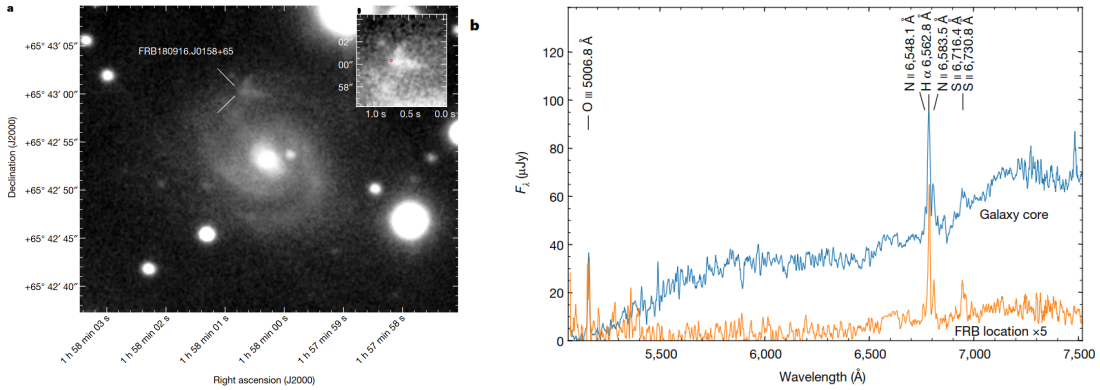

Figure 12.6: *Observations performed with the Gemini-North telescope from [273]. Left: Image of the host galaxy with the position of FRB 180916.J0158+65 marked by a red circle. Right: spectrum (corrected by the sky contribution) of the 5 arcsec region around the host galaxy core (blue) and spectrum of the 2 arcsec region around the location of FRB 180916.J0158+65 (orange) multiplied by 5 that show that the star-forming clump and the host galaxy core are at the same redshift.*

MAGIC performed a short campaign of 2.4h together with radio, soft and hard X-rays and radio. On the night of 14th September 2021 a FRB was detected by uGMRT simultaneous to our observations. Unfortunately, no burst was detected in X-rays, optical nor VHE; but we are providing differential and integral ULs on the persistent VHE emission, integral VHE ULs within the 10 ms window surrounding the FRB TOA, optical light curves covering 200 ms around the TOA with an integration window of 2ms and ULs on optical burst emission.

12.3.0.1 Observations

MAGIC observations of the source FRB 180916.J0158+65 took place on the night of 14-15th September 2021. The VHE observations were performed in ON mode simultaneous to CPIX observations. The background conditions changed in the 2.4h in which the observations took place, with high, medium and low background illumination levels due to the Moon as is sumarized in table 12.3. The FRB occurred over medium Moon illumination levels. In these conditions, the low-energy threshold of MAGIC VHE observations increases significantly. For this reason the provided upper limits are not as good as they could be if the night-sky background illumination had been lower.

Analysis period	Date	Mode	CPIX	Observation time (h)	Zenith range (deg)	NSB level
ST.03.16_5-8	2021 09 15	ON	ON	0.9	50-62	High
ST.03.16_3-5	2021 09 15	ON	ON	0.9	35-62	Medium
ST.03.15_2-3	2021 09 15	ON	ON	0.6	35-50	Low

Table 12.3: *Summary of observations for FRB 180916, with a total of 2.4 h of observation time and three background illumination levels.*

12.3.0.2 Results

A non-standard analysis was performed for MAGIC VHE data to properly take into account the effects of higher background illumination. The performance of MAGIC under this conditions is explored in [281]. The main sources of noise under these conditions are the statistical fluctuations due to NSB photons, PMT after pulses and electronic noise. The noise caused by the background photons increases with the square root of the NSB (following Poisson statistics). The rate of PMT after pulses increases linearly with the NSB. The electronic noise does not increase with NSB as long as the HV remains unchanged (for observations with extremely high background illumination levels, reduced HV is employed to avoid degrading the PMTs). For the analysis, three levels of NSB were defined according to the mean DC and the mean and RMS of the pedestal events distribution. For each NSB level different cleaning level factors and size cuts were applied.

In order to account for the different types of counterparts predicted for these sources, we performed similar searches than those performed for FRB 121102 [138]: burst-like emission in both VHE and optical and persistent emission in VHE.

In order to find the optimal size of the signal region in theta^2 and hadroness cut, a study was performed to maximize the background rejection and gamma-ray acceptance for VHE burst in ms timescales. Figure 12.7 shows the distribution of gamma Cut Efficiency (gCE) which accounts for the relationship between the rejected background and the accepted gamma rays among the MC events, for several combinations of Cherenkov image sizes and defined signal regions in theta^2. On the other hand, figure 12.8 shows the minimum events necessary for a 5σ detection of a 10ms VHE burst with the same size and theta^2 as the previous plot, with a background frequency of events extracted from the data with the most NSB (ST.03.16_5-8). For data with such high NSB a cut of size > 150 phe is required (as seen in [281]). For this size, the cuts that returned the best acceptance ($\sim$ 50%) were found for hadroness < 0.4 and theta^2 < 0.14 deg^2. The minimum number of events for these cuts is 4.

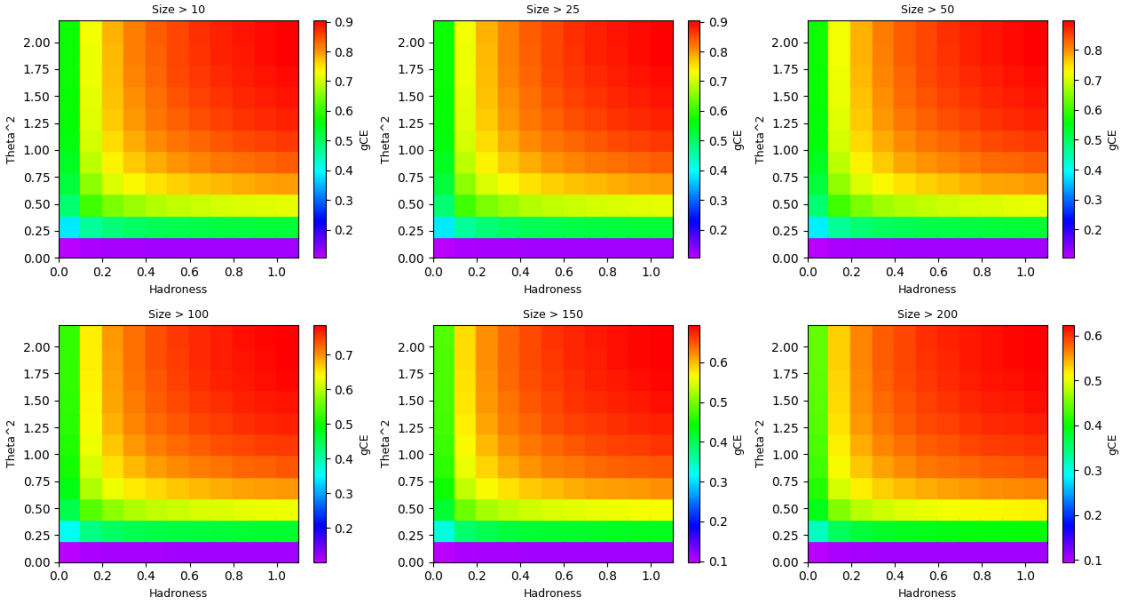

Figure 12.7: *2D-distributions of acceptance of gamma-ray events of the MC simulations for different cuts in size, theta^2 and hadroness.*

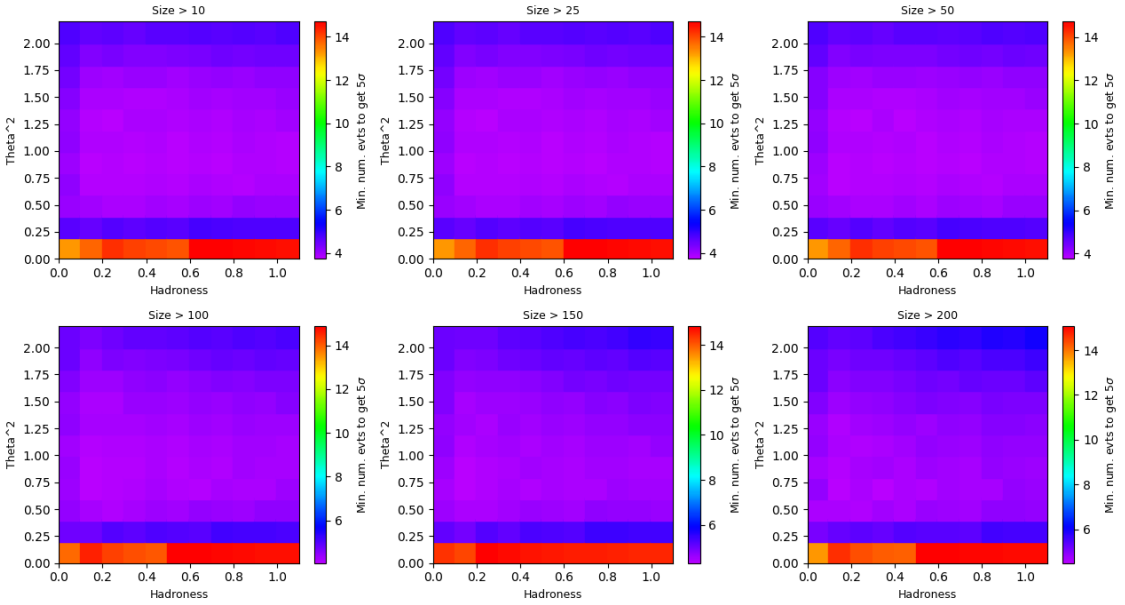

Figure 12.8: *2D-distributions of minimum number of events to get a 5σ detection in a 10 ms window for different cuts in size, theta^2 and hadroness..*

The differential ULs for VHE persistent emission were obtained for the three NSB levels were combined for photon indexes 2 and 4, as seen in figure 12.9. Due to the NSB conditions, the threshold is not as low as for observations performed in dark conditions, starting at E = 200 GeV.

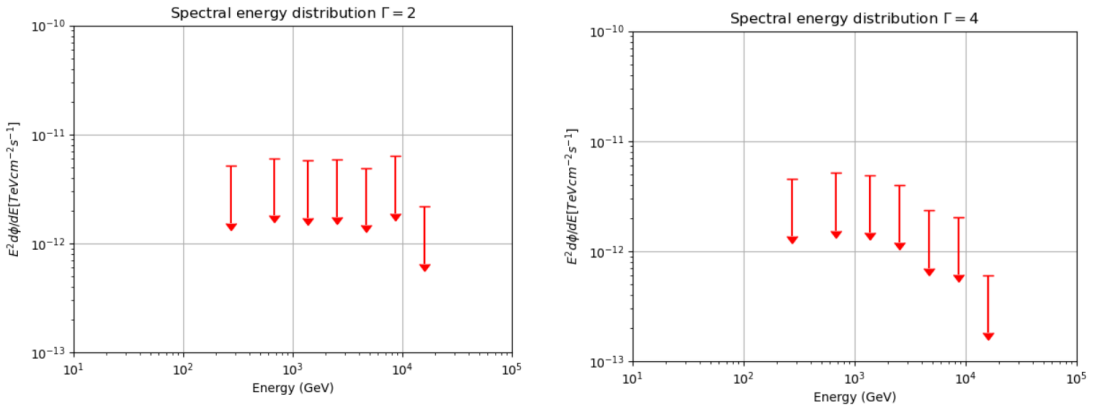

Figure 12.9: *Differential ULs for FRB 180916 for energies greater than 200 GeV and spectral indexes 2 (left) and 4 (right).*

Integral ULs have also been calculated for the persistent VHE for energies E > 200, 500 and 1000 GeV as shown in table 12.4 for the combined 2.4 h of observations.

UL Eth	Int. Flux UL (95% CL Γ = 2) [10^{-12} cm^{-2}s^{-1}]	Int. Flux UL (95% CL Γ = 4) GeV>GeV [10^{-12} cm^{-2}s^{-1}]
200	5.78	9.81
500	4.14	4.80
1000	1.68	1.61

Table 12.4: *Integral ULs on the persistent VHE emission for FRB 180916.J0158+65 for spectral indexes 2 and 4 and energies E > 200, 500 and 1000 GeV.*

The VHE integral ULs on persistent VHE emission obtained for FRB 121102 [138] for E > 1000 GeV were $0.37 \cdot 10^{-12}$ cm^{-2}s^{-1} and $0.33 \cdot 10^{-12}$ cm^{-2}s^{-1} for spectral indexes 2 and 4 respectively are more constraining than the ones found for this source, due to the higher NSB conditions and less integrated observing time (22 h for FRB 121102), even though FRB 180916 is closer.

In order to find the integral ULs for VHE burst within the 10 ms time window surrounding the TOA of the FRB, the same procedure than for FRB 121102 was followed [138]. Assuming that the number of photons within a 10 ms time window follows a Poisson distribution, we do not expect any background events in said window. Therefore, we would need (with 95% CL and 30% systematic uncertainty) an excess of 3.56 events, so this is the number of events that we use in our UL calculations. We provide the integral fluxes ULs for three energy thresholds and two photon indexes are shown in table 12.5.

UL Eth	Int. Flux UL (95% CL $\Gamma = 2$) [10^{-7} cm^{-2}s^{-1}]	Int. Flux UL (95% CL $\Gamma = 4$) GeV>GeV [10^{-7} cm^{-2}s^{-1}]
200	4.18	64.44
500	1.66	4.17
1000	0.99	1.23

Table 12.5: *Integral ULs for VHE burst emission within 10 ms around the TOA for FRB 180916.J0158+65, for spectral indexes 2 and 4 and energies E > 200, 500 and 1000 GeV.*

The VHE integral ULs on burst VHE emission obtained for FRB 121102 for 10 ms time windows [138] for E > 1000 GeV were 0.41 $\cdot 10^{-7}$ cm^{-2}s^{-1} and 0.36 $\cdot 10^{-7}$ cm^{-2}s^{-1} for spectral indexes 2 and 4 respectively. Similarly to for VHE persistent emission ULs, the limits for FRB 121102 are more constraining than the ones found for this source.

Instead of focusing on the 10 ms around the TOA of the FRB, an unbiased search of 10 ms bursts was performed. As stated before, the necessary number of events to get a 5 σ detection in time windows of 10 ms is 4 (with size > 150 phe, theta^2 < 0.14 as the signal region and hadroness < 0.40). In this case only the UL for the lowest energy threshold E > 200 GeV and photon index 2 was calculated. The integral UL obtained is $5.06 \cdot 10^{-7} cm^{-2} s^{-1}$.

Since CPIX optical observations were performed simultaneously to the VHE observations, optical analysis is possible. Figure 12.10 shows MAGIC CPIX light-curve covering 200 ms around the TOA of the FRB with an integration window (binning) of 2 ms (both to reduce CPIX noise and to match the time binning used by X-rays partners).

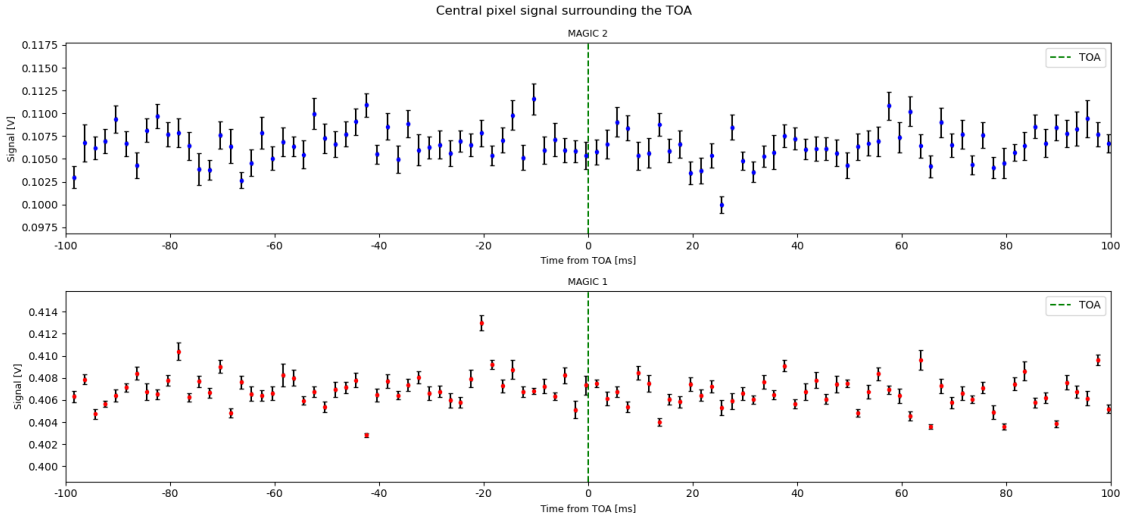

Figure 12.10: *MAGIC CPIX light-curve around ±100 ms of the TOA. The voltage measured from MAGIC 2 CPIX (top) and MAGIC 1 (bottom) is shown in bins of 2 ms to reduce CPIX noise.*

In order to calculate the optical ULs for burst emission unassociated with the FRB, we used an empirical expression that allows to transform the voltage from MAGIC's CPIX

to magnitudes (see expression 1 from [138]). The expression has been calibrated using recent data from the Crab Pulsar as shown in section 11.2. The resulting ULs for optical burst emission in table 12.6 have been obtained for each of the telescopes/CPIX, for no integration time (0.1 ms), and integration windows 1 ms and 10 ms, in both magnitudes in U band and mJy.

	Integration windows		
Telescope/CPIX	0.1 ms	1 ms	10ms
MAGIC 1	13.52 mag/16.1 mJy	14.06 mag/9.83 mJy	15.09 mag/3.80 mJy
MAGIC 2	13.13 mag/23.1 mJy	14.00 mag/10.4 mJy	15.08 mag/3.84 mJy

Table 12.6: *Optical burst emission ULs for FRB 180916 for both CPIX systems and three integration windows (0.1, 1 and 10 ms) in magnitudes and mJy.*

These ULs for optical burst emission are worse than the ones found for FRB 121102 of 8.6 and 3.2 mJy for 1 and 10 ms respectively [138]. This is somewhat expected since FRB 180916 observations were performed in worse conditions, but its closer distance could favour better constrains in the future.

13. Conclusions and prospects

The analysis for three repeating sources of FRB have been reported: SGR 1935+2154 (galactic), FRB 20200120E (extragalactic) and FRB 180916 (extragalactic). Their repeating nature, even periodic for FRB 180916, has allowed for the organization of MWL campaigns in radio, optical, X-rays and gamma rays. In some cases, exploratory campaigns were performed while others were triggered by high activity from the sources. For most observations, no FRB was detected strictly simultaneously to MAGIC observations, so no analysis have been performed for short VHE and optical emission as their significance would be heavily affected by the number of trials. In the case of FRB 180916 a burst was detected simultaneous to MAGIC VHE and optical observations, so analysis in short timescales was performed. Still, several searches were performed for the sources. No optical absorption was considered.

For the galactic magnetar SGR 1935+2154 several emission mechanisms were expected from literature: the detection of optical and VHE emission in case of a giant flare since Fermi detected one of these events in HE, the detection of short optical flares as expected from [223] and VHE persistent emission from the surrounding SNR G57.2+00.8, which would be the first detected SNR powered by a magnetar. For this source, no detection was found for persistent VHE emission. Integral flux ULs were calculated for persistent VHE emission at several energies. The integral UL found at $E > 600$ GeV of $0.42 \cdot 10^{-12}$ cm^{-2}s^{-1} is more constraining than the one found by HESS of $1.5 \cdot 10^{-12}$ cm^{-2}s^{-1} [262], probably because their accumulated observation time was 2 h and our is 14.8 h. The non-detections in VHE suggests that IC processes are being suppressed within the magnetar vicinity. This could be the case if the gamma-ray emission is happening very close to the surface of the magnetar, suffering pair-production and photon splitting processes, producing strong cut-offs in MeV and GeV [262]. It is worth to note that if a giant burst was detected in future observing campaigns for this source, given its short distance, the limits imposed to the optical luminosity simultaneous to FRBs would be several orders of magnitude better than the limits reported for FRB 121102 [138] since the SGR is $\sim$108000 times closer. Still, it is likely we will need to wait for the next generation of IACTs (CTA) to properly constrain these models.

Recent works place closest known extragalactic source of FRBs, FRB 20200120E, in the globular cluster [PR95] 30244 of M81 or in the Milky Way halo [264]. Three main FRB engines have been proposed: a highly magnetized neutron star in a binary system, a compact binary system in which components are interacting magnetically or a binary millisecond pulsar with a strong magnetic field [264]. Even though no persistent emission is expected in any of these scenarios nor has been detected so far in any wavelength, a search for VHE persistent emission was performed in order to constrain the emission in this wavelength. This search within the full 17 h of observations returned integral ULs for persistent VHE emission for E > 100, 300 and 600 GeV fo 6.77 $\cdot 10^{-12}$, 1.61 $\cdot 10^{-12}$ $cm^{-2}s^{-1}$ and 0.29 $\cdot 10^{-12}$ $cm^{-2}s^{-1}$, respectively. These ULs are more constraining than the ones found for SGR 1935+2154 for E > 100 and 600 GeV even though this source is at a longer distance but not for E > 300 GeV.

For the extragalactic source FRB 180916, which was the first repeating FRB source known to display periodic episodes of activity. The periodic nature of this source has been suggested to be caused by the same mechanisms proposed for FRB 121102 but in a more evolved system or by the interaction of a neutron star magnetosphere with a nearby strong plasma stream [273]. A FRB was detected simultaneous to MAGIC observations, so similar searches than the ones performed for FRB121102 were performed [138]: VHE persistent emission (even though it is not expected in the SNR powered by a young magnetar scenario because the system would be too old and the emission would have faded), VHE burst emission around 10 ms of the TOA, unbiased VHE burst emission of 10 ms over the full dataset and optical burst emission. No detection was found for any of the searches for the 2.4 h of observations, but ULs has been set for each of them. Unlike for the other FRB sources, observations were performed under intermediate and high background illumination levels, therefore a non-standard analysis was performed to take into account the noise contribution from the NSB, meaning that the found ULs are worse than if observations would have been performed in dark conditions. For VHE persistent emission limits were calculated at energy thresholds higher than for the sources due to the high illumination levels. The ULs found for optical burst emission are worse than the ones found for FRB 121102 of 8.6 and 3.2 mJy for 1 and 10 ms respectively [138], but not by much. This is somewhat expected since FRB 180916 observations were performed with high background illumination levels, but its closer distance to us than FRB 121102 could favour better constrains in the future.

It is expected that the results here presented will be cross-checked by the MAGIC Collaboration and be included in future publications. A publication for the source FRB 180916 is already in preparation for which I will be one of the corresponding authors.

Main conclusions

In this thesis I have reported the results from the implementation of the intensity interferometry technique with an upgraded setup in the MAGIC telescopes, along with the results from more than 400 h of observations of which I have been the official scheduler for the past 2 years. I have also reported the results of 33 h of observation campaigns of three FRB sources, for which one of them a FRB was detected simultaneously to MAGIC observations.

Main contributions with the MAGIC stellar intensity interferometer:

- I developed a software tool to find the AMC focusing parameters for the pixels used for intensity interferometry observations, reaching concentrations of more than 85% of starlight.

- I developed a software tool to find the hardware delays added by each channel cable length.

- I built a catalogue of about 400 stars by cross-referencing and filtering three preexisting catalogues of modeled and measured angular diameters. I used said catalogue to define reference (diameter previously measured) in order to calibrate the setup and candidate (diameter not previously measured) stars. It is the catalogue used for intensity interferometry observations with the MAGIC telescopes and it is being expanded with new science cases.

- I developed a scheduling tool with the aforementioned catalogue used as input in order to allocate the extra 300 h a year within MAGIC Moon-breaks, achieving 400 h of observations in 2 years, only interrupted by a volcano eruption.

- I developed an analysis pipeline independently from other analizers within the MAGIC intensity interferometry working group, obtaining very similar, compatible results that will be shown in an upcoming publication of which I will be a corresponding author.

- Most of the 400 h of data has been analyzed and presented in this work by calculating the angular diameter for 5 reference stars and 16 candidate stars assuming a UD model. Some of the calculated diameters have the best precision to date in blue band.

- I performed several successful consistency tests to ensure the quality of the obtained angular diameters.

- I also reported the systematics found for intensity interferometry observations, amounting to less than 5% for any given measurement. These values will also be reported in an upcoming publication of which I will be a corresponding author, and that I have already showed in a summarized way as a proceeding in the latest International Cosmic Ray Conference [282].

Main fast radio bursts contributions:

- For SGR 1935+2154: no FRB was detected simultaneous to MAGIC observations during the 2020 campaign of 14.8 h. I performed a search for VHE persistent emission via non-standard analysis of MAGIC VHE data. No VHE emission was detected. I obtained integral flux ULs for energies E > 100, 300 and 600 GeV of $17.17 \cdot 10^{-12}$, $1.50 \cdot 10^{-12}$ cm^{-2}s^{-1} and $0.42 \cdot\cdot 10^{-12}$ cm^{-2}s^{-1}. The integral flux UL at E > 600 GeV of $0.42 \cdot 10^{-12}$ cm^{-2}s^{-1} is more constraining than the one previously reported in the literature of $1.5 \cdot 10^{-12}$ cm^{-2}s^{-1} by HESS.

- For FRB 20200120E: no FRB was detected simultaneous to MAGIC observations during the campaigns of 2021 and 2022 of 6.3 and 10.7 h. I performed a search for VHE persistent emission via non-standard analysis of MAGIC VHE data. No detection was found for VHE persistent emission. Integral flux limits were calculated for E > 100, 300 and 600 GeV of $6.77 \cdot 10^{-12}$ cm^{-2}s^{-1}, $1.61 \cdot 10^{-12}$ cm^{-2}s^{-1} and $0.29 \cdot 10^{-12}$ cm^{-2}s^{-1}. The ULs found for E > 100 and 600 GeV are even more constraining for VHE persistent emission than the ones found for SGR 1925+2154 even though the SGR is closer, but not for E > 300 GeV.

- For FRB 180916: a FRB was detected simultaneous to MAGIC observations by uGMRT during a short campaign of 2.4 h in 2021. I performed several counterpart searches, obtaining different results: 1) differential ULs on the persistent VHE emission. 2) Integral ULs on the persistent VHE emission were found to be less constraining than those for FRB 121102, probably due worse observing conditions and less integrated observation time, even though the source is closer than FRB 121102. 3) VHE integral ULs within the 10 ms time window surrounding the TOA were also found to be less constraining than those for FRB 121102, similarly than for VHE persistent emission ULs. 4) Unbiased search for 10 ms VHE bursts, which retrieved an UL of $5.06 \cdot 10^{-7}$ cm^{-2}s^{-1} for spectral index 2 and energies greater than 200 GeV. 5) Optical light curve with the CPIX, that showed no bursts in 2 ms bins around 200 ms from the TOA. 6) Optical burst emission, which was not found, so ULs were obtained for both telescopes' CPIX and 0.1, 1 and 10 ms integration time windows. The found ULs are once again less constraining than those found for

FRB 121102 for MAGIC 2 CPIX of 8.6 and 3.2 mJy versus the ones from this work of 10.4 and 3.84 mJy. A publication is in process with radio and X-ray partners of which I will be one of the corresponding authors.

- I reported preliminary prospects of VHE and optical emission for the three FRB sources in a summarized way as a proceeding in the latest Scientific Meeting of the Spanish Astronomical Society [283].

With the fast evolution of both the intensity interferometry technique and searches for FRB counterparts it is possible that I have left out some of the most recently discovered science cases for intensity interferometry and models for FRB emission at the moment of defending this thesis. Still, I hope that readers of this work find it useful as an introduction to the non-standard analyses of intensity interferometry observations and FRB counterpart searches with the MAGIC telescopes. I am personally looking forward to see how these two apparently unrelated fields evolve in a parallel way to the development of newer IACT observatories such as CTA or other kinds of observatories, inducing advances in fast-reading detectors and other electronic components.

Conclusiones generales

En esta tesis he reportado los resultados de la implementación de la técnica de interferometría de intensidad con el sistema mejorado en los telescopios MAGIC, así como los resultados de más de 400 horas de observación que he programado a lo largo de los dos últimos 2 años como la planificadora de observaciones de interferometría de intensidad ofical de los telescopios MAGIC. También he mostrado el análisis de 33 horas de observaciones divididas en varias campañas para tres fuentes de pulsos rápidos en radio, habiéndose detectado un pulso en radio simultáneo a observaciones de MAGIC para una de las fuentes.

Mis contribuciones principales al interferómetro de intensidad estelar de MAGIC han sido:

- He desarrollado una herramienta de sofware para encontrar los parámetros de ajuste de los espejos con óptica activa, los cuales se usan para enfocar la luz a los píxeles con los que se han realizado las observaciones de interferometría de intensidad, alcanzando concentraciones de luz de más del 85%.

- He desarrollado una herramienta de software para encontrar el retraso temporal causado por las diferencias en longitud de cables que unen los píxeles con el correlador.

- He construido un catálogo de unas 400 estrellas por medio de referencias cruzadas entre tres catálogos de diámetros angulares estelares estimados y medidos. He usado este catálogo para definir estrellas de referencia para calibrar el instrumento (estrellas para las que existe una medida directa previa) y estrellas candidatas (estrellas para las que no existe una medida directa previa). Este es el catálogo usado para planificar y realizar observaciones de interferometría de intensidad con los telescopios MAGIC y está siendo ampliado constantemente según nuevos casos científicos son propuestos.

- He desarrollado una herramienta de sofware que usa el catálogo mencionado anteriormente para asignar las 300 horas extra al año durante los descansos de Luna de MAGIC, alcanzando 400 horas de observaciones en los últimos dos años, sólo interrumpidas por la erupción de un volcán.

- He desarrollado una cadena de análisis independiente de otros miembros del grupo de trabajo de interferometría de intensidad de MAGIC, obteniendo resultados muy similares y compatibles que serán mostrados en una publicación próxima de la que seré una de los autores correspondientes.

- La mayor parte de las 400 horas de datos ha sido analizada y presentada en esta tesis, siendo calculados los diámetros angulares estelares asumiendo un modelo de disco uniforme para 5 de las 7 estrellas de referencia y 16 estrellas candidatas. Algunos de los diámetros obtenidos son los más precisos hasta la fecha en banda azul.

- He realizado varias pruebas de consistencia exitosas para garantizar la calidad de los diámetros angulares obtenido.

- También he mostrado las fuentes de sistemáticos encontradas para observaciones de interferometría de intensidad con los telescopios MAGIC. Acumuladas, devuelven unos sistemáticos de menos del 5% para cualquier medida. Este estudio también será mostrado en la próxima publicación de la que seré autora correspondiente, y parte de ello lo he mostrado de forma resumida en la última conferencia internacional de rayos cósmicos (IRCR) en forma de proceeding [282].

Mis contribuciones principales a pulsos rápidos en radio han sido:

- Para SGR 1935+2154: no fue detectado ningún pulso rápido en radio simultáneo a las observaciones de MAGIC tomadas en la campaña de 2020 por 14.8 horas. He realizado una búsqueda de emisión persistente en muy alta energía por medio de un análisis no estándard de datos de MAGIC de muy alta energía. No ha sido detectada emisión persistente de muy alta energía. Sin embargo, he obtenido límites superiores de flujo integral para energías E > 100, 300 and 600 GeV de $17.17{\cdot}10^{-12}$, $1.50{\cdot}10^{-12}$ $cm^{-2}s^{-1}$ y $0.42{\cdot}10^{-12}$ $cm^{-2}s^{-1}$. El límite superior obtenido para E > 600 GeV de $0.42{\cdot}10^{-12}$ $cm^{-2}s^{-1}$ es más restrictivo que el reportado en la literatura por HESS de $1.5{\cdot}10^{-12}$ $cm^{-2}s^{-1}$.

- Para FRB 20200120E: no fue detectado ningún pulso rápido en radio simultáneo a las observaciones de MAGIC tomadas en las campañas de 2021 y 2022 de 6.3 y 10.7 horas. He realizado una búsqueda de emisión persistente en muy alta energía similar que para SGR 1935+2154, sin encontrar detección. He calculado los límites superiores para el flujo integral para energías E > 100, 300 and 600 GeV of $6.77 \cdot 10^{-12}$ $cm^{-2}s^{-1}$, $1.61{\cdot}10^{-12}$ $cm^{-2}s^{-1}$ y $0.29{\cdot}10^{-12}$ $cm^{-2}s^{-1}$. Los límites encontrados para E > 100 y 600 GeV son más restrictivos que los encontrados para SGR 1935+2154 a pesar de que el SGR está más cerca, pero no lo son para E > 300 GeV.

- Para FRB 180916: un pulso rápido en radio fue detectado por uGMRT simultáneo to observaciones de MAGIC durante la campaña corta de 2.4 horas en 2021. He realizado varias búsquedas de contrapartidas, obteniendo resultados variados: 1) límites superiores para el flujo diferencial para emisión persistente en muy alta energía. 2) Límites superiores para el flujo integral de emisisón persistente en muy

alta energía que resultan menos restrictivos que los encontrados para el FRB 121102, probablemente debido a que estas medidas se han realizado con niveles de iluminación de fondo mayores y por menos tiempo, y a pesar de que esta fuente es más cercana que FRB 121102. 3) Límites superiores para el flujo integral de muy alta energía en 10 ms alrededor del tiempo de llegada del pulso en radio, también menos restrictivos que los encontrados para FRB 121102. 4) Búsqueda insesgada de pulsos de 10 ms en muy alta energía, que resulta en un límite superior integral de $5.06{\cdot}10^{-7}$ $\mathrm{cm}^{-2}\mathrm{s}^{-1}$ para índice espectral 2 y energías mayores de 200 GeV, de nuevo, menos restrictivo que el encontrado para FRB 121102. 5) Curva de luz con datos del los CPIX, con ningún pulso observado en bins de 2 ms en los 200 ms alrededor del tiempo de llegada del FRB. 6) Pulsos ópticos, que no han sido encontrados, así que límites superiores han sido calculados para ventanas de integración (bines temporales) de 0.1, 1 y 10 ms. Los límites obtenidos son de nuevo menos restrictivos que los encontrados para el FRB 121102: con 8.6 and 3.2 mJy contra los calculados para este trabajo de 10.4 and 3.84 mJy. Una publicación en conjunto con los compañeros en radio y rayos X está en proceso, y yo sería una de las autoras correspondientes.

- Mostré perspectivas preliminares de contrapartidas en óptico y muy alta energía para estas tres fuentes en forma de proceeding para la última reunión de la Sociedad Española de Astronomía [283].

Dada la rápida evolución de la técnica de interferometría de intensidad y las búsquedas de contrapartidas para pulsos rápidos en radio, es posible que haya dejado fuera de este trabajo los resultados más recientes en el momento de defender esta tesis. Aún así, espero que los lectores encuentren este trabajo útil para inciarse en los análisis no estándar de interferometría de intensidad y búsquedas de contrapartidas para pulsos rápidos en radio con los telescopios MAGIC. Personalmente, espero con entusiasmo ver cómo estos dos campos aparantemente no relacionados entre sí evolucionan de forma paralela gracias a la construcción de nuevos observatorios (como CTA para IACTs), que seguramente se traduzcan en avances en detectores cada vez más rápidos y mejores componentes electrónicos.

A. Intensity interferometry visibility curves

In this section the contrast/visibility curves are presented for all the intensity interferometry targets described in chapter II.

A.1 Reference stellar angular diameter measurements

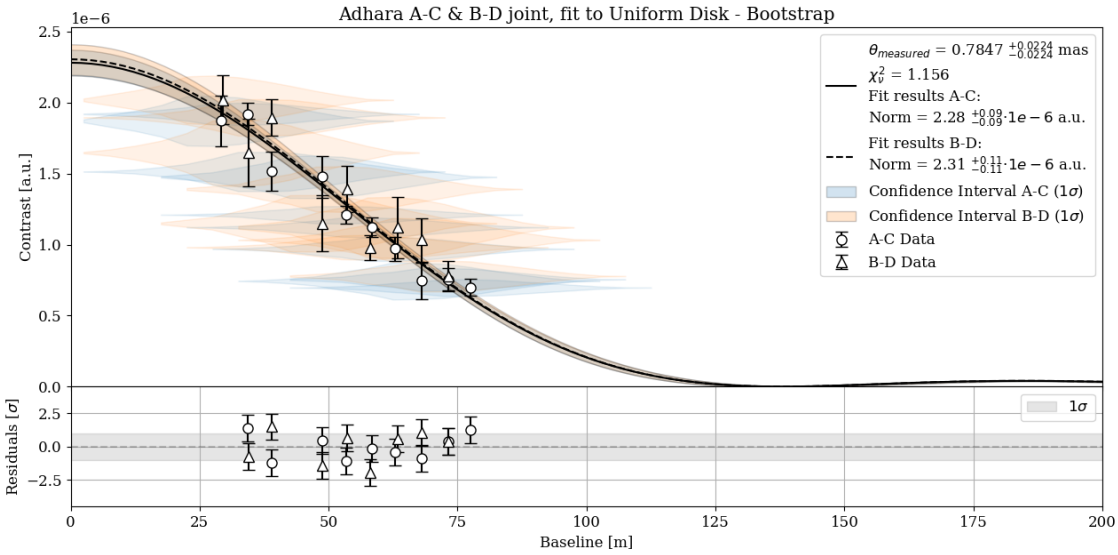

Figure A.1: Bootstrap fit for contrast vs baseline for Adhara.

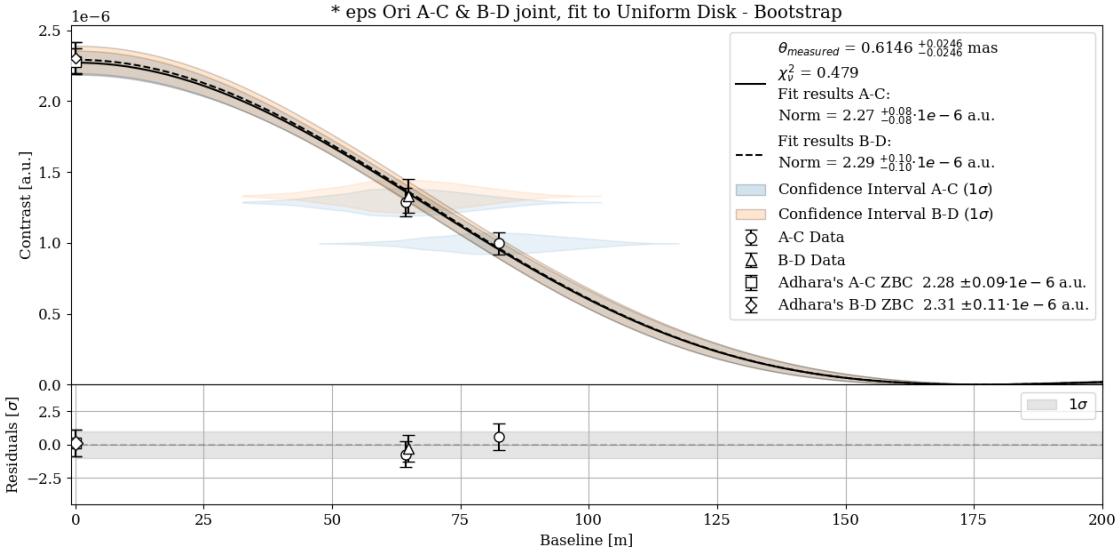

Figure A.2: Bootstrap fit for contrast vs baseline for eps Ori.

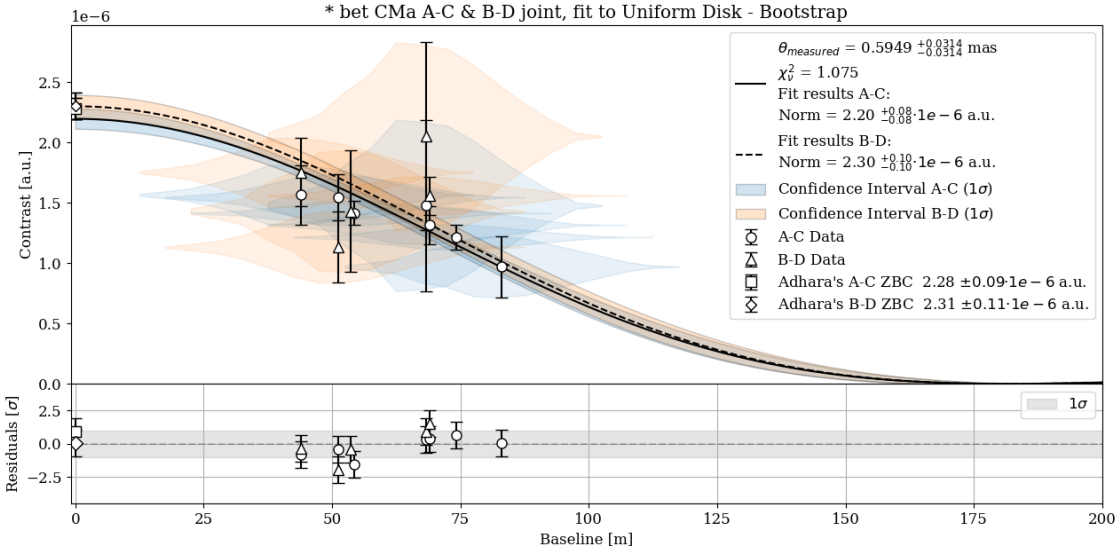

Figure A.3: Bootstrap fit for contrast vs baseline for bet CMa.

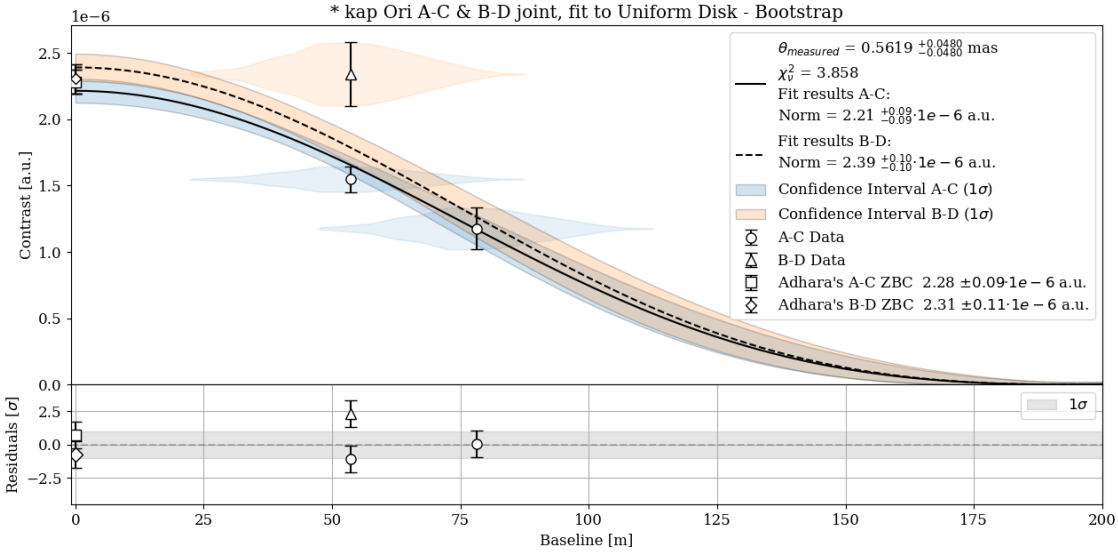

Figure A.4: Bootstrap fit for contrast vs baseline for kap Ori.

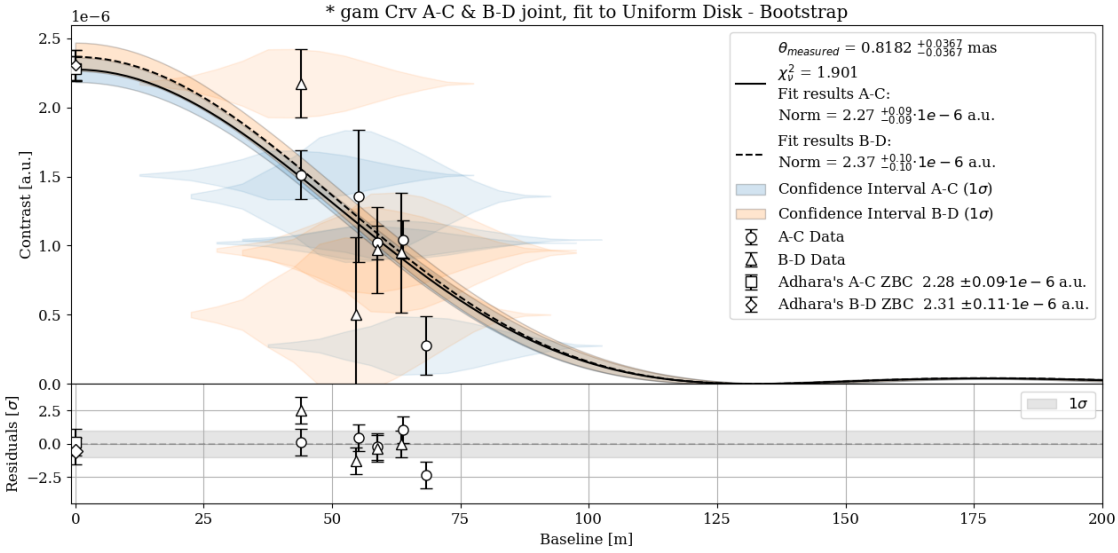

Figure A.5: Bootstrap fit for contrast vs baseline for gam Crv.

A.2 New stellar angular diameter measurements

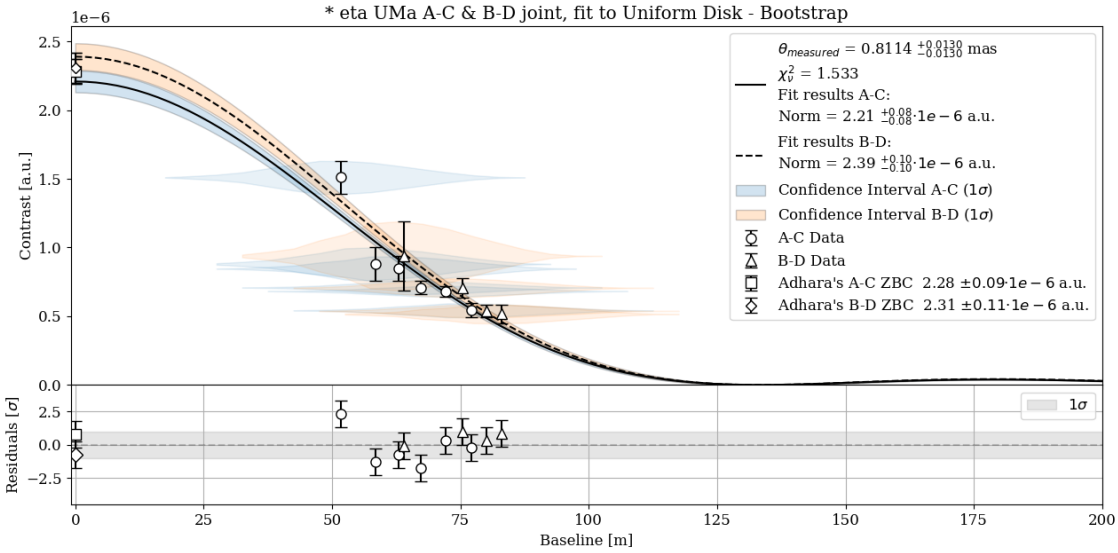

Figure A.6: Bootstrap fit for contrast vs baseline for eta UMa.

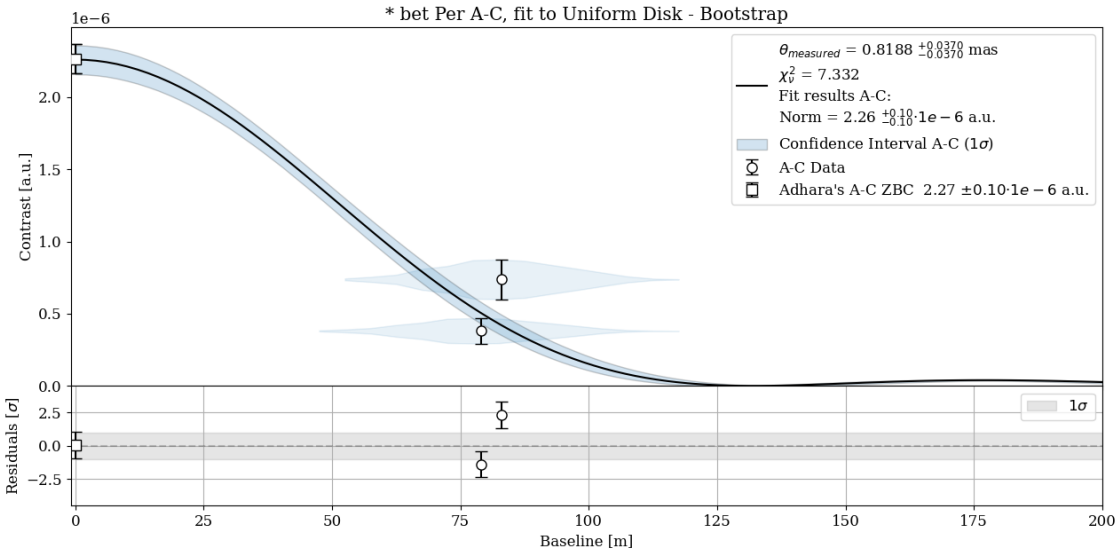

Figure A.7: Bootstrap fit for contrast vs baseline for bet Per.

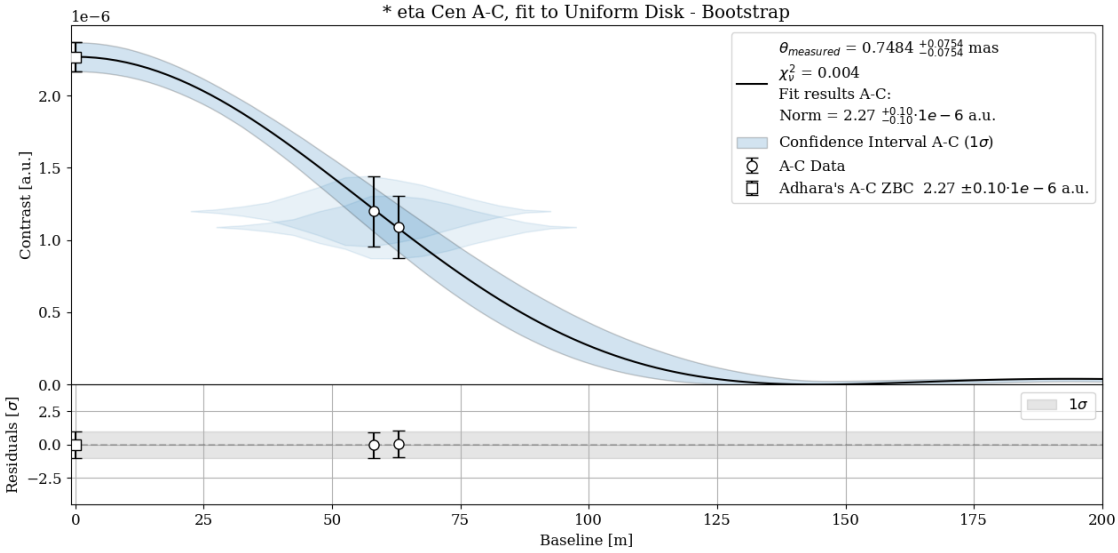

Figure A.8: Bootstrap fit for contrast vs baseline for eta Cen.

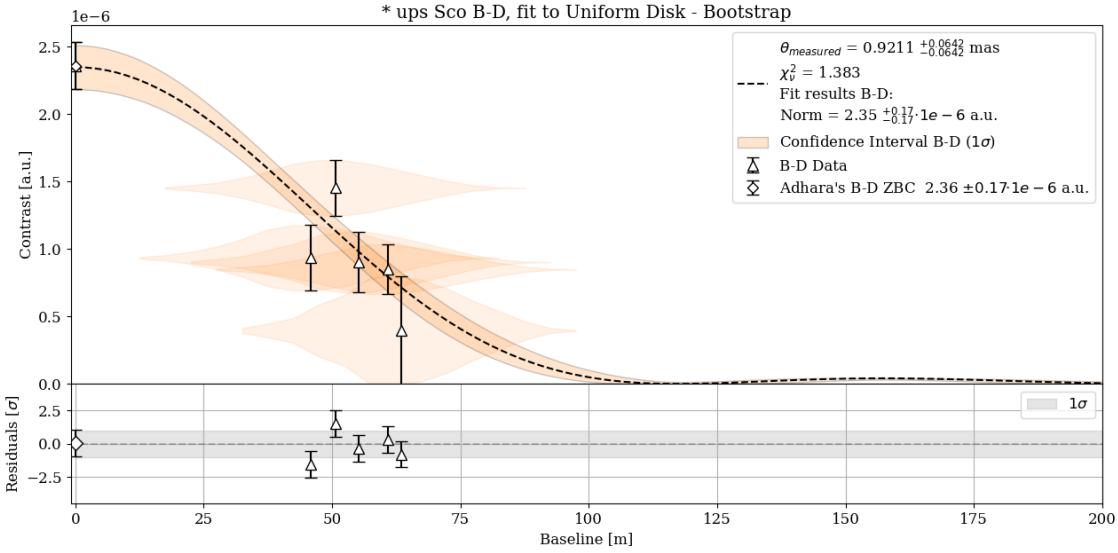

Figure A.9: Bootstrap fit for contrast vs baseline for ups Sco.

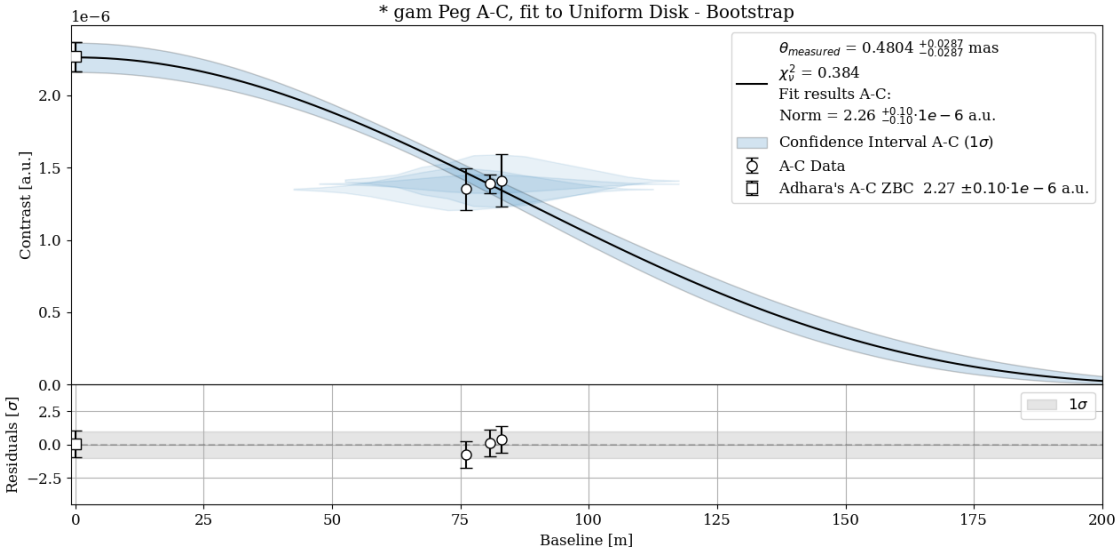

Figure A.10: Bootstrap fit for contrast vs baseline for gam Peg.

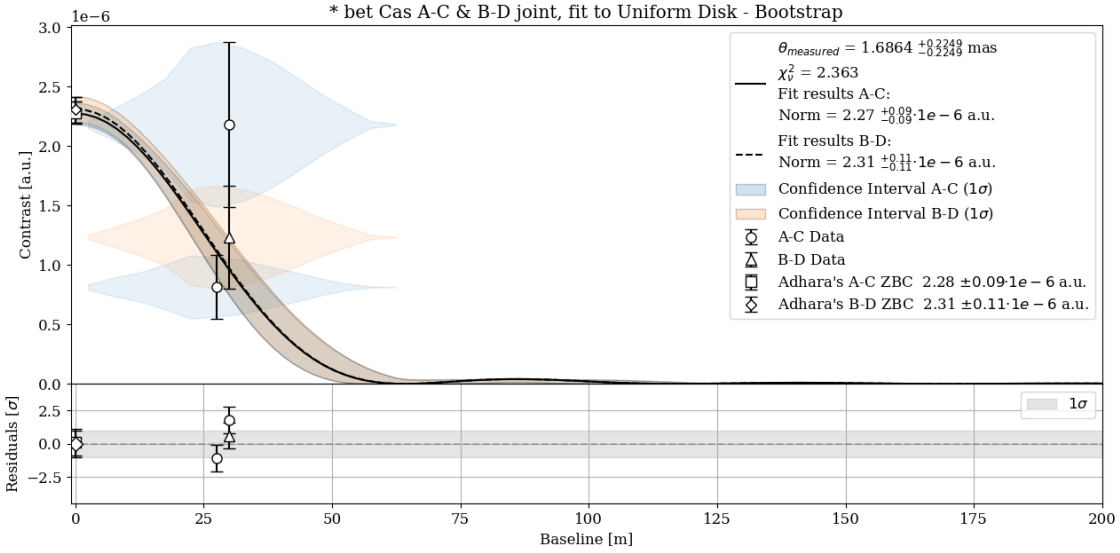

Figure A.11: Bootstrap fit for contrast vs baseline for bet Cas.

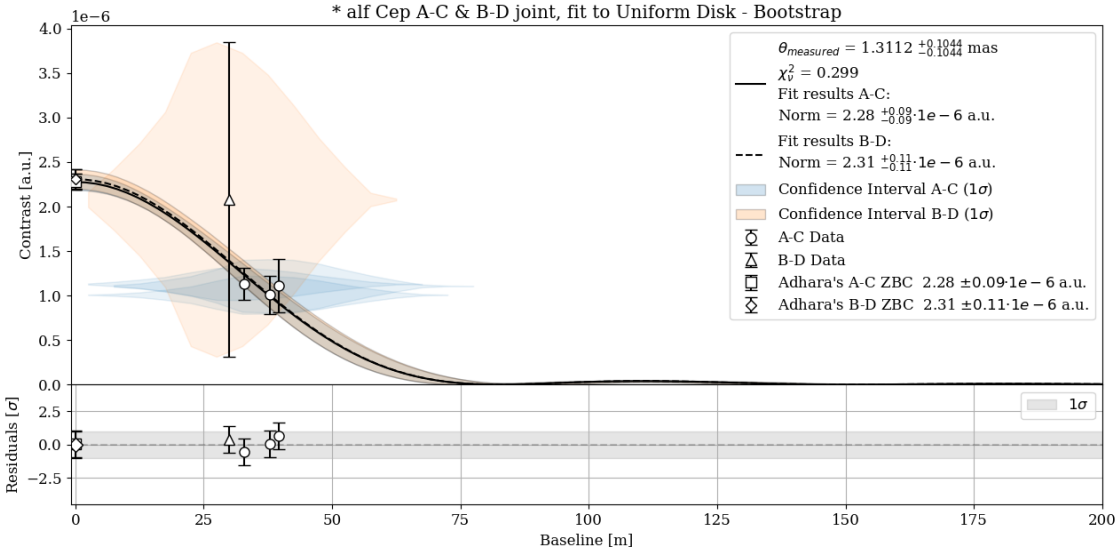

Figure A.12: Bootstrap fit for contrast vs baseline for alf Cep.

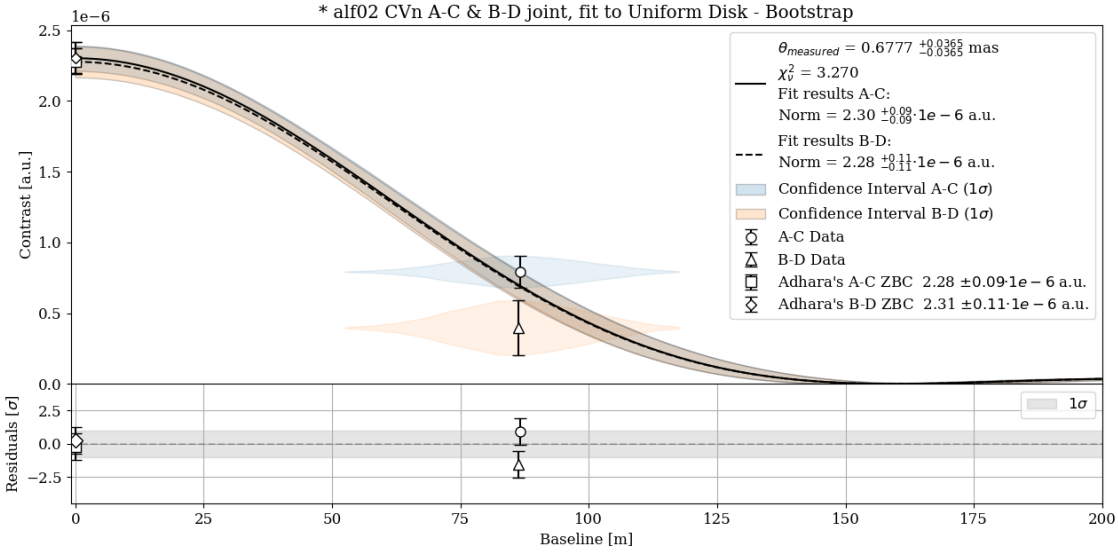

Figure A.13: Bootstrap fit for contrast vs baseline for alf02 CVn.

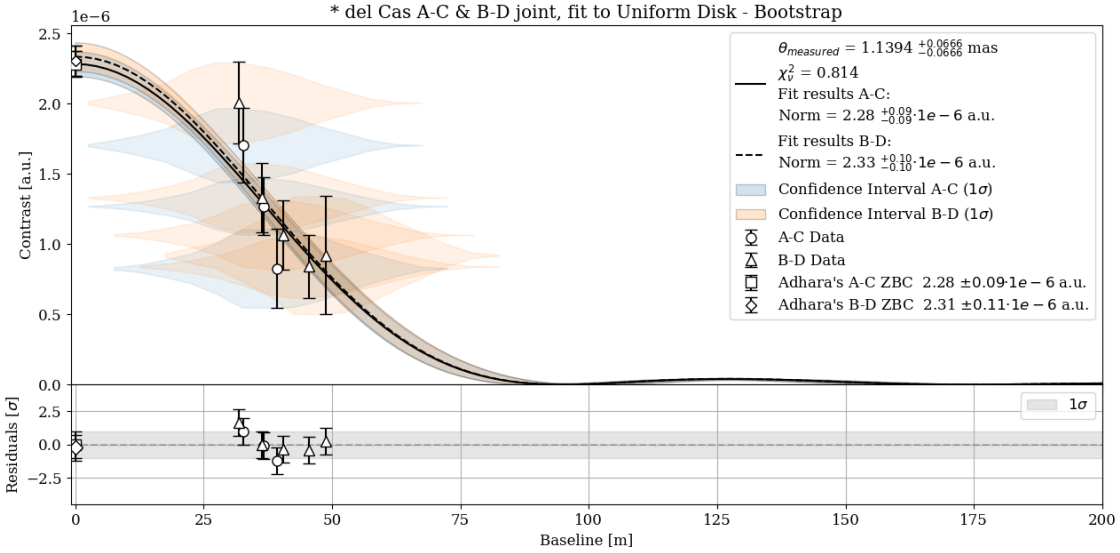

Figure A.14: Bootstrap fit for contrast vs baseline for del Cas.

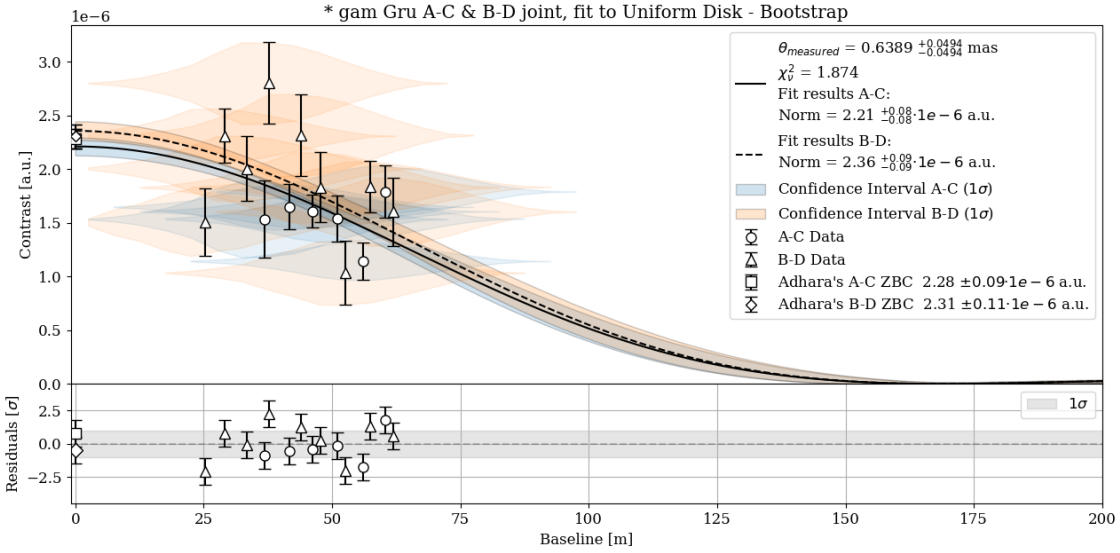

Figure A.15: Bootstrap fit for contrast vs baseline for gam Gru.

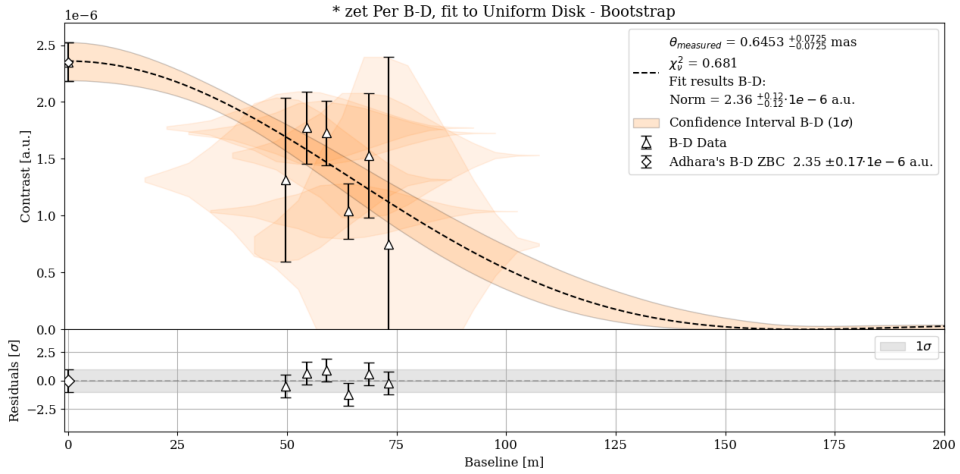

Figure A.16: Bootstrap fit for contrast vs baseline for zet Per.

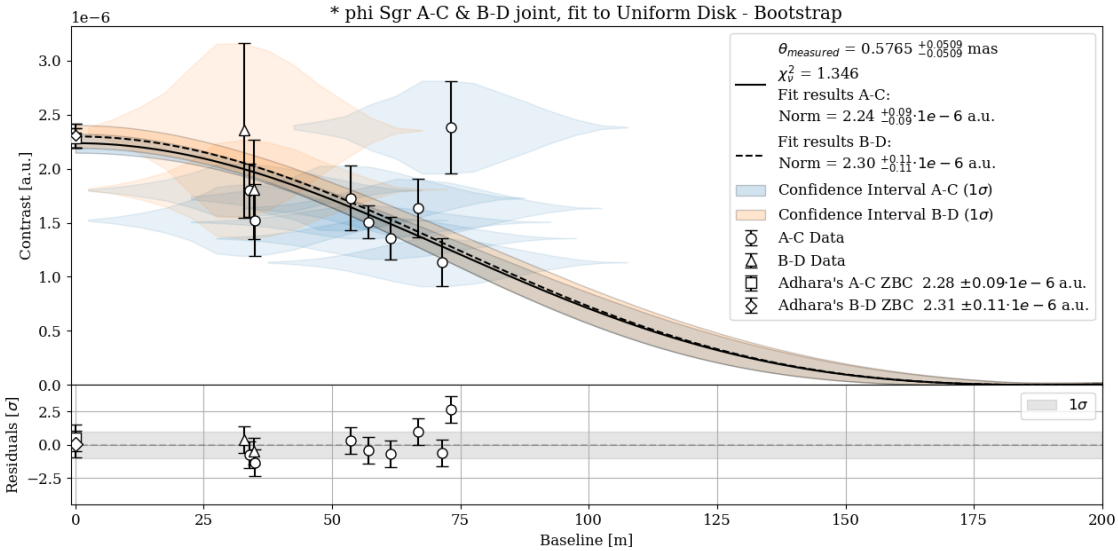

Figure A.17: Bootstrap fit for contrast vs baseline for phi Sgr.

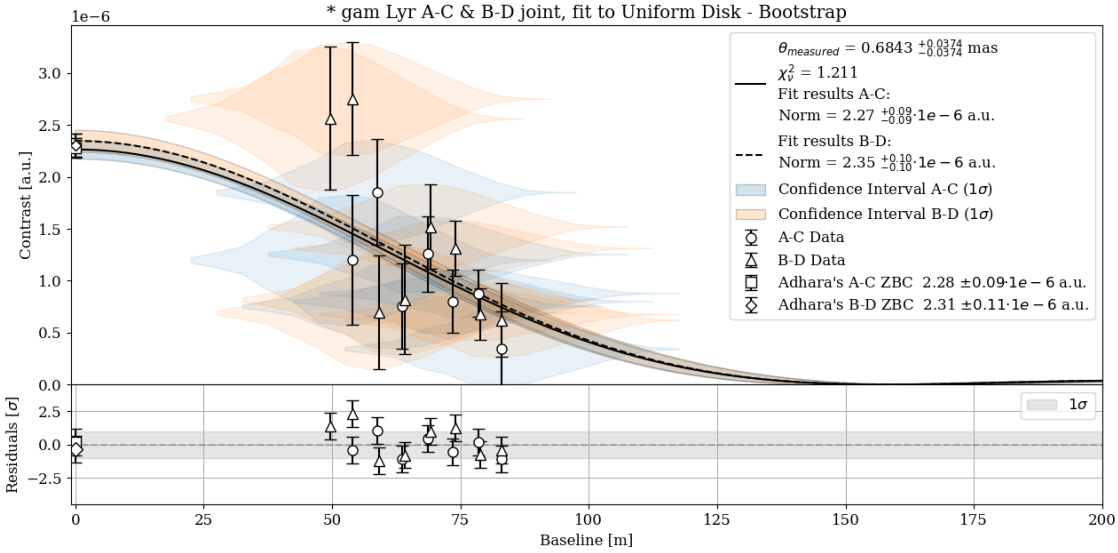

Figure A.18: Bootstrap fit for contrast vs baseline for gam Lyr.

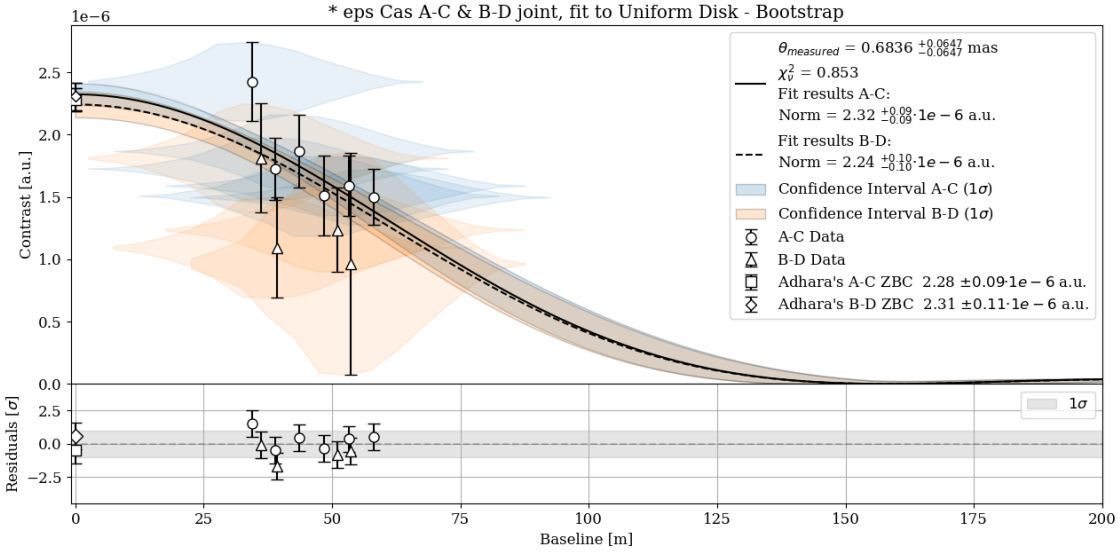

Figure A.19: Bootstrap fit for contrast vs baseline for eps Cas.

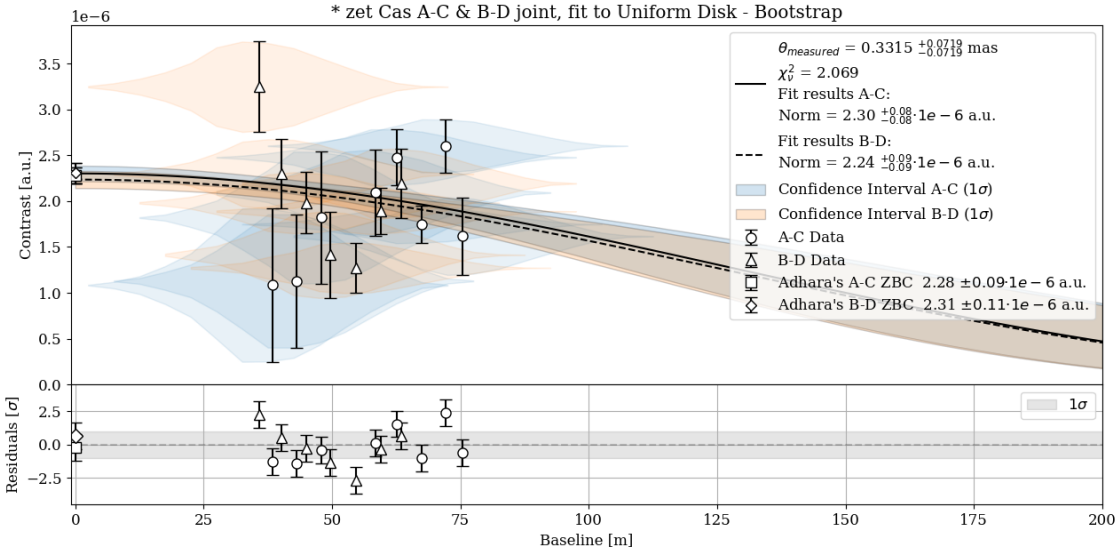

Figure A.20: Bootstrap fit for contrast vs baseline for zet Cas.

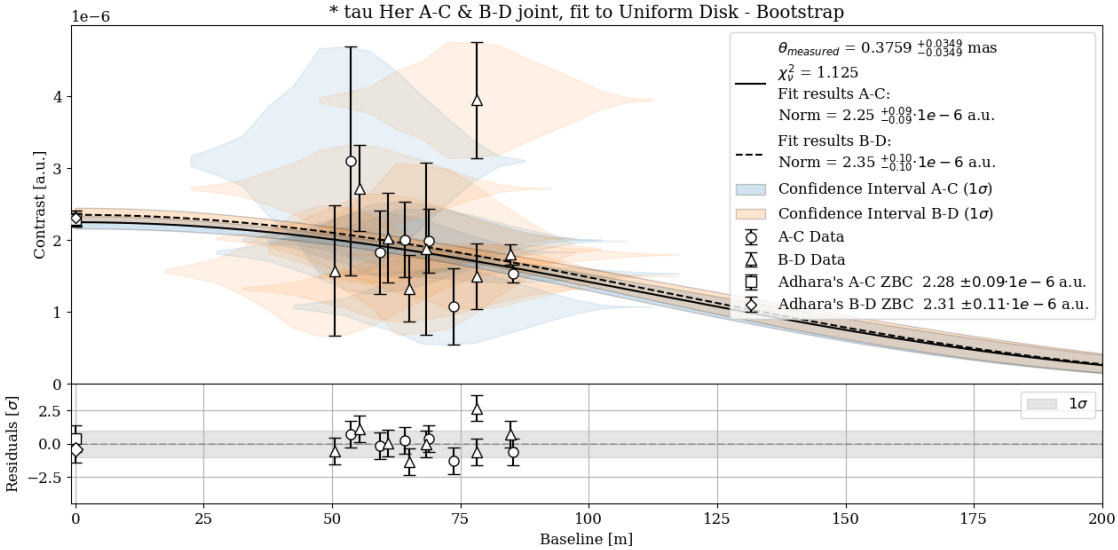

Figure A.21: Bootstrap fit for contrast vs baseline for tau Her.

B. Publications

List of articles or contributions in national and international conferences published or in preparation during the course of this work. I include first the contributions about intensity interferometry and fast radio bursts of which I am a corresponding author, and then some of the contributions in which I am included for having fulfilled collaboration duties for MAGIC, LST and CTA.

B.1 Contributions as a corresponding author about intensity interferometry

Jiménez, I. (2020, July). High angular resolution at optical wavelengths using the Intensity interferometry technique in the MAGIC telescopes. In XIV. 0 Scientific Meeting (virtual) of the Spanish Astronomical Society (p. 228).

Delgado, C., Acciari, V. A., Colombo, E., Cortina, J., Diaz Ginzo, C., Fink, D., ... & MAGIC Collaboration. (2021). Intensity interferometry with the MAGIC telescopes. In 37th International Cosmic Ray Conference (ICRC 2021) (Vol. 395, p. 693). SISSA.

Cortina, J., Acciari, V. A., Biland, A., Colombo, E., Da Costa, C., Delgado, C., ... & Zampieri, L. (2022, August). First measurements and upgrade plans of the MAGIC intensity interferometer. In Optical and Infrared Interferometry and Imaging VIII (Vol. 12183, pp. 127-141). SPIE.

Fiori, M., Naletto, G., Zampieri, L., Martínez, I. J., & Wunderlich, C. (2022). Investigating the accuracy achievable in reconstructing the angular sizes of stars through stellar intensity interferometry observations. Astronomy & Astrophysics, 666, A48.

Martínez, I. J., Acciari, V. A., Cifuentes, A., Colombo, E., Cortina, J., Delgado, C., ... & Zampieri, L. (2023). Update on the performance of the MAGIC Intensity Interferometer.

Publication in preparation about the performance of the MAGIC stellar intensity

interferometer.

B.2 Contributions as a corresponding author about fast radio bursts

López-Oramas, A., Jiménez Martínez, I., Hassan, T., Hoang, J., Inoue, S., Arbet-Engels, A., ... & MAGIC Collaboration. (2021). Monitoring the magnetar SGR 1935+ 2154 with the MAGIC telescopes. In 37th International Cosmic Ray Conference (ICRC 2021) (Vol. 395, p. 783). SISSA.

Jiménez Martínez, I. (2023). Constraining VHE and optical emission from Fast Radio Bursts with the MAGIC telescopes. Highlights of Spanish Astrophysics XI, 141.

Publication in preparation about FRB 180916.

B.3 Contributions as a member of the MAGIC, LST and CTA collaborations

Sakurai, S., Bhattacharyya, W., Dorner, D., Grespan, P., Morcuende, D., Prandini, E., ... & FACT Collaboration. (2021). Studying the long-term spectral and temporal evolution of 1ES 1959+ 650. In 37th International Cosmic Ray Conference (ICRC 2021) (Vol. 395, p. 858). SISSA.

Heckmann, L., Paneque, D., Gasparyan, S., Cerruti, M., Sahakyan, N., Arbet-Engels, A., ... & Fermi-LAT Collaboration. (2021). Multi-messenger characterization of Mrk501 during historically low X-ray and gamma-ray activity. In 37th International Cosmic Ray Conference (ICRC 2021) (Vol. 395, p. 844). SISSA.

Abe, H., Aguasca, A., Agudo, I., Antonelli, L. A., Aramo, C., Armstrong, T., ... & Murase, K. (2022, March). First follow-up of transient events with the CTA Large Size Telescope prototype. In 37th International Cosmic Ray Conference. 12-23 July 2021. Berlin (p. 838).

Arbet-Engels, A., Paneque, D., Heckmann, L., Biland, A., Bretz, T., Hildebrand, D., ... & Multi-wavelength Collaborators. (2021). Unveiling the complex correlation patterns in Mrk 421. In 37th International Cosmic Ray Conference (ICRC 2021) (Vol. 395, p. 834). SISSA.

Longo, F., Berti, A., Bosnjak, Z., Donini, A., Fukami, S., Green, J. G., ... & Antonelli, L. A. (2021, July). Upper limits on the very high energy emission from GRBs observed by MAGIC. In Proceedings of the 37th International Cosmic Ray Conference—PoS (ICRC2021), Berlin, Germany (pp. 12-23).

Acciari, V. A., Ansoldi, S., Antonelli, L. A., Arbet Engels, A., Artero, M., Asano, K., ...

& Puljak, I. (2022, March). Multiwavelength monitoring of gravitationally lensed blazar QSO B0218+ 357 between 2016 and 2020. In 37th International Cosmic Ray Conference. 12-23 July 2021. Berlin (p. 819).

Zarić, D., Green, D., Strzys, M., Vovk, I., Arbet-Engels, A., Biland, A., & MAGIC Collaboration. (2021). MAGIC observations of HESS J1809-193 using the Very Large Zenith Angle technique at energies above TeV. In 37th International Cosmic Ray Conference (ICRC 2021) (Vol. 395, p. 818). SISSA.

Ceribella, G., López-Moya, M., Mirzoyan, R., Arbet-Engels, A., Biland, A., & MAGIC Collaboration. (2021). MAGIC detection of Geminga: an Inverse Compton tail?. In 37th International Cosmic Ray Conference (ICRC 2021) (Vol. 395, p. 816). SISSA.

Manganaro, M., Seglar-Arroyo, M., Becerra González, J., Sanchez, D., Cerruti, M., Tavecchio, F., ... & Fermi-LAT Collaboration. (2021). MAGIC and HESS detect VHE gamma rays from the blazar OT081 for the first time: a deep multiwavelength study. In 37th International Cosmic Ray Conference (ICRC 2021) (Vol. 395, p. 815). SISSA.

Lopez-Coto, R., Moralejo, A., Artero, M., Baquero, A., Bernardos, M., Contreras, J. L., ... & Vuillaume, T. (2021). Physics Performance of the Large-Sized Telescope prototype of the Cherenkov Telescope Array. arXiv preprint arXiv:2109.03515.

Loporchio, S., Lindfors, E., Fallah Ramazani, V., D'Ammando, F., Arbet Engels, A., Di Venere, L., ... & Cutini, S. (2022, March). Discovery of TXS 1515-273 at VHE gamma-rays and modelling of its Spectral Energy Distribution. In 37th International Cosmic Ray Conference (ICRC 2021) (Vol. 395, p. 801). SISSA.

Suda, Y., Artero, M., Asano, K., Berti, A., Nava, L., Noda, K., ... & MAGIC Collaboration. (2021). Observation of a relatively low luminosity long duration GRB 201015A by the MAGIC telescopes. In 37th International Cosmic Ray Conference (ICRC 2021) (Vol. 395, p. 797). SISSA.

Oka, T., Saito, T., Strzys, M., Arbet-Engels, A., Biland, A., & MAGIC Collaboration. (2021). Resolving the origin of very-high-energy gamma-ray emission from the PeVatron candidate SNR G106. 3+ 2.7 using MAGIC telescopes. In 37th International Cosmic Ray Conference (ICRC 2021) (Vol. 395, p. 796). SISSA.

Otero-Santos, J., Dorner, D., Morcuende, D., Paneque, D., Fallah Ramazani, V., Prandini, E., ... & Fermi-LAT Collaboration. (2021). BL Lac object 1ES 0647+ 250, a decade of MWL observations. In 37th International Cosmic Ray Conference (ICRC 2021) (Vol. 395, p. 792). SISSA.

Fukami, S., Berti, A., Loporchio, S., Suda, Y., Nava, L., Noda, K., ... & MAGIC Collaboration. (2021). Very-high-energy gamma-ray emission from GRB 201216C detected by MAGIC. In 37th International Cosmic Ray Conference (ICRC 2021) (Vol. 395, p. 788). SISSA.

Berti, A., Bosnjak, Z., Covino, S., Fukami, S., Inoue, S., Longo, F., ... & MAGIC Collaboration. (2021). Shedding light on the highest energy emission from GRBs with MAGIC observations. In 37th International Cosmic Ray Conference (ICRC 2021) (Vol. 395, p. 787). SISSA.

Molina, E., López-Oramas, A., Hadasch, D., & Hoang, J. (2022). Recent MAGIC results on Galactic binaries. arXiv preprint arXiv:2209.10226.

D'Amico, G., Kerszberg, D., Martinez, M., Perennes, C., Rico, J., Terzić, T., ... & No Collaboration. (2021). Recent results on LIV studies using MAGIC telescopes from the observation of GRB 190114C. In 37th International Cosmic Ray Conference (ICRC 2021) (Vol. 395, p. 785). SISSA.

López-Oramas, A., Green, D., Arbet-Engels, A., Biland, A., & MAGIC Collaboration. (2021). Understanding the origin of the extended gamma-ray emission and the physical nature of HESS J1841-055 using observations at TeV energies with the MAGIC telescopes. In 37th International Cosmic Ray Conference (ICRC 2021) (Vol. 395, p. 782). SISSA.

Noda, K., Nava, L., Inoue, S., Fukami, S., Palatiello, M., Berti, A., ... & Fermi-LAT Collaboration. (2021). MAGIC observations of the nearby short GRB 160821B. In 37th International Cosmic Ray Conference (ICRC 2021) (Vol. 395, p. 776). SISSA.

D'Ammando, F., Angioni, R., Orienti, M., Sitarek, J., Nozaki, S., Lindfors, E., ... & MAGIC Collaboration. (2021). Multiwavelength observations in 2019-2020 of a new very-high-energy gamma-ray emitter: the flat spectrum radio quasar QSO B1420+ 326. In 37th International Cosmic Ray Conference (ICRC 2021) (Vol. 395, p. 775). SISSA.

Grespan, P., Jacquemont, M., López-Coto, R., Miener, T., Nieto-Castaño, D., & Vuillaume, T. (2021). Deep-learning-driven event reconstruction applied to simulated data from a single Large-Sized Telescope of CTA. arXiv preprint arXiv:2109.14262.

Ohtani, Y., Berti, A., Depaoli, D., Di Pierro, F., Green, D., Heckmann, L., ... & Vovk, I. (2021). Cross-calibration and combined analysis of the CTA-LST prototype and the MAGIC telescopes. arXiv preprint arXiv:2108.05140.

Kobayashi, Y., Okumura, A., Cassol, F., Katagiri, H., Sitarek, J., Gliwny, P., ... & Nogami, Y. (2021). Camera Calibration of the CTA-LST prototype. arXiv preprint arXiv:2108.05035.

Blanch, O., Delgado, C., Saito, T., Batković, I., Becerra Gonzalez, J., Jiménez Martínez, I., ... & Montaruli, T. (2022, March). Commissioning of the camera of the first Large Size Telescope of the Cherenkov Telescope Array. In 37th International Cosmic Ray Conference. 12-23 July 2021. Berlin (p. 718).

Alispach, C. M., Abe, H., Aguasca, A., Agudo, I., Antonelli, L. A., Aramo, C., ... & Mrakovcic, K. (2022, March). Reconstruction of extensive air shower images of the Large Size Telescope prototype of CTA using a novel likelihood technique. In 37th International

Cosmic Ray Conference. 12-23 July 2021. Berlin (p. 716).

Foffano, L., Carosi, A., Dalchenko, M., Heller, M., Della Volpe, D., & Montaruli, T. (2021). Monitoring the pointing of the prototype LST-1 using star reconstruction in the Cherenkov camera. arXiv preprint arXiv:2108.00699.

Abe, H., Aguasca, A., Agudo, I., Antonelli, L. A., Aramo, C., Armstrong, T., ... & Murase, K. (2022, March). Analysis of the Cherenkov Telescope Array first Large Size Telescope real data using convolutional neural networks. In 37th International Cosmic Ray Conference (p. 703).

Di Tria, R., Di Venere, L., Giordano, F., Green, D., Hahn, A., Pantaleo, F. R., ... & MAGIC Collaboration. (2021). Analysis of the W 44 Supernova Remnant and its surroundings with Fermi-LAT and MAGIC. In 37th International Cosmic Ray Conference (ICRC 2021) (Vol. 395, p. 642). SISSA.

Babic, A., Baquero, A., Batković, I., Becerra Gonzalez, J., Besenrieder, J., Bökenkamp, H., ... & Teshima, M. (2021). Search for Gamma-ray Line emission from Dark Matter annihilation in the Galactic Centre with the MAGIC telescopes.

Maggio, C., Kerszberg, D., Ninci, D., Vitale, V., Arbet-Engels, A., Biland, A., & MAGIC Collaboration. (2021). Upper limits on the WIMP annihilation cross section from a joint analysis of dwarf spheroidal satellite galaxy observations with the MAGIC telescopes. In 37th International Cosmic Ray Conference (ICRC 2021) (Vol. 395, p. 512). SISSA.

Temnikov, P., Verguilov, V., Maneva, G., Mirzoyan, R., Baack, D., Arbet-Engels, A., ... & Magic Collaboration. (2021). Protons Spectrum from MAGIC Telescopes data. In 37th International Cosmic Ray Conference (ICRC 2021) (Vol. 395, p. 231). SISSA.

Acciari, V. A., Aniello, T., Ansoldi, S., Antonelli, L. A., Engels, A. A., Artero, M., ... & Prandini, E. (2022). Investigating the Blazar TXS 0506+ 056 through Sharp Multiwavelength Eyes During 2017–2019. The Astrophysical Journal, 927(2), 197.

Adams, C. B., Benbow, W., Brill, A., Buckley, J. H., Capasso, M., Chromey, A. J., ... & Jouvin, L. (2021). Observation of the Gamma-Ray Binary HESS J0632+ 057 with the HESS, MAGIC, and VERITAS Telescopes. The Astrophysical Journal, 923(2), 241.

Arbet-Engels, A., Prandini, E., Ventura, S., Fallah Ramazani, V., Cerruti, M., Arcaro, C., ... & FACT Collaboration. (2021). Extreme blazars under the eyes of MAGIC. In 37th International Cosmic Ray Conference (ICRC 2021) (Vol. 395, p. 865). SISSA.

Abe, H., Abe, S., Acciari, V. A., Agudo, I., Aniello, T., Ansoldi, S., ... & Ohtani, Y. (2023). Multimessenger Characterization of Markarian 501 during Historically Low X-Ray and -Ray Activity. The Astrophysical Journal Supplement Series, 266(2), 37.

Abe, S., Aguasca-Cabot, A., Agudo, I., Crespo, N. A., Antonelli, L. A., Aramo, C.,

... & Marsella, G. (2023). Multiwavelength study of the galactic PeVatron candidate LHAASO J2108+ 5157. Astronomy & Astrophysics, 673, A75.

Abe, H., Abe, S., Acciari, V. A., Agudo, I., Aniello, T., Ansoldi, S., ... & Oka, T. (2022). MAGIC observations provide compelling evidence of the hadronic multi-TeV emission from the putative PeVatron SNR G106. 3+ 2.7. arXiv preprint arXiv:2211.15321.

Abe, H., Abe, S., Acciari, V. A., Aniello, T., Ansoldi, S., Antonelli, L. A., ... & Paneque, D. (2023). Search for Gamma-Ray Spectral Lines from Dark Matter Annihilation up to 100 TeV toward the Galactic Center with MAGIC. Physical Review Letters, 130(6), 061002.

Acciari, V. A., Agudo, I., Aniello, T., Ansoldi, S., Antonelli, L. A., Engels, A. A., ... & Pavletić, L. (2023). A lower bound on intergalactic magnetic fields from time variability of 1ES 0229+ 200 from MAGIC and Fermi/LAT observations. Astronomy & Astrophysics, 670, A145.

Acciari, V. A., Aniello, T., Ansoldi, S., Antonelli, L. A., Engels, A. A., Arcaro, C., ... & Pavletić, L. (2022). Long-term multi-wavelength study of 1ES 0647+ 250. arXiv preprint arXiv:2211.13268.

Abe, H., Abe, S., Acciari, V. A., Aniello, T., Ansoldi, S., Antonelli, L. A., ... & Paiano, S. (2022). Gamma-ray observations of MAXI J1820+ 070 during the 2018 outburst. Monthly Notices of the Royal Astronomical Society, 517(4), 4736-4751.

Adams, C. B., Batista, P., Benbow, W., Brill, A., Brose, R., Buckley, J. H., ... & Ishio, K. (2022). Multiwavelength observations of the blazar VER J0521+ 211 during an elevated TeV gamma-ray state. The Astrophysical Journal, 932(2), 129.

Acciari, V. A., Ansoldi, S., Antonelli, L. A., Arbet Engels, A., Artero, M., Asano, K., ... & Pihet, M. (2022). Proton acceleration in thermonuclear nova explosions revealed by gamma rays. Nature Astronomy, 6(6), 689-697.

López-Oramas, A., Manganaro, M., Strišković, J., Acciari, V. A., Ansoldi, S., Antonelli, L. A., ... & Priyadarshi, C. (2022, March). meetTheMAGICians: Science communication and visibility of young researchers. In 37th International Cosmic Ray Conference (p. 1389).

Acciari, V. A., Ansoldi, S., Antonelli, L. A., Arbet Engels, A., Artero, M., Asano, K., ... & Puljak, I. (2021, July). Searching for VHE gamma-ray emission associated with IceCube neutrino alerts using FACT, HESS, MAGIC, and VERITAS. In Proceedings of 37th International Cosmic Ray Conference—PoS (ICRC2021).

Stamerra, A., Salafia, O. S., Berti, A., Covino, S., D'Elia, V., Miceli, D., ... & MAGIC Collaboration. (2021). Follow-up observations of GW170817 with the MAGIC telescopes. In 37th International Cosmic Ray Conference (ICRC 2021) (Vol. 395, p. 944). SISSA.

Heller, M., Armstrong, T., Bellato, M., Bergnoli, A., Bernardos, M., Bernasconi, E.,

... & Tajima, H. (2021). Development of an advanced SiPM camera for the Large Size Telescope of the Cherenkov Telescope Array Observatory. Development, 12, 23.

Acciari, V. A., Ansoldi, S., Antonelli, L. A., Arbet Engels, A., Artero, M., Asano, K., ... & Puljak, I. (2022, March). Multi-epoch monitoring of TXS 0506+ 056 with MAGIC and MWL partners. In 37th International Cosmic Ray Conference. 12-23 July 2021. Berlin (p. 875).

Mazin, D. (2021). Status and results of the prototype LST of CTA. arXiv preprint arXiv:2108.06005.

Acciari, V. A., Ansoldi, S., Antonelli, L. A., Asano, K., Babić, A., Banerjee, B., ... & Sahakyan, N. (2021). Multiwavelength variability and correlation studies of Mrk 421 during historically low X-ray and -ray activity in 2015–2016. Monthly Notices of the Royal Astronomical Society, 504(1), 1427-1451.

Green, J. G., Seglar-Arroyo, M., Consortium, C., Abe, K., Abe, S., Acharyya, A., ... & Dörner, J. (2023). Chasing Gravitational Waves with the Chereknov Telescope Array. arXiv preprint arXiv:2310.07413.

Abe, H., Abe, S., Acciari, V. A., Agudo, I., Aniello, T., Ansoldi, S., ... & Ohtani, Y. (2023). MAGIC detection of GRB 201216C at $z = 1.1$. arXiv preprint arXiv:2310.06473.

Abe, H., Abe, S., Acciari, V. A., Agudo, I., Aniello, T., Ansoldi, S., ... & Moroni, P. G. (2023). Multi-year characterisation of the broad-band emission from the intermittent extreme BL Lac 1ES 2344+ 514. arXiv preprint arXiv:2310.03922.

Abe, H., Abe, K., Abe, S., Acciari, V. A., Aguasca-Cabot, A., Agudo, I., ... & Houles, J. (2023). Performance of the joint LST-1 and MAGIC observations evaluated with Crab Nebula data.

Abe, H., Abe, K., Abe, S., Aguasca-Cabot, A., Agudo, I., Crespo, N. A., ... & Majumdar, P. (2023). Observations of the Crab Nebula and Pulsar with the Large-sized Telescope Prototype of the Cherenkov Telescope Array. The Astrophysical Journal, 956(2), 80.

Abe, K., Abe, S., Acero, F., Acharyya, A., Adam, R., Aguasca-Cabot, A., ... & Dumora, D. (2023). Prospects for γ-ray observations of the Perseus galaxy cluster with the Cherenkov Telescope Array.

Bibliography

[1] WL Kraushaar and GW Clark. “Search for primary cosmic gamma rays with the satellite Explorer XI”. In: *Physical Review Letters* 8.3 (1962), page 106 (cited on page 16).

[2] GW Clark, GP Garmire, and WL Kraushaar. “Observation of high-energy cosmic gamma rays”. In: *Astrophysical Journal, vol. 153, p. L203* 153 (1968), page L203 (cited on page 16).

[3] CE Fichtel, DA Kniffen, and RC Hartman. *Celestial diffuse gamma radiation above 30 MeV observed by SAS-2*. Technical report. 1973 (cited on page 16).

[4] HA Mayer-Hasselwander et al. “COS-B observation of the Milky Way in high-energy gamma rays”. In: *Ann. NY Acad. Sci., 9th Texas Symposium on Relativistic Astrophysics*. Volume 336. 1980, pages 211–222 (cited on page 16).

[5] Trevor C Weekes et al. “Observation of tev gamma-rays from the crab nebula using the atmospheric cherenkov imaging technique”. In: *Astrophysical Journal* 342 (1989), pages 379–395 (cited on page 16).

[6] Michael S Briggs et al. “BATSE observations of the large-scale isotropy of gamma-ray bursts”. In: *arXiv preprint astro-ph/9509078* (1995) (cited on page 16).

[7] E Costa. “X–ray afterglow of gamma–ray bursts with BeppoSAX”. In: *Astronomy and Astrophysics Supplement Series* 138.3 (1999), pages 425–429 (cited on page 16).

[8] Alessandro De Angelis. “Atmospheric ionization and cosmic rays: studies and measurements before 1912”. In: *Astroparticle Physics* 53 (2014), pages 19–26 (cited on page 16).

[9] Charles Augustin Coulomb. *Premier-[troisième] mémoire sur l’electricité et le magnétisme*. Académie Royale des sciences, 1785 (cited on page 16).

[10] Michael Faraday. “Experimental Researches in Electricity”. In: 2 (1844) (cited on page 16).

[11] Julius Elster and H Geitel. “Ueber Elektricitätszerstreuung in der Luft”. In: *Annalen der Physik* 307.7 (1900), pages 425–446 (cited on page 16).

[12] Domenico Pacini. “Penetrating radiation at the surface of and in water”. In: *arXiv preprint arXiv:1002.1810* (2010) (cited on page 16).

[13] Victor Francis Hess. “Über Beobachtungen der durchdringenden Strahlung bei sieben Freiballonfahrten”. In: *Z. Phys.* 13 (1912), page 1084 (cited on page 16).

[14] Robert Andrews Millikan and G Harvey Cameron. “High frequency rays of cosmic origin III. Measurements in snow-fed lakes at high altitudes”. In: *Physical Review* 28.5 (1926), page 851 (cited on page 17).

[15] GA Bazilevskaya. “Once again about origin of the solar cosmic rays”. In: *Journal of Physics: Conference Series*. Volume 798. 1. IOP Publishing. 2017, page 012034 (cited on page 17).

[16] AI Podgorny et al. “The spectrum of solar relativistic cosmic ray measurements and numerical simulation”. In: *Journal of Physics: Conference Series*. Volume 798. 1. IOP Publishing. 2017, page 012027 (cited on page 17).

[17] Terry D Oswalt and Gerard Gilmore. *Planets, Stars and Stellar Systems: Volume 5: Galactic Structure and Stellar Populations*. Springer, 2013 (cited on page 18).

[18] Rafael Alves Batista et al. “Open questions in cosmic-ray research at ultrahigh energies”. In: *Frontiers in Astronomy and Space Sciences* 6 (2019), page 23 (cited on page 18).

[19] Kenneth Greisen. “End to the cosmic-ray spectrum?” In: *Physical Review Letters* 16.17 (1966), page 748 (cited on page 18).

[20] Georgi T Zatsepin and Vadem A Kuz’min. “Upper limit of the spectrum of cosmic rays”. In: *Soviet Journal of Experimental and Theoretical Physics Letters* 4 (1966), page 78 (cited on page 18).

[21] Igor Oya Vallejo. “Observation of active galatic nuclei with the Magic telescope”. In: (2010) (cited on pages 20–23, 116).

[22] GR Choppin et al. “Absorption of nuclear radiation”. In: *Radiochem. Nucl. Chem* 1 (2002), pages 123–165 (cited on pages 24, 25).

[23] Alberto Franceschini, Giulia Rodighiero, and Mattia Vaccari. “Extragalactic optical-infrared background radiation, its time evolution and the cosmic photon-photon opacity”. In: *Astronomy & Astrophysics* 487.3 (2008), pages 837–852 (cited on page 24).

[24] Alberto Dominguez et al. “Extragalactic background light inferred from AEGIS galaxy-SED-type fractions”. In: *Monthly Notices of the Royal Astronomical Society* 410.4 (2011), pages 2556–2578 (cited on page 24).

[25] FW Stecker and ST Scully. “A simple analytic treatment of the intergalactic absorption effect in blazar gamma-ray spectra”. In: *The Astrophysical Journal* 652.1 (2006), page L9 (cited on page 24).

[26] Daniel Mazin. “Constraints on Extragalactic Background Light from Cherenkov telescopes: status and perspectives for the next 5 years”. In: *AIP Conference Proceedings*. Volume 1112. 1. American Institute of Physics. 2009, pages 111–120 (cited on page 24).

[27] Kouichi Hirotani. "Particle accelerator in pulsar magnetospheres: super-Goldreich-Julian current with ion emission from the neutron star surface". In: *The Astrophysical Journal* 652.2 (2006), page 1475 (cited on page 25).

[28] Frank M Rieger, Valentí Bosch-Ramon, and Peter Duffy. "Fermi acceleration in astrophysical jets". In: *The Multi-Messenger Approach to High-Energy Gamma-Ray Sources*. Springer. 2007, pages 119–125 (cited on page 26).

[29] JP Hulss and Ch Wiebusch. "Search for signatures of extra-terrestrial neutrinos with a multipole analysis of the AMANDA-II sky-map". In: *The IceCube Collaboration: contributions to the 30 th International Cosmic Ray Conference (ICRC 2007)*. 2007, page 111 (cited on page 26).

[30] Subrahmanyan Chandrasekhar. "The maximum mass of ideal white dwarfs". In: *Astrophysical Journal, vol. 74, p. 81* 74 (1931), page 81 (cited on page 27).

[31] Donald E Osterbrock and Gary J Ferland. *Astrophysics Of Gas Nebulae and Active Galactic Nuclei*. University science books, 2006 (cited on page 27).

[32] GF Krymskii. "A regular mechanism for the acceleration of charged particles on the front of a shock wave". In: *Akademiia Nauk SSSR Doklady*. Volume 234. 1977, pages 1306–1308 (cited on page 28).

[33] URL: https://hubblesite.org/contents/media/images/2005/37/1823-Image.html (cited on page 28).

[34] URL: https://www.nasa.gov/mission_pages/GLAST/news/crab-flare.html (cited on page 28).

[35] A Giuliani et al. "Neutral pion emission from accelerated protons in the supernova remnant W44". In: *The Astrophysical Journal Letters* 742.2 (2011), page L30 (cited on page 28).

[36] Markus Ackermann et al. "Detection of the characteristic pion-decay signature in supernova remnants". In: *Science* 339.6121 (2013), pages 807–811 (cited on page 28).

[37] T Jogler and S Funk. "Revealing W51C as a cosmic ray source using Fermi-LAT data". In: *The Astrophysical Journal* 816.2 (2016), page 100 (cited on page 28).

[38] Soheila Abdollahi et al. "Fermi large area telescope fourth source catalog". In: *The Astrophysical Journal Supplement Series* 247.1 (2020), page 33 (cited on pages 29, 36).

[39] Stefano Ansoldi et al. "Teraelectronvolt pulsed emission from the Crab Pulsar detected by MAGIC". In: *Astronomy & Astrophysics* 585 (2016), A133 (cited on pages 29, 125).

[40] Ester Aliu et al. "Observation of pulsed γ-Rays above 25 GeV from the Crab Pulsar with MAGIC". In: *Science* 322.5905 (2008), pages 1221–1224 (cited on page 30).

[41] L Maraschi and A Treves. "A model for LSI 61 303". In: *Monthly Notices of the Royal Astronomical Society* 194.1 (1981), 1P–5P (cited on page 30).

[42] IF Mirabel and LF Rodriguez. "A superluminal source in the Galaxy". In: *Nature* 371.6492 (1994), pages 46–48 (cited on page 30).

[43] IF Mirabel and LF Rodriguez. “Microquasars in our Galaxy”. In: *Nature* 392.6677 (1998), pages 673–676 (cited on page 30).

[44] Fermi-LAT Collaboration, AA Abdo, et al. “Fermi LAT Observations of LS I+ 61deg303: First Detection of an Orbital Modulation in GeV Gamma Rays, 701 (Aug., 2009) L123–L128”. In: *arXiv preprint arXiv:0907.4307* 50 () (cited on page 30).

[45] Fermi LAT Collaboration et al. “Modulated high-energy gamma-ray emission from the microquasar Cygnus X-3”. In: *Science* 326.5959 (2009), pages 1512–1516 (cited on pages 30, 31).

[46] Felix Aharonian et al. “Discovery of the binary pulsar PSR B1259-63 in very-high-energy gamma rays around periastron with HESS”. In: *Astronomy & Astrophysics* 442.1 (2005), pages 1–10 (cited on page 30).

[47] Jordı Albert et al. “Variable very-high-energy gamma-ray emission from the microquasar LS I+ 61 303”. In: *science* 312.5781 (2006), pages 1771–1773 (cited on page 30).

[48] Jordı Albert et al. “Periodic Very High Energy γ-Ray Emission from LS I+ 61 303 Observed with the MAGIC Telescope”. In: *The Astrophysical Journal* 693.1 (2009), page 303 (cited on page 30).

[49] AU Abeysekara et al. “Very-high-energy particle acceleration powered by the jets of the microquasar SS 433”. In: *Nature* 562.7725 (2018), pages 82–85 (cited on page 30).

[50] URL: https://www.nasa.gov/mission_pages/chandra/a-stellar-circle-of-life.html (cited on page 31).

[51] Fermi-LAT Collaboration et al. “Gamma-ray emission concurrent with the nova in the symbiotic binary V407 Cygni”. In: *Science* 329.5993 (2010), pages 817–821 (cited on page 31).

[52] Fermi-LAT Collaboration. “Fermi establishes classical novae as a distinct class of gamma-ray sources”. In: *Science* 345.6196 (2014), pages 554–558 (cited on page 31).

[53] CC Cheung et al. “Fermi-LAT gamma-ray detections of classical Novae V1369 Centauri 2013 and V5668 Sagittarii 2015”. In: *The Astrophysical Journal* 826.2 (2016), page 142 (cited on page 31).

[54] E Aliu et al. “VERITAS Observations of the Nova in V407 Cygni”. In: *The Astrophysical Journal* 754.1 (2012), page 77 (cited on page 31).

[55] Victor A Acciari et al. “Proton acceleration in thermonuclear nova explosions revealed by gamma rays”. In: *Nature Astronomy* 6.6 (2022), pages 689–697 (cited on page 31).

[56] Stefan J Wagner, HESS collaboration, et al. “Detection of VHE gamma-ray emission from the recurrent nova RS Ophiuchi with HESS”. In: *The Astronomer’s Telegram* 14844 (2021), page 1 (cited on page 31).

[57] A Aguasca-Cabot et al. “RS Ophiuchi nova outburst detection by the LST-1”. In: (2022) (cited on page 31).

[58] PH Tam, Chung Y Hui, and Albert K H Kong. "Gamma-ray emission from globular clusters". In: *arXiv preprint arXiv:1207.7267* (2012) (cited on page 31).

[59] Aous A Abdo et al. "A population of gamma-ray emitting globular clusters seen with the Fermi Large Area Telescope". In: *Astronomy & Astrophysics* 524 (2010), A75 (cited on page 31).

[60] Attila Abramowski et al. "Search for very-high-energy γ-ray emission from Galactic globular clusters with HESS". In: *Astronomy & Astrophysics* 551 (2013), A26 (cited on page 31).

[61] Fermi LAT Collaboration et al. "Fermi detection of a luminous γ-ray pulsar in a globular cluster". In: *Science* 334.6059 (2011), pages 1107–1110 (cited on page 31).

[62] JHK Wu et al. "Search for pulsed γ-ray emission from globular cluster M28". In: *The Astrophysical Journal Letters* 765.2 (2013), page L47 (cited on page 31).

[63] Andrea M Ghez et al. "High proper-motion stars in the vicinity of Sagittarius A*: Evidence for a supermassive black hole at the center of our galaxy". In: *The Astrophysical Journal* 509.2 (1998), page 678 (cited on page 32).

[64] Aous A Abdo et al. "Fermi/large area telescope bright gamma-ray source list". In: *The Astrophysical Journal Supplement Series* 183.1 (2009), page 46 (cited on page 32).

[65] Felix Aharonian et al. "Very high energy gamma rays from the direction of Sagittarius A". In: *Astronomy & astrophysics* 425.1 (2004), pages L13–L17 (cited on page 32).

[66] J Albert et al. "Observation of gamma rays from the galactic center with the MAGIC telescope". In: *The Astrophysical Journal* 638.2 (2006), page L101 (cited on page 32).

[67] Karl Kosack et al. "TeV gamma-ray observations of the galactic center". In: *The Astrophysical Journal* 608.2 (2004), page L97 (cited on page 32).

[68] F Aharonian et al. "Discovery of very-high-energy γ-rays from the Galactic Centre ridge". In: *Nature* 439.7077 (2006), pages 695–698 (cited on page 32).

[69] Kevork N Abazajian. "The consistency of Fermi-LAT observations of the galactic center with a millisecond pulsar population in the central stellar cluster". In: *Journal of Cosmology and Astroparticle Physics* 2011.03 (2011), page 010 (cited on page 32).

[70] Chris Gordon and Oscar Macias. "Dark matter and pulsar model constraints from Galactic Center Fermi-LAT gamma-ray observations". In: *Physical Review D* 88.8 (2013), page 083521 (cited on page 32).

[71] Kazunori Akiyama et al. "First Sagittarius A* Event Horizon Telescope results. I. The shadow of the supermassive black hole in the center of the Milky Way". In: *The Astrophysical Journal Letters* 930.2 (2022), page L12 (cited on page 32).

[72] Meng Su, Tracy R Slatyer, and Douglas P Finkbeiner. "Giant gamma-ray bubbles from Fermi-LAT: active galactic nucleus activity or bipolar galactic wind?" In: *The Astrophysical Journal* 724.2 (2010), page 1044 (cited on pages 32, 33).

[73] Gregory Dobler et al. “The Fermi haze: a gamma-ray counterpart to the microwave haze”. In: *The Astrophysical Journal* 717.2 (2010), page 825 (cited on page 32).

[74] Meng Su and Douglas P Finkbeiner. “Evidence for gamma-ray jets in the Milky Way”. In: *The Astrophysical Journal* 753.1 (2012), page 61 (cited on page 32).

[75] LHAASO Collaboration*† et al. “Peta–electron volt gamma-ray emission from the Crab Nebula”. In: *Science* 373.6553 (2021), pages 425–430 (cited on pages 33, 34).

[76] Zhen Cao et al. “Ultrahigh-energy photons up to 1.4 petaelectronvolts from 12 γ-ray Galactic sources”. In: *Nature* 594.7861 (2021), pages 33–36 (cited on page 33).

[77] C Megan Urry and Paolo Padovani. “Unified schemes for radio-loud active galactic nuclei”. In: *Publications of the Astronomical Society of the Pacific* 107.715 (1995), page 803 (cited on pages 34, 35).

[78] Grzegorz Madejski and Marek Sikora. “Gamma-ray observations of active galactic nuclei”. In: *Annual Review of Astronomy and Astrophysics* 54 (2016), pages 725–760 (cited on page 34).

[79] Charles Dennison Dermer and Berrie Giebels. “Active galactic nuclei at gamma-ray energies”. In: *Comptes Rendus Physique* 17.6 (2016), pages 594–616 (cited on page 34).

[80] Volker Beckmann and Chris Shrader. *Active galactic nuclei*. John Wiley & Sons, 2012 (cited on page 35).

[81] Adam Goldstein et al. “An ordinary short gamma-ray burst with extraordinary implications: Fermi-GBM detection of GRB 170817A”. In: *The Astrophysical Journal Letters* 848.2 (2017), page L14 (cited on page 36).

[82] “Teraelectronvolt emission from the γ-ray burst GRB 190114C”. In: *Nature* 575.7783 (2019), pages 455–458 (cited on page 36).

[83] Rosalba Perna, Davide Lazzati, and Matteo Cantiello. “Ultra-long Gamma-Ray Bursts from the Collapse of Blue Supergiant Stars: An End-to-end Simulation”. In: *The Astrophysical Journal* 859.1 (2018), page 48 (cited on page 36).

[84] Fabio Acero et al. “Detection of gamma rays from a starburst galaxy”. In: *Science* 326.5956 (2009), pages 1080–1082 (cited on page 36).

[85] “A connection between star formation activity and cosmic rays in the starburst galaxy M82”. In: *Nature* 462.7274 (2009), pages 770–772 (cited on page 36).

[86] AA Abdo et al. “Detection of gamma-ray emission from the starburst galaxies M82 and NGC 253 with the Large Area Telescope on Fermi”. In: *The Astrophysical journal letters* 709.2 (2010), page L152 (cited on page 36).

[87] Aous A Abdo et al. “Fermi large area telescope first source catalog”. In: *The Astrophysical Journal Supplement Series* 188.2 (2010), page 405 (cited on page 36).

[88] J-P Lenain et al. “Seyfert 2 galaxies in the GeV band: jets and starburst”. In: *Astronomy & Astrophysics* 524 (2010), A72 (cited on page 36).

[89] Shao-Qiang Xi et al. “Detection of gamma-ray emission from the Coma cluster with Fermi Large Area Telescope and tentative evidence for an extended spatial structure”. In: *Physical Review D* 98.6 (2018), page 063006 (cited on page 37).

[90] Vardan Baghmanyan et al. “Detailed study of extended γ-ray morphology in the vicinity of the Coma cluster with Fermi Large Area Telescope”. In: *Monthly Notices of the Royal Astronomical Society* 516.1 (2022), pages 562–571 (cited on page 37).

[91] P Sreekumar et al. “Observations of the Large Magellanic Cloud in high-energy gamma rays”. In: *The Astrophysical Journal* 400 (1992), pages L67–L70 (cited on page 37).

[92] AA Abdo et al. “Observations of the large magellanic cloud with Fermi”. In: *Astronomy & Astrophysics* 512 (2010), A7 (cited on page 37).

[93] Markus Ackermann et al. “Deep view of the Large Magellanic Cloud with six years of Fermi-LAT observations”. In: *Astronomy & Astrophysics* 586 (2016), A71 (cited on page 37).

[94] RHD Corbet et al. “A luminous gamma-ray binary in the large magellanic cloud”. In: *The Astrophysical Journal* 829.2 (2016), page 105 (cited on page 37).

[95] Nu Komin et al. “HESS observations of the Large Magellanic Cloud”. In: *arXiv preprint arXiv:1201.0639* (2012) (cited on page 37).

[96] HESS collaboration. “The exceptionally powerful TeV γ-ray emitters in the Large Magellanic Cloud”. In: *Science* 347.6220 (2015), pages 406–412 (cited on page 37).

[97] AA Abdo et al. “Detection of the Small Magellanic Cloud in gamma-rays with Fermi/LAT”. In: *Astronomy & Astrophysics* 523 (2010), A46 (cited on page 37).

[98] Aous A Abdo et al. “Fermi Large Area Telescope observations of Local Group galaxies: detection of M 31 and search for M 33”. In: *Astronomy & Astrophysics* 523 (2010), page L2 (cited on page 37).

[99] Markus Ackermann et al. “Observations of M31 and M33 with the fermi large area telescope: a galactic center excess in andromeda?” In: *The Astrophysical Journal* 836.2 (2017), page 208 (cited on pages 37, 38).

[100] URL: http://www.robgendlerastropics.com/M31-HST-Subaru-NOAO-RC.html (cited on page 38).

[101] V Schonfelder et al. “Instrument description and performance of the imaging gamma-ray telescope COMPTEL aboard the Compton Gamma-Ray Observatory”. In: *Astrophysical Journal Supplement Series* (1993) (cited on page 39).

[102] Christoph Winkler et al. “The INTEGRAL mission”. In: *Astronomy & Astrophysics* 411.1 (2003), pages L1–L6 (cited on page 39).

[103] Kevin Bennett. “COS-B: the highlights”. In: *Nuclear Physics B-Proceedings Supplements* 14.2 (1990), pages 23–34 (cited on page 40).

[104] DJ Thompson et al. “Calibration of the energetic gamma-ray experiment telescope (EGRET) for the Compton gamma-ray observatory”. In: *Astrophysical Journal Supplement Series (ISSN 0067-0049), vol. 86, no. 2, p. 629-656.* 86 (1993), pages 629–656 (cited on page 40).

[105] M Tavani et al. “The AGILE mission”. In: *Astronomy & Astrophysics* 502.3 (2009), pages 995–1013 (cited on page 40).

[106] WB Atwood et al. “The large area telescope on the Fermi gamma-ray space telescope mission”. In: *The Astrophysical Journal* 697.2 (2009), page 1071 (cited on page 40).

[107] Markus Ackermann et al. “The Fermi large area telescope on orbit: event classification, instrument response functions, and calibration”. In: *The Astrophysical Journal Supplement Series* 203.1 (2012), page 4 (cited on page 40).

[108] Peter F Michelson, William B Atwood, and Steven Ritz. “Fermi Gamma-ray Space Telescope: high-energy results from the first year”. In: *Reports on Progress in Physics* 73.7 (2010), page 074901 (cited on page 40).

[109] AA Moiseev et al. “Compton-pair production space telescope (ComPair) for MeV gamma-ray astronomy”. In: *arXiv preprint arXiv:1508.07349* (2015) (cited on page 40).

[110] F Lebrun et al. “The Gamma Cube: a novel concept of gamma-ray telescope”. In: *Space Telescopes and Instrumentation 2014: Ultraviolet to Gamma Ray*. Volume 9144. SPIE. 2014, pages 88–99 (cited on page 41).

[111] François Lebrun et al. “The Gamma Cube: a new way to explore the gamma-ray sky”. In: *10th INTEGRAL Workshop: A Synergistic View of the High-Energy Sky*. 2015 (cited on page 41).

[112] Juan Cortina and Carlos Delgado. “Detecting gamma rays with high resolution and moderate field of view: the air Cherenkov technique”. In: *arXiv preprint arXiv:2306.06415* (2023) (cited on page 41).

[113] A Borione et al. “A large air shower array to search for astrophysical sources emitting γ-rays with energies $\geq$ 1014 eV”. In: *Nuclear Instruments and Methods in Physics Research Section A: Accelerators, Spectrometers, Detectors and Associated Equipment* 346.1-2 (1994), pages 329–352 (cited on page 42).

[114] R Mirzoyan et al. “The first telescope of the HEGRA air Cherenkov imaging telescope array”. In: *Nuclear Instruments and Methods in Physics Research Section A: Accelerators, Spectrometers, Detectors and Associated Equipment* 351.2-3 (1994), pages 513–526 (cited on pages 42, 43).

[115] XA Huo et al. “Tibet-AS gamma Experiment”. In: *Proceedings of the 21st International Cosmic Ray Conference. Volume 2 (OG Sessions), p. 427*. Volume 2. 1990, page 427 (cited on page 42).

[116] G Di Sciascio, Lhaaso Collaboration, et al. “The LHAASO experiment: from gamma-ray astronomy to cosmic rays”. In: *Nuclear and particle physics proceedings* 279 (2016), pages 166–173 (cited on page 42).

[117] Milagro Collaboration et al. “Status of the Milagro Gamma Ray Observatory”. In: *arXiv preprint astro-ph/0110513* (2001) (cited on page 42).

[118] AU Abeysekara et al. “Daily monitoring of TeV gamma-ray emission from Mrk 421, Mrk 501, and the Crab Nebula with HAWC”. In: *The Astrophysical Journal* 841.2 (2017), page 100 (cited on page 42).

[119] Albrecht Karle et al. “Design and performance of the angle integrating Čerenkov array AIROBICC”. In: *Astroparticle Physics* 3.4 (1995), pages 321–347 (cited on page 42).

[120] URL: https://www.mpi-hd.mpg.de/hfm/HEGRA/scint_and_air.gif (cited on page 42).

[121] DA Lewis. "Optical characteristics of the Whipple Observatory TeV gamma-ray imaging telescope". In: *Experimental Astronomy* 1 (1990), pages 213–226 (cited on page 43).

[122] R_ Enomoto et al. "Design study of CANGAROO-III, stereoscopic imaging atmospheric Cherenkov telescopes for sub-TeV γ-ray detection". In: *Astroparticle Physics* 16.3 (2002), pages 235–244 (cited on page 43).

[123] James Anthony Hinton, Hess Collaboration, et al. "The status of the HESS project". In: *New Astronomy Reviews* 48.5-6 (2004), pages 331–337 (cited on pages 43, 45).

[124] J. Aleksić and al. "The major upgrade of the MAGIC telescopes, Part I: The hardware improvements and the commissioning of the system". In: *Astrop. Phys.* 72 (2016), page 61 (cited on pages 43–45).

[125] J. Aleksić and al. "The major upgrade of the MAGIC telescopes, Part II: A performance study using observations of the Crab Nebula". In: *Astrop. Phys.* 72 (2016), page 76 (cited on pages 43, 45).

[126] TC Weekes et al. "VERITAS: the very energetic radiation imaging telescope array system". In: *Astroparticle Physics* 17.2 (2002), pages 221–243 (cited on pages 43, 45).

[127] H Anderhub et al. "Design and operation of FACT–the first G-APD Cherenkov telescope". In: *Journal of Instrumentation* 8.06 (2013), P06008 (cited on page 43).

[128] CTA-LST Project et al. "Observations of the Crab Nebula and Pulsar with the Large-Sized Telescope Prototype of the Cherenkov Telescope Array". In: *arXiv preprint arXiv:2306.12960* (2023) (cited on pages 43, 45).

[129] URL: https://veritas.sao.arizona.edu/whipple (cited on page 43).

[130] Alexander Aab et al. "The pierre auger observatory upgrade-preliminary design report". In: *arXiv preprint arXiv:1604.03637* (2016) (cited on page 43).

[131] Xin-Hua Ma et al. "LHAASO Instruments and Detector technology". In: *Chinese Physics C* 46.3 (2022), page 030001 (cited on pages 43, 44).

[132] J. Aleksić et al. "The major upgrade of the MAGIC telescopes, Part II: A performance study using observations of the Crab Nebula". In: *Astroparticle Physics* 72 (Jan. 2016), pages 76–94. DOI: 10.1016/j.astropartphys.2015.02.005. arXiv: 1409.5594 [astro-ph.IM] (cited on pages 44, 95).

[133] URL: https://apod.nasa.gov/apod/ap200724.html (cited on page 45).

[134] F Di Pierro et al. "Performance of joint gamma-ray observations with MAGIC and LST-1 telescopes". In: (2023) (cited on page 45).

[135] J Hinton et al. "Precision measurement of optical pulsation using a Cherenkov telescope". In: *Astroparticle Physics* 26.1 (2006), pages 22–27 (cited on page 45).

[136] F Lucarelli et al. "The central pixel of the MAGIC telescope for optical observations". In: *Nuclear Instruments and Methods in Physics Research Section A: Accelerators, Spectrometers, Detectors and Associated Equipment* 589.3 (2008), pages 415–424 (cited on pages 45, 124).

[137] W Benbow et al. “Direct measurement of stellar angular diameters by the VERITAS Cherenkov telescopes”. In: *Nature astronomy* 3.6 (2019), pages 511–516 (cited on pages 45, 46, 125).

[138] Magic Collaboration et al. “Constraining very-high-energy and optical emission from FRB 121102 with the MAGIC telescopes”. In: *Monthly Notices of the Royal Astronomical Society* 481.2 (2018), pages 2479–2486 (cited on pages 45, 46, 114, 115, 127, 128, 131, 137, 139–143).

[139] AU Abeysekara et al. “A search for brief optical flashes associated with the SETI target KIC 8462852”. In: *The Astrophysical Journal Letters* 818.2 (2016), page L33 (cited on page 46).

[140] IceCube Collaboration et al. “Multimessenger observations of a flaring blazar coincident with high-energy neutrino IceCube-170922A”. In: *Science* 361.6398 (2018), eaat1378 (cited on page 46).

[141] Victor A Acciari et al. “Measurement of the extragalactic background light using MAGIC and Fermi-LAT gamma-ray observations of blazars up to z= 1”. In: *Monthly Notices of the Royal Astronomical Society* 486.3 (2019), pages 4233–4251 (cited on page 46).

[142] H Abdalla et al. “The HESS Galactic plane survey”. In: *Astronomy & Astrophysics* 612 (2018), A1 (cited on page 46).

[143] “Acceleration of petaelectronvolt protons in the Galactic Centre”. In: *Nature* 531.7595 (2016), pages 476–479 (cited on page 46).

[144] BS Acharya et al. “Introducing the CTA concept”. In: *Astroparticle physics* 43 (2013), pages 3–18 (cited on page 46).

[145] Cta Consortium et al. *Science with the Cherenkov Telescope Array*. World Scientific, 2018 (cited on page 46).

[146] A Acharyya et al. “Monte Carlo studies for the optimisation of the Cherenkov Telescope Array layout”. In: *Astroparticle Physics* 111 (2019), pages 35–53 (cited on page 46).

[147] Juan Cortina. “Status of the large size telescopes of the Cherenkov Telescope Array”. In: *arXiv preprint arXiv:1907.10146* (2019) (cited on page 46).

[148] Markus Garczarczyk et al. “Status of the medium-sized telescope for the cherenkov telescope array”. In: *arXiv preprint arXiv:1509.01361* (2015) (cited on page 46).

[149] Teresa Montaruli, Giovanni Pareschi, and Tim Greenshaw. “The small size telescope projects for the Cherenkov Telescope Array”. In: *arXiv preprint arXiv:1508.06472* (2015) (cited on page 46).

[150] T Hassan et al. “MAGIC sensitivity to millisecond-duration optical pulses”. In: *arXiv preprint arXiv:1708.07698* (2017) (cited on pages 46, 124–127).

[151] Vik Dhillon et al. “First light with HiPERCAM on the GTC”. In: *Ground-based and Airborne Instrumentation for Astronomy VII*. Volume 10702. SPIE. 2018, pages 157–167 (cited on page 46).

[152] MH Fizeau. "On the hypotheses relating to the luminous æther, and an experiment which appears to demonstrate that the motion of bodies alters the velociety with which light propagates itself in their interior". In: *The London, Edinburgh, and Dublin Philosophical Magazine and Journal of Science* 2.14 (1851), pages 568–573 (cited on page 48).

[153] M. Stéphan. "Sur l'extrême petitesse du diamètre apparent des étoiles fixes". In: *Comptes rendus hebdomadaires des séances de l'Académie des sciences* 78 (1874), pages 1008–1012 (cited on page 48).

[154] Albert A Michelson. "I. On the application of interference methods to astronomical measurements". In: *The London, Edinburgh, and Dublin Philosophical Magazine and Journal of Science* 30.182 (1890), pages 1–21 (cited on page 49).

[155] Albert A Michelson and Francis G Pease. "Measurement of the diameter of Alpha-Orionis by the interferometer". In: *Proceedings of the National Academy of Sciences* 7.5 (1921), pages 143–146 (cited on page 49).

[156] R. Hanbury-Brown and R. Q. Twiss. "A Test of a New Type of Stellar Interferometer on Sirius". In: *Nature* 178 (1956), page 1046 (cited on page 49).

[157] J. Davis R. Hanbury-Brown and L. R. Allen. "The Angular Diameters of 32 Stars". In: *MNRAS* 167-1 (1974), pages 121–136 (cited on pages 49, 63, 64, 88).

[158] R Hanbury Brown, J Davis, and LR Allen. "The Effects of Čerenkov Light Pulses on a Stellar Intensity Interferometer". In: *Monthly Notices of the Royal Astronomical Society* 146.4 (1969), pages 399–409 (cited on page 49).

[159] JE Grindlay et al. "First results of a Southern Hemisphere search for gamma ray sources at ET> 3x1011 eV". In: *Proceeding sof the 13th International Cosmic Ray Conference, Volume 1, 439.* Volume 1. 1973 (cited on page 49).

[160] JE Grindlay et al. "Evidence for the detection of gamma rays from Centaurus A at gamma-ray energies above 300 GeV". In: *Astrophysical Journal, vol. 197, Apr. 1, 1975, pt. 2, p. L9-L12. Research supported by the Smithsonian Institution, Australian Research Grants Committee, and University of Sidney* 197 (1975), pages L9–L12 (cited on page 49).

[161] Antoine Labeyrie, Stephen G Lipson, and Peter Nisenson. *An introduction to optical stellar interferometry*. Cambridge University Press, 2006 (cited on pages 50, 52).

[162] A Richard Thompson, James M Moran, and George W Swenson. *Interferometry and synthesis in radio astronomy*. Springer Nature, 2017 (cited on page 50).

[163] Hideya Gamo. "Triple correlator of photoelectric fluctuations as a spectroscopic tool". In: *Journal of Applied Physics* 34.4 (1963), pages 875–876 (cited on page 51).

[164] Dainis Dravins. "Intensity interferometry: optical imaging with kilometer baselines". In: *Optical and Infrared Interferometry and Imaging V*. Volume 9907. SPIE. 2016, pages 128–139 (cited on page 51).

[165] Carlos Delgado et al. "Intensity interferometry with the MAGIC telescopes". In: *37th International Cosmic Ray Conference (ICRC 2021)*. Volume 395. SISSA. 2021, page 693 (cited on pages 55, 76, 106).

[166] Juan Cortina et al. “First measurements and upgrade plans of the MAGIC intensity interferometer”. In: *Optical and Infrared Interferometry and Imaging VIII*. Volume 12183. SPIE. 2022, pages 127–141 (cited on pages 55, 106, 108).

[167] VA Acciari et al. “Optical intensity interferometry observations using the MAGIC Imaging Atmospheric Cherenkov Telescopes”. In: *Monthly Notices of the Royal Astronomical Society* 491.2 (2020), pages 1540–1547 (cited on pages 55, 65, 106, 107).

[168] Juan Cortina et al. “First measurements and upgrade plans of the MAGIC intensity interferometer”. In: *Optical and Infrared Interferometry and Imaging VIII*. Edited by Antoine Mérand, Stephanie Sallum, and Joel Sanchez-Bermudez. Volume 12183. Society of Photo-Optical Instrumentation Engineers (SPIE) Conference Series. Aug. 2022, 121830C, page 121830C. DOI: 10.1117/12.2629876. arXiv: 2209.14844 [astro-ph.IM] (cited on page 56).

[169] Samuel J Swihart et al. “A Catalog of Calibrator Stars for Next-generation Optical Interferometers”. In: *The Astronomical Journal* 153.1 (2016), page 16 (cited on pages 61, 102).

[170] L Bourges et al. “VizieR Online Data Catalog: JMMC Stellar Diameters Catalogue-JSDC. Version 2 (Bourges+, 2017)”. In: *VizieR Online Data Catalog* (2017), pages II–346 (cited on pages 61, 102).

[171] Daniel Bonneau et al. “SearchCal: a virtual observatory tool for searching calibrators in optical long baseline interferometry-I. The bright object case”. In: *Astronomy & Astrophysics* 456.2 (2006), pages 789–789 (cited on pages 61, 102).

[172] D Bonneau et al. “SearchCal: a Virtual Observatory tool for searching calibrators in optical long-baseline interferometry-II. The faint-object case”. In: *Astronomy & Astrophysics* 535 (2011), A53 (cited on pages 61, 102).

[173] X Delfosse and D Bonneau. “Determination of stellar diameter from photometry in the JMMC Evolutive Search Calibrator”. In: *SF2A-2004: Semaine de l’Astrophysique Francaise* (2004), page 181 (cited on page 61).

[174] J Diaz-Cordoves, A Claret, and A Gimenez. “Linear and non-linear limb-darkening coefficients for LTE model atmospheres.” In: *Astronomy and Astrophysics Supplement, v. 110, p. 329* 110 (1995), page 329 (cited on page 61).

[175] A Claret, J Diaz-Cordoves, and A Gimenez. “Linear and non-linear limb-darkening coefficients for the photometric bands RIJH K.” In: *Astronomy and Astrophysics Supplement, v. 114, p. 247* 114 (1995), page 247 (cited on page 61).

[176] Alain Chelli et al. “Pseudomagnitudes and differential surface brightness: Application to the apparent diameter of stars”. In: *Astronomy & Astrophysics* 589 (2016), A112 (cited on page 62).

[177] Marc Wenger et al. “The SIMBAD astronomical database-The CDS reference database for astronomical objects”. In: *Astronomy and Astrophysics Supplement Series* 143.1 (2000), pages 9–22 (cited on pages 63, 88).

[178] A. U. Abeysekara and al. “Demonstration of stellar intensity interferometry with the four VERITAS telescopes”. In: *Nature Astronomy* 4 (2020), pages 1164–1169 (cited on pages 63, 88).

[179] OF Hamamatsu NIR. "PHOTOMULTIPLIER TUBES, Basics and Applications, Third Edition". In: () (cited on page 81).

[180] J. Aleksić et al. "Performance of the MAGIC stereo system obtained with Crab Nebula data". In: *Astroparticle Physics* 35.7 (Feb. 2012), pages 435–448. DOI: 10.1016/j.astropartphys.2011.11.007. arXiv: 1108.1477 [astro-ph.IM] (cited on page 95).

[181] R. Hanbury-Brown. *The Intensity Interferometer: Its Application to Astronomy*. London: Taylor & Francis, 1974 (cited on page 95).

[182] Gerard T van Belle. "Interferometric observations of rapidly rotating stars". In: *The Astronomy and Astrophysics Review* 20 (2012), pages 1–49 (cited on pages 103, 104, 106).

[183] Kathryn D Gordon et al. "Angular sizes, radii, and effective temperatures of b-type stars from optical interferometry with the chara array". In: *The Astrophysical Journal* 873.1 (2019), page 91 (cited on pages 103, 105).

[184] AB Underhill et al. "Effective temperatures, angular diameters, distances and linear radii for 160 O and B stars". In: *Monthly Notices of the Royal Astronomical Society* 189.3 (1979), pages 601–605 (cited on pages 103–105).

[185] S Soderhjelm. "Geometry and dynamics of the Algol system". In: *Astronomy and Astrophysics, vol. 89, no. 1-2, Sept. 1980, p. 100-112.* 89 (1980), pages 100–112 (cited on page 103).

[186] F Baron et al. "Imaging the algol triple system in the H band with the CHARA interferometer". In: *The Astrophysical Journal* 752.1 (2012), page 20 (cited on page 103).

[187] Eduardo Janot-Pacheco et al. "Multi-periodicity of the Be star η Centauri from spectroscopic and photometric observations". In: *Astronomy and Astrophysics Supplement Series* 137.3 (1999), pages 407–418 (cited on page 104).

[188] CAL Bailer-Jones et al. "Estimating distances from parallaxes. V. Geometric and photogeometric distances to 1.47 billion stars in Gaia Early Data Release 3". In: *The Astronomical Journal* 161.3 (2021), page 147 (cited on page 104).

[189] Feb ESA. *The Hipparcos and Tycho Catalogues*. 1997 (cited on page 104).

[190] Carolin Waltraud Wunderlich et al. "Fast photodetectors and their role in measuring star diameters with the MAGIC intensity interferometer". In: (2023) (cited on page 104).

[191] Przemysław Walczak and Jadwiga Daszyńska-Daszkiewicz. "Complex asteroseismology of the hybrid B-type pulsator γ Pegasi: A test of stellar opacities". In: *Astronomische Nachrichten* 331.9-10 (2010), pages 1057–1060 (cited on page 104).

[192] A Baglin et al. "Delta Scuti stars." In: *Astronomy and Astrophysics, Vol. 23, p. 221-240* 23 (1973), pages 221–240 (cited on page 104).

[193] X Che et al. "Colder and hotter: interferometric imaging of β Cassiopeiae and α Leonis". In: *The Astrophysical Journal* 732.2 (2011), page 68 (cited on page 104).

[194] G Guiglion et al. "Understanding the dynamical structure of pulsating stars: The Baade-Wesselink projection factor of the δ Scuti stars AI Velorum and β Cassiopeiae". In: *Astronomy & Astrophysics* 550 (2013), page L10 (cited on page 104).

[195] DJ Hutter et al. “Surveying the Bright Stars by Optical Interferometry. I. A Search for Multiplicity among Stars of Spectral Types FK”. In: *The Astrophysical Journal Supplement Series* 227.1 (2016), page 4 (cited on page 104).

[196] Tyler E Nordgren et al. “Stellar angular diameters of late-type giants and supergiants measured with the Navy Prototype Optical Interferometer”. In: *The Astronomical Journal* 118.6 (1999), page 3032 (cited on page 104).

[197] James B Kaler. *The hundred greatest stars*. Springer, 2002 (cited on page 104).

[198] BV Kukarkin et al. “The third edition containing information on 20437 variable stars discovered and designated till 1968.” In: *General Catalogue of Variable Stars* (1971), page 0 (cited on page 104).

[199] May G Pedersen et al. “Diverse Variability of O and B Stars Revealed from 2-minute Cadence Light Curves in Sectors 1 and 2 of the TESS Mission: Selection of an Asteroseismic Sample”. In: *The Astrophysical journal letters* 872.1 (2019), page L9 (cited on page 105).

[200] Floor Van Leeuwen. “Validation of the new Hipparcos reduction”. In: *Astronomy & Astrophysics* 474.2 (2007), pages 653–664 (cited on page 105).

[201] Janet Rountree Lesh. “The kinematics of the Gould Belt: an expanding group?” In: *Astrophysical Journal Supplement, vol. 17, p. 371 (1968)* 17 (1968), page 371 (cited on page 105).

[202] M Challouf et al. “Measurements of eight early-type stars angular diameters using VEGA/CHARA interferometer”. In: *SF2A-2014: Proceedings of the Annual meeting of the French Society of Astronomy and Astrophysics*. 2014, pages 471–474 (cited on page 105).

[203] WILLIAM P Bidelman. “A list of early-type shell stars”. In: *Be and Shell Stars* 70 (1976), pages 457–465 (cited on page 105).

[204] A Andrillat, M Jaschek, and C Jaschek. “A survey of Be stars in the infrared. II-Determination of envelope dimensions”. In: *Astronomy and Astrophysics Supplement Series (ISSN 0365-0138), vol. 84, no. 1, July 1990, p. 11-28.* 84 (1990), pages 11–28 (cited on page 105).

[205] Luis A Balona and Dogus Ozuyar. “Pulsation among TESS A and B stars and the Maia variables”. In: *Monthly Notices of the Royal Astronomical Society* 493.4 (2020), pages 5871–5879 (cited on page 105).

[206] NN Samus’ et al. “General catalogue of variable stars: Version GCVS 5.1”. In: *Astronomy Reports* 61 (2017), pages 80–88 (cited on page 105).

[207] Duncan R Lorimer et al. “A bright millisecond radio burst of extragalactic origin”. In: *Science* 318.5851 (2007), pages 777–780 (cited on pages 110, 111).

[208] LG Spitler et al. “Fast radio burst discovered in the Arecibo pulsar ALFA survey”. In: *The Astrophysical Journal* 790.2 (2014), page 101 (cited on pages 110, 114).

[209] BC Andersen et al. “CHIME/FRB discovery of eight new repeating fast radio burst sources”. In: *The Astrophysical Journal Letters* 885.1 (2019), page L24 (cited on pages 110, 134, 135).

[210] KM Rajwade et al. "Possible periodic activity in the repeating FRB 121102". In: *Monthly Notices of the Royal Astronomical Society* 495.4 (2020), pages 3551–3558 (cited on pages 110, 114).

[211] "Periodic activity from a fast radio burst source". In: *Nature* 582.7812 (2020), pages 351–355 (cited on pages 110, 134).

[212] BC Andersen et al. "A bright millisecond-duration radio burst from a Galactic magnetar". In: *arXiv preprint arXiv:2005.10324* (2020) (cited on pages 110, 129).

[213] Shotaro Yamasaki, Tomonori Totani, and Kenta Kiuchi. "Repeating and non-repeating fast radio bursts from binary neutron star mergers". In: *Publications of the Astronomical Society of Japan* 70.3 (2018), page 39 (cited on page 110).

[214] Jedrzej A Jawor and Thomas M Tauris. "Modelling spin evolution of magnetars". In: *Monthly Notices of the Royal Astronomical Society* 509.1 (2022), pages 634–657 (cited on page 111).

[215] Sandro Mereghetti. "The strongest cosmic magnets: soft gamma-ray repeaters and anomalous X-ray pulsars". In: *The Astronomy and Astrophysics Review* 15.4 (2008), pages 225–287 (cited on page 111).

[216] Jian Li et al. "Gamma-ray upper limits on magnetars with six years of Fermi-LAT observations". In: *The Astrophysical Journal* 835.1 (2017), page 30 (cited on pages 111, 131).

[217] Jelena Aleksić et al. "Observations of the magnetars 4U 0142+ 61 and 1E 2259+ 586 with the MAGIC telescopes". In: *Astronomy & Astrophysics* 549 (2013), A23 (cited on page 111).

[218] Daniele Viganò, Diego F Torres, and Jonatan Martín. "A systematic synchro-curvature modelling of pulsar γ-ray spectra unveils hidden trends". In: *Monthly Notices of the Royal Astronomical Society* 453.3 (2015), pages 2599–2621 (cited on page 111).

[219] C Elenbaas et al. "Magnetar giant flare high-energy emission". In: *Monthly Notices of the Royal Astronomical Society* 471.2 (2017), pages 1856–1872 (cited on page 112).

[220] "High-energy emission from a magnetar giant flare in the Sculptor galaxy". In: *Nature Astronomy* 5.4 (2021), pages 385–391 (cited on pages 112, 130).

[221] Steven E Boggs et al. "The giant flare of 2004 December 27 from SGR 1806–20". In: *The Astrophysical Journal* 661.1 (2007), page 458 (cited on page 112).

[222] Valentina Fioretti et al. "The Cherenkov Telescope Array sensitivity to the transient sky". In: *arXiv preprint arXiv:1907.08018* (2019) (cited on page 113).

[223] Yuan-Pei Yang, Bing Zhang, and Jian-Yan Wei. "How bright are fast optical bursts associated with fast radio bursts?" In: *The Astrophysical Journal* 878.2 (2019), page 89 (cited on pages 113, 125, 130, 142).

[224] Alexander Stefanescu et al. "Very fast optical flaring from a possible new Galactic magnetar". In: *AIP Conference Proceedings*. Volume 1133. 1. American Institute of Physics. 2009, pages 491–496 (cited on pages 113, 114).

[225] B Marcote et al. "The repeating fast radio burst FRB 121102 as seen on milliarcsecond angular scales". In: *The Astrophysical Journal Letters* 834.2 (2017), page L8 (cited on page 114).

[226] S Chatterjee et al. "A direct localization of a fast radio burst and its host". In: *Nature* 541.7635 (2017), pages 58–61 (cited on page 114).

[227] CG Bassa et al. "FRB 121102 is coincident with a star-forming region in its host galaxy". In: *The Astrophysical Journal Letters* 843.1 (2017), page L8 (cited on page 114).

[228] Shriharsh P Tendulkar et al. "The host galaxy and redshift of the repeating fast radio burst FRB 121102". In: *The Astrophysical Journal Letters* 834.2 (2017), page L7 (cited on page 114).

[229] Paul Scholz et al. "A Repeating Fast Radio Burst: Radio and X-ray Follow-up Observations of FRB 121102". In: *AAS/High Energy Astrophysics Division# 15* 15 (2016), pages 105–03 (cited on pages 114, 115).

[230] T Bretz, R Wagner, MAGIC collaboration, et al. "The MAGIC analysis and reconstruction software". In: *Proceedings of the 28th International Cosmic Ray Conference. July 31-August 7, 2003. Tsukuba, Japan. Under the auspices of the International Union of Pure and Applied Physics (IUPAP). Editors: T. Kajita, Y. Asaoka, A. Kawachi, Y. Matsubara and M. Sasaki, p. 2947*. Volume 5. 2003, page 2947 (cited on page 116).

[231] Jürgen Albert et al. "VHE γ-Ray Observation of the Crab Nebula and its Pulsar with the MAGIC Telescope". In: *The Astrophysical Journal* 674.2 (2008), page 1037 (cited on pages 116, 118, 125).

[232] Rene Brun and Fons Rademakers. "ROOT—An object oriented data analysis framework". In: *Nuclear instruments and methods in physics research section A: accelerators, spectrometers, detectors and associated equipment* 389.1-2 (1997), pages 81–86 (cited on page 116).

[233] D Nieto. "Dark matter constrains from high energy astrophysical observations". PhD thesis. PhD thesis. Universidad Complutense de Madrid, Spain, 2012 (cited on page 116).

[234] Mireia Nievas Rosillo. "Observaciones de la emisión en muy altas energías de blazars a distancias; Observaciones de la emisión en muy altas energías de blazars a distancias; Observations of the very high energy emission from blazars at cosmological distances". In: *Ph. D. Thesis* (2018) (cited on pages 116, 123).

[235] R Mirzoyan. "On the calibration accuracy of light sensors in atmospheric Cherenkov fluorescence and neutrino experiments". In: *International Cosmic Ray Conference*. Volume 7. 1997, page 265 (cited on page 117).

[236] A Michael Hillas. "Cerenkov light images of EAS produced by primary gamma". In: *19th Intern. Cosmic Ray Conf-Vol. 3*. OG-9.5-3. 1985 (cited on page 117).

[237] Mathieu de Naurois and Daniel Mazin. "Ground-based detectors in very-high-energy gamma-ray astronomy". In: *Comptes Rendus Physique* 16.6-7 (2015), pages 610–627 (cited on page 118).

[238] M Gaug et al. “Atmospheric Monitoring for the MAGIC Telescopes”. In: *arXiv preprint arXiv:1403.5083* (2014) (cited on page 120).

[239] Christian Fruck et al. “A novel LIDAR-based atmospheric calibration method for improving the data analysis of MAGIC”. In: *arXiv preprint arXiv:1403.3591* (2014) (cited on page 120).

[240] T-P Li and Y-Q Ma. “Analysis methods for results in gamma-ray astronomy”. In: *Astrophysical Journal, Part 1 (ISSN 0004-637X), vol. 272, Sept. 1, 1983, p. 317-324.* 272 (1983), pages 317–324 (cited on pages 122, 123).

[241] Filippo Ambrosino et al. “Optical pulsations from a transitional millisecond pulsar”. In: *Nature Astronomy* 1.12 (2017), pages 854–858 (cited on page 125).

[242] H Bradt et al. “X-ray and optical observations of the pulsar NP 0532 in the Crab nebula”. In: *Nature* 222.5195 (1969), pages 728–730 (cited on page 125).

[243] AA Abdo et al. “A population of gamma-ray millisecond pulsars seen with the Fermi Large Area Telescope”. In: *Science* 325.5942 (2009), pages 848–852 (cited on page 125).

[244] T Hassan and M Daniel. “Proving the outstanding capabilities of Imaging Atmospheric Cherenkov Telescopes in high time resolution optical astronomy”. In: *36th International Cosmic Ray Conference (ICRC2019)*. Volume 36. 2019, page 692 (cited on page 125).

[245] F Spada et al. “The radius discrepancy in low-mass stars: single versus binaries”. In: *The Astrophysical Journal* 776.2 (2013), page 87 (cited on page 125).

[246] Megumi Shidatsu et al. “X-ray and optical monitoring of state transitions in MAXI J1820+ 070”. In: *The Astrophysical Journal* 874.2 (2019), page 183 (cited on page 125).

[247] Dimitrios Psaltis, Tomaso Belloni, and Michiel van der Klis. “Correlations in quasi-periodic oscillation and noise frequencies among neutron star and black hole x-ray binaries”. In: *The Astrophysical Journal* 520.1 (1999), page 262 (cited on page 125).

[248] Ph Uttley. “The relationship between optical and x-ray variability in Seyfert Galaxies”. In: *AGN Variability from X-rays to Radio Waves*. Volume 360. 2006, page 101 (cited on page 125).

[249] AF Cook et al. “Flux of optical meteors down to M pg=+ 12”. In: *Monthly Notices of the Royal Astronomical Society* 193.3 (1980), pages 645–666 (cited on page 126).

[250] MD Campbell-Brown. “Solar cycle variation in radar meteor rates”. In: *Monthly Notices of the Royal Astronomical Society* 485.3 (2019), pages 4446–4453 (cited on page 126).

[251] MAGIC COLLABORATION. et al. “The timing system of the MAGIC telescope”. In: *International Journal of Modern Physics A* 20.29 (2005), pages 7012–7015 (cited on page 126).

[252] C Germanà et al. “Aqueye optical observations of the Crab Nebula pulsar”. In: *Astronomy & Astrophysics* 548 (2012), A47 (cited on pages 126, 127).

[253] AG Lyne, RS Pritchard, and F Graham Smith. “23 years of Crab pulsar rotational history”. In: *Monthly Notices of the Royal Astronomical Society* 265.4 (1993), pages 1003–1012 (cited on page 126).

[254] M Stamatikos et al. “GRB 140705A: Swift detection of a short burst.” In: *GRB Coordinates Network* 16520 (2014), page 1 (cited on page 129).

[255] Gian Luca Israel et al. “The discovery, monitoring and environment of SGR J1935+ 2154”. In: *Monthly Notices of the Royal Astronomical Society* 457.4 (2016), pages 3448–3456 (cited on page 129).

[256] S Mereghetti et al. “INTEGRAL discovery of a burst with associated radio emission from the magnetar SGR 1935+ 2154”. In: *The Astrophysical Journal Letters* 898.2 (2020), page L29 (cited on page 129).

[257] Ping Zhou et al. “Revisiting the distance, environment, and supernova properties of snr g57. 2+ 0.8 that hosts sgr 1935+ 2154”. In: *The Astrophysical Journal* 905.2 (2020), page 99 (cited on page 129).

[258] M Bailes et al. “Multifrequency observations of SGR J1935+ 2154”. In: *Monthly Notices of the Royal Astronomical Society* 503.4 (2021), pages 5367–5384 (cited on page 130).

[259] JWT Hessels et al. “Monitoring the magnetar SGR 1935+ 2154 with the MAGIC telescopes”. In: (2021) (cited on page 130).

[260] Weiwei Zhu et al. “FAST detection of radio bursts and pulsed emission from SGR J1935+ 2154”. In: *The Astronomer’s Telegram* 14084 (2020), page 1 (cited on page 130).

[261] Wolfgang A Rolke, Angel M López, and Jan Conrad. “Limits and confidence intervals in the presence of nuisance parameters”. In: *Nuclear Instruments and Methods in Physics Research Section A: Accelerators, Spectrometers, Detectors and Associated Equipment* 551.2-3 (2005), pages 493–503 (cited on pages 131, 134).

[262] H Abdalla et al. “Searching for TeV gamma-ray emission from SGR 1935+ 2154 during its 2020 X-ray and radio bursting phase”. In: *The Astrophysical Journal* 919.2 (2021), page 106 (cited on pages 132, 142).

[263] M Bhardwaj et al. “A nearby repeating fast radio burst in the direction of M81”. In: *The Astrophysical Journal Letters* 910.2 (2021), page L18 (cited on page 132).

[264] F Kirsten et al. “A repeating fast radio burst source in a globular cluster”. In: *Nature* 602.7898 (2022), pages 585–589 (cited on pages 132, 133, 143).

[265] Piet Hut et al. “Binaries in globular clusters”. In: *Publications of the Astronomical Society of the Pacific* 104.681 (1992), page 981 (cited on page 132).

[266] David Pooley et al. “Dynamical formation of close binary systems in globular clusters”. In: *The Astrophysical Journal* 591.2 (2003), page L131 (cited on page 132).

[267] Frank Verbunt. “Binary evolution and neutron stars in globular clusters”. In: *Arxiv preprint astro-ph/0210057* (2002) (cited on page 132).

[268] Fabrice Mottez and Philippe Zarka. “Radio emissions from pulsar companions: a refutable explanation for galactic transients and fast radio bursts”. In: *Astronomy & Astrophysics* 569 (2014), A86 (cited on page 132).

[269] Fabrice Mottez, Philippe Zarka, and Guillaume Voisin. "Repeating fast radio bursts caused by small bodies orbiting a pulsar or a magnetar". In: *Astronomy & Astrophysics* 644 (2020), A145 (cited on page 132).

[270] Iminhaji Ablimit and Xiang-Dong Li. "Formation of binary millisecond pulsars by accretion-induced collapse of white dwarfs under wind-driven evolution". In: *The Astrophysical Journal* 800.2 (2015), page 98 (cited on page 132).

[271] S Ye Claire et al. "Millisecond pulsars and black holes in globular clusters". In: *The Astrophysical Journal* 877.2 (2019), page 122 (cited on page 132).

[272] Navin Sridhar et al. "Periodic fast radio bursts from luminous X-ray binaries". In: *The Astrophysical Journal* 917.1 (2021), page 13 (cited on page 132).

[273] Benito Marcote et al. "A repeating fast radio burst source localized to a nearby spiral galaxy". In: *Nature* 577.7789 (2020), pages 190–194 (cited on pages 135, 136, 143).

[274] Ben Margalit and Brian D Metzger. "A concordance picture of FRB 121102 as a flaring magnetar embedded in a magnetized ion–electron wind nebula". In: *The Astrophysical Journal Letters* 868.1 (2018), page L4 (cited on page 135).

[275] Brian D Metzger, Ben Margalit, and Lorenzo Sironi. "Fast radio bursts as synchrotron maser emission from decelerating relativistic blast waves". In: *Monthly Notices of the Royal Astronomical Society* 485.3 (2019), pages 4091–4106 (cited on page 135).

[276] Yu. Lyubarsky. "A model for fast extragalactic radio bursts." In: 442 (July 2014), pages L9–L13. DOI: 10.1093/mnrasl/slu046. arXiv: 1401.6674 [astro-ph.HE] (cited on page 135).

[277] Andrei M. Beloborodov. "A Flaring Magnetar in FRB 121102?" In: *The Astrophysical Journal Letters* 843.2 (July 2017), page L26. DOI: 10.3847/2041-8213/aa78f3. URL: https://dx.doi.org/10.3847/2041-8213/aa78f3 (cited on page 135).

[278] D Michilli et al. "An extreme magneto-ionic environment associated with the fast radio burst source FRB 121102". In: *Nature* 553.7687 (2018), pages 182–185 (cited on page 135).

[279] Bing Zhang. "A "Cosmic Comb" Model of Fast Radio Bursts". In: *The Astrophysical Journal Letters* 836.2 (Feb. 2017), page L32. DOI: 10.3847/2041-8213/aa5ded. URL: https://dx.doi.org/10.3847/2041-8213/aa5ded (cited on page 135).

[280] Bing Zhang. "FRB 121102: A Repeatedly Combed Neutron Star by a Nearby Low-luminosity Accreting Supermassive Black Hole". In: *The Astrophysical Journal Letters* 854.2 (Feb. 2018), page L21. DOI: 10.3847/2041-8213/aaadba. URL: https://dx.doi.org/10.3847/2041-8213/aaadba (cited on page 135).

[281] M.L. Ahnen et al. "Performance of the MAGIC telescopes under moonlight". In: *Astroparticle Physics* 94 (Sept. 2017), pages 29–41. DOI: 10.1016/j.astropartphys.2017.08.001. URL: https://doi.org/10.1016%2Fj.astropartphys.2017.08.001 (cited on page 137).

[282] I Jiménez Martínez et al. “Update on the performance of the MAGIC Intensity Interferometer”. In: (2023) (cited on pages 145, 148).

[283] I Jiménez Martínez. “Constraining VHE and optical emission from Fast Radio Bursts with the MAGIC telescopes”. In: *Highlights of Spanish Astrophysics XI* (2023), page 141 (cited on pages 146, 149).

Magnetar illustration for the Fast Radio Bursts chapter is by Maciej Rebisz and picture of the MAGIC telescopes for the Main conclusions is by Robert Wagner, Max Planck Institute for Physics, Munich.

List of Acronyms

ADC Analog-to-Digital Converter. 96
AGN Active Galactic Nuclei. 16, 22, 23, 26, 32, 34, 35, 135, 192
AIROBICC AIrshower Observation By Angle Integrating Cherenkov Counters. 42, 43, 192
AMC Active Mirror Control. 8, 47, 55–60, 77, 97
AOI Angle Of Incidence. 97, 196

BH Black Hole. 34

CCD Charge-coupled Device. 120
CL Confidence Level. 131, 134, 139, 140
CMB Cosmic Microwave Background. 18, 22, 31, 37
CPIX Central Pixel. 12, 115, 124–127, 130, 135, 136, 140, 197
CPS Central Pixel System. 124
CR Cosmic Ray. 17, 18, 28, 32, 41, 117
CTA Cherenkov Telescope Array. 43, 45
CUDA Compute Unified Device Architecture. 56

DC Direct Current. 57, 75–82, 96–98, 194
DM Dispersion Measurement. 129
DT Discriminator Threshold. 117

EAS Extense Atmospheric Shower. 23, 39, 41, 42, 55, 57
EBL Extragalactic Background Light. 24
EHT Event Horizon Telescope. 32, 192

FACT First G-APD Cherenkov Telescope. 43
FBs Fermi Bubbles. 33, 192
FFT Fast Fourier Transform. 56
FOB Fast Optical Burst. 125
FOV Field Of View. 39, 69, 98
FRB Fast Radio Burst. 9, 11, 12, 14, 109, 110, 114, 115, 125, 127, 129, 130, 132–134, 136, 139, 197

FSRQ Flat Spectrum Radio Quasars. 34

GBM Gamma-ray Burst Monitor. 40, 192
GPU Graphic Processing Unit. 56, 75, 96
GRB Gamma Ray Burst. 16, 21, 35, 36, 40, 192

HDD Hard Disk Drive. 56
HE High Energy. 28–32, 34, 36, 37, 41, 111, 112, 125, 130
HEGRA High Energy Gamma Ray Astronomy. 42, 43, 192
HESS High Energy Stereoscopic System. 30, 31, 37, 43, 45, 49
HV High Voltage. 80, 81, 97, 194

IACT Imaging Atmospheric Cherenkov Telescope. 16, 29, 43–45, 49, 55, 95, 112, 117, 125
IC Inverse Compton. 29, 37, 125, 142
ISM Interstellar Medium. 27

LE Low Energy. 41
LHASSO Large High Altitude Air Shower Observatory. 43, 44, 192
LMC Large Magellanic Cloud. 37
LST Large-Sized Telescope. 31, 43, 45
LUT Look-Up Tables. 97

MAGIC Major Atmospheric Gamma Imaging Cherenkov Telescope. 8, 30, 31, 43, 45, 47, 49, 53, 55–61, 76, 80, 83, 85, 97, 98, 114, 115, 117, 120, 124, 126, 135, 193, 195, 197
MSPs Millisecond Pulsars. 31, 32
MWL Multi-wavelength. 135

NSB Night-Sky Background. 76, 98, 117, 120, 137

PMT Photomultiplier Tube. 42, 43, 55, 56, 63, 65, 75, 80, 81, 83, 96, 97, 117
PWNe Pulsar Wind Nebulae. 28

QE Quantum Efficiency. 97
QSO Quasi-Stellar Objects. 35

RF Random Forest. 130
RM Rotation Measure. 135

S/N Signal-to-Noise. 65
SFR Star Formation Ratio. 36, 37
SGR Soft Gamma Repeater. 9, 109, 110, 113, 114, 129–131, 197
SiPM Silicon Photomultiplier. 43
SMC Small Magellanic Cloud. 37
SNR Super Nova Remnants. 23, 25, 27, 28, 30, 32, 125, 129, 130, 197
SSD Solid-Dtate Drive. 56

TOA Time Of Arrival. 115, 127, 136, 197

UD Uniform Disk. 64, 87

uGMRT upgraded Giant Metrewave Radio Telescope. 135, 136, 145, 148
UHE Ultra High Energy. 18, 33, 41, 42
UL Upper Limit. 114, 131, 134, 139, 140

VCSels Vertical-Cavity Surface-Emitting Lasers. 96
VERITAS Very Energetic Radiation Imaging Telescope Array System. 43, 45, 49, 63, 88, 199
VHE Very High Energy. 24, 25, 30–32, 34, 36, 37, 41–43, 45, 55, 57, 61, 71, 75, 80, 111, 112, 114–117, 119, 125, 130, 136, 139, 140, 192, 200

ZBC Zero Baseline Correlation. 9, 51, 52, 59, 76, 87–89, 93–96, 195, 196

List of Figures

List of Tables